Development of low-noise visible near-infrared fiber-based supercontinuum source

Etienne Genier

To cite this version:

Etienne Genier. Development of low-noise visible near-infrared fiber-based supercontinuum source. Optics / Photonic. Université Bourgogne Franche-Comté, 2020. English. NNT : 2020UBFCD049 . tel-03369754

HAL Id: tel-03369754
https://theses.hal.science/tel-03369754

Submitted on 7 Oct 2021

THÈSE DE DOCTORAT

DE L'ÉTABLISSEMENT UNIVERSITÉ BOURGOGNE FRANCHE-COMTÉ

PRÉPARÉ À L'UNIVERSITÉ DE FRANCHE-COMTÉ

École doctorale n° 37

Sciences Pour l'Ingénieur et Microtechnique

Doctorat d'Optique et Photonique

par

ETIENNE GENIER

Development of a low-noise visible near-infrared fiber-based supercontinuum source

Développement de sources supercontinuum fibrées visible proche-infrarouge pour applications en tomographie optique cohérente

Thèse présentée et sountenue à Besançon, le 26 Novembre 2020

Composition du Jury:

MUSSOT ARNAUD	Professeur, Laboratoire PhLAM, Université de Lille, Lille	Rapporteur
HEIDT ALEXANDER	Associate Professor, Institute of Applied Physics, University of Bern, Bern	Rapporteur
JACQUOT MAXIME	Professeur, Institut FEMTO-ST, Université de Franche-Comté, Besançon	Examinateur
BANG OLE	Professor, DTU Fotonik, Technical University of Denmark, Lyngby	Examinateur
KLIMCZAK MARIUSZ	Assistant Professor, Faculty of Physics, University of Warsaw, Warsaw	Examinateur
BOWEN PATRICK	Ph.D, NKT Photonics, Birkerød	Invité
DUDLEY JOHN	Professeur, Institut FEMTO-ST, Université de Franche-Comté, Besançon	Codirecteur de thèse
SYLVESTRE THIBAUT	Directeur de Recherche CNRS, Institut FEMTO-ST, Besançon	Directeur de thèse

ACKNOWLEDGEMENTS

This thesis would not have existed without the support of the funding program of the European Union H2020 Innovative Training Network SUPUVIR (SUPercontinuum broadband light sources covering UV to IR applications). This thesis mainly took place at NKT Photonics A/S, Birkerød, DTU Fotonik, Lyngby, and also at FEMTO-ST Institute, Besançon.

First of all, I thank my whole team of supervisors: Dr. Patrick Bowen, Dr. Thibaut Sylvestre, Prof. Ole Bang, Dr. Peter Moselund, and Prof. John Dudley, all of you provide me so much both on the professional and personal aspects. Thibaut, you support me so much since my master degree, without your help I would never be what I am today. Peter, you gave me the opportunity to be involved in this amazing project and helped me when I struggled with the beautiful danish language. Patrick, you were always there to encourage, assist, and push me during these three years in the good and bad phases, I could never dream about a better mentor. Ole, thank you for trying me so hard, I discovered my limits were far away from what I initially thought. John, despite the distance you were always available for me, thank you for keeping an eye on me.

Also, I express my gratitude to Prof. Arnaud Mussot and Dr. Alexander Heidt who reviewed my Ph.D manuscript and for their pertinent comments. Furthermore, I am grateful to Prof. Maxime Jacquot, Prof. Ole Bang and Dr. Mariusz Klimczak for accepting to be examiners.

I would like to give a special thanks to my SUPUVIRA's fellows, especially to Kyei, Manoj, Marcello, Solveig, and Xavier. I have so much memories with you guys, I will never forget our workshops spent together. Obviously, I want to thank all my colleagues with whom I shared so much both at work and outside: Benjamin, Sacha, Callum, Laurent, Rasmus, Abbu, Mikkel, Tobias ...

Finally, I want to thank my family and all those who accompanied me during this chapter of my life. Tusind tak

I dedicate this thesis manuscript to those who never stop believing in me.

LIST OF ABBREVIATIONS

	Signification		Signification
AC	Autocorrelation	ANDi	All-normal dispersion
CGNLSEs	Coupled generalized nonlinear Schrödinger equations	CW	Continuous wave
DFT	Dispersive Fourier transform	DSF	Dispersion-shifted fiber
DW	Dispersive wave	ESA	Electrical spectrum analyzer
ESR	Equivalent spectral resolution	FWHM	Full width at half maximum
FWM	Four-wave mixing	GNLSE	Generalized nonlinear Schrödinger equation
HCF	Hollow-core fiber	PBG	Photonic bandgap
IR	Infrared	LMA	Large mode area
MFD	Mode-field diameter	MI	Modulation instability
NLSE	Nonlinear Schrödinger equation	OPM	One photon per mode
OSA	Optical spectrum analyzer	OWB	Optical wave-breaking
PCF	Photonic crystal fiber	PER	Polarization extinction ratio
PM	Polarization maintaining	PMI	Polarization modulation instability
RIN	Relative intensity noise	RMS	Root mean square
SC	Supercontinuum	SIF	Step-index fiber
SNR	Signal-to-noise ratio	SPM	Self-phase modulation
SRS	Stimulated Raman scattering	SSFS	Soliton self-frequency shift
SPM	Self-phase modulation	TBP	Time-bandwidth product
TIR	Total intern reflection	UV	Ultraviolet
WDM	Wavelength division multiplexers	X-FROG	Cross-correlation frequency resolved optical grating
XPM	Cross-phase modulation	XPMI	Cross-phase modulation instability
ZDW	Zero dispersion wavelength		

CONTENTS

Introduction **1**

1 Introduction to light propagation in photonic crystal fibers **7**

1.1 Photonic crystal fibers 8
  1.1.1 Guiding mechanisms in standard optical fibers 8
  1.1.2 Fabrication and parameters of PCF 9
  1.1.3 Attenuation 12
  1.1.4 Chromatic dispersion 14
  1.1.5 Modal birefringence 16
1.2 Nonlinear pulse propagation in photonic crystal fibers 17
  1.2.1 Scalar generalized nonlinear Schrödinger equation 17
  1.2.2 Self-phase modulation 18
  1.2.3 Four-wave mixing 21
  1.2.4 Modulation instability 22
  1.2.5 Temporal optical solitons 23
  1.2.6 Dispersive waves 24
  1.2.7 Stimulated Raman scattering 25
  1.2.8 Vector generalized nonlinear Schrödinger equation 26
  1.2.9 Cross-phase modulation 27
  1.2.10 Supercontinuum generation 28

2 Noise sources and their impact on all-normal dispersion supercontinuum generation **33**

2.1 Noise characterization of supercontinuum generation 34
2.2 Known limits of coherent supercontinuum generation 41

2.3 All-normal dispersion polarization-maintaining silica fiber 47
2.4 Effect of technical noise on relative intensity noise and temporal coherence 49

3 Cross-phase modulation instability seeded by supercontinuum generation 63

3.1 Experimental investigations of XPMI in femtosecond ANDi SC generation . 64
3.2 Theoretical investigation of XPMI generation 70
3.3 Numerical investigation of XPMI generation 72
3.4 Real-time noise SC measurements 77

4 Development of a low-noise supercontinuum system 83

4.1 First system: low-average power laser 84
4.2 Second system: high-power, long pulse duration and nonlinear compression 93
4.3 Third system: high power, short pulse duration 99

5 General conclusion 107

6 Bibliography 111

GENERAL INTRODUCTION AND OUTLINE

Nonlinear optical effects are remarkable physical phenomena that can occur when a high-intensity light beam propagates through an optical medium [1]. A supercontinuum (SC) appears when a collection of nonlinear optical effects acts together upon a pump laser beam and induces a tremendous broadening of the initial spectrum. The first observations of SC generation have been reported in the visible region in bulk material, by Alfano and Shapiro in 1970 [2, 3]. Due to the complexity of the SC system, the applications of this technology were extremely limited. In the nineties, Russell *et al.* developed the concept of photonic crystal fibers thus the SC generation field evolved drastically due to their higher light confinement capabilities [4]. Since, a number of different fields such as spectroscopy, optical coherence tomography, use SC sources due to the octave-spanning bandwidth properties of this spatially coherent white "laser". Furthermore, Hall and Hänsch obtained a Nobel prize in 2005 in frequency metrology where they used a fiber SC system [5]. So far, there is a competition to obtain the broadest SC bandwidth, in the infrared region, using different materials for the photonic crystal fibers such as chalcogenide, ZBLAN, or even hollow-core fiber filled with different gases or nonlinear liquids. The main issue with typical SC generation, i.e. pumping a fiber in the anomalous dispersion regime, appears when one investigates its temporal coherence and noise properties. Indeed, the anomalous dispersion SC spectrum can be extremely incoherent due to the stimulation of the noise through the nonlinear effect of modulation instability and Raman scattering [1]. In 2010, Heidt *et al.* investigated the SC generation when pumping a photonic crystal fiber exhibiting normal dispersion at every wavelength present in the SC bandwidth [6]. In this case, it has been proven by authors of Ref. [7] that only the nonlinear effects of self-phase modulation and optical wave-breaking are responsible for the spectral broadening of the initial pulse, which are both known to be highly coherent [8]. However, later investigations have shown that the stimulated Raman scattering nonlinear effect can ruin the coherence of ANDi SC generation at high peak power or long pulse duration, thus limiting the SC bandwidth extension [9]. Furthermore, in Ref. [10] the authors have demonstrated pumping an ANDi photonic crystal fiber (PCF) that does not maintain the polarization state of the beam during the propagation, leads to the detrimental effect of polarization modulation instability (PMI). This nonlinear effect corresponds to the vector aspect of modulation instability, which is known to amplify noisy components in ANDi SC.

The main objective of this Ph.D is to overcome these two main limitations and to develop a fully compact polarization-stable and low-noise ANDi supercontinuum system, which potentially could be used for several applications such as optical coherent tomography and metrology. Using a 190 fs laser at 1040 nm and a polarization-maintaining ANDi PCF, we demonstrate in this work the generation of an octave-spanning, smooth, ultra-flat (bandwidth of 720 nm at -3 dB), linearly polarized (polarization extinction ratio up to 17 dB) and extremely stable (average relative intensity noise of 0.54 %/nm) supercontinuum. Comparing this system to ones already reported [**?**, 10, 11], we find that ours has, to the best of our knowledge, the lowest average SC ANDi RIN value ever reported. A detailed numerical study is also presented about the impact of pump laser amplitude noise on the coherence of the SC generated in ANDi PCFs. We further report the observation of cross-phase modulation instability in PM ANDi PCF based SC generation.

This thesis manuscript summarizes the main research results obtained during this Ph.D and it is divided into the following chapters:

The first chapter of this manuscript focuses on the modeling of pulse propagation in photonic crystal fibers. We begin by defining the optical and geometrical properties of photonic crystal fibers with and without a maintaining of the polarization state. Then we will describe the equations governing the propagation of intense-enough pulses to reach the nonlinear regime in photonic crystal fibers along one optical axis or taking into account the input polarization. Finally, we will introduce the concept of SC generation, especially in the case of femtosecond pulses pumping a polarization-maintaining all-normal dispersion photonic crystal fiber.

The second chapter deals with the different numerical and experimental methods used to characterize the noise properties of coherent SC light. We will describe different kinds of noise and their impacts on the relative intensity noise or the degree of coherence of the SC generation. We demonstrate, in particular, that taking into account the amplitude noise and the pulse duration fluctuations of the laser, both separately and combined, the SC coherence degree decreases when either the pulse duration or fiber length is increased. Thus, the available parameter space to achieve a low-noise SC generation is extremely narrow. We show that for a typical mode-locked laser, in which the noise of peak power and pulse duration are anticorrelated, their combined impact on the SC noise is generally smaller than in isolation. This means that the SC noise is smaller than the noise of the mode-locked pump laser itself, a fact that was recently observed in experiments but not explained until now.

The third chapter presents a SC system allowing us to investigate the cross-phase modulation instability in polarization-maintaining fiber seeded by SC generation. Then, we studied the impact of input polarization on this nonlinear effect and also the effect on an output polarizer on the SC generation while pumping at 45° of the fiber's axis. Furthermore, we use two noise measurement methods, dispersive Fourier transform and pulse train analysis with an oscilloscope, to investigate the noise of the SC as a function on the input polarization and then deduce the cross-phase modulation instability has no real impact on the relative intensity noise of the SC.

In chapter four, we describe three experimental setups to achieve an ultra-low-noise SC system using three different pump lasers. We investigate experimentally the impact of pulse duration and peak power on the SC bandwidth and relative intensity noise. We demonstrate we could achieve a system with an average relative intensity noise ten times lower than a commercial one using a commercially available seed, which has been nonlinearly compressed, even though the emitting pulses are not transformed limited or using directly another system to pump our dedicated fiber.

Finally, we conclude this manuscript reviewing the salient results of our work. We will highlight the different points of our system that can be improved to achieve an even better low noise level SC. Besides, we mention briefly different applications needing a low-noise SC system which could be fulfilled by our systems and we give some outlooks to further overcome the issues and improve the performances of all-normal dispersion SC generation.

These Ph.D works led to national and international publications, listed in the following paragraph.

ARTICLES

1. E. Genier, P. Bowen, T. Sylvestre, J. M. Dudley, P. M. Moselund, and O. Bang, "Amplitude noise and coherence degradation of femtosecond supercontinuum generation in all-normal-dispersion fibers," Journal of the Optical Society of America B 36, A161-A167 (2019)

2. E. Genier, A. N. Ghosh, S. Bobba, P. Bowen, P. M. Moselund, O. Bang, J. M. Dudley, and T. Sylvestre, "Cross-Phase Modulation Instability in PM ANDi Fiber-Based Supercontinuum Generation," Optics Letters, 45(13), 3545-3548.

3. E. Genier, S. Grelet, P. Bowen, T. Sylvestre, J. M. Dudley, P. M. Moselund, and O. Bang, "Ultra-flat low-noise visible near-IR ANDi supercontinuum source," Submitted to Optics Letters.

NATIONAL AND INTERNATIONAL CONFERENCES

1. Etienne Genier, Patrick Bowen, Thibaut Sylvestre, John Dudley, Peter M. Moselund and Ole Bang, “Coherence degradation and noise properties of all-normal dispersion femtosecond supercontinuum generation” International OSA Networks for Students (IONS) Scandinavia 2018, Copenhagen, Denmark, and Lund, Sweden, 7 June 2018.

2. Etienne Genier, Patrick Bowen, Thibaut Sylvestre, John Dudley, Peter M. Moselund and Ole Bang, “RIN in All-Normal Dispersion Supercontinuum Generation” Danish Optical Society, Copenhagen, Denmark, 28 January 2019.

3. Etienne Genier, Patrick Bowen, Thibaut Sylvestre, John Dudley, Peter M. Moselund and Ole Bang, “Noise Evolution in All-Normal Dispersion Supercontinuum Generation” CLEO Europe, Munich, Germany, 25 June 2019.

4. Etienne Genier, Amar N. Ghosh, Bobba Swetha, Patrick bowen, Peter M. Moselund, Ole Bang, John M. Dudley and Thibaut Sylvestre, “Cross-Phase Modulation Instability in PM ANDi Fiber-Based Supercontinuum Generation” CLEO US, San Jose, 11 May 2020.

SYMPOSIUM AND WORKSHOPS

1. Etienne Genier, Patrick Bowen, Thibaut Sylvestre, John Dudley, Ole Bang and Peter M. Moselund, "Low noise visible-near-infrared supercontinuum sources for optical coherent tomography applications," Future Prospects for Photonics on Mid-Infrared Light Sources and Applications Symposium, Tampere, Finland, 14 December 2017.

2. Etienne Genier, Patrick Bowen, Thibaut Sylvestre, Ole Bang, Peter M. Moselund, "Low-noise supercontinuum sources for UHR-PS-OCT applications," ShapeOCT meeting, Lyngby, Denmark, 26 February 2018.

3. Etienne Genier, Patrick Bowen, Thibaut Sylvestre, John Dudley, Ole Bang and Peter M. Moselund, "Limits of femtosecond All-Normal Dispersion Supercontinuum Generation," ShapeOCT meeting, Lyngby, Denmark, 3 December 2018.

4. Etienne Genier, Patrick Bowen, Thibaut Sylvestre, John Dudley, Ole Bang and Peter M. Moselund “Femtosecond All-Normal Dispersion Supercontinuum Generation and amplitude noise” Besancon meeting, Besancon, France, 14 December 2018.

1

INTRODUCTION TO LIGHT PROPAGATION IN PHOTONIC CRYSTAL FIBERS

This introduction chapter is written to provide a review of the characteristics of an optical fiber. Then, we will introduce several nonlinear effects, which can occur in a single-mode fiber, and are responsible for the spectral broadening of a laser. The first section describes the physical properties of optical fibers such as optical losses, spatial modes, waveguide and material dispersion, and birefringence. Furthermore, specific attention will be given to the dispersion profiles due to their impact on the nonlinear effects. The second section focuses on nonlinear effects resulting from the interaction of a powerful electromagnetic field with a dielectric medium. From this interaction two main nonlinear effects will be introduced: the optical Kerr effect and the stimulated Raman scattering (SRS). Finally, we will introduce the different dynamics leading to the supercontinuum generation and the equation governing the nonlinear propagation of optical pulse: the generalized nonlinear Schrödinger equation.

1.1/ PHOTONIC CRYSTAL FIBERS

1.1.1/ GUIDING MECHANISMS IN STANDARD OPTICAL FIBERS

According to the refraction law, a beam light going from one medium with a high refractive index to a medium with a lower refractive index, launched with a sufficiently small incidence angle will be totally reflected during the propagation, as shown in Fig. 1.1. From this principle, it is possible to guide light in an optical fiber over long distances and minimal losses.

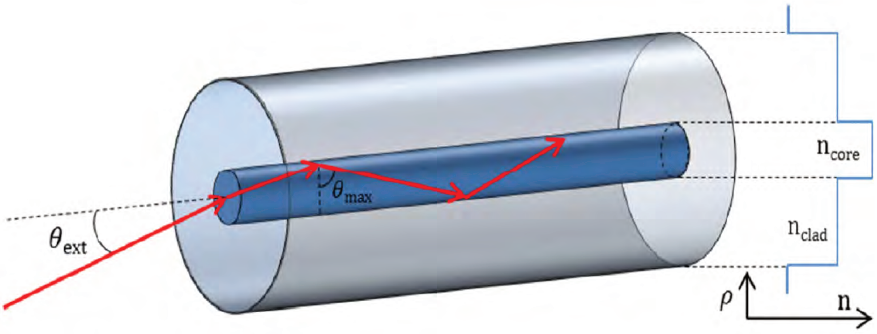

Figure 1.1: Geometry and ray-guiding schematic of an optical fiber showing refraction at the air-glass interface, and total internal reflection at the core-cladding interface. The step-index contrast between the core and cladding refractive indices is indicated to the right as a function of the radial coordinate ρ. Extracted from [12].

A conventional single-mode fiber or step-index fiber (SIF) is composed by its core (high refractive index, n_{core}) and by a surrounding medium (low refractive index, n_{clad}), called the cladding. In order to be guided in the fiber, the maximum input angle, θ_{max}, is defined as [13, 14]:

$$\sin(\theta_{max}) = \sqrt{n_{core}^2 - n_{clad}^2}. \tag{1.1}$$

Another important parameter which characterizes an optical fiber is its normalized frequency, V, defined as [13]:

$$V = \frac{2\pi}{\lambda} a \sqrt{n_{core}^2 - n_{clad}^2}, \tag{1.2}$$

where a is the core diameter of the fiber and λ the wavelength of the light coupled in the fiber. When V is lower than 2.405 [13], the optical fiber can support only one spatial mode (the fundamental one) and is also called single-mode fiber. To fulfill this condition the core diameter and the core-cladding index difference have to be very small, $\sim \mu$m and $\sim 10^{-2}$, respectively. As a consequence of the normalized frequency equation, one can define the lowest wavelength at which a given optical fiber is single-mode, λ_c, called the cut-off wavelength, defined as [15]:

$$\lambda_c = \frac{2\pi a}{V_c} \sqrt{n_{core}^2 - n_{clad}^2}, \tag{1.3}$$

with $V_c = 2.405$ the cut-off V number.

1.1.2/ FABRICATION AND PARAMETERS OF PCF

The emergence of photonic crystal fibers (PCF), also known as holey fiber or microstructured optical fiber, in the nineties, revolutionized the field of nonlinear optics and supercontinuum generation [16]. Usually, the typical design of a PCF is based on a periodic hexagonal lattice of capillaries forming a cladding area with a defect in the center of this region forming the core (the defect is made by "removing" one or more capillaries), as depicted in Fig. 1.2.

PCF are usually fabricated with a single material and used a pattern of rods with different material in the cladding to lower the average index of the cladding and confine the light to the core of the fiber [17]. The typical fabrication process of PCF is depicted in Fig. 1.3. where we can see the stack-and-draw technique. Usually, the cladding structure of the PCF is hexagonally shaped as shown in Fig. 1.2. This type of structure is normally characterized by its pitch, Λ, which corresponds to the hole-to-hole average distance, the hole diameter, d and the relative hole size, d/Λ, which is the diameter of the holes divided by the pitch.

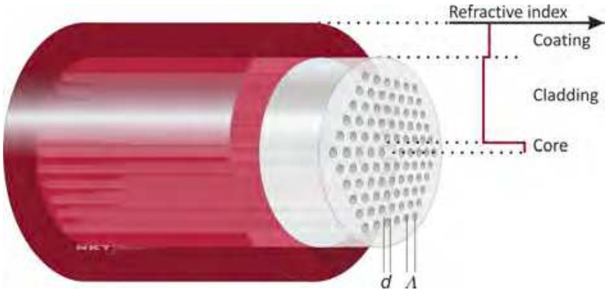

Figure 1.2: Cross-section of a solid-core photonic crystal fiber with hexagonal lattice of air holes in a silica glass background. The pitch Λ and the hole diameter d are represented so as the evolution of the refractive index as a function of the position on the fiber. Extracted from [18].

As explained above, the cladding of the PCF is composed of air holes and silica glass so the refractive index is not the same across the facet. The light guiding mechanisms in this solid-core PCF is similar to all solid standard optical fibers and uses total internal reflexion (TIR). However, Eq. 1.2 for SIF can not be used anymore. Thus, it is useful to define the effective refractive index of the PCF n_{FSM} representing the air fraction impact on the refractive index of the cladding, this is shown in Fig. 1.4 (a). Furthermore, the parameter V_{eff} for a PCF is defined as [19,20]:

$$V_{eff} = \frac{2\pi}{\lambda} a_{eff} \left(n_{eff}^2 - n_{FSM}^2 \right), \tag{1.4}$$

with a_{eff} is the radius of the effective core in μm and n_{eff} the refractive index of the core. For a PCF with a big relative hole size (d/Λ), this one can support the propagation of higher-order modes if the ratio λ/Λ is inferior to 1.

The number of modes support by a PCF depends on the two ratios d/λ and λ/Λ. When the air fraction is very small ($d/\Lambda < 0.45$) the PCF is single-mode whatever the

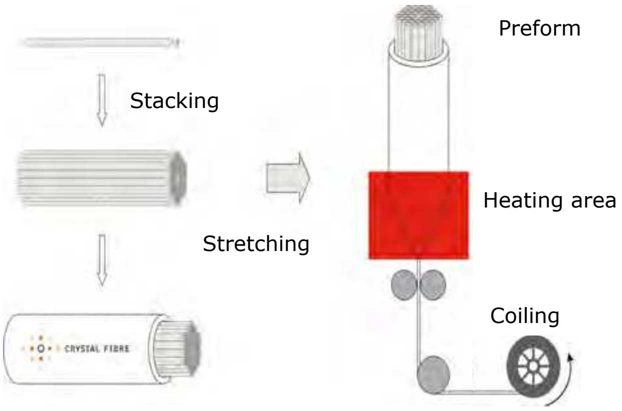

Figure 1.3: Schematic of the PCF fabrication via the stacking and drawing method

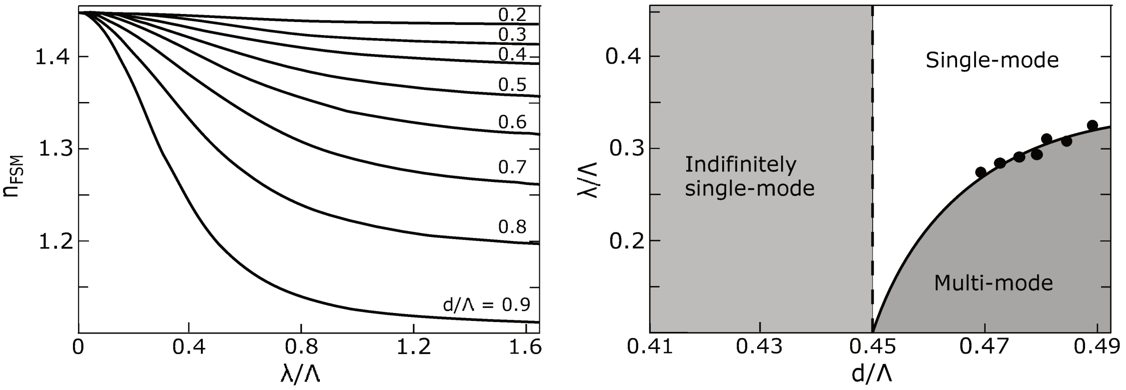

Figure 1.4: (a) Representation of the effective refractive index of a PCF as a function of λ/Λ for value of d/λ going from 0.2 to 0.9 [21]. Representation of the three functioning regimes as a function of d/λ and λ/Λ. The curve and dots correspond to $V_{eff} = 0.245$ and to the measure of Ref. [22], respectively.

wavelengths launched into the PCF (see Fig. 1.4 (b)). Thus, it is possible to obtain single-mode propagation with huge effective areas at telecom wavelengths [23], which is the principle of large mode area (LMA) fiber. In this thesis, LMA fiber has been used as the first stage of nonlinear pulse compression (followed by chirp mirrors), see Sec. 4.2.

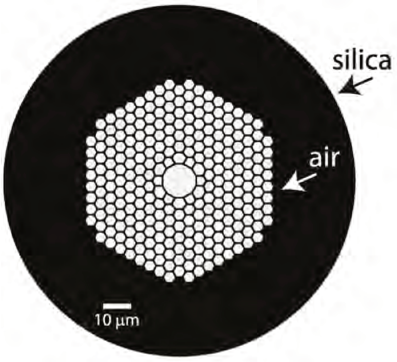

Figure 1.5: Schematic of a hollow core fiber cross section.

There are different kinds of PCFs like hollow-core photonic bandgap fibers when the fiber is composed of a hollow core, which is surrounded by air holes in a hexagonal shape as represented in Fig. 1.5 [17]. In this kind of fiber, the refraction law can not be applied due to the low-index of the core compared to the cladding. Thus, the mechanism governing the propagation of the light in hollow-core fiber (HCF) is the photonic band-gap (PBG) effect. These fibers are usually used to transport high optical power because the light is essentially guided in air, which involves a small nonlinear coefficient ($n_{2,air} \sim 10^{-26}$ m^2/W) [23]. In this thesis, hollow-core fiber has been used for linear pulse compression, see Sec. 4.1.

1.1.3/ ATTENUATION

The optical power transmitted through an optical fiber (PCF in our case) is limited by the losses during the propagation. The fiber losses are characterized by the attenuation coefficient α given by [13]

$$\alpha_{dB} = -\frac{10}{L}\log_{10}\left(\frac{P_{out}}{P_0}\right) \quad \Rightarrow \quad P_{out} = P_0 e^{-\alpha L}, \tag{1.5}$$

where P_0 is the input power, P_{out} the transmitted power, L the fiber length in m, α_{dB} and α the attenuation coefficient in dB/km and 1/km, respectively. Furthermore, we have to take into account the wavelength dependence of the loss in the fiber, which comes from several phenomena split into three categories: scattering, confinement, and absorption.

The scattering losses include the contribution of the Rayleigh and imperfection-induced scatterings (surface roughness, microdeformation, hole size and pitch longitudinal variations). The Rayleigh scattering loss arises due to the density fluctuations in the refractive index of the fiber, which are much smaller than the optical wavelength. The equation governing the Rayleigh scattering has an inverse dependence with the optical wavelength to the power 4 as:

$$\alpha_{Ray} = \frac{A_{Ray}}{\lambda^4} \tag{1.6}$$

where $A_{Ray} = 1.3$ dB/km/$\mu\mathrm{m}^4$.

The imperfection scattering losses are inherently present in the fiber fabrication process but don't have any wavelength dependence [24]. The contribution of the imperfection scattering loss has been estimated to 1 dB/km at 1 μm for silica fiber.

The confinement loss depends heavily on the fiber structure and results from a leakage of the core mode to the cladding [25]. The structure dependence is the following: the confinement loss increases when the core size decreases and decreases when the number of rings holes increases or the relative hole size increases as well. The confinement loss can be obtained from the imaginary part of the effective refractive index of the fiber:

$$\alpha_{leak} = \frac{20}{\ln(10)}\frac{2\pi}{\lambda}\mathrm{Im}(\mathrm{n_{eff}}), \tag{1.7}$$

The ultraviolet (UV) and infrared (IR) absorption losses depend on the glass material used for the fiber (fused-silica in our case) and are related to the electronic and vibrational resonances in the UV and mid-infrared regions, respectively. The contribution of both absorption phenomena scale exponentially with the photon energy and can be expressed as [26, 27]:

$$\alpha_{UV} = A_{UV} e^{\frac{\lambda_{UV}}{\lambda}}, \qquad \alpha_{IR} = A_{IR} e^{-\frac{\lambda_{IR}}{\lambda}}, \tag{1.8}$$

where, $A_{UV} = 0.001$ dB/km, $\lambda_{UV} = 4.67\ \mu$m, $A_{IR} = 6 \times 10^{11}$ dB/km and $\lambda_{IR} = 47.8\ \mu$m. The impurities transfer in the fiber fabrication process also leads to some absorption peaks. Thus, a purification step is added in the fabrication process to reduce this contribution. The main absorption impurities come from the presence of water particles in the fiber, which has a main peak at 1345 nm. The impurity loss due to the absorption of water can be expressed as [26, 27]:

$$\alpha_{OH}(\lambda) = \frac{A_{OH}}{1 + \left(\frac{\lambda - 1385}{16}\right)^2} \tag{1.9}$$

where A_{OH} is the peak value of the OH absorption. Finally, when we take into account all these loss contributions, we obtain the following equation [26]

$$\alpha(\lambda) = \alpha_{Ray}(\lambda) + \alpha_{imp} + \alpha_{UV}(\lambda) + \alpha_{IR}(\lambda) + \alpha_{OH}(\lambda) + \alpha_{leak}(\lambda). \tag{1.10}$$

which can be represented on the following graph:

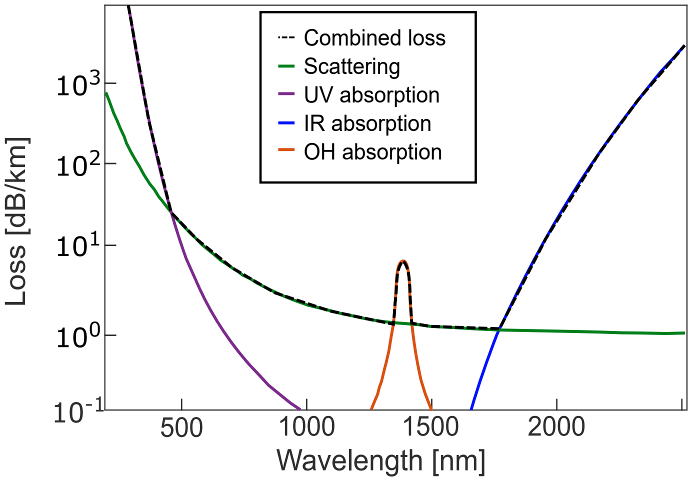

Figure 1.6: Combined loss profile including scattering loss, UV, IR and OH absorption.

1.1.4/ CHROMATIC DISPERSION

In the linear regime, when a light beam interacts with a dielectric material, the optical properties of the material depend on the optical frequency of the beam. This dependency of the linear refraction index $n(\omega)$ is called the chromatic dispersion and involves the spectral components of the light travel at different speeds in the material. Thus, when a pulse with a finite spectral bandwidth propagates in a dispersive medium, the chromatic dispersion induces a temporal broadening of the initial pulse. The chromatic dispersion is given by the contribution of the material dispersion and the waveguide dispersion [28]. The material dispersion can be approximated by the Sellmeier equation, which for silica glass is [13, 29]:

$$n^2(\lambda) = 1 + \sum_{j=1}^{m} \frac{B_j \omega_j^2}{\omega_j^2 - \omega^2}. \tag{1.11}$$

Using the experimental data given by [30], the solutions of the equation 1.11 with visible to near-IR light and $m = 3$ is:

$$\begin{aligned} &B_1 = 0.6961663, \quad B_2 = 0.4079426, \quad B_3 = 0.8974794 \\ &\lambda_1 = 0.06840403\,\mu\text{m}, \quad \lambda_2 = 0.1162414\,\mu\text{m}, \quad \lambda_3 = 9.896161\,\mu\text{m}. \end{aligned} \tag{1.12}$$

Mathematically, the effect of chromatic dispersion can be modeled in the frequency domain by expanding the propagation constant β in a Taylor series around the pump frequency ω_0:

$$\beta(\omega) = n(\omega)\frac{\omega}{c} = \beta_0 + \beta_1(\omega - \omega_0) + \frac{1}{2}\beta_2(\omega - \omega_0)^2 + ... + \frac{1}{m!}\beta_m(\omega - \omega_0)^m, \tag{1.13}$$

where

$$\beta_m = \frac{d^m\beta}{d\omega^m}\Big|_{\omega=\omega_0} \qquad (m = 0, 1, 2, 3...), \tag{1.14}$$

and with $\beta_0 = \frac{n(\omega_0)\omega_0}{c}$ the propagation constant and $n(\omega_0)$ the refraction index at the frequency ω_0. In equation 1.13 the most important parameters are β_1 which is the inverse of the group velocity and β_2, which is the group velocity dispersion (GVD). The group velocity characterizes the velocity of the pulse envelope in the medium while the GVD represents the dispersion or temporal broadening of the group velocity. The higher-order dispersion terms have to be taken into account especially when the GVD is very close to the zero-dispersion wavelength (ZDW).

For the pulse propagation in optical fiber, another parameter is often used: the dispersion parameter $D(\lambda)$ in picosecond per kilometer of fiber and per nanometer:

$$D(\lambda) = -\frac{\lambda}{c}\frac{d^2n}{d\lambda^2} = \frac{-2\pi c}{\lambda^2}10^6\beta_2. \qquad (\mathrm{ps.nm^{-1}.km^{-1}}). \tag{1.15}$$

When D is negative, this is the normal dispersion regime ($\beta_2 > 0$), the longer wavelengths travel faster than shorter wavelengths whereas when D is positive, anomalous dispersion regime ($\beta_2 < 0$), longer wavelengths travel slower than shorter wavelengths. Furthermore, in the linear regime, an unchirped pulse propagating along an optical fiber undergoes temporal broadening regardless of the sign of the D (β_2) parameter.

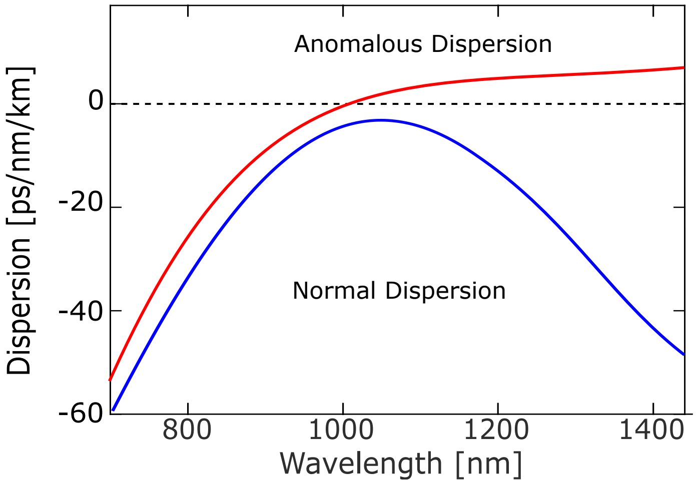

Figure 1.7: Typical dispersion profile for a PCF exhibiting all-normal dispersion values over the entire wavelength range (solid blue) and for one presenting a ZDW at 1 μm (solid red).

In the context of PCFs, it is easy to tailor the GVD profile using the additional degrees of freedom provided by d and d/Λ. From this fine control, several GVD profiles can be obtained or tailored: moving the ZDW of the fiber over a wide range of wavelengths (from 500 nm to 1.5 μm), having a normal dispersion profile over a large bandwidth or several ZDWs. In Fig. 1.7, the dispersion profile of a typical PCF with a ZDW located at 1000 nm is shown as well as the dispersion profile of an all-normal dispersion PCF.

Finally, the parameter L_D can be introduced to estimate when the dispersion starts to be important for a given fiber length. This parameter is defined as the fiber length at which the initial Gaussian pulse width broadens by a factor of $\sqrt{2}$ and has the following equation:

$$L_D = \frac{T_0^2}{|\beta_2|}, \tag{1.16}$$

where T_0 is the initial pulse width measured at 1/e of the maximum pulse intensity.

1.1.5/ MODAL BIREFRINGENCE

In addition to the attenuation and dispersion, the birefringence is another important property of optical fibers. It is extremely difficult to fabricate perfectly circular optical fiber due to the small deviations in the fabrication process. These deviations induce the creation of two degenerate optical modes, which introduce the birefringence. This is the reason for which, the fundamental optical mode of a single-mode fiber corresponds to two degenerated modes and are orthogonally polarized. There are two kinds of birefringence: phase one and group one. In this paragraph, we talk only about the phase birefringence (B_m). This birefringence is defined by the refractive index difference between the two polarization axes or can be given by the difference between the propagation constants of each orthogonal polarization axes (x, y):

$$B_m = \Delta n = |n_x - n_y|, \quad \Delta\beta = \beta_x - \beta_y = \frac{\Delta n(\omega)\omega}{c}, \tag{1.17}$$

where $\Delta n = n_x - n_y$ is the refractive index difference between two orthogonal polarizations of the same mode, i.e, the birefringence. Thus, a linearly polarized beam aligned on the axis with the lowest value (fast axis) will propagate faster than the axis with the highest value (slow axis). These two particular axes are called the principal fiber axes. Typically, the birefringence induced only by the imperfection of the fiber process is weak $\Delta n \sim 10^{-6} - 10^{-5}$. Furthermore, these fibers are usually called weakly birefringent fibers. In order to keep the polarization state of a beam during the propagation, mechanical stresses are usually used around the core of the fiber during the fabrication process (using rods). These polarization-maintaining (PM) fiber have high birefringence value, $\Delta n > 10^{-4}$, and are called "Panda" or "Bow-tie" and are represented in Fig. 1.8.

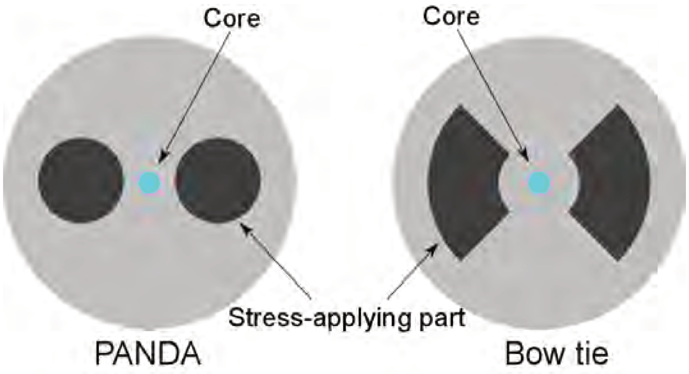

Figure 1.8: Schematic of polarization-maintaining PCFs. The stress-induced by the big air holes (panda or bow-tie structure) are used to create the phase birefringence. Extracted from [31].

When launching the input beam at 45° degrees of the principal axes in a PM fiber, two orthogonal modes periodically exchange their power while propagating inside a fiber with beat length L_B which is given by:

$$L_B = \frac{2\pi}{\Delta\beta} = \frac{\lambda}{\Delta n}. \tag{1.18}$$

During the propagation, the polarization state of the beam will change from linear to elliptic to circular and to linear again. After a beating length period, the beam will retrieve its original polarization state. For a weakly birefringent fiber ($\Delta n = 10^{-6}$) at 1μm, the beat length is $L_B = 1$ m but has arbitrary meaning since the birefringence is caused by fiber imperfections and is thus changing throughout the fibre, while for a highly birefringent PCF with $\Delta n = 5\times10^{-4}$, like the one used in this thesis, the beat length is $L_B = 2$ mm. Nevertheless, the beat length can only be defined in the linear regime because the interaction between polarizations is affected by nonlinearities at high power. This intensity-dependent polarization effect is called the nonlinear birefringence [13].

1.2/ NONLINEAR PULSE PROPAGATION IN PHOTONIC CRYSTAL FIBERS

1.2.1/ SCALAR GENERALIZED NONLINEAR SCHRÖDINGER EQUATION

The first model used in this thesis to simulate the nonlinear propagation of pulses in PCF is the well-known Generalized Nonlinear Schrödinger Equation (GNLSE) solved with a split-step Fourier method using Matlab. With this model, we assume the electrical field is polarized along only one axis of the fiber without any interaction with the other one (scalar case). This assumption can be used only while pumping on one axis of a PM-fiber with a linearly polarized laser having a high polarization extinction degree. The scalar GNLSE equation is usually derived from the wave equation including the third-order nonlinear polarization and it is finally given by [1,32–36]:

$$\frac{\partial A}{\partial z} = -\frac{\alpha(\omega)}{2}A + \sum_{k\geq 2}\frac{i^{k+1}}{k!}\beta_k\frac{\partial^k A}{\partial T^k} + i\gamma\left(1 + i\tau_0\frac{\partial}{\partial T}\right)\left(A\int_{-\infty}^{+\infty}R(T')|A(z,T-T')|^2 dT'\right), \tag{1.19}$$

where A is the complex amplitude field as $E = Ae^{(-iwt+kz)}$, the two first terms of the right-hand side of the equation model the linear losses and the dispersion of the fiber using a series of Taylor coefficients (up to 10^{th} order) while the last term models the nonlinear effects including both optical Kerr effect and Raman scattering. γ is the nonlinear coefficient expressed as:

$$\gamma = \frac{2\pi n_2}{\lambda A_{eff}}, \tag{1.20}$$

where n_2 is the nonlinear index of the fiber, and A_{eff} the spatial mode effective area evaluated at the input wavelength. The nonlinear index is assumed to be frequency independent and equal to $2.6 \times 10^{-20}\ m^2 W^{-1}$ for silica fiber [13]. The effective mode area is defined as:

$$A_{eff}(\omega) = \frac{\left(\iint_{\infty}^{\infty} |F(x, y, \omega)|^2 dxdy\right)^2}{\iint_{\infty}^{\infty} |F(x, y, \omega)|^4 dxdy}, \tag{1.21}$$

where $F(x, y, \omega)$ is the transverse modal distribution. This equation can be simplify for a Gaussian mode and is given by:

$$A_{eff} = \pi R_{core}^2, \tag{1.22}$$

where R_{core} is the core radius of the fiber. The temporal derivation of the field envelope in Eq. 1.19 corresponds to the self-steepening phenomenon with its characteristic time scale $\tau_0 = 1/\omega_0$ (ω_0 being the input pulse angular frequency). Another consequence of the Kerr effect on a short optical pulse is the intensity dependence of the group velocity that leads to the phenomena of self-steepening and optical shock wave formation [13]. The intensity dependence of group velocity causes the peak of the pulse to slow down more than the edges of the pulse, leading to the steepening of the trailing edge of the pulse. When the edge becomes infinitely steep, the intensity changes instantaneously, and eventually, it leads to form an optical shock wave and a strong asymmetric spectrum. Finally, $R(t)$ corresponds to the nonlinear Raman response function and can be written as:

$$R(t) = f_R \delta(t) + (1 - f_R)\, h_R(t), \tag{1.23}$$

which includes the instantaneous electronic response $\delta(t)$ and the delayed Raman $h_R(t)$ corresponding to molecular vibrations. The nonlinear Raman response is normalized as $\int_0^{\infty} h_R(t)dt = 1$, and fractional contribution f_R of the delayed Raman response is typically equal to 0.18 for fused silica [1].

1.2.2/ SELF-PHASE MODULATION

In order to introduce some of the basic nonlinear effects in PCF, we can further simplify the GNLSE by removing the higher dispersion terms, self-steepening, loss and delayed Raman response. After this simplification, we obtain the simplest form of the nonlinear

Schrödinger equation (NLSE):

$$\frac{\partial A(z,T)}{\partial z} = -\frac{i\beta_2}{2}\frac{\partial^2 A(z,T)}{\partial T^2} + i\gamma|A(z,T)|^2 A(z,T). \tag{1.24}$$

The first nonlinear effect in the context of femtosecond supercontinuum (SC) generation is the self-phase modulation (SPM). This phenomenon leads to a spectral broadening of short optical pulses as a result of the intensity dependence of the refractive index $n = n_0 + n_2 I(t)$, with n_0 and n_2 the linear and nonlinear refractive index, respectively [3,37]. The SPM can be studied in depth by neglecting the dispersion term ($\beta_2 = 0$) in the NLSE which leads to the following general solution:

$$A(z,T) = A(0,T)\exp\left[i\phi_{NL}(z,T)\right], \qquad \phi_{NL} = \gamma|A(0,T)|^2 z = \gamma P(T)z, \tag{1.25}$$

where $P(t)$ is the pulse power distribution. From equation 1.25, we can understand that a nonlinear phase shift $\phi_{NL}(t)$ is induced on a pulse when it is propagating along with the fiber. The maximum nonlinear phase shift ϕ_{max} occurs at the center of the pulse (maximum peak power) and is given by $\phi_{max} = \gamma P_0 L$, with P_0 the pulse's peak power. Due to this nonlinear phase shift, the spectral bandwidth of the pulse will broaden during the propagation while the temporal profile of the pulse will stay invariant. The parameter L_{NL}, nonlinear characteristic length, can be introduced to estimate when the nonlinear process becomes important. This one is defined as:

$$L_{NL} = \frac{1}{\gamma P_0}. \tag{1.26}$$

Due to the SPM effect, the temporal profile of the pulse doesn't change but is affected by a time-dependent nonlinear phase shift, called $\phi_{NL}(z,t)$, which induces a time-varying instantaneous frequency, i.e a frequency chirp, defined as:

$$\delta\omega(t) = -\frac{\partial\phi_{NL}(z,t)}{\partial t}. \tag{1.27}$$

Thus, the instantaneous optical frequency varies across the temporal profile of the pulse as:

$$\omega(z,t) = \omega_0 + \delta\omega(z,t) = \omega_0 - \gamma\frac{\partial|A(0,t)|^2}{\partial t}z. \tag{1.28}$$

From this equation, one can understand the frequency chirp induced by SPM is nonlinear in time because it is proportional to the time derivative of the initial temporal power profile [13]. Thus, SPM creates new spectral components whose separation from ω_0 increases with peak power, propagation distance, nonlinearity and steepness of the pulse, this is shown in Fig. 1.9 (a) and 1.9 (b) for a secant hyperbolic pulse with different input pulse duration or peak power. At the trailing pulse edge, where the slope of the intensity profile is negative the spectrum is broadened towards blue-shifted shorter wavelength, while at the leading edge of the pulse, where the slope of the rising intensity profile is positive, the spectrum is broadened towards red-shifted longer wavelength.

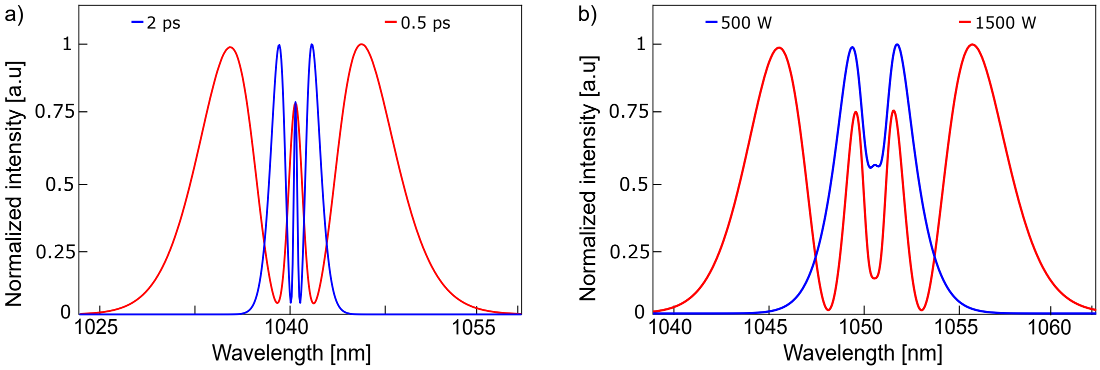

Figure 1.9: Broadening induced by self-phase modulation as a function of (a) pulse duration with $P_0 = 1$ kW and (b) peak power with $T_0 = 100$ fs. For this simulation, an unchirped secant hyperbolic is used as input profile with $\beta_2 = 0$ and $L = 20$ cm.

Another way to study SPM-induced spectral broadening is to plot the pulse spectrogram in order to represent the time-frequency correlations within the pulse, which represents the induced frequency chirp. Fig 3.13 shows the spectrogram of a 400 fs secant hyperbolic pulse with an input peak power of 8 kW after 15 cm of propagation. We can clearly

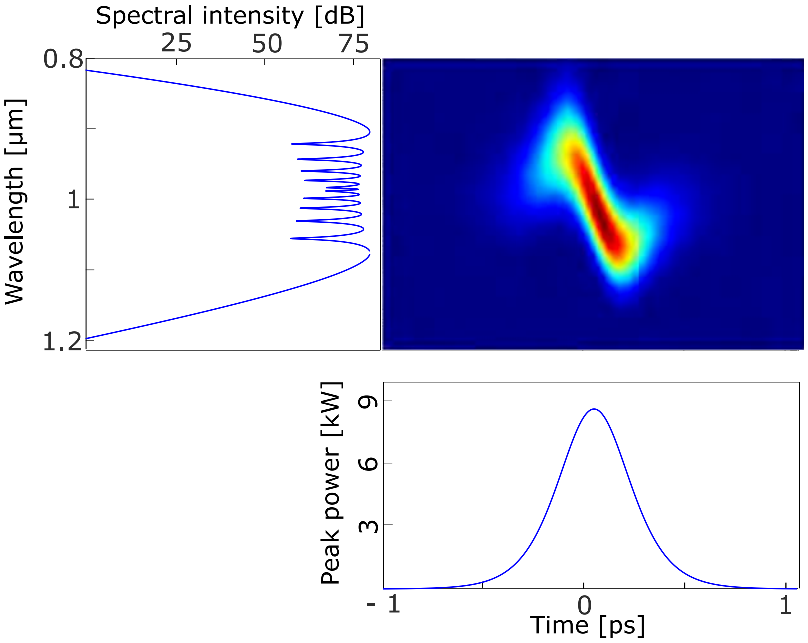

Figure 1.10: Spectrogram of a SPM spectrum with $T_0 = 400$ fs, $P_0 = 8$ kW, $L = 15$ cm, and $\gamma = 0.0268\ (W.m)^{-1}$.

notice the temporal pulse shape remains unaffected while the spectral pulse shape undergoes an oscillatory structure. These oscillatory features are explained because identical spectral components are present at the same time and thus will interfere with each other.

1.2.3/ FOUR-WAVE MIXING

From a quantum point of view, four wave mixing (FWM) consists of the annihilation of two photons of frequency ω_1, ω_2 and the creation of two other frequency-detuned photons at ω_3 and ω_4, shown in Fig. 1.11 (a) satisfying two fundamental laws: the energy conservation and the momentum conservation as follows [13, 38]:

$$\begin{aligned} &\hbar\omega_4 + \hbar\omega_3 = \hbar\omega_2 + \hbar\omega_1 \\ &\Delta\beta = \beta(\omega_4) + \beta(\omega_3) - \beta(\omega_2) - \beta(\omega_1) = 0, \end{aligned} \tag{1.29}$$

where $\hbar$ is the reduced Planck's constant and β is the propagation constant of each photon. The momentum conservation implies a phase matching condition for FWM to appear. An interesting aspect of the FWM appears when strong pump waves have the same frequency ($\omega_1 = \omega_2 = \omega_P$) and create photon pair at frequencies ω_S and ω_i, which represent respectively a Stokes/signal and an anti-Stokes/idler wave (see Fig.1.11 (b)). In such a case, we talk about degenerate FWM. This photon pair is frequency symmetric compared to the pump frequency with a frequency shift defined as $\Omega_S = \omega_p - \omega_s = \omega_i - \omega_p$, where the Stokes wave is the wave created with a lower frequency than the pump and the anti-Stokes wave is the one which has a higher frequency [39]. In this case, we get the following phase-matching condition:

$$\Delta\beta = \beta(\omega_p - \Omega_S) + \beta(\omega_p + \Omega_S) + 2\beta(\omega_p) = \beta(\omega_s) + \beta(\omega_i) - 2\beta(\omega_p) = 0. \tag{1.30}$$

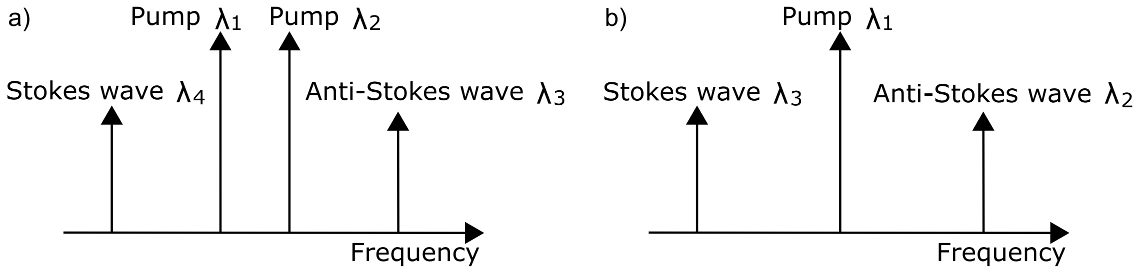

Figure 1.11: Schematic of four waves mixing for (a) 2 pump waves and (b) 1 pump wave (degenerated case)

A deeper analysis of FWM will be introduced in chapter 3 when we will explain the phenomenon of cross-phase modulation instability. FWM is an ubiquitous process in χ^3 media involved in modulation instability, parametric amplification, optical wave breaking, dispersive waves, photon pair generation,...

1.2.4/ MODULATION INSTABILITY

The modulation instability (MI) nonlinear effect generates sidebands around the pump in the frequency domain (through the interaction between nonlinear and dispersive effects) [13]. In the time domain, MI leads to the amplification of a weak perturbation (quantum noise, background noise or weak seed signal) and thus induces a break up of the main pulse into shorter ones, for quasi-continuous wave (CW) pulse or a temporal modulation for CW pulse. This phenomenon can be understood as a FWM but, in the case of MI, the anti-Stokes and Stokes frequencies are generated through the quantum noise, as shown in Fig. 1.12.

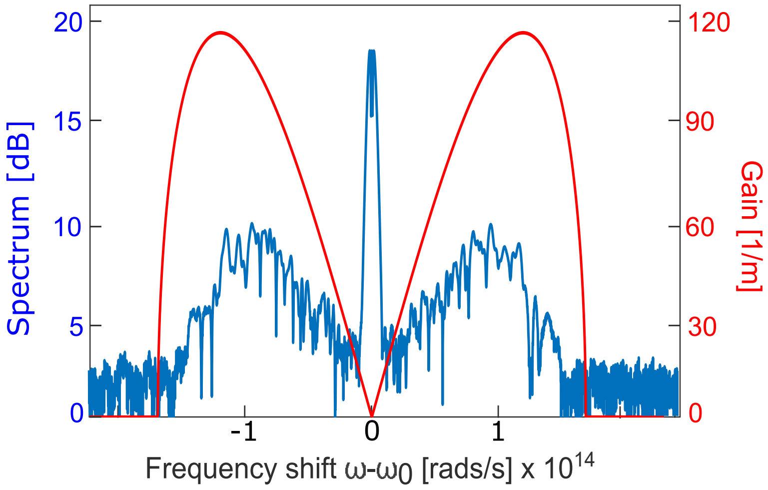

Figure 1.12: Numerical simulation of modulation instability sidebands (blue) for an initial secant pulse with $T_0 = 5ps$ and $P_0 = 2$ kW using NLSE equation. The theoretical MI gain (red) is also calculated. The fiber parameters in the simulation are: $\gamma = 0.027$ (W.m)$^{-1}$, $\beta_2 = -0.1$ ps^2/m, and $L = 20$ cm.

Theoretically, MI is studied by adding a small perturbation to the steady-state solution of the NLSE (Eq. 1.24) as:

$$A(z,t) = \sqrt{P_0 + a(z,t)}e^{i\gamma P_0 z}, \tag{1.31}$$

where $a(z,t) = a_1 \exp^{[i(Kz-\Omega t)]} + a_2 \exp^{[-i(Kz-\Omega t)]}$, and K and Ω are the wave number and the frequency of the perturbation, respectively. Inserting the perturbed equation (Eq. 1.31) into the NLSE equation (Eq. 1.24), a dispersion relation for K can be obtained:

$$K = \pm\frac{1}{2}|\beta_2\Omega|\sqrt{\Omega^2 + sign(\beta_2)\Omega_c^2}, \tag{1.32}$$

where $\Omega_c = 4\gamma P_0/|\beta_2|$. Scalar MI can not occur while pumping in the normal dispersion regime and thus the field envelope is stable against any perturbation because $sign(\beta_2) = 1$, which means K is always a real number for every Ω. However, while pumping in the anomalous dispersion regime ($sign(\beta_2) = -1$) K is imaginary for $|\Omega| < |\Omega_c|$ and thus the condition for MI generation is satisfied. In this case, the maximum scalar MI gain $g_{max} = 2\gamma P_0$ [13] is located at two symmetric frequencies around the pump with the following frequency shift:

$$\Omega_{MI} = \pm\sqrt{\frac{2\gamma P_0}{|\beta_2|}} \tag{1.33}$$

This is shown in Fig. 1.12 where we can see the generation of symmetric MI sideband compared to the pump obtained by solving the NLSE equation with the following input parameters: $\gamma = 0.027$ (W.m)$^{-1}$, $\beta_2 = -0.1$ ps^2/m, and $L = 20$ cm.

1.2.5/ TEMPORAL OPTICAL SOLITONS

A temporal optical soliton is an optical pulse that preserves its shape and duration when propagating in a nonlinear optical fiber. A soliton is generated when the linear chirp from GVD is compensated by the nonlinear chirp induced by SPM. This compensation appears only in the anomalous dispersion regime, i.e. when β_2 is negative, because their respective contribution has an opposite sign [13]. In the normal dispersion regime, i.e. β_2 positive, their respective contribution has the same sign thus it is impossible to generate bright soliton (only dark soliton) [40].

Solitons are solutions of NLSE and their temporal electric field envelopes satisfy the following equation [13]

$$A(z,t) = N sech\left(\frac{t}{t_0}\right)\exp\left(-i\frac{|\beta_2|}{2t_0}z\right), \tag{1.34}$$

where t_0 is the pulse width measured at 1/e of the pulse intensity and N is the soliton number defined as [1, 13]

$$N = \sqrt{\frac{L_D}{L_{NL}}} = \sqrt{\frac{\gamma P_0 T_0^2}{|\beta_2|}}. \tag{1.35}$$

When $N = 1$, the soliton is called fundamental soliton, this case appears when the dispersion and the nonlinearity compensate each other ($L_D = L_{NL}$). Thus, a fundamental soliton has its temporal and spectral profiles unaffected during the propagation. On the other hand, when $N > 1$ we talked about higher-order solitons. These higher-order solitons evolve periodically with propagation, i.e. they recover their initial temporal (and spectral) shape after the soliton period length defined as $z_{sol} = \pi L_D/2$ [1]. The issue with higher-order solitons compared to the fundamental soliton is their stability. Indeed, in the presence of small perturbation such as self-steepening or higher-order dispersion terms higher-order solitons are highly unstable and will break up into N fundamental solitons that shed some energy in the form of dispersive waves. This phenomenon is called soliton fission and is defined by the soliton fission length $L_{fiss} \approx L_D/N$.

1.2.6/ DISPERSIVE WAVES

A specific aspect of the FWM, in the context of supercontinuum generation, is the phenomenon of dispersive wave generation. Under the Raman self-frequency shift and higher-order dispersion, a soliton becomes unstable and can shed some radiations in the form of weak waves, called dispersive waves (DW) [1]. This transfer depends on the matching of the phase velocity of the two waves and the spectral covering between them. Therefore, this transfer is proportional to the spectral overlap between the soliton and the generated wave [41]. Thus, the more the soliton is separated from the zero-dispersion wavelength the more the wavelength satisfying the phase matching would be in a strong normal dispersion regime and the more the covering would be limited, decreasing the created wave amplitude. The phenomenon of DW generation contributes to spreading the spectrum towards the normal dispersion regime, i.e. generation of shorter wavelengths compared to the input one, in fiber.

The resonance frequency can be calculated from a phase-matching argument involving the soliton linear and nonlinear phase, and the linear phase of a quasi-CW component at a different frequency [41–43]. According to [1], for a soliton with a peak power P_S, frequency ω_s, and group velocity $v_{g,s}$, a DW can be generated at the frequency ω_{DW} if :

$$\beta(\omega_s) - \frac{\omega_S}{v_{g,S}} + (1 - f_R)\gamma P_S = \beta(\omega_{DW}) - \frac{\omega_{DW}}{v_{g,s}} \tag{1.36}$$

The frequency shift $\Omega = \omega_S - \omega_{DW}$ between soliton and DW can be approximated, if fourth-order dispersion and f_R are neglected, by [13]

$$\Omega \approx -\frac{3\beta_2}{\beta_3} + \frac{\gamma P_S \beta_3}{3\beta_2^2} \tag{1.37}$$

where β_2 and β_3 are the second and third-order dispersion coefficients of the fiber at the soliton frequency.

1.2.7/ STIMULATED RAMAN SCATTERING

The stimulated Raman scattering (SRS) phenomenon is a scattering process corresponding to a resonant excitation, by an intense electromagnetic field, of molecular vibrational states. Through this nonlinear effect, the optical field transmits a little part of its energy to the dielectric medium inducing the creation of optical phonons. Thus, SRS is an inelastic scattering and thus transfers this energy to other optical frequencies shifted by the frequency of the phonon, as shown in Fig. 1.13. This shift is given by the phase-matching corresponding to the amplification of the spontaneous scattering Raman noise.

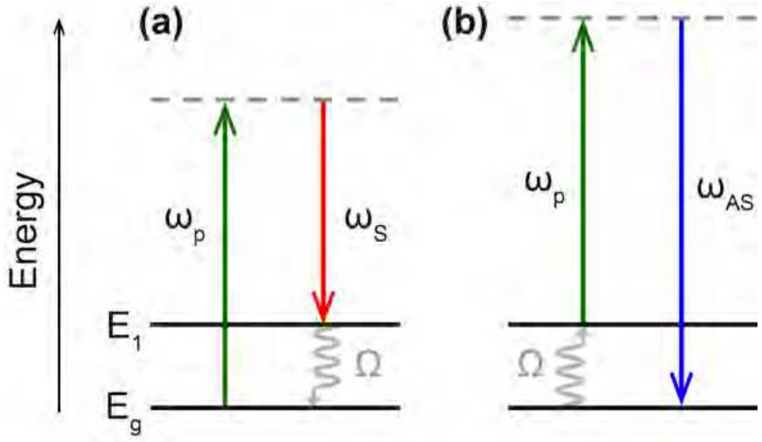

Figure 1.13: Virtual energy level diagram for generation of (a) Stokes (ω_S) and (b) anti-Stokes (ω_{AS}) frequencies. The phonon frequency is Ω.

As explained above, SRS is a phenomenon related to the vibrational modes of the molecules. Thus, this nonlinear effect is not instantaneous and its response time, in silica fiber, is around 75 fs [44].

The stimulated Raman gain spectrum in silica spreads on more than 40 THz bandwidth with maximum efficiency at $\nu_{Raman} = 13.2$ THz [45]. When an intense optical field with a frequency ν_0 propagates in an optical fiber, a Stokes wave arises around the frequency $\nu_0 - \Omega$ and growths exponentially as a function of the fiber length (more details are given in Sec. 2.2). The power of this Stokes wave is similar to the pump one from a threshold given by [13]:

$$P_{th}^{Raman} > \frac{16A_{eff}}{g_R L_{eff}}, \tag{1.38}$$

where g_R is the Raman gain and equal, for silica fiber, to $1.\ 10^{-13}$ m.W^{-1}, and L_{eff} is the effective length and equal to $1 - e^{-\alpha L}$.

Another phenomenon resulting from the Raman scattering can appear when soliton generation conditions are respected: the Soliton Self-Frequency Shift (SSFS) [46]. This phenomenon induces a shift to a higher wavelength of emitted solitons. The effect comes from the soliton spectrum covering the Raman gain band thus it only appears when the soliton has an enough larger spectrum so of short temporal length, in general in femtosecond regime. This soliton frequency shift is given by: $d\nu_R/dz \propto |\beta_2|/T_0^4$ [46]. The factors of proportionality depend on the pulse length of the soliton if this one is shorter than 76 fs one can use the formula described in [47] or in [13] for pulse longer than 76 fs (the threshold of 76 fs corresponds to the oscillation period of silica [47]). A deeper explanation of SRS will be introduced in Sec. 2.2.

1.2.8/ VECTOR GENERALIZED NONLINEAR SCHRÖDINGER EQUATION

All previous equations and nonlinear effects were based on the scalar GNLSE, which has for the main assumption that all the waves are polarized along the same axis and never move away from it during the propagation. Thus, no polarization (vector) effects could be investigated with this model. Therefore, another model used during this thesis is the vector GNLSE, also called coupled GNLSEs. This model allows an investigation of polarization effects when a single-mode birefringent fiber is used. Furthermore, cross-phase modulation instability is presented as an appropriate example of nonlinear polarization effects. This phenomenon is investigated deeply in Chapter 3. Finally, the vector GNLSEs are given, in the time domain, by [13]

$$\begin{aligned}
&\frac{\partial A_{x,y}}{\partial z} + \frac{\alpha}{2}A_{x,y} + \beta_{1x,y}\frac{\partial A_{x,y}}{\partial T} - \sum_{k\gg 2}\frac{i^{k+1}}{k!}\beta_k^{x,y}\frac{\partial^k A_{x,y}}{\partial T^k} = i\gamma\left(1 + i\tau_{shock}\frac{\partial}{\partial T}\right)\\
&\left\{(1-f_r)\left(|A_{x,y}|^2 + \frac{2}{3}|A_{y,x}|^2\right) + f_R A_{x,y}(z,t)\int_{-\infty}^{T} h_R(T-T')|A_{x,y}(z,T-T')|^2 dT'\right.\\
&\left.+\frac{i\gamma}{3}A_{x,y}^{*}A_{y,x}^{2}\exp^{i\Delta\beta z}\right\},
\end{aligned} \tag{1.39}$$

where x and y correspond to each linear polarization field envelopes, A_x and A_y, respectively, and $\Delta\beta = \beta_{0x} - \beta_{0y} = 2\pi/L_B$. In these equations, we neglect the orthogonal Raman gain. Furthermore, Eq. 1.19 is similar to the scalar GNLSE (Eq. 1.17) but we take into account the effect of cross-phase modulation (red part of the equation) and FWM between both polarizations (blue part). The FWM term can be neglected if the birefringence is high enough ($> 10^{-4}$), which is the case for PM fiber, because its sign will change often during the propagation and its average contribution tends toward zero [13]. Unlike, in non-PM fiber, the FWM term has to be taken into account because it is responsible for the polarization modulation instability (PMI) effect.

1.2.9/ CROSS-PHASE MODULATION

In the CGNLSE equations, we introduced the concept of cross-phase modulation (XPM). This effect appears when an optical pulse experiences a nonlinear phase shift induced by the interaction with another co-propagating optical pulse with a different frequency or polarization state. Thus, the nonlinear phase shift depends on its intensity through the SPM effect and by the intensity of the co-propagating pulse. Finally, the total nonlinear phase shift acquired by an optical field co-propagating with another one is given by:

$$\phi_j^{NL}(z,t) = \gamma \left(|A_j(0,t)|^2 + 2|A_{3-j}(0,t)|^2 \right) z, \tag{1.40}$$

where $j = 1, 2$ corresponds to each optical field. Furthermore, one can notice that the nonlinear phase shift induces by XPM is twice as strong as the SPM one for co-polarized different frequency waves. The XPM factor is 2/3 for cross-polarized waves as in birefringent optical fibers.

The XPM phenomenon can be efficient only if the two optical pulses overlap, in time, with each other. Thus, the nonlinear phase shift induced by XPM stops when each optical pulse will walk-off from each other. In order to determine when the walk-off appears, we can define the effective length at which the nonlinear interaction between the two waves ceases, this length is defined as:

$$L_W = \frac{T_0}{|\Delta\beta_1|}, \tag{1.41}$$

where $\Delta\beta_1$ is the group-velocity mismatch of the two waves. Some care is required while using this equation because we need to put $\Delta\beta_1$ in context, in order to avoid mistakes. Thus, the group velocity mismatch is different for the following cases:
- In multimode fiber, it characterizes the group velocity speed difference between two or more modes.
- In single-mode fiber with optical pulses traveling with different wavelength
- In our case, optical pulses traveling with orthogonal polarizations but having the same wavelength. Thus, the group velocity mismatch depends on the fiber birefringence as

written in Eq. 1.18. The XPM phenomenon is responsible for the cross-phase modulation instability, which will be further investigated in Chap. 3.

1.2.10/ SUPERCONTINUUM GENERATION

Now that we introduced different nonlinear effects that can occur in PCF, we can go through the concept of supercontinuum (SC) generation. An SC appears when a collection of nonlinear processes act together upon a pump beam in order to cause a dramatic broadening of the initial pump spectrum [1]. As explained before, there are two important parameters to take into account in order to predict which nonlinear effects will take place for the spectral broadening: the dispersion and the input pulse duration. If the fiber used has an anomalous dispersion area and one pump close to the ZDW of this fiber, the nonlinear effects responsible for the spectral broadening will be:

- In the femtosecond regime: SPM, soliton and dispersive wave generation, and SSFS
- In the pico-nanosecond regime: MI and SRS

If the fiber has an all-normal dispersion (ANDi) profile across the whole SC bandwidth and is single-mode, SC is generated by:

- In the femtosecond regime: SPM and optical wave-breaking (OWB)
- In the pico-nanosecond regime: cascaded SRS and FWM

Figure 1.14 shows a typical spectral evolution of femtosecond SC generation while pumping a fiber close to the zero-dispersion wavelength (ZDW) with an input pulse duration of 50 fs, 10 kW peak power and $\beta_2 = -11$ ps$^2/km$ (a), and with an input pulse duration of 50 fs, 50 kW peak power, a fiber having an ANDi profile with $\beta_2 = 5.33$ ps$^2/km$ (b).

As we can see, the anomalous pumping leads to the presence of several dips in the spectrum while with an ANDi pumping the spectrum remains smooth and flat. The advantage to use anomalous pumping is to get a very large multi-octave wavelength span. For instance, it can go up to 8 μm in the mid-infrared [48]) with a relatively small input peak power ($<$ 20 kW). The trade-off with this technique is the temporal (and thus the frequency) spectrum is not stable especially when the soliton number $N > 16$ [1], leading to a noisy and low coherent SC source. On the contrary, ANDi SC generation has the advantage to be theoretically coherent and stable when SRS is not present [6] but needs a very high peak power in order to obtain a broad spectrum in areas where the dispersion is not very close to zero (1.8 μm with 400 kW peak power [6]). This issue can be fixed with better engineering of the dispersion profile (easier at 1.5 μm than at 1 μm). In this thesis, we will focus only on femtosecond ANDi SC generation at 1 μm.

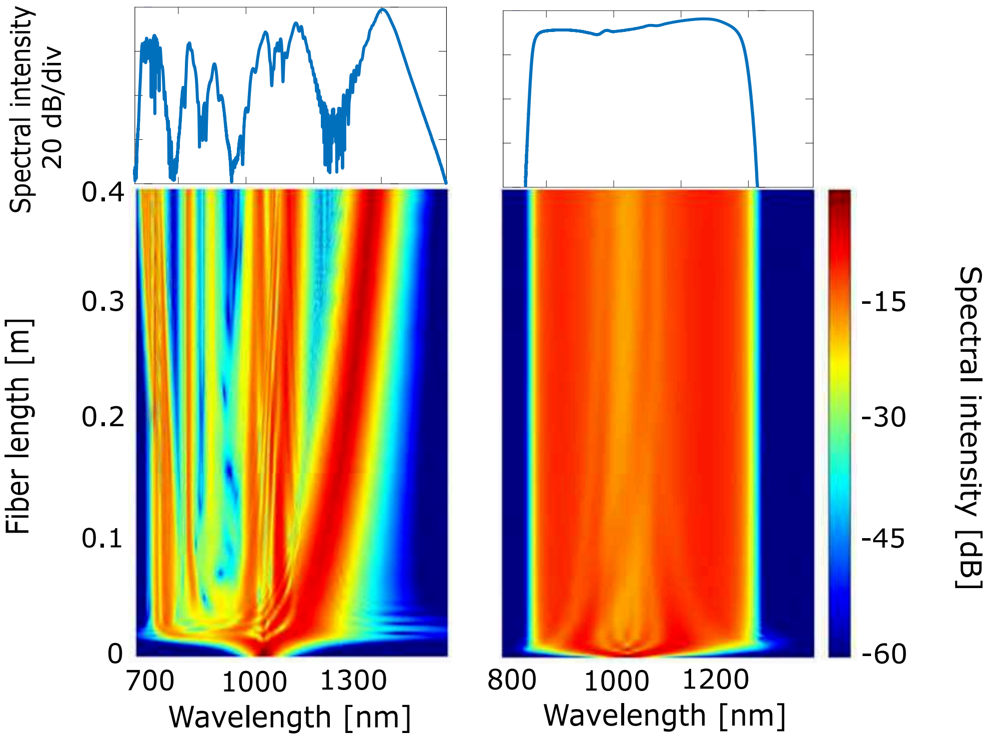

Figure 1.14: Numerical simulations of (a) anomalous and (b) ANDi SC evolution as a function of fiber length. The input parameters are: 50 fs input pulse duration with 10 kW input peak power and $\beta_2 = -11$ ps$^2/km$ for (a) and 50 fs input pulse duration with 50 kW input peak power $\beta_2 = 5.27$ ps$^2/km$ for (b).

We will now explain deeply the mechanisms governing fs ANDi SC generation. For that, the temporal and spectral SC spectra at different fiber lengths are shown in Fig. 1.15. The initial parameters used in this simulation are 150 fs full width half maximum (FWHM) secant pump pulse centered at 1054 nm with 100 kW peak power using a parabolic ANDi profile with a minimum of dispersion of $\beta_2 = 5.935 \times 10^{-27} s^2/m$, and a constant nonlinear parameter $\gamma = 25.5\ W^{-1}km^{-1}$. Before going into detail with the SCG in ANDi fibers, there are some general features to consider:

- The group velocity increases with wavelength, i.e. longer wavelengths travel faster than shorter wavelengths
- Eventually, the dispersion increases at longer wavelengths, crossing the ZDW, which can induce the generation of soliton and thus ruined the coherent SC generation [11].
- Spectral broadening at shorter or longer wavelengths than the pump wavelength

corresponds to the leading or trailing edge of the pulse in the time domain, respectively.

- The chirp induced by SPM and GVD have the same sign and therefore the pulse broadens continuously in the time domain, which results in peak power reduction that limits the spectral broadening. Thus, the maximum spectral broadening is achieved when pumping at the point of minimum absolute dispersion. Furthermore, ANDi fibers have been engineered and fabricated to have as low dispersion as possible for maximizing the spectral broadening [49].
- In parabolic-like ANDi fibers, the sign of β_2 and β_4 is positive and therefore scalar MI cannot occur. Care must be taken when using flat-dispersion ANDi fibers as β_4 can be negative depending on the wavelength.

Using femtosecond pulses the spectral broadening at the beginning of the fiber is governed by the SPM nonlinear effect (see Fig. 1.15 (a) and (b)). To help the understanding of this example, it is useful to estimate the linear and nonlinear characteristic lengths using our input parameters. The dispersion length is $L_D = 1.3$ m and is much longer than the nonlinear length $L_{NL} = 0.38$ cm. Thus the initial dynamics are governed by the nonlinear effect, SPM in this case. As previously explained, the initial spectral broadening due to SPM can be enhanced or reduced with the input peak power or nonlinearity.

In the normal dispersion regime, the longer wavelengths travel faster than the shorter ones. Thereby, after some propagation distance, overlap in time appears between the trailing/leading edge of the pulse and the main blue/red peaks of the SPM spectrum. As a result, new wavelengths are generated on both sides of the spectrum. This phenomenon is called optical wave breaking (OWB) [6, 8]. The first signatures of OWB appear at 3 cm in the short wavelength side of the spectrum as shown in Fig. 1.15 (c) and on the right side of the temporal spectrum (Fig. 1.15 (d)), in the form of temporal oscillations. In the long-wavelength side, OWB generates new wavelengths after 5 cm as shown in Fig. 1.15 (e) and on the left side of the temporal spectrum (Fig. 1.15 (f)).

The new frequencies generated by OWB are obtained via a degenerate FWM: $\omega_{OWB} = 2\omega_{pump} - \omega_{SPM}$, where ω_{pump} is the pump frequency and ω_{SPM} the frequency of the SPM redder/bluer peaks of the spectrum. Some energy is transferred to the OWB frequency while the frequency components overlap in time until the energy of the tails of the pump is completely depleted. Another feature of OWB is displayed in Fig. 1.15 (d) and (f) in which the pulse undergoes interference in the leading (d) and trailing (f) edge of the pulse in the time domain. This corresponds to the OWB development at short/long wavelengths, as a result of the overlap of different frequencies in time. The interference in the time domain ceases with further propagation, when OWB is over (Fig. 1.15 (h)).

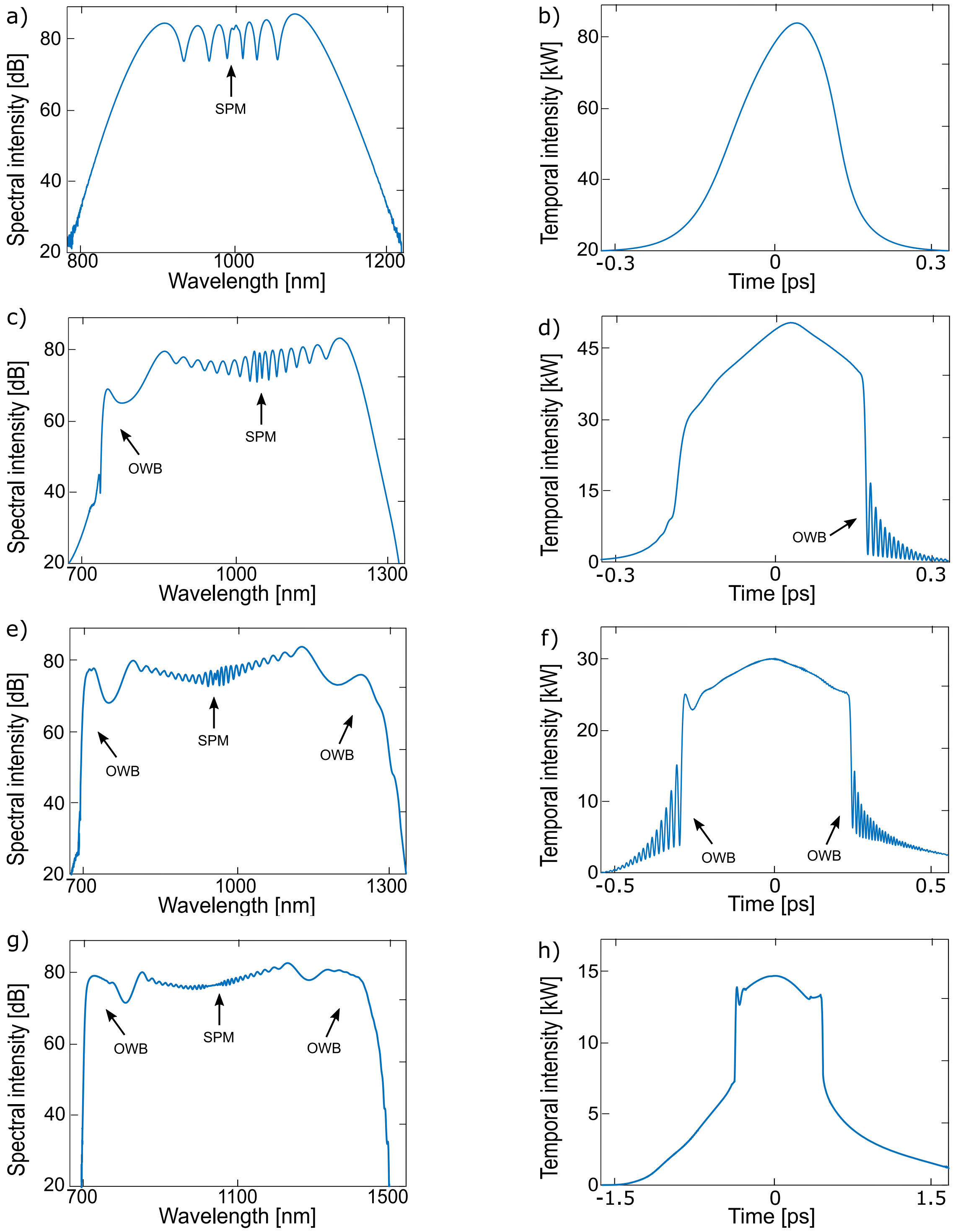

Figure 1.15: Typical temporal and spectral evolution of fs SC generation in ANDi fibers for (a,b) 2 cm, (c,d) 3 cm, (e,f) 5 cm, and (g,h) 10 cm.

The reason for OWB to occur earlier at shorter than at longer wavelengths is related to the shape of the dispersion curve. In the short wavelength region, the dispersion is steeper than at long wavelengths, in this example. This means that the group velocity difference between the pump (1054 nm) and the outermost red/blue-shifted SPM peak (1163 nm / 886 nm in this case) is larger in the short-wavelength region than in the long-wavelength region. As a result, the overlap in time between those frequencies and the consequent OWB frequency generation takes place earlier in the short wavelength region. Besides, self-steepening enhances the OWB generation at short wavelengths [50] by inducing an intensity dependence on the group velocity. In fact, when self-steepening, Raman and higher-order dispersion terms are removed, the spectral broadening is generated symmetrically in frequency [8]. A characteristic length can be defined for Gaussian pulses to predict the onset of OWB [8]:

$$L_{WB} \approx 1.1\frac{L_D}{N} = 1.1T_0\sqrt{\frac{1}{\gamma P_0 \beta_2}} \tag{1.42}$$

For our parameters, the OWB length is $L_{WB} = 2$ mm, which gives an estimation of the OWB onset. This analytical OWB length is given in Eq. 1.42 was derived for a constant β_2. Therefore, the asymmetries in OWB generation due to the group velocity difference, self-steepening and Raman are not taken into account.

After the onset of OWB on both sides of the spectrum, all the frequencies are located in one unique temporal position. Further propagation, therefore, leads to stretching of the pulse in time and no more spectral broadening as shown in Fig. 1.15 (f) at 10 cm. For this example, the SCG is fully developed after less than 12 cm, and thus longer fiber length is not needed. However, under other conditions, such as longer pump pulses, the OWB distance increases, and therefore more fiber length is required to obtain the broadest spectrum possible. Also note that not only in our example but also in general, a single pulse in the time domain is maintained at the output of the fiber with linear phase [6], which can be compressed to ultra-short (single cycle) pulses [**?**, 51].

In conclusion, spectrally flat and pulse-preserving SC can be obtained by using ANDi fibers. The phenomena governing SCG using ANDi fibers are SPM and OWB, which generate new frequencies coherently [6, 8], and therefore allow for potentially coherent and low noise SC [6, 51]. Ideally, short pump pulses and high peak powers are preferably used in order to generate the broadest ANDi SC with the shortest possible fiber length.

In the next chapter, we will investigate in detail all source of noise and their impact on ANDi SC supercontinuum.

2

NOISE SOURCES AND THEIR IMPACT ON ALL-NORMAL DISPERSION SUPERCONTINUUM GENERATION

In this chapter, we will discuss and investigate all noise sources and their impact on the supercontinuum noise and its coherence. Several theoretical studies about SC coherence have been reported in anomalous dispersion fiber, covering pulse durations from fs up to continuous wave, and including several kinds of noise, such as quantum noise added as a photon with random phase noise in the frequency domain (one photon per mode), Wigner-representation based quantum noise was also added in the time domain as amplitude and phase noise, Raman noise, and polarization noise [1, 52–62]. This is not the case for theoretical studies of ANDi SC generation, which have mostly considered only the quantum noise [6, 9], except for a recent work of Gonzalo *et al.* [10], in which relative intensity noise was experimentally and numerically compared for ANDi SC generation with 170 fs pump pulses. In this study, it was found that quantum noise was too weak to describe the experimentally observed noise, whereas adding 1 % amplitude fluctuations of the laser gave better agreement with the experimental results. This important result underlines that while pump laser noise traditionally has contributed little to the noise levels in incoherently broadened anomalous dispersion fiber SC generation, it is extremely important in coherently broadened ANDi SC generation.

Unfortunately, Gonzalo *et al.* just briefly mentioned the effect of pure amplitude noise of the pump laser for one specific pulse duration and fiber length and no specific simulation including the amplitude noise was shown and no general study was conducted [10].

2.1/ NOISE CHARACTERIZATION OF SUPERCONTINUUM GENERATION

There are two main metrics used to analyze the noise properties of a laser or a SC: the first-order spectral coherence function and the relative intensity noise (RIN). In this chapter, we will describe how both functions are defined, how they are numerically implemented and how they are measured experimentally.

The first-order spectral coherence function is defined as [1, 9, 10, 63]

$$|g_{12}(\omega)| = \left| \frac{\left\langle \tilde{A}_i^*(\omega)\tilde{A}_j(\omega) \right\rangle_{i\neq j}}{\sqrt{\left\langle \left|\tilde{A}_i(\omega)\right|^2 \right\rangle \left\langle \left|\tilde{A}_j(\omega)\right|^2 \right\rangle}} \right|, \tag{2.1}$$

where $\left[A_i(\omega), A_j(\omega)\right]$ represent independent pairs of the complex spectral amplitude of a SC spectrum, and angle brackets indicate an ensemble average over independent SC pairs generated from the N simulations with different noise seeds. The first-order spectral coherence function returns a value between 0 (low coherence) and 1 (high coherence) for each frequency. Furthermore, the spectrally averaged coherence can also be calculated as [1,9,10,63] :

$$\langle |g_{12}| \rangle = \frac{\int_0^\infty |g_{12}(\omega)| \left\langle \left|\tilde{A}_i(\omega)\right|^2 \right\rangle d\omega}{\int_0^\infty \left\langle \left|\tilde{A}_i(\omega)\right|^2 \right\rangle d\omega} \tag{2.2}$$

which gives $0 \leqslant \langle |g_{12}| \rangle \leqslant 1$ for an ensemble of SC and indicates the average stability of the whole SC spectrum. The first-order spectral coherence function evaluates a mix of phase and amplitude fluctuations. Numerically, the first-order spectral coherence can be measured using the ratio between the standard deviation and the average of an ensemble of SC as demonstrated in App. 1 [63]:

$$|g_{12}(\omega)| = \frac{\left|\left\langle \tilde{A}(\omega) \right\rangle\right|^2}{\left\langle \left|\tilde{A}(\omega)\right|^2 \right\rangle}. \tag{2.3}$$

From this alternative formulation, we can interpret $|g_{12}(\omega)|$ as the modulus of the mean field squared normalized to the mean spectrum.

Unlike the first-order spectral coherence function, the RIN formula gives only the intensity fluctuations of the SC without taking into account effects of phase fluctuations. The RIN formula is described as the ratio between the standard deviation of the SC ensemble divided by its mean [10]:

$$\mathrm{RIN}(\omega) = \frac{\sigma(\omega)}{\mu(\omega)}. = \frac{\sqrt{\langle \left(|\tilde{A}_i(\omega)|^2 - \langle |\tilde{A}_i(\omega)|^2 \rangle \right)^2 \rangle}}{\langle |\tilde{A}_i(\omega)|^2 \rangle}. \tag{2.4}$$

The spectrally averaged RIN can be calculated as [1,9,10,63] :

$$\langle RIN \rangle = \frac{\int_0^\infty RIN(\omega) \left\langle \left|\tilde{A}_i(\omega)\right|^2 \right\rangle d\omega}{\int_0^\infty \left\langle \left|\tilde{A}_i(\omega)\right|^2 \right\rangle d\omega}, \tag{2.5}$$

which indicates the average pulse-to-pulse fluctuations over the whole SC bandwidth. Experimentally, there are several methods used to measure pulse-to-pulse fluctuations of a laser or an SC. In general, in order to fully characterize these fluctuations, the noise measurement method should quantify both the phase and the amplitude of the laser/SC pulse. However, it is very difficult to have access to the phase fluctuations of a pulse. Thus, the majority of the noise measurement techniques are designed to quantify only the intensity fluctuations of the pulse. Hopefully, for many applications, it is not useful to resolve the phase. There are four techniques commonly used to measure the RIN of an SC:

- RIN measurement using a fast photodiode and an oscilloscope [11]
- Noise spectral density measurement using an electrical spectrum analyzer (ESA) [**?**]
- Dispersive Fourier Transform (DFT) technique [64]
- Cross-correlation frequency-resolved optical grating (X-FROG) [65]

Single-shot, X-FROG, unlike the other technique, is used for measuring the spectral amplitude and phase of ultrashort laser pulses [65–67]. Thus, this method can provide a shot-to-shot characterization of the pulse in both time and frequency. X-FROG system has been used to measure the complete bandwidth of the SC for a single pulse. The issue with X-FROG setup is its complexity compared to other noise measurement methods and could be very limited, in terms of wavelength range, regarding the various component needed to characterize a whole SC bandwidth. In this thesis, we used the three first techniques to measure our pulse-to-pulse fluctuations in amplitude.

These methods are based on the same approach: via a photodiode, the laser/SC light is converted into electrical current. Then, using a fast oscilloscope, we can analyze the electrical pulse train emitted by the photodiode and thus determine the average and standard deviation of this pulse train, as described in Fig. 2.1.

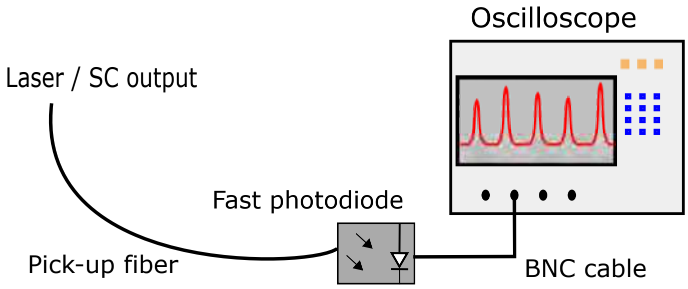

Figure 2.1: Schematic of noise measurement techniques based on fast photodiode and oscilloscope.

The concept of the DFT technique is rather similar but uses an intermediate dispersive fiber to stretch the pulses and analyze their spectra in real-time [64]. It can be described as follows: when a pulse propagates in a linear dispersive medium with a high quadratic spectral phase the pulse will stretch linearly and will look like its Fourier transform, as shown in Fig. 2.2. Indeed, according to the Fourier theory where, in the spatial domain, the diffraction pattern of an arbitrary spatial mask in the far-field will give the spatial Fourier transform of the initial mask [68].

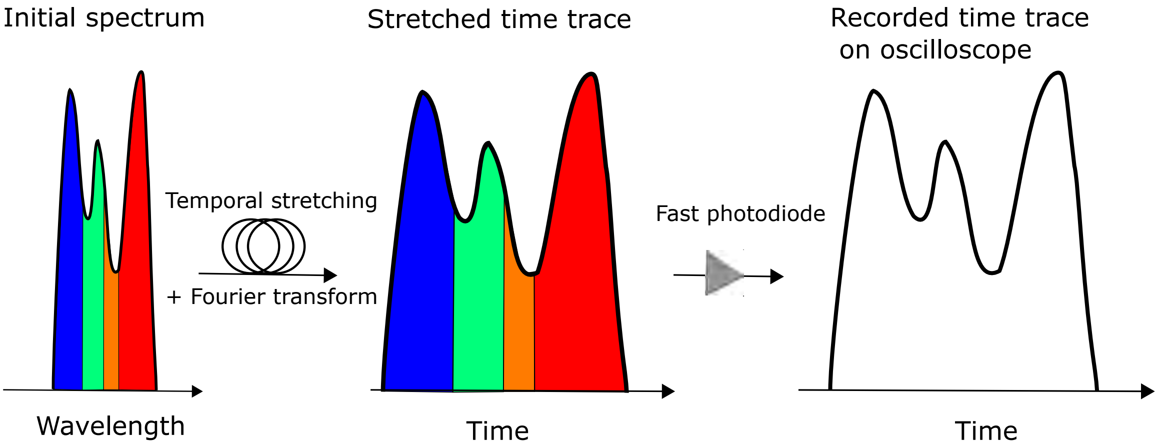

Figure 2.2: Schematic of dispersive Fourier transform principle. Fluctuations of the initial spectrum are real-time resolved using an ultrafast detection optoelectronic system (photodiode + oscilloscope).

If we consider an initial temporal field $A(t)$ and its Fourier transform $\tilde{A}(\omega)$, propagating over a distance z in a dispersive fiber having a quadratic dispersion β_{2s}, after a sufficient propagation in the approximation of stationary phase (as defined in [69]), we obtain a time stretch output pulse $A_z(t)$ defined as [69]:

$$A_z(t) \approx \tilde{A}(t/\beta_{2s}z)\exp\left(\frac{-it^2}{2\beta_{2s}z}\right). \tag{2.6}$$

Thus, we obtain an output time-stretched pulse with an intensity profile similar to the initial spectrum:

$$|A_z(t)|^2 \approx |\tilde{A}(t/\beta_{2s}z)|^2 \tag{2.7}$$

This principle is described schematically in Fig. 2.2 where we can find the different steps of the dispersive Fourier transform technique. Finally, the equivalent spectral resolution (ESR) represents the spectral bandwidth for which the RIN is integrated during the DFT measurement and is given by [69]:

$$\delta\lambda = \frac{1}{B|D|z}, \tag{2.8}$$

where B is the photodiode or scope bandwidth, D the dispersion in ps/nm/km of the stretching fiber and z the fiber stretching length. We have to notice that the ESR is frequency-dependent thus the RIN value given by DFT measurements could be different from one edge of the spectrum to the other one especially the RIN value should be higher close to the ZDW of the stretching fiber because the integrated bandwidth will be shorter.

In practice, to perform a DFT measurement, one needs a fast photodiode with high sensitivity and a fast oscilloscope which can resolve every pulse without any overlapping. One can use different stretching elements in order to temporally spread the pulse: prism, chirped-mirrors, grating, fiber [70]. We notice that experimentally, to have a linear propagation (avoiding nonlinear effect), we could have to reduce the power of the input field.

For this thesis, the DFT technique has been used to investigate pulse-to-pulse noise fluctuations in PM-ANDi SC generation and especially the impact of the input polarization on the SC RIN. More details regarding this experiment are provided in Chapter 3.

Another way to measure the RIN of a laser (or an SC) is to use directly a fast photodiode and a fast oscilloscope to record the pulse train, this one will measure the pulse-to-pulse intensity fluctuations [10, 71]. In order to obtain a spectrally resolved RIN (for the SC case), one can use a tunable bandpass filter before the photodiode, as shown in Fig. 2.3. The impact of the bandwidth on RIN measurements will be discussed later. This measurement technique has been used to study the statistic behavior of rogue wave characteristics with a ps pumped SC [64, 72].

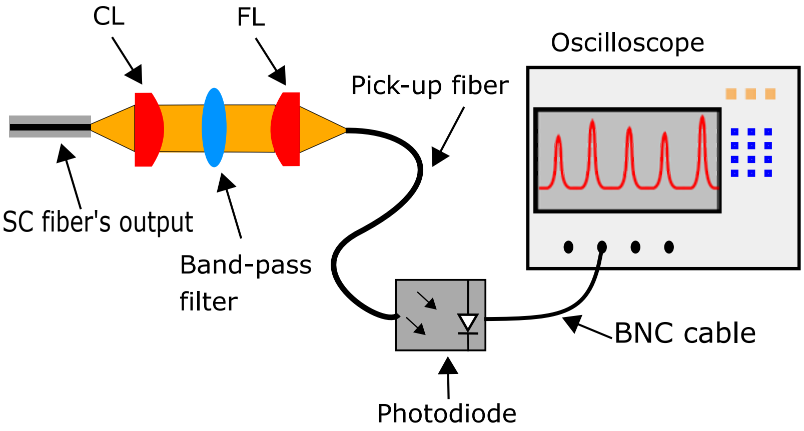

Figure 2.3: Schematic of the spectrally resolved RIN measurement setup using collimating lens (CL), focussing lens (FL) and band-pass filters.

To correctly use this measurement method, we have to fulfill the following condition [73]:

$$T_{rep} \geqslant T_{PD} \geqslant T_0, \tag{2.9}$$

where T_{rep} is the inverse of the repetition rate (12.5 ns for a laser emitting pulses at 80 MHz repetition rate), T_{PD} is the FWHM of the photodiode response function and T_0 the FWHM of the input pulse. To obtain this condition, one need to know that the voltage response of the photodiode, $V(t)$ is proportional to the convolution of the photodiode response function with the incident intensity:

$$V(t) \propto \int_{-T_{rep}/2}^{T_{rep}/2} PD(t-\tau)|A(t)|^2 d\tau, \tag{2.10}$$

where $A(t)$ is the amplitude of the measured field, and $PD(t)$ is the photodiode response function. We have to notice the response time of the photodetector is much longer than the input pulse duration. Therefore the input pulse can be approximated to a Dirac function. Thus, the entire pulse goes through the photodector before this one responds. Thus, the detector only sees integrated energy of the pulse as the amplitude of the delta function:

$$|A(t)|^2 \propto E_0\delta(t), \tag{2.11}$$

where E_0 is the pulse energy. Finally, inserting Eq. 2.11 in Eq. 2.10, we obtain the following relationship:

$$V(t) \propto E_0 \int_{-T_{rep}/2}^{T_{rep}/2} PD(t-\tau)\delta(t)d\tau \propto E_0 PD(t) \tag{2.12}$$

Thus, the peak signal recorded on the oscilloscope is directly related to the optical energy of the pulse and the shape of the signal is given by the impulse response of the photodiode.

The ESA method also uses a fast photodiode but is used in order to measure the signal-to-noise-ratio (SNR) over a wide range of frequency in the electrical Fourier domain. The noise values given by an ESA are in $V/\sqrt{Hz}$. Thus, to compare them to the direct measurement with an oscilloscope, we have to transform the noise spectral density (NSD) to RIN. The first step, to normalized the NSD, is to divide it by the DC voltage given by a voltmeter. The unit of the NSD is now: $1/\sqrt{Hz}$. Now, we have to take the square of the NSD to convert it in $1/Hz$. Finally, we have to integrate the NSD of the frequency range going from the "minimum frequency" given by the ESA to the first harmonic of the laser. The transformations are written with the following equation:

$$RIN = \int_{f_1}^{f_2} \left(\frac{NSD}{V_{DC}}\right)^2 df, \tag{2.13}$$

where f_1 and f_2 represent the minimum frequency and the first harmonic frequency of the laser, respectively.

A quicker way to determine the RIN value from the NSD, given by [73], is to find the noise level of the flat part, RIN_{flat} of the normalized NSD spectrum, in unit of $\sqrt{Hz}$, and multiplied it with the repetition rate of the laser, f_{rep} :

$$RIN_{rms} \approx \sqrt{f_{rep} RIN_{flat}} \tag{2.14}$$

This approximation can only be used with high repetition rate laser because the flat part can be difficult to determine as the first harmonic can stretch all the way down to zero while using low repetition rate laser.

Like the method using an oscilloscope, to determine the spectrally resolved RIN of an SC spectrum with an ESA, one needs to use band-pass filters. During this thesis, ESA measurements were performed to determine the noise level of the laser itself, which means no band-pass filters were needed.

Each method described previously has its pros and cons. The X-FROG method is the only one that gives information on the temporal and frequency spectrum of the source. Thus, with this method, we can determine if the system is transform-limited, its RIN value, and its spectrogram but this method can be very complex to set-up. The DFT method has the advantage to give directly the spectrally resolved RIN (limited by the dispersion and length of the stretching fiber, and bandwidth of the photodiode, Eq. 2.8). Furthermore, it is very easy to obtain the statistical behavior of each wavelength bin (L-shape for optical rogue waves ...). The main issue with this technique is to use the appropriate stretching element. Indeed, considering the stretching device is an optical fiber, one needs to be very careful about the specification of the fiber. This one must have the same sign across the whole SC bandwidth (to avoid overlapping of the frequencies), the stretched pulse has to be shorter than the inverse of the repetition rate of the laser, the photodiode should have a high sensitivity to obtain a good signal-to-noise ratio and the cut-off wavelength of the fiber should be below the blue edge of the spectrum. The oscilloscope method needs band-pass filters to measure the spectrally resolved SC RIN and several photodiodes to cover the entire spectral bandwidth, i.e the silicon detects from 400 nm to 1100 nm, and the InGaAs from 800 nm to 1700 nm. This method is very quick and easy to set-up but the RIN results depend heavily on the band-pass filter bandwidth. An advantage to measure the RIN based on an oscilloscope detection is to confirm that the pulses look as expected, i.e. expected shape without ringing in the signal due to bandwidth limitations. A clear benefit of frequency-domain measurements is the ability to locate the frequency of the high noise regions. This can lead to the identification of the noise source, i.e. mechanical vibrations or power supplies, which in turn can lead to the elimination of these noise sources. Furthermore, a spectrum analyzer directly measuring in the frequency domain can operate with a narrow band filter, leading to excellent dynamic range and sensitivity. Also, analysis in the frequency domain can provide detailed information on the timing jitter. Finally, Tab. 2.1 summarizes the pros and cons of each technique.

	Average RIN	Spectrally resolved RIN	Frequency RIN spectrum	Difficulty to set-up	Pulse shape
X-Frog	✓	✓	X	✓	✓
DFT	✓	✓	X	✓	✓
Oscilloscope	✓	With filters	X	X	✓
ESA	With integration	With filters	✓	X	X

Table 2.1: Summary of the pros and cons for each noise measurement techniques.

2.2/ KNOWN LIMITS OF COHERENT SUPERCONTINUUM GENERATION

Previous studies on ANDi SC generation have already been reported [6, 9–11, 49, 74] presenting this particular case of SC generation with different configurations. In two of them, it has been reported that ANDi SC generation could not be as perfect as predicted [9, 10]. Indeed, theoretically, fs ANDi SC generation is predicted to be a fully coherent process to generate new wavelengths via SPM and OWB but this assumption is true only in a certain measure. In this section, we will give a short review of different phenomena that have to be taken into account to obtain a low-noise ANDi SC spectrum.

In Heidt *et al* [9], the authors established the first limit of ANDi SC generation, which is inherent to this method. This limit is the input pulse duration of the laser pumping an ANDi fiber. Figure 2.4 shows the logarithmic spectra and the corresponding coherence plot as a function of the input pulse duration (T_{FWHM} going from 50 fs to 5 ps) for an input peak power of 5 kW.

We observe for subpicosecond input pulse duration, the spectral dynamic is governed by coherent nonlinear effects: SPM and OWB (the coherence value is 1 across the whole spectral bandwidth). If the input pulse duration increases but the fiber length remains the same, the spectral bandwidth will be reduced because the new wavelengths by OWB can not be generated ($L_{WB} > 1$ m using Eq. 1.42). Furthermore, we can notice decoherence on the red wavelength side of the SC spectrum, which can be attributed to the SRS. For longer input pulse duration ($T_{FWHM} = 5$ ps), the spectral broadening dynamics is governed by SPM and cascaded SRS. In this case, only the SPM area of the spectrum remains coherent but the decoherence is not only due to the SRS but also to Raman assisted parametric FWM [9, 74–76].

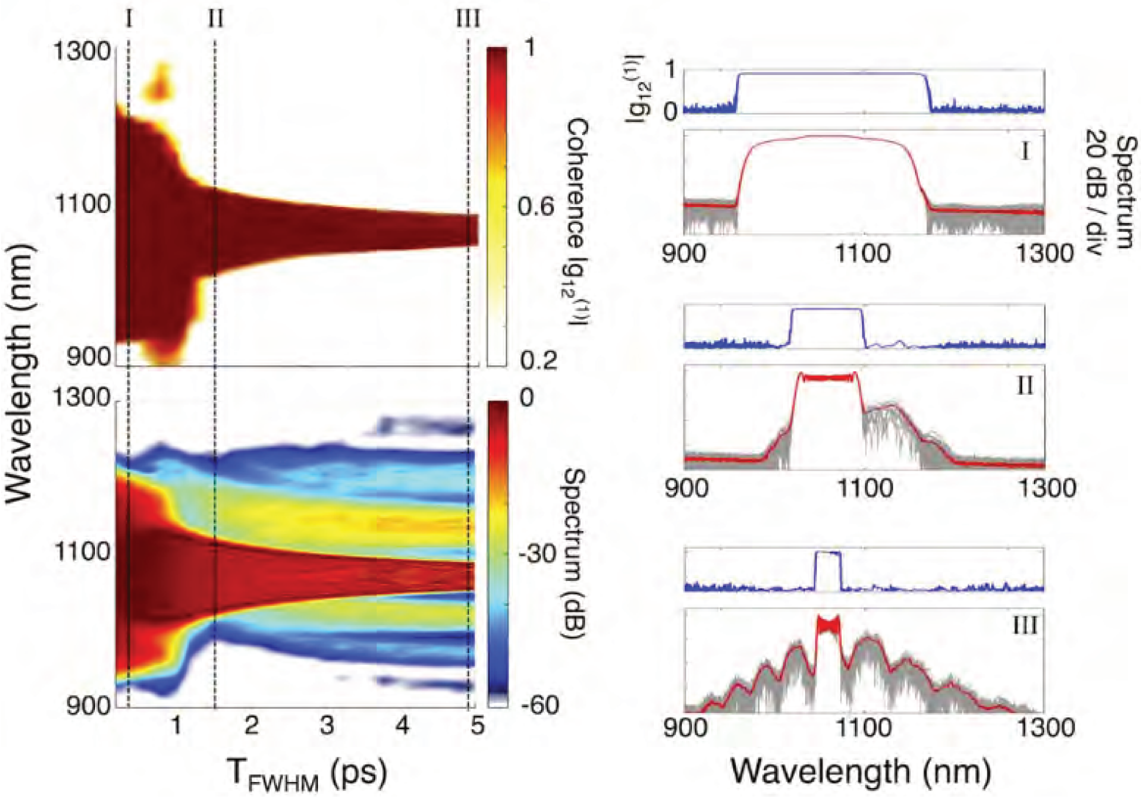

Figure 2.4: (left) SC mean spectral intensity (bottom) and corresponding spectral coherence (top) generated by a 5 kW peak power pump pulse after 1 m propagation as a function of input pulse duration T_{FWHM}. (right) Detail from (a) marked in positions I, II, and III corresponding to 200 fs, 1500 fs, and 5000 fs pulse duration, respectively. The mean spectrum is displayed in red, while the intensity fluctuations are visualized by displaying an ensemble of 20 independent simulations with different noise seeds in gray. Extracted from [9].

After this investigation of the main effects involved in the decoherence of ANDi SC generation, the authors investigate the impact of higher input peak power ($\sim$ 100 kW), i.e octave generation, on the spectral coherence, for $T_{FWHM} < 1$ ps ($N \leq 400$). The nonlinear effects responsible for spectral broadening are still the SPM and the OWB. It is evident the OWB characteristic length determines when the coherent ANDi SC generation is concluded and doesn't evolve anymore. In this regime, the maximum spectral bandwidth $\Delta\omega_{coh}$ is independent of the input pulse duration and depends only on [77]:

$$\Delta\omega_{coh} \propto \sqrt{\frac{\gamma P_0}{\beta_2}}. \tag{2.15}$$

From this equation, one can understand with a given fiber, the spectral bandwidth is only power-dependent but only for a sufficient large fiber length. Indeed, as discussed above, for a longer input pulse duration one needs to use a longer fiber length to obtain the wavelength generated by OWB. Furthermore, one can define a coherence length, L_{coh}, for which the average SC coherence is higher than 0.9 ($\langle g_{12} \rangle > 0.9$). This parameter is very large for short input pulse duration, as shown in Fig. 2.5.

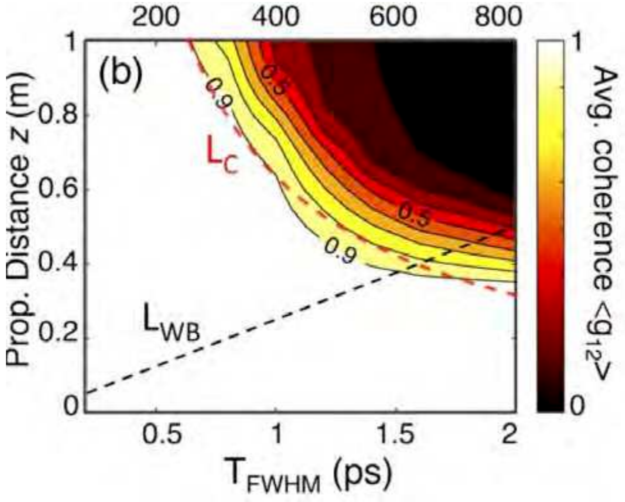

Figure 2.5: Average spectral coherence of SC pulses generated with an input peak power of 100 kW as a function of pump pulse duration and propagation distance. The wave breaking distance (dashed black line) and the coherence length (dashed red line) are also represented.

For $N \sim 250$, $L_{WB} < L_{coh}$, and a long fiber length, i.e. $L > 4L_{WB}$, the noise-seeded SRS phenomenon starts to appear. For even longer propagation length, like in the low-power case, Raman assisted FWM quickly spreads the noise also to the short wavelength side. The presence of SRS and FWM components and their overlap with the main pulse now cause noisy interference structures and large pulse-to-pulse fluctuations in both the spectral and temporal domain. the process responsible for the decoherence of the SC is the SRS as explained previously.

For $N \sim 650$, $L_{WB} > L_{coh}$, the decoherence process appears before the full spectral bandwidth of the ANDi SC is obtained. In this case, a nonlinear mixing between the SPM components, SRS, and Raman assisted FWM can be obtained due to the overlap in time of these three components. This overlap will generate new wavelengths through what can be called incoherent OWB. Therefore, coherence is never established across the SC bandwidth.

Thus, according to [9], in order to obtain a low-noise/highly coherent SC spectrum, one needs to pump an ANDi fiber with an input pulse duration shorter than 1 ps for peak power of 100 kW.

In Bravo et at [74], the authors explain that it is very important to use the measured Raman gain spectrum to estimate the coherence of numerical ANDi SC generation.

The nonlinear response of silica, $R(t)$, can be expressed as:

$$R(t) = (1 - f_R)\delta(t) + f_r h_R(t) = (1 - f_R)\delta(t) + f_r \left[R_a(t) + R_B(t)\right], \tag{2.16}$$

where f_R represents the fractional Raman contribution [44]. The first term of this equation characterizes the instantaneous electronic response while the second one is the delayed nuclear response of the material. Furthermore, h_R represents the isotropic R_a and anisotropic R_B contribution [13,45,78]. There are different Raman functions that can be used to simulate this nonlinear effect. Here is a short review of the 3 main ones which are also shown in Fig. 2.6:

- Measured Raman Gain

  This model is based on the experimental Raman Gain of silica measured at $\lambda_p^R = 526$ nm. Several similar Raman gains have also been measured at other pump wavelengths [45,79]. In this case, the fractional contribution f_R is equal to 0.18.

- Standard model

  This model is the simplest one and has been used largely in the literature and can be written as [80]

  $$h_R(t) = \frac{\tau_1^2 + \tau_2^2}{\tau_1 \tau_2^2} \exp\left(-\frac{t}{\tau_2}\right) \sin\left(\frac{t}{\tau_1}\right) \tag{2.17}$$

  with $\tau_1 = 12.2$ fs and $\tau_2 = 32$ fs. The issue with this simple model is the underestimate Raman gain for frequency shift below 10 THz and overestimate it above 15 THz.

- Q-Lin model

  This model developed by [45] corrects the underestimation of the Raman gain for frequency below 10 THz but still overestimate it above 15 THz. This model is expressed as:

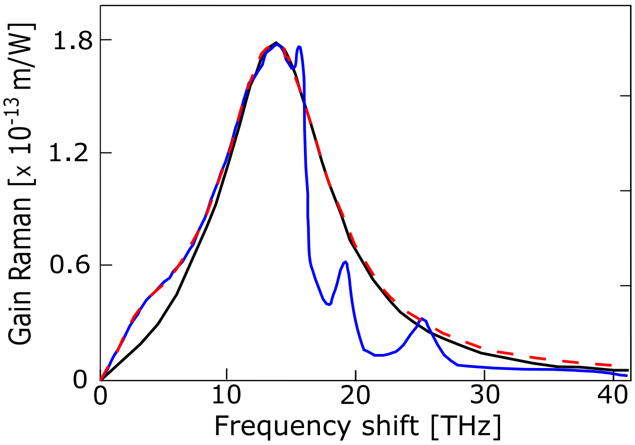

Figure 2.6: Raman gain measured at $\lambda_p^R = 526$ nm (solid blue), Classic model (solid black), and Q. Lin model (dashed red).

$$h_R(t) = f_a h_a(t) + (f_c h_a(t) + f_b h_b(t)), \tag{2.18}$$

with,

$$h_a(t) = \frac{\tau_1^2 + \tau_2^2}{\tau_1 \tau_2^2} \exp\left(-\frac{t}{\tau_2}\right) \sin\left(\frac{t}{\tau_1}\right), \quad \text{and} \quad h_b(t) = \left(\frac{2\tau_b - \tau}{\tau_b^2}\right) \exp\left(-\frac{\tau}{\tau_b}\right), \tag{2.19}$$

where $\tau_b = 96$ fs, $f_a = 0.75$, $f_b = 0.21$, $f_c = 0.04$, and $f_R = 0.245$.

As discussed before and in [66], FWM and SRS can interact with each other to generate incoherent OWB. The efficiency of this interaction is given by the mix-parametric Raman (MPR) gain and is expressed as [66, 76, 81, 82]

$$g^*(\Omega) = 2\gamma P_0 \mathrm{Re}\left[\sqrt{K(2q-k)}\right], \tag{2.20}$$

where $K = -\Delta\beta/(2\gamma P_0)$ is the linear phase mismatch normalized to the nonlinear contribution to the mismatch, $\Delta\beta = \beta_2\Omega^2 + \beta_4\Omega^4/12 + ...$ and $q = 1 - f_R + f_R h_R(-\Omega)$.

Thus, to suppress the influence of MPR on the spectral coherence of ANDi fs SC generation, one needs to use a short input pulse duration (< 400 fs) or a flat dispersion profile close to the ZDW, or a high input peak power [9, 74]. Furthermore, we highlight in all our simulations we use the measured Raman gain.

Another phenomenon that can lead to a degradation of the coherence of ANDi SC spectrum is the polarization modulation instability (PMI). This nonlinear effect is the vectorial aspect of the well-known scalar MI, which has been described in 1.2.4. Bravo *et al* [10] investigate this phenomenon and its impact on ANDi SC generation and its coherence. This section will give a short review of their investigations.

The vectorial aspect of the PMI phenomenon induces that the scalar GNLSE can not be used anymore because this model assumes all the light is polarized along with one fiber's axis and doesn't exchange its energy with the other one. Thus, in order to investigate the impact of PMI on ANDi SC generation, one needs to use a vectorial model of the GNLSE as the one described in 1.2.8. Experimental studies of PMI effects in ANDi SC generation have already been reported in weakly birefringent ANDi PCF [83, 84] but no one before [10] investigates this phenomenon in depth. Thus, in order to study this phenomenon, one needs to use a code solving the CGNLSE and align the input pulse off axes to generate PMI and especially at 45° of both fiber's axes to maximize its gain [85].

To investigate only the impact of PMI on ANDi SC generation, the authors limit the range of their simulation from 50 fs to 500 fs to suppress the impact on SRS as discussed before. Figure 2.7. demonstrates the coherent and noise properties of ANDi SC generation obtained up to 500 fs with a fiber length of 1 m with an input peak power of 44 kW. We find that for a pulse duration longer than 120 fs the decoherence process starts to appears due to the PMI effect when this one is taken into account via a vectorial model. About the RIN of the SC, this one scales drastically with the input pulse duration. Thus, one needs to use a pulse duration shorter than 120 fs to keep a low-noise SC generation. Also, to limit the impact of PMI using a long pulse duration of ≈ 300 fs, one can use a shorter fiber length ($\approx 5cm$) at the cost of the spectral bandwidth.

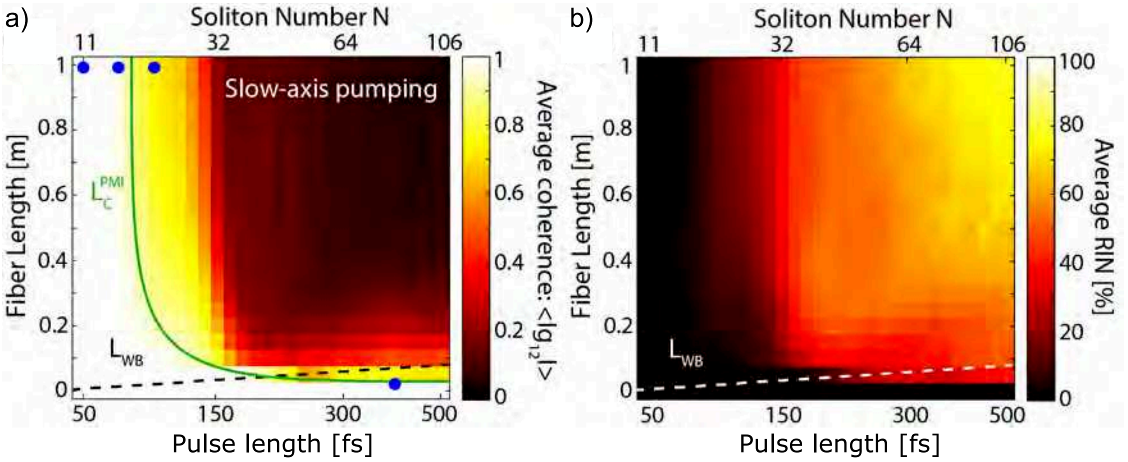

Figure 2.7: (a) Spectrally averaged coherence and (b) RIN for an ensemble of 20 simulations with an input peak power of 44 kW with input polarization along the slow-axis as a function of pulse length and fiber length using CGNLSEs solver. Extracted from [10].

Thereby, in order to limit/suppress the PMI influence, one needs to use either a femtosecond laser pumping a PM-ANDi fiber to avoid any transfer of energy from one polarization to the other one.

Finally, knowing the limitations and how to avoid them, we decided to use during this thesis a PM-ANDi PCF and different femtosecond lasers going from 90 fs to 400 fs.

2.3/ ALL-NORMAL DISPERSION POLARIZATION-MAINTAINING SILICA FIBER

In this section, we will present the PM-ANDi PCF used during this thesis. This fiber is the so-called NL-1050-NEG-PM-2 from NKT Photonics. This fiber is the PM version of the commercially available NL-1050-NEG-1 ANDi PCF. The non-PM version is well known and has been largely used in the literature [6, 51, 86, 87]. The non-PM version has been used, for the moment, for two papers [88, 89], and this will be discussed in this chapter and the next ones.

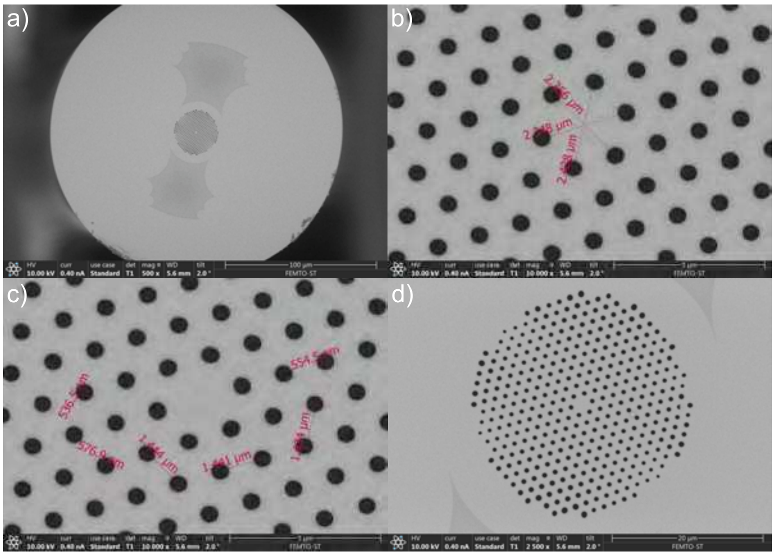

Figure 2.8: Scanning electron microscope image of the PM-ANDi PCF. a) Full image of the fiber. b) Values of the core diameter. c) Values of the pitch and hole diameter d) Zoom on the fiber facet.

Figure 2.8. presents the scanning electron microscope image of the NL-1050-NEG-PM-1, used during all this Ph.D. Furthermore, in the rest of this manuscript, this fiber will be called PM-ANDi PCF. We can notice on this image two rods in borosilicate, which induce stress to create the polarization-maintaining effect.

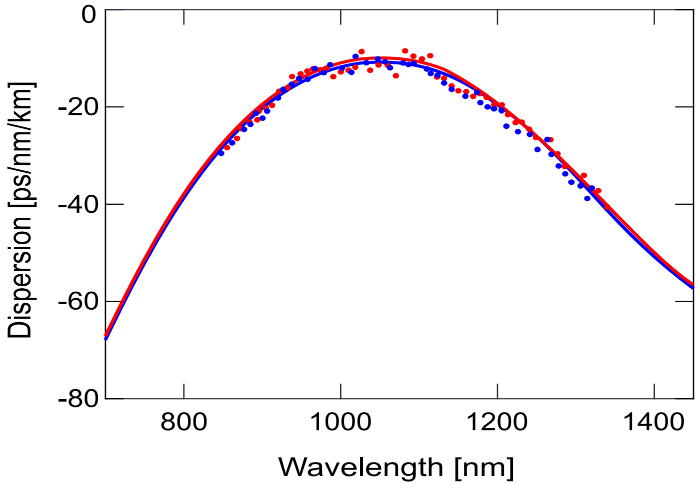

Figure 2.9: Measured dispersion profile of the NL-1050-NEG-1 PM ANDi PCF for the slow axis (red dots) and fast axis (blue dots), and their fitted dispersion profiles

From these images, we measure an average hole size of 550 nm, and an average pitch of 1.44 μm. Furthermore, we can calculate the air fraction of our fiber $d/\Lambda \approx 0.38$, with a 10 rings hexagonal structure. Thus, from Eq. 1.4, we can determine that our fiber is endlessly single-mode (d/Λ = 0.38 $<$ 0.45).

The dispersion profile of our fiber was measured using white light interferometry, as described in [90] and shown in Fig. 2.9 (red and blue dots). We can see the average dispersion profile is slightly smaller on the slow axis than on the fast axis but the uncertainties on their values are also high so we can - within experimental error - assume the same dispersion profile for both polarizations (dashed blue curve in Fig. 2.10).

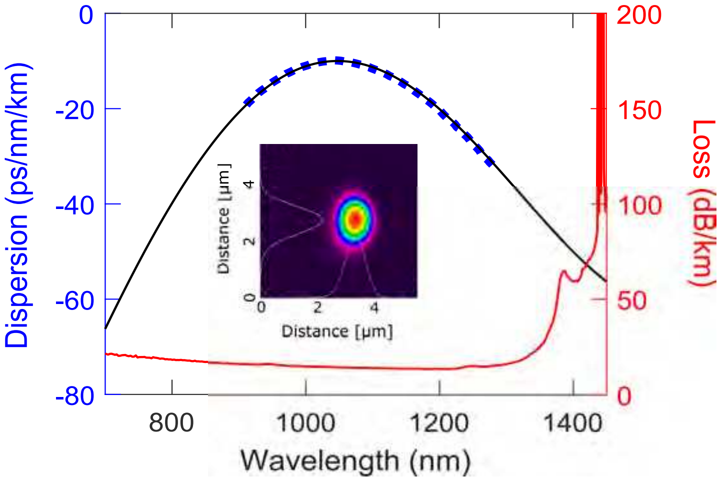

Figure 2.10: Average measured (dashed blue) and modelled (solid black) dispersion profile, and measured fiber loss profile (solid red) of the NL-1050-NEG-1 PM ANDi PCF. The inset shows the MFD measurement.

The calculated dispersion profile was obtained using COMSOL Multiphysics (black curve in Fig. 2.10). As expected, the small holes of the PCF give a confinement loss edge (red curve in Fig. 2.10) significantly below the material loss edge, here found to be at 1450 nm this will significantly influence the long-wavelength part of the intensity and noise profiles. The stressed-induced rods used to obtain the PM version of this fiber give rise to an asymmetry of the mode field diameter (MFD) along each optical axis, as shown in inset in Fig. 2.10 . Due to this asymmetry, the nonlinear coefficient on each axis is different (0.0272 $m^{-1}W^{-1}$ for the slow axis and 0.0255 $m^{-1}W^{-1}$ for the fast axis) thus the SC bandwidth should be broader on the slow axis than on the fast axis.

2.4/ EFFECT OF TECHNICAL NOISE ON RELATIVE INTENSITY NOISE AND TEMPORAL COHERENCE

This subsection will focus on a numerical study where we use a single-polarization scalar model in the form of the standard GNLSE to model the propagation of the envelope function. We choose to ignore the effect induced by polarization instability like PMI to investigate, in isolation, the effects of technical noise on the RIN/coherence of fs ANDi SC generation.

The first noise considered in this study is the well-known quantum noise δ_{QN} arising from vacuum fluctuations. This quantum noise is modeled semiclassically as the standard one-photon per mode (OPM) white noise and commonly used in numerical simulations of SCG [1,62] (this model is always used in all simulations performed in this thesis). This model has been introduced by R. G. Smith [62] where he demonstrated that including this noise model on the input fields accounted for the observed Raman amplification of spontaneous emission in the optical fiber. The principle of this model is to add to the initial condition in the Fourier domain a photon with random phase and intensity in each spectral bin.

The envelope of the one-photon-per-mode field in the frequency domain is written as [62]:

$$\delta_{\mathrm{QN}} = \sqrt{\hbar\omega_m/\Delta\Omega}e^{2i\pi\Phi_m}, \tag{2.21}$$

where $\hbar$ is the reduced Planck's constant, Φ_m is a random number, Gaussian distributed in the interval [0,1] in each angular frequency bin ω_m and having a bin size $\Delta\Omega$. The noise is transformed back to the time domain and added to the input envelope field as:

$$E_0 = A_0 + \mathscr{F}^{-1}\left(\delta_{QN}\right), \tag{2.22}$$

with $A_0 = \sqrt{P_0}\mathrm{sech}\left(t/T_0\right)$, and $\mathscr{F}^{-1}$ the inverse Fourier transform.

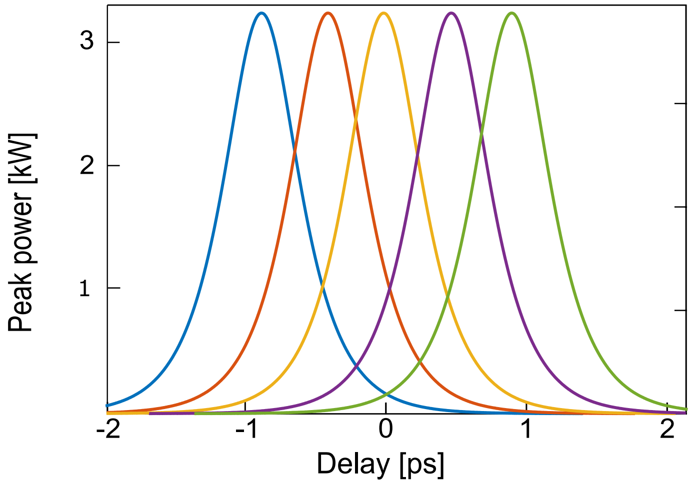

Figure 2.11: Representation of the timing jitter effect showing the delay between pulses in the time domain. The maximum timing jitter value is 1 ps.

Another source of noise presents in mode-locked laser is the timing jitter which can be modeled by doing a convolution with a Dirac function in the time domain of the input field or multiplying it with a frequency-phase in the Fourier domain which could be written as:

$$E(t+\tau) = E(t) \otimes \delta(t-\tau) = \mathscr{F}^{-1}\left(\tilde{E}(\nu)e^{i\tau f}\right), \tag{2.23}$$

where τ represents the timing jitter value of the laser and $\mathscr{F}^{-1}$ the inverse Fourier transform. A more physical way to understand the timing jitter effect is to picture it as a variation of the repetition rate of the laser which means the duration between two emitted pulses will be different from pulse to pulse as described in Fig. 2.11. As an example, if you consider a mode-locked laser with a repetition rate of 10 MHz and with a timing jitter value of 1 ns, it will mean the duration between two pulses will vary from 99 ns to 101 ns.

Fortunately, timing jitter in femtosecond mode-locked lasers can be very small which is especially true for the lasers used in this study (hundreds of attosecond, see Fig. 2.12). The Origami LP femtosecond laser datasheet can be found in [91]. Thus, we can neglect this effect when we will investigate the technical noise effect on the SC RIN and coherence.

In addition to timing jitter, amplitude noise/intensity noise, arising from fluctuations in the laser pump's diode of a laser can be a problem to obtain a low-noise SC system as

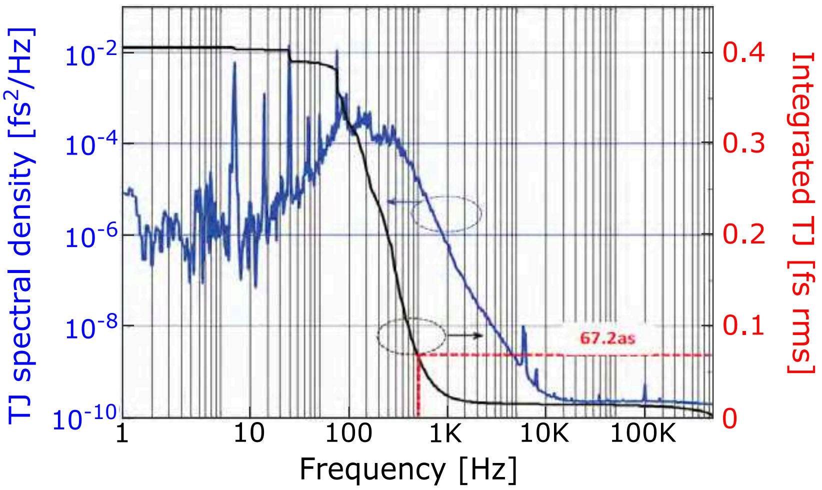

Figure 2.12: Measured timing jitter (TJ) spectral density for an Origami 15 LP from NKT Photonics and its integrated timing jitter for the frequency range f= 1 Hz-1 MHz.

nonlinear effects are strongly dependent on the pulse intensity. The equation describing the amplitude noise of the laser is given by:

$$E_{AN}(t) = E(t) \times (1 + \delta_{AN}), \tag{2.24}$$

the laser amplitude fluctuations described by $\delta_{\mathrm{AN}} = \Psi$, where Ψ is a single random value for each input pulse, extracted from a Gaussian distribution with a zero mean and a standard deviation equal to the root mean square (RMS) amplitude noise of the modeled laser, given by the manufacturer of the laser. This amplitude noise effect is represented in Fig. 2.13 using an amplitude noise value of 5%. Also, typical commercially available mode-locked lasers report an intensity noise value of 1% thus we need to find a formula

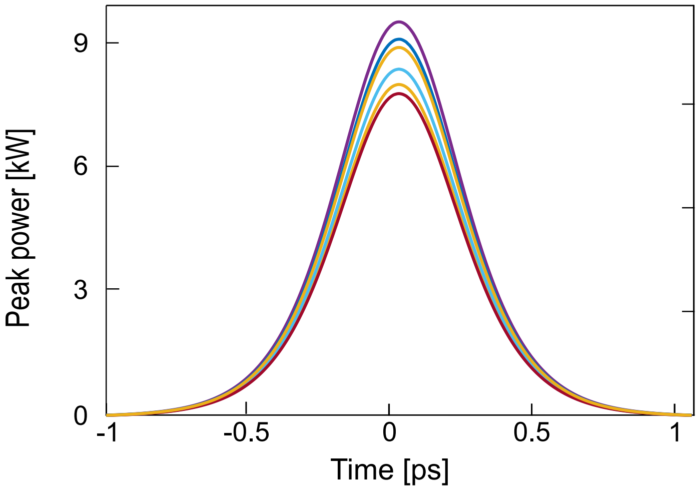

Figure 2.13: Representation of the amplitude noise effect showing the peak power difference in the time domain. The maximum output intensity noise value is 10 %.

linking intensity noise and amplitude noise in order to compare both:

$$\begin{aligned} I_{AN} = E_{AN}^2 &= I(t) * (1+\delta_{AN})^2 \quad \delta_{AN} << 1 \\ &\approx I(t) * (1+2\delta_{AN}) \\ &\approx I(t) * (1+\delta_I) \\ &\Rightarrow \delta_I \approx 2\delta_{AN}. \end{aligned} \tag{2.25}$$

Thus, there is a factor 2 between RIN and amplitude noise. Finally, in this study, we will consider a range of RMS amplitude noise going from 0.1% to 2%.

To correctly consider the effects of laser amplitude fluctuations on the SC, it is important to take into account any correlated fluctuations of the pulse duration, which occur in a mode-locked laser. This is important to model, as pulse duration fluctuations will subtly affect the efficiency of SPM, and thus the output spectral shape and width. To estimate the correlation of the fluctuations, we use the deterministic correlation between average power and spectral bandwidth experimentally measured in an Origami 10 fs mode-locked laser, shown in Fig. 2.14. Assuming a fixed repetition rate and a state of anomalous dispersion soliton mode-locking, producing approximately transform-limited sech-shaped pulses, we then find the linearized relation between peak power and pulse length (more detailed in App. 2). Assuming then that this relation holds during the fluctuations, we obtain the following relationship:

$$\delta_{T_0} = -0.8 * \delta_{\mathrm{AN}}, \tag{2.26}$$

where δ_{T_0} is a Gaussian distribution centered in 0 having a standard deviation equal to 0.8 times δ_{AN}. The peak power and pulse duration of a mode-locked laser are thus anti-correlated, which is extremely important for the SC noise, as we shall see in the following. We note that the value of 0.8 is specific to the laser considered, but can be generalized for other kinds of lasers.

Thus, when both noise terms are included our initial condition becomes:

$$A\,(0,t) = \sqrt{P_0(1+\delta_{\mathrm{AN}})}\mathrm{sech}\,(t/(T_0(1-0.8\times\delta_{\mathrm{AN}}))) + \mathscr{F}^{-1}\{\delta_{\mathrm{QN}}\}. \tag{2.27}$$

Here and in the following the Fourier transform of a function is denoted by a tilde and defined as $\tilde{A}(z,\omega) = \int_{-\infty}^{\infty} A(z,t)\exp(i[\omega-\omega_0]t)dt$, where ω_0 is the pump angular frequency.

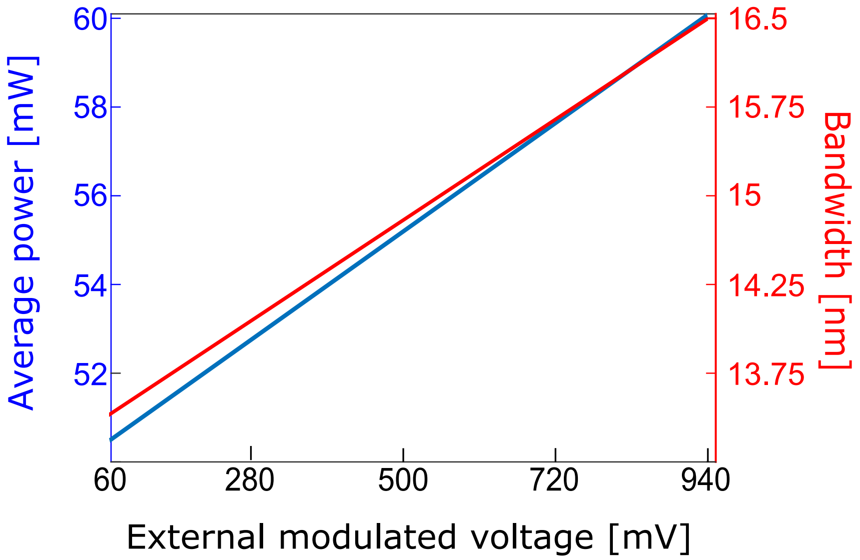

Figure 2.14: Average power (blue curve) and bandwidth (red curve) of the Origami LP as a function of the external modulated voltage.

In previous papers talking about coherence and/or RIN in ANDi SC generation [6, 10], it appears the authors choose an ensemble size of 20 pulses to calculate the coherence or the RIN of their SC without explaining why they choose this number. Thus, we decided to investigate the impact of the ensemble size on the RIN and coherence values. For this, we performed 10 sets of independent SC simulations for different ensemble sizes (2, 5, 10, 20 and 40) to calculate the mean and standard deviation of the average RIN and coherence value. We used for these simulations the following input parameters: pulse duration $T_0 = 400$ fs, peak power $P_0 = 100$ kW, fiber length $L = 40$ cm, amplitude noise $\delta_{AN} = 0.5$ % and the dispersion profile of our PM-ANDi fiber. We choose a pulse duration where the SRS starts to appear in order to highlight the ensemble size's impact on the RIN/coherence value. Thus, Fig. 2.15 shows the evolution of the mean and standard deviation (std) of the RIN and g_{12} parameter of our SC generation.

We demonstrate in Fig. 2.15 that the mean of the coherence/RIN decreases/increases when the ensemble size increases (from 0.74 to 0.47 for the coherence and from 4.41 % to 5.1 % for the RIN). In statistics, if the ensemble size is high enough, the mean should not change whatever the size of the ensemble [92]. In our case, the ensemble size doesn't satisfy this condition thus the mean of this ensemble can vary. Furthermore, it is normal that the mean's evolution of the coherence and RIN are anti-correlated because when the RIN is high the coherence of an SC drops. Also, we observe that, as expected, the standard deviation of our ensemble reduces when this one increases (from 0.2 to 0.01 for the coherence and from 2.08 to 0.056 for the RIN). In theory, the decrease in the standard deviation should follow a curve in $\sqrt{N}$, where N is the ensemble size [92].

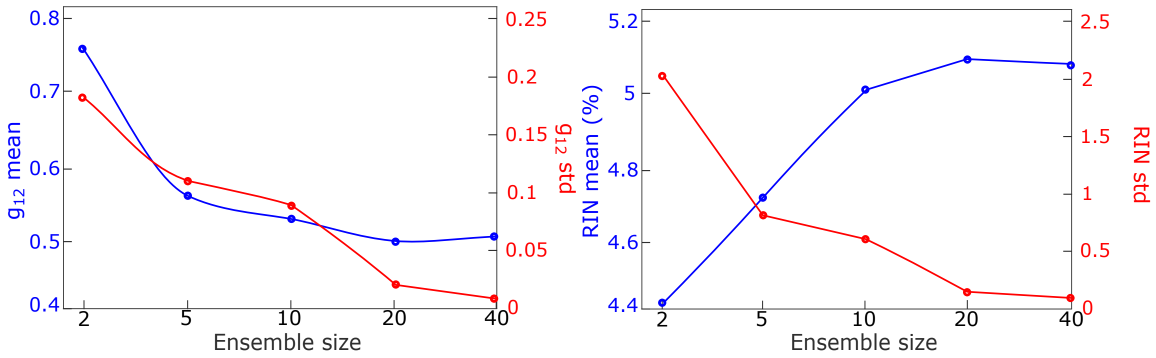

Figure 2.15: a) Evolution of the g_{12} mean (blue dots) and standard deviation (red dots) value as a function of the ensemble size. b) Evolution of the RIN mean (blue dots) and standard deviation (red dots) value as a function of the ensemble size. The input simulation parameters are: $T_0 = 400$ fs, $P_0 = 100$ kW, $L = 40$ cm, $\delta_{AN} = 0.5$ % and dispersion profile of our PM-ANDi fiber.

We can notice there is a small difference between the RIN and g_{12} mean and std values between an ensemble of 20 or 40. Of course, in order to obtain a better accuracy of the RIN/coherence value, one should use a bigger ensemble size but the trade-off appears in the computation time needed for these simulations (the better the longer). Thus, we decided, for all our simulations, to use an ensemble size of 20 SC, which allows us to compare our results to the ones already published [6, 10]. After this brief explanation of the impact of the ensemble size, we will investigate the impact of technical noise on the RIN/coherence of an SC.

In Fig. 2.16, we show the numerically found SC spectrum out of 1m of ANDi fiber generated by a pump laser with an average peak power and pulse duration of P_0 = 100

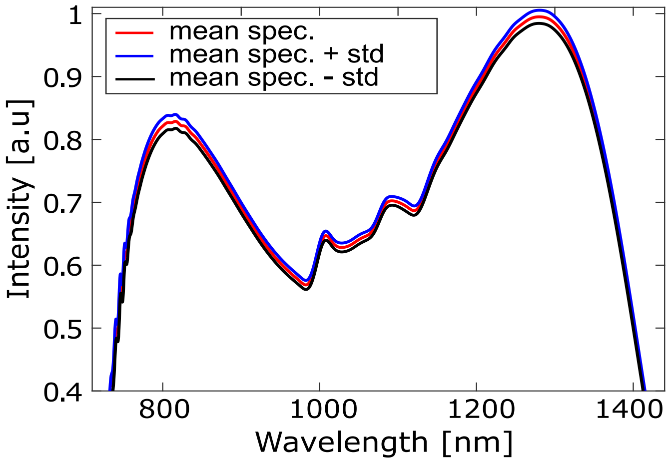

Figure 2.16: Numerical SC spectra generated in 1 m of ANDi fiber with a 1054 nm pump with an average peak power and pulse duration of P_0=100kW and T_0=50 fs, respectively. An amplitude noise of 0.5% was used, corresponding to a pulse duration noise of 0.4%.

kW and T_0 = 50 fs, respectively, and an amplitude and corresponding anti-correlated pulse duration noise of 0.5 % and 0.4 %, respectively. We used an ensemble of 20 simulated pulses to calculate the mean and standard deviation for each wavelength and show in Fig. 1(b) the mean and the mean +/- the standard deviation. The results show that with only a small pump laser amplitude noise of 0.5%, fluctuations in the SC spectrum are already noticeable. The calculations were repeated with 40 and 80 pulses in the ensemble and no noticeable change was found, which means that the statistics can be trusted (as shown in Fig. 2.15).

In ANDi SC generation, it has been shown that the pulse duration, fiber length, and peak power have a critical influence on the noise properties [6, 10], e.g., the anticipated coherent spectra are only obtained for sufficiently short pulse durations and fiber lengths. To see the effect of pump laser amplitude noise on the coherence and the requirements on the fiber length and pulse parameters, we simulate a wide parameter space and calculate for each case the spectrally averaged coherence given by [1, 9] and discussed previously.

In Fig. 2.17, we plot the color-coded spectrally averaged coherence $\langle|g_{12}|\rangle$ versus the pulse duration and fiber length, for a fixed weak amplitude noise of 0.3% (giving an anti-correlated pulse duration noise of 0.24%). As is typical of ANDi-SC sources, the coherence decreases when either the pulse duration or fiber length is increased [9, 10]. However, unlike earlier single-polarization studies without amplitude noise, we observe in Fig. 2.17 a considerably limited range of parameters where the noise is low, defined

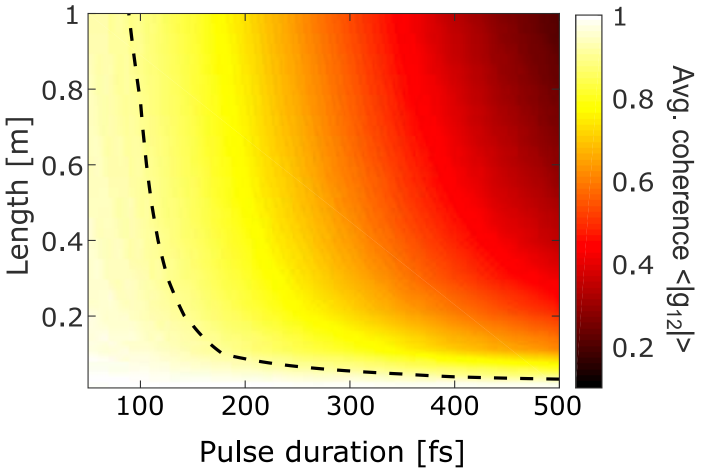

Figure 2.17: Average spectral coherence $\langle|g_{12}|\rangle$ of SC pulses generated with P_0=100 kW peak power pump pulses as a function of pump pulse duration T_0 and propagation distance for an amplitude noise value of 0.3 % (pulse duration noise 0.24 %). The dotted line indicates the limit $\langle|g_{12}|\rangle$=0.9.

as when the spectrally averaged coherence $\langle|g_{12}|\rangle$ is higher than 0.9 (dashed line in Fig. 2.17). In particular, good coherence is seen to require pulse durations below 100 fs, which is an order of magnitude shorter than the corresponding limit found without this even weak laser amplitude noise of 0.3% [9, 10].

In Fig. 2.18, we show the low noise limit $\langle|g_{12}|\rangle = 0.9$ for amplitude noise levels between 0.1-1 % (pulse duration noise from 0.08 to 0.8%). From Fig. 2.18 we see that for amplitude noise levels higher than 1% an average coherence of 0.9 cannot be obtained for any reasonable fiber length. From this, we can see clearly the dramatically limiting effect that the addition of standard laser noise levels has on the coherence parameter space. Significantly, Fig. 2.18 does not show a contour line for the case when only OPM noise is present because there is no loss of coherence observable until pulse durations as long as 1 ps, as also shown by Heidt *et al.* [9].

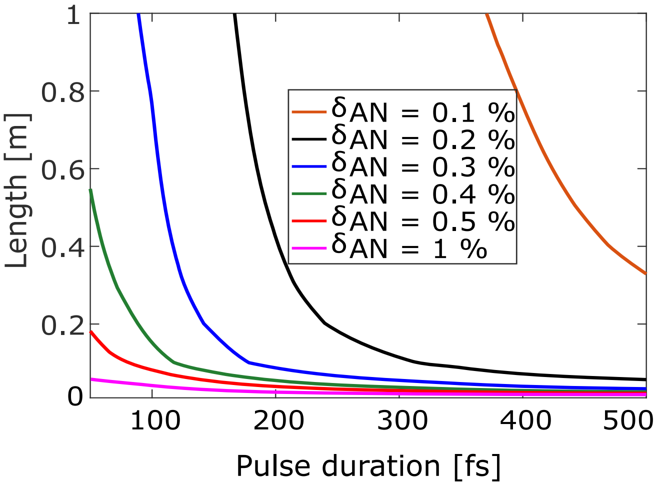

Figure 2.18: Limit $\langle|g_{12}|\rangle$=0.9 for a range of amplitude noise values from 0.1-1 % (pulse duration noise 0.08-0.8%).

It is interesting to look into the specific spectral structure of the ANDi noise. To do so we consider the experimentally more relevant RIN, which is typically used to characterize the noise of an SC source and defined in 2.4. Figure 2.19 shows the mean of the intensity spectrum and the RIN(ω) of an SC generated with 100 kW, 50 fs pulses at 1054 nm for a reasonably long fiber length of 1 m for pump laser amplitude noise levels of 0.1, 0.5, and 1.0%.

We see that in all cases the RIN is low for the majority of the bandwidth, but increases strongly at the edges as expected. Two things are interesting to note: First, for the weaker amplitude noise levels of 0.1 and 0.5%, the RIN at the red edge is significantly lower than the RIN at the corresponding blue edge (e.g., the 0.6 intensity level for 0.5%

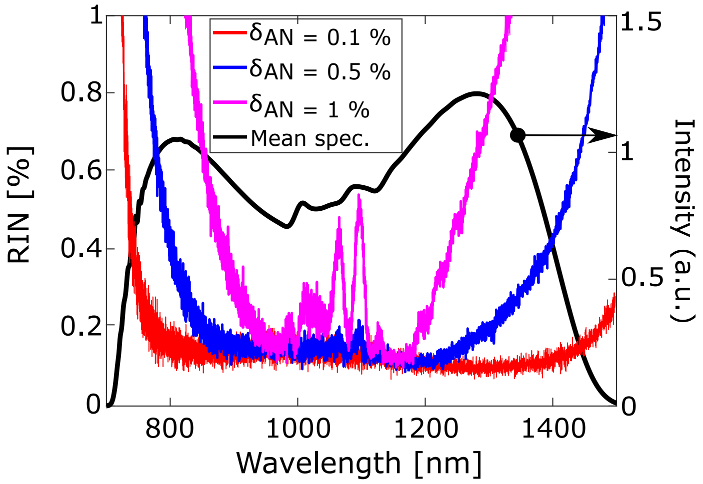

Figure 2.19: RIN profiles for different amplitude noise values and mean spectral profile out of 1 m of ANDi fiber pumped with 100 kW peak power, 50 fs long pulses at 1054 nm.

noise). This is because the loss at the red edge is much higher than at the blue edge due to the strongly increasing confinement loss at 1450 nm. Indeed, if we omit fiber losses from our model, we find similar RIN values at the two spectral edges. We note that the impact of the long-wavelength loss edge was studied previously in conventional anomalous dispersion SC generation, in which it was also found to reduce the noise, here, by suppressing rogue wave generation [93].

Secondly, we see in Fig. 2.19 a signature of peaks in the spectrum being correlated with peaks in the RIN profile. This correlation becomes even more pronounced at shorter fiber lengths where SPM is dominating, and generates a periodic spectrum and RIN

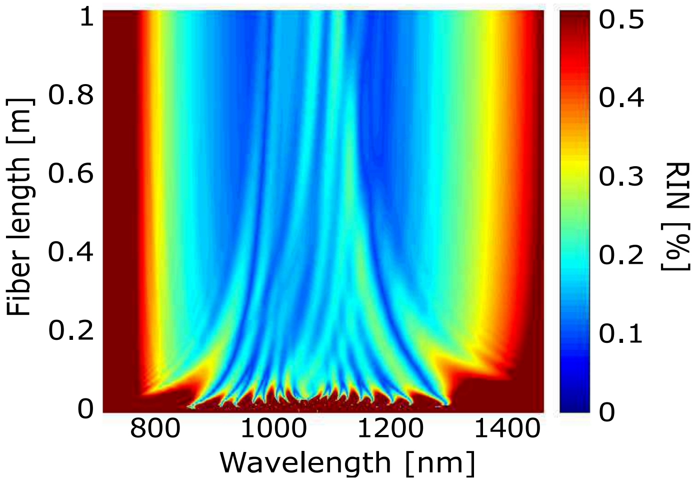

Figure 2.20: Evolution of the RIN along the fiber length for an amplitude noise value of 0.5% (pulse duration noise 0.4%). NB: The color map has a dynamic range limited to a RIN equal to 0.5%, meaning RIN data is only visible for wavelengths 800-1430 nm.

profile, as is visible in the initial 20 cm of the propagation shown in Fig. 2.20, which is a colormap of the spectral RIN evolution as a function of the fiber length. We note that while the average RIN increases during the propagation, the spectrally resolved RIN in the central region of the spectrum decreases with the propagation, with the higher RIN quotients being pushed to the edges of the spectrum.

In Fig. 2.21 we show the mean spectrum and the RIN profile after 10 cm of propagation and draw vertical lines from the peaks in the RIN profile to the corresponding point in the mean spectrum (OPM noise was removed for better clarity). The correlation is very clear here as a closely matched periodicity and it appears that when SPM is dominating the influence of amplitude and pulse duration noise is to generate strong RIN peaks close to the fringes with a maximum slope in the spectrum. We again used 20 pulses in the ensemble and the calculations were repeated with 40 and 80 pulses in the ensemble, which revealed no noticeable change. This means that the RIN statistics is converged and can be trusted.

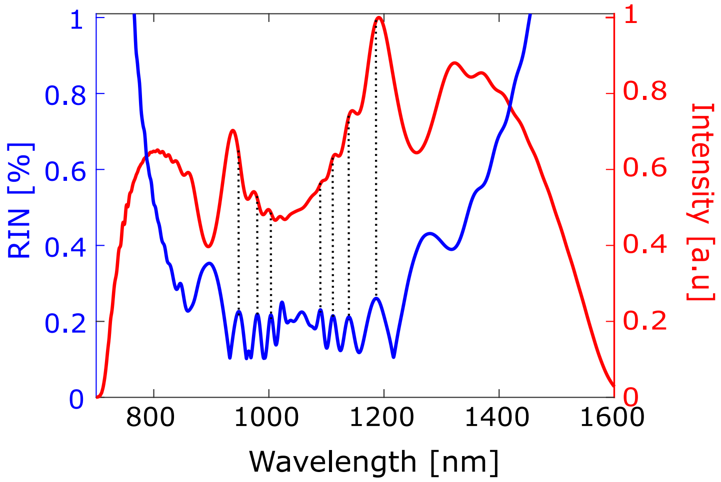

Figure 2.21: RIN profile (blue line) and mean spectrum (red line) of an ensemble of 20 pulses after 10 cm of fiber with 100 kW peak power, 50 fs pulse duration at 1054 nm for an amplitude noise value of 0.5 % (pulse duration noise of 0.4%).

A very interesting and counter-intuitive fact seen in Figs. 2.19 and 2.21 is that across the bandwidth, away from the edges, the noise level of the generated ANDi SC is lower than the laser amplitude noise imposed on the initial condition. This has, in fact, also been observed experimentally in a recent work on ANDi SC generation with a 1550 nm mode-locked laser [11], but never explained. To explain it we need to look deeper into the SPM-based SC generation and the effects of the anti-correlated amplitude and pulse duration noise separately and together.

Let us consider the exact solution for SPM, which with our initial condition is given by $A(z,t) = \sqrt{P_0}\mathrm{sech}(t/T_0)\exp(i\gamma P_0 \mathrm{sech}^2(t/T_0)z)$. Expanding the sech^2 function in the exponent around its maximum derivative, which corresponds to the maximum frequency shift, one finds $\phi(x) = \mathrm{sech}^2(x) \approx \phi_0 + \phi_1(x - x_0) + \phi_2(x - x_0)^2$, where $x_0 = 0.66$, $\phi_1 = -0.77$, and $\phi_2 = 0$. This gives the Fourier transform

$$|\tilde{A}(\omega)|^2 = P_0 T_0^2 \left| \int_0^{+\infty} \mathrm{sech}(x) \left(e^{i(\omega-\omega_0+\Delta\omega)T_0 x} + e^{-i(\omega-\omega_0+\Delta\omega)T_0 x} \right) dx \right|^2 , \tag{2.28}$$

where the frequency shift is given by $\Delta\omega = -0.77\gamma P_0 z/T_0$. This expression can be used to study the RIN due to amplitude and pulse duration noise, which is basically how much $|\tilde{A}(\omega)|^2$ changes under a change in P_0 and/or T_0.

First of all, we see that the frequency shift increases with increasing peak power and/or decreasing pulse duration, as is well-known. Thus an increasing (decreasing) peak power and correlated decreasing (increasing) pulse duration will act together on the frequency shift and lead to a strongly increasing (decreasing) frequency shift. This will in itself lead to a periodic change in the spectral intensity $|\tilde{A}(\omega)|^2$ and thus a periodic RIN.

Let us now look at two simple special cases: (1) At the input $z = 0$ the frequency shift is zero and the solution becomes $|\tilde{A}(\omega)|^2 = \pi^2 P_0 T_0^2 \mathrm{sech.}^2(\pi T_0[\omega - \omega_0]/2)$. Since T_0 will decrease when P_0 increases (and vice versa) according to Eq. (2), we see that at the center frequency the amplitude and anti-correlated pulse duration noise act against each other, i.e., they will tend to eliminate each other. (2) If we consider sufficiently large propagation distances, so that the frequency shift $\Delta\omega$ is large, then we can neglect the first (second) exponential in Eq. (6) when $\omega \approx \omega_0 + \Delta\omega$ ($\omega \approx \omega_0 - \Delta\omega$), because the exponential will be rapidly oscillating. In other words, the two outer slopes in the SPM spectrum can be treated in isolation. In this case, the approximate solution for the long-wavelength SPM slope is $|\tilde{A}(\omega)|^2 = (\pi^2/4)P_0 T_0^2 \mathrm{sech}^2(\pi T_0[\omega - \omega_0 + \Delta\omega]/2)$. At the peak, we, therefore, see that again the amplitude and anti-correlated pulse duration will act oppositely and tend to cancel each other. The fact that the RIN is lower than the pump laser amplitude noise is thus to be expected from theory and due to the anti-correlated pulse duration noise.

Finally, Fig. 2.22 compares the impact of the different noise sources including OPM, pulse duration, and amplitude noise, on the RIN spectrum. We clearly see when all the noise sources are included (blue curve) the RIN level is lower than in isolation (red and pink curves), except for OPM noise (black curve).

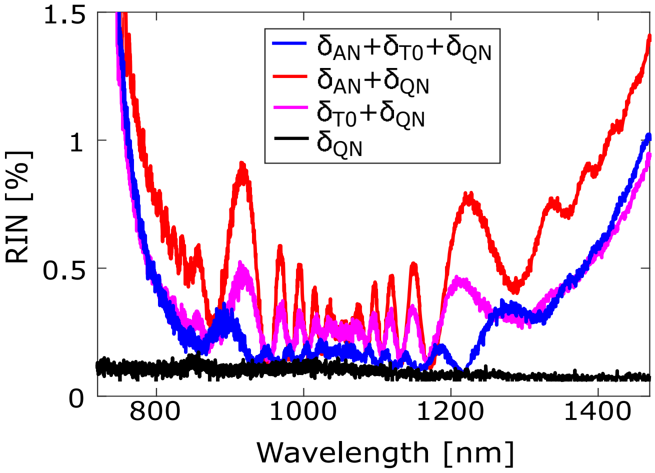

Figure 2.22: RIN spectra as a function of the input noise : OPM only (black line), amplitude noise plus OPM noise (red line), pulse duration noise plus OPM (pink line) and amplitude noise plus pulse duration noise and OPM (blue line).

With this final statement, we need to understand how noise suppression and coherence collapse fit together. For this, Fig. 2.23 depicts the input vs output RIN/intensity in the spectral domain a) and time domain b). We observe a clear noise suppression between the input and output of the fiber in both domains. Thus, the only explanation for the coherence degradation is an increase of the phase noise, which counterbalances the RIN suppression. Also, if we take a look at Eq. 2.28, we understand that fluctuations in P_0 and/or T_0 introduce(s) linear phase fluctuation i.e timing jitter. Furthermore, the timing jitter is linearly proportional to the RIN of the pump laser (and to input pulse duration fluctuations). Also, we note that the impact of timing jitter-induced by RIN and/or pulse duration fluctuations on the compression factor in ANDi SC generation has been recently investigated by Sierro *et al* [94].

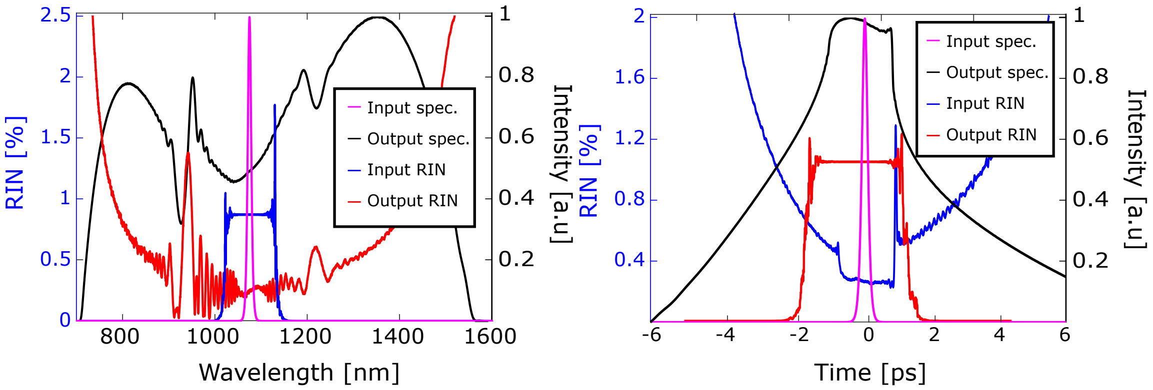

Figure 2.23: Comparison between input and output RIN/intensity in a) spectral domain and b) temporal domain with the following input parameters: pulse duration T_0 = 190 fs, peak power P_0= 35 kW, fiber length L = 80 cm and amplitude noise δ_{AN} = 1 %.

In conclusion, we have presented a detailed numerical study of the impact of pump laser amplitude noise on the coherence of the SC generated in ANDi PCFs with femtosecond high peak power mode-locked pump lasers. In particular, we have shown that considering nominal values of amplitude noise drastically affects the SC coherence on the spectral edges. Indeed, when only one-photon-per-mode quantum noise is taken into account, the coherence first starts to degrade for pulse durations above 1.2 ps, while if a weak pump laser amplitude noise of 0.5 % is taken into account, the degradation starts already at a pulse duration of $\sim$ 50 fs.

We have looked into the specific spectral profile of the RIN of a typical low-noise ANDi SC (50 fs pulse duration, 100 kW peak power) and found that it strongly increases towards the spectral edges of the SC, as expected, but much less so on the red edge than the blue edge. We found that this is due to the noise suppression effect of the long-wavelength confinement loss edge of the ANDi PCF, occurring already at 1450 nm due to the small holes of the typical ANDi PCF we considered.

In the central part of the low-noise ANDi SC, we demonstrated that the peaks in the SC spectrum are correlated with the peaks in the RIN spectrum and that this correlation is especially apparent at shorter fiber length where SPM is dominating and the RIN profile is periodic. In particular, we demonstrated numerically that the SC noise in the central part is lower than the considered pump laser amplitude noise and that this is due to a competition between the amplitude and anti-correlated pulse duration noise, which in combination gives a lower noise than in isolation. We confirmed analytically that this should be so and that it is due to the anti-correlation of the amplitude and pulse duration of the pump laser. Furthermore, we determined that the timing jitter is the main responsible of coherence degradation when we take into account amplitude noise and/or pulse duration fluctuations.

This study of the absolute values and finer details of SC noise in ANDi fibers is of substantial value to potential applications, such as optical coherence tomography (OCT) and metrology, which require ultra-low-noise SC light sources. Indeed, this study constitutes the first in-depth look into the effect of technical noise sources on the ANDi SC process and provides grounds for further research to achieve a better understanding of these physically complex processes.

3

CROSS-PHASE MODULATION INSTABILITY SEEDED BY SUPERCONTINUUM GENERATION

In this chapter, we investigate SC generation in a PM-ANDi silica photonic crystal fiber with a Ti:Sa femtosecond pulsed mode-locked laser (Coherent Chameleon) with the intention to suppress PMI. However, in doing this, we discovered the generation of a sideband outside the SC bandwidth which was not observed in previous PM-ANDi SC generation [95, 96]. We identify this sideband as the result of cross-phase modulation instability (XPMI) process that builds up from coherent SC generation and OWB [97]. As described in [98, 99], XPMI is usually observed when a beam is launched at a 45° from the principal axis of highly birefringent fiber. This beam is then split into two linearly polarized modes on each axis that will nonlinearly interact with each other to generate two frequency-detuned and cross-polarized four-wave mixing sidebands [98]. However, this XPMI process has never been observed before through the stimulation of fs-SC generation but only via spontaneous generation of the interaction of picosecond or nanosecond pulses.

3.1/ EXPERIMENTAL INVESTIGATIONS OF XPMI IN FEMTOSECOND ANDI SC GENERATION

The experimental setup used to observe and analyze SC and XPMI generation in the PM-ANDi PCF is shown in Fig 3.1. As a pump laser, we used a Ti:Sa femtosecond pulsed laser (Coherent Chameleon) tunable from 680 nm - 1080 nm, delivering 200 fs pulse duration at an 80 MHz rate with a maximum average power of 450 mW at 1040 nm. The output power is controlled using a variable neutral density filter (ND). A half-wave plate is used to turn the input polarization state at the fiber input while the polarizer at the output of the fiber is used to observe the spectral content of the light of each axis. A 40x microscope objective is used to couple the light into the 40 cm of PM-ANDi PCF. A set of 2 aspheric lenses is used to collimate the output beam and then focus it on the multimode pick-up fiber.

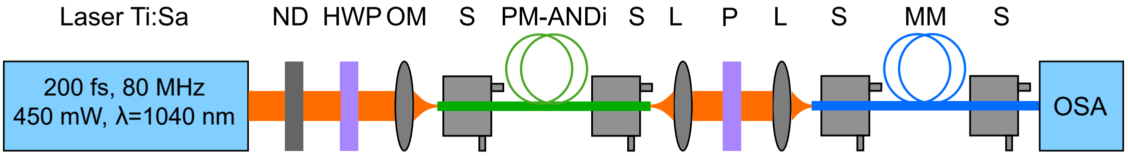

Figure 3.1: Schematic of the setup, including a wavelength tunable Ti:Sa femtosecond laser, a variable neutral density filter (ND), a half wave plate (HWP), a 40x microscope objective (OM), aspheric lenses (L), 3D translation stages (S), 40 cm of all normal dispersion PCF (PM-ANDi), a polarizer (P), 2 m of multimode pick-up fiber (MM), and an optical spectrum analyzer (OSA).

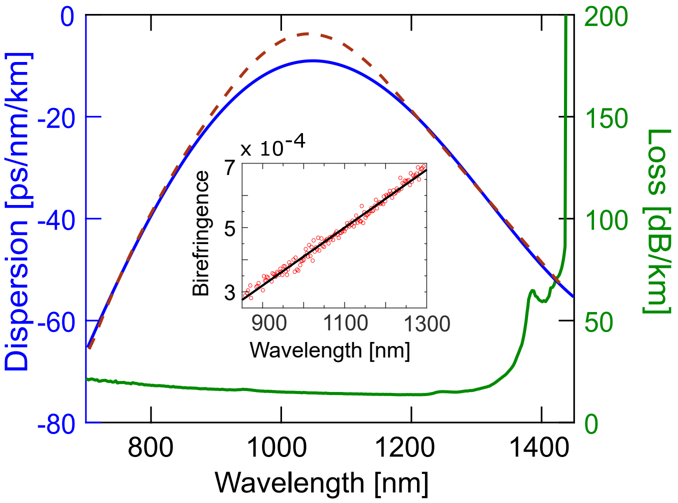

Figure 3.2: Comsol (solid blue) and modeled (dash brown) dispersion profiles, and fiber losses (solid green) of the NL-1050-NE-PM ANDi PCF. The inset shows the dispersion of the group birefringence: the linear fitting (solid black) and measured data (circles red).

The fiber's dispersion profile, shown in Fig. 3.2 (blue curve), is again the one from the PM-ANDi fiber. The polarization-maintaining effect of this fiber is stress-rod induced, with a slight degree of core-ellipticity that causes a linearly increasing birefringence [100] which goes from 2.5.10^{-4} at 850 nm to 6.8.10^{-4} at 1300 nm, as shown in the inset in Fig. 3.2 (red circles).

We pumped the fiber at 1040 nm, at the maximum dispersion wavelength (MDW), thus we should expect the broadest SC spectrum for a given power and input angle. Figure 3.3 shows the spectral evolution while pumping on the slow axis (blue curve), fast axis (yellow curve) and at 45° to both axes (brown curve). The broadest SC spectrum (bandwidth at -20 dB is 460 nm) is obtained by pumping on the slow axis while the narrowest is obtained by pumping at 45° to both axes. The spectrum generated when pumping on the fast axis is narrower than when pumping on the slow axis, which could be due to core ellipticity inducing a difference in the mode field diameter and thus in the nonlinear coefficient. The SC spectrum obtained when pumping at 45° to both axes is the narrowest. This result is expected because only half the power is available for spectral broadening in each axis and due to the temporal walk-off, which tends to eliminate the influence of cross-phase modulation [101]. Interestingly a sideband appears at 1360 nm, which is strongest when pumping at 45° and which we identify as XPMI. When pumping on the slow axis, the sideband intensity is reduced by 12 dB but is still clearly observable. Finally, when pumping on the fast axis the sideband appears to be completely suppressed with an extinction of at least 25 dB.

To understand the appearance of this sideband and the efficiencies regarding the input

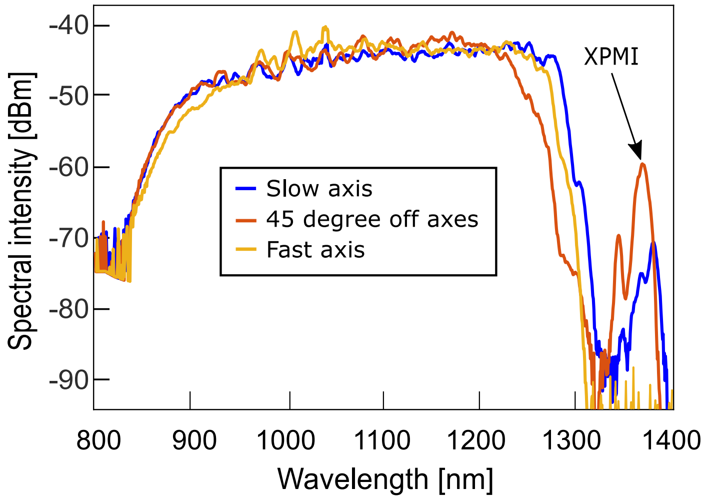

Figure 3.3: Experimental SC spectra in the PM-ANDi fiber for different input polarizations with 220 mW output power.

polarization angle, let us recall that the phase-matching conditions for XPMI should give rise to a Stokes sideband on the slow axis and an anti-Stokes sideband on the fast axis because of positive (normal) GVD [99, 102]. This means to stimulate the generation of an idler-pumped sideband on the Stokes side of the spectrum we need energy in the pump (on both axes) and energy on the anti-Stokes sideband (aligned to the fast axis). Furthermore, it is not theoretically possible to obtain an XPMI process if the beam is polarized linearly along with one of the axes of the fiber as the process requires interaction between light on both axes. Experimentally, we used a laser with a polarization extinction ratio (PER) of 40 dB and injected the light into an end-collapse highly birefringent fiber. This seed laser is not isolated, thus in order to protect it from back reflections, we decided to collapse the holes of the PM-ANDi PCF to limit the amount of power going back in the laser cavity. To collapse them, we used an FFS-2000 Fusion Splicing Workstation from Vytran (see App. 3). Using this filament splicer, the fiber's facet is heated (we can control the collapsed length by increasing the duration/power of the electrical arc) and the fiber holes collapse.

At the output, we measure a maximum achievable PER of 17 dB, which has a relatively even distribution over the whole SC bandwidth and depicted in Fig. 3.4. This shows that, at some point in the propagation, light has deviated from the input axis to become distributed moreover both axes, probably due to the collapse of the fiber holes. Thus, it is possible to observe a Stokes sideband at 1360 nm when the input beam is almost aligned on the slow axis, though the efficiency of this sideband will be much lower than when the beam is aligned at 45° of the axis, as shown in Fig. 3.3.

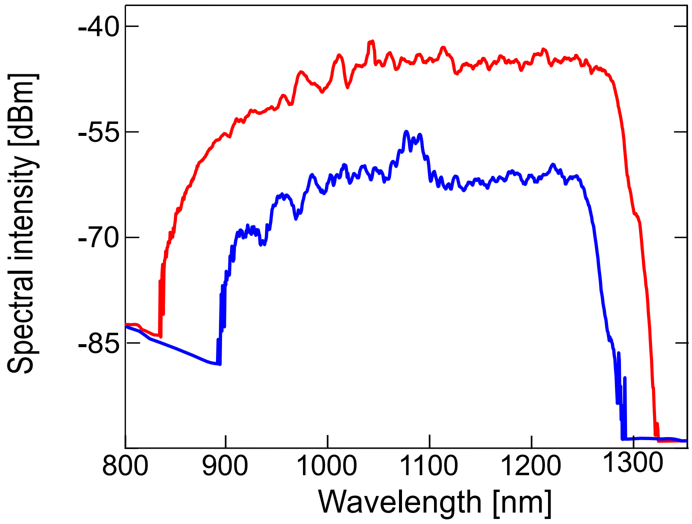

Figure 3.4: Experimental SC spectra with an half-wave plate aligned on the fast axis. The red curve shows the spectrum recorded when the polarizer is aligned on the fast axis while the blue curve shows the one recorded when it is aligned on the slow axis. The difference between both curves provides the PER.

Figure 3.5 shows the evolution of the SC spectrum as a function of the pump power for an input polarization at 45° to both axes obtained via the half-wave plate (HWP). As expected in ANDi SC generation, the broadening is limited by the dispersion of the fiber and the peak power available. The SC bandwidth is 430 nm at -20 dB (845 nm - 1275 nm) for an average output power of 220 mW. The XPMI sideband grows and slightly broadens to longer wavelengths when increasing the coupled power. It starts to appear only when SC extends past 1200 nm and when the OWB also starts to appear (See green spectrum in Fig. 3.5). In addition, there is no observable anti-Stokes sideband

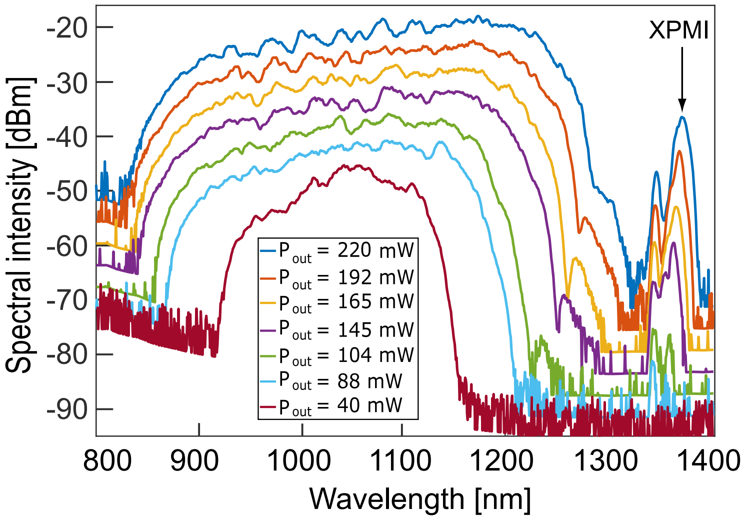

Figure 3.5: SC evolution for different pump power while pumping at 45° from the two axes (power offset for clarity).

outside the SC, even when observing the spectrum over a wide bandwidth (600 nm - 2000 nm). We can further notice a little red-shift of the XPMI peak when the coupled power increases that can be explained by the corresponding spectral broadening of the SC and its evolution of spectral power density [103].

Adding a polarizer at the output of the fiber to analyze the sideband polarization angle, in Fig. 3.6, we show the SC spectrum measured after the polarizer as a function of the polarizer angle at a maximum of output power (220 mW average power). We can see the 3 spectra obtained by aligning the polarizer on the slow axis (blue curve), fast axis (red curve) and at 45° of the axes (pink curve) have a similar bandwidth and shape. We observe the most powerful sideband when the polarizer is aligned on the slow axis and a 10 dB suppression when aligning the polarizer at 45° of the axes. Finally, aligning the polarizer on the fast axis totally suppresses the sideband, confirming that the sideband is polarized along the slow axis.

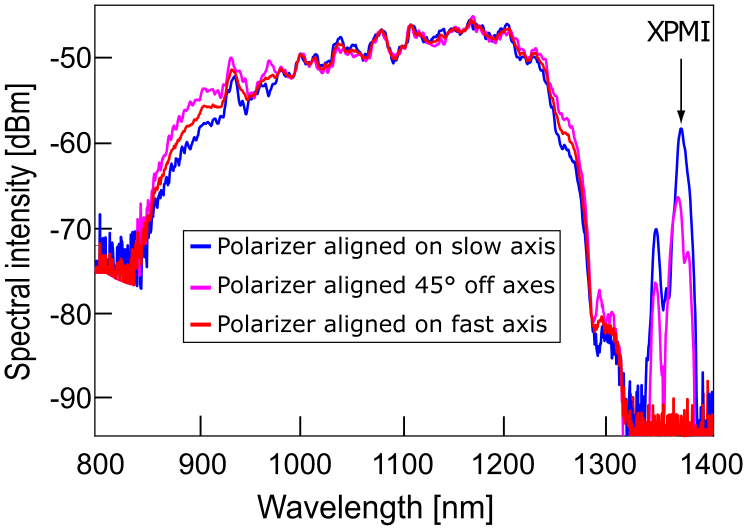

Figure 3.6: SC evolution for different polarizer orientations while pumping at 45° from the two axes.

We also investigate the impact of the input wavelength on the XPMI generation. For this, we tune the pump laser wavelength down to 910 nm to get more input power. Indeed, the output power of the laser is around 2 W at 910 nm, which is four times more than pumping at 1040 nm. This also enables us to investigate different phase-matching conditions for XPMI by measuring the SC dynamics as a function of the input wavelength, power and polarization. However, we must highlight that our HWP is not properly working at this wavelength. Indeed, we obtain an average PER of only 12 dB (before the fiber) compared to the 40 dB PER measured at 1040 nm. Therefore, we suspect that the input polarization is slightly elliptical at the fiber input which could explain the results below.

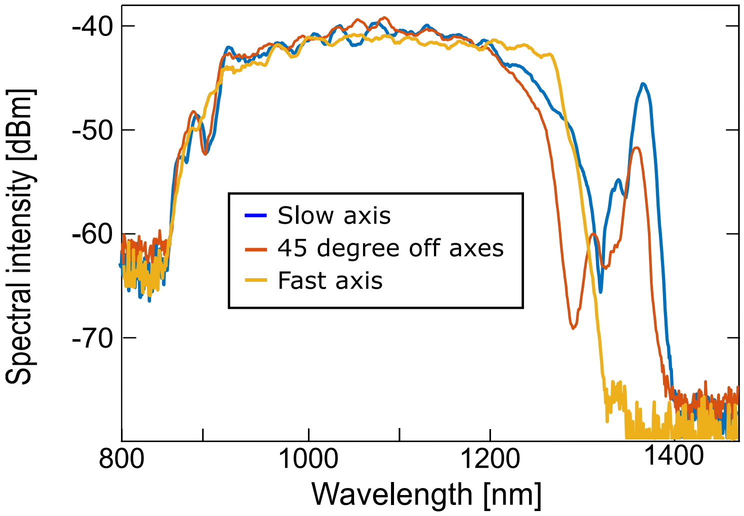

Figure 3.7: Experimental SC spectra for a pump wavelength at 910 nm for different input polarizations with 400 mW output power.

Figure 3.7 shows the SC spectrum for different input polarization while pumping at 910 nm. The broadest SC spectrum (bandwidth at -20 dB is 453 nm, going from 858 nm to 1311 nm) is again obtained by pumping on the slow axis while the narrowest is obtained by pumping at 45° (417 nm at -20 dB), going from 858 nm to 1275 nm). The fast axis bandwidth is between the two others, 437 nm at - 20 dB going from 858 to 1295 nm. We find the spectral broadening evolution is highly asymmetric because we are pumping far away from the minimum dispersion wavelength (on the blue side of the parabolic dispersion curve). Furthermore, The XPMI sideband still doesn't appear when pumping on the fast axis. The sideband is more powerful when pumping on the slow than on off-axis, which could be due to the input elliptical polarization from the HWP.

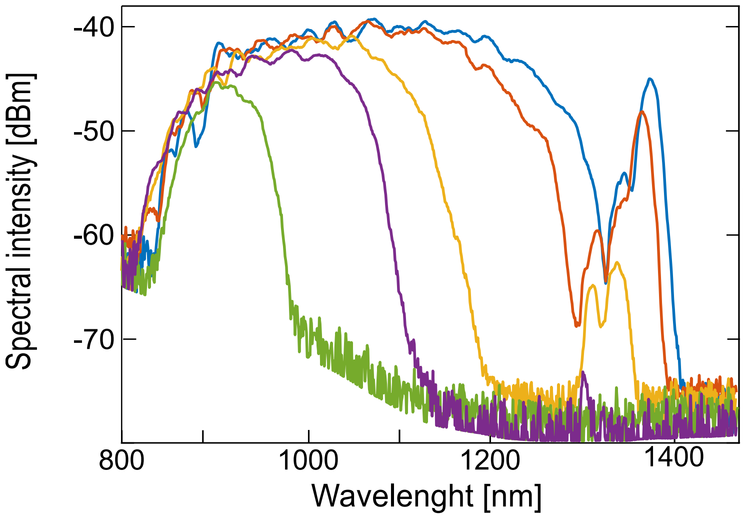

Figure 3.8: Experimental SC spectra while pumping at 910 nm on the slow axis for different output power going from 16 mW (green curve) to 392 mW (blue curve).

To investigate the behavior of the XPMI sideband. We plot the evolution of the SC spectrum for different input power when polarizing the optical field on the slow axis, as shown in Fig. 3.8. In this figure, we can clearly see the asymmetric evolution of the spectral bandwidth, which is due to pumping far away from the MDW on the blue side of the parabolic dispersion curve. We observe, the XPMI sideband appears only when the SC spans up to 1080 nm, for an output average power of 90 mW (purple curve) at 1300 nm. We observe a wide tunability of the XPMI sideband from 1300 nm up to 1380 nm when we increase the injected power (up to 392 mW average output power).

3.2/ THEORETICAL INVESTIGATION OF XPMI GENERATION

To get further into details, we investigate theoretically the XPMI generation. The XPMI theory is derived from the vector NLSE (Eq. 1.39 without the Raman term), which leads to the following coupled equations (assuming the same dispersion affects all waves) [13]:

$$\begin{aligned} \frac{\partial A_1}{\partial z} &= -\beta_{1x}\frac{\partial A_1}{\partial t} - i\frac{\beta_2}{2}\frac{\partial A_1}{\partial t^2} + i\gamma\left(|A_1|^2 + \frac{2}{3}|A_2|^2\right)A_1 + \frac{1}{3}i\gamma A_2^2 A_1^* e^{i\Delta\beta z} \\ \frac{\partial A_2}{\partial z} &= -\beta_{1x}\frac{\partial A_2}{\partial t} - i\frac{\beta_2}{2}\frac{\partial A_2}{\partial t^2} + i\gamma\left(|A_2|^2 + \frac{2}{3}|A_1|^2\right)A_2 + \frac{1}{3}i\gamma A_1^2 A_2^* e^{i\Delta\beta z}, \end{aligned} \tag{3.1}$$

where $\beta_{1x,1y}$ represent the inverse of the group velocity of each wave having different polarization state (x, y), β_2 is the group velocity dispersion, and $\Delta\beta$ is given by $\Delta\beta = \beta_{1x} - \beta_{1y}$. If $\Delta\beta$ is big (huge birefringent), the exponential term oscillates strongly and its effect is negligible for propagation distance higher than the beat length (see Sec. 1.1.5). Therefore, we can neglect this term and the coupled NLSEs become:

$$\begin{aligned} \frac{\partial A_1}{\partial z} &= -\beta_{1x}\frac{\partial A_1}{\partial t} - i\frac{\beta_2}{2}\frac{\partial A_1}{\partial t^2} + i\gamma\left(|A_1|^2 + \frac{2}{3}|A_2|^2\right)A_1 \\ \frac{\partial A_2}{\partial z} &= -\beta_{1y}\frac{\partial A_2}{\partial t} - i\frac{\beta_2}{2}\frac{\partial A_2}{\partial t^2} + i\gamma\left(|A_2|^2 + \frac{2}{3}|A_1|^2\right)A_2. \end{aligned} \tag{3.2}$$

Now, using the instability method described in Ref. [104]. Because the considered fiber is highly birefringent (>10^{-4}), the powers, $P_1 = |A_1|^2$ and $P_2 = |A_2|^2$, do not evolve with z during the propagation . Thereby, the stationary solution of Eqs. 3.2 is given by:

$$\begin{aligned} A_1 &= \sqrt{P_1}\exp(i\gamma\left(P_1 + \frac{2}{3}P_2\right)z) \\ A_2 &= \sqrt{P_2}\exp(i\gamma\left(P_2 + \frac{2}{3}P_1\right)z). \end{aligned} \tag{3.3}$$

Introducing a perturbation in the stationary solution, we obtain:

$$\begin{aligned} A_1 &= \left(\sqrt{P_1} + u(z,t)\right)\exp(i\gamma\left(P_1 + \frac{2}{3}P_2\right)z) \\ A_2 &= \left(\sqrt{P_2} + v(z,t)\right)\exp(i\gamma\left(P_2 + \frac{2}{3}P_1\right)z), \end{aligned} \tag{3.4}$$

where u, v represent the perturbation of each field components. Inserting, Eq. 3.4 in 3.2, we obtain the equation of propagation of our perturbations u, v:

$$\begin{aligned} \frac{\partial u}{\partial z} &= -\beta_{1x}\frac{\partial u}{\partial t} - i\frac{\beta_2}{2}\frac{\partial u}{\partial t^2} + i\gamma\left(P_1(u+u^*) + \frac{2}{3}\sqrt{P_1 P_2}(v+v^*)\right) \\ \frac{\partial v}{\partial z} &= -\beta_{1y}\frac{\partial v}{\partial t} - i\frac{\beta_2}{2}\frac{\partial v}{\partial t^2} + i\gamma\left(P_2(v+v^*) + \frac{2}{3}\sqrt{P_1 P_2}(u+u^*)\right) \end{aligned} \tag{3.5}$$

The modulation approach can be written as:

$$\begin{aligned} u(z,t) &= u_s(z)\exp(i\Omega t) + u_i(z)\exp(-i\Omega t) \\ v(z,t) &= v_s(z)\exp(i\Omega t) + v_i(z)\exp(-i\Omega t), \end{aligned} \tag{3.6}$$

where $\Omega = \omega_s - \omega_0 < 0$ is the frequency of the perturbation. In the frequency domain, this modulation of the amplitude induces the generation of symmetric sidebands around the pump (of frequency ω_0. $u_i(u_s)$ represents the amplitude of the anti-Stokes (Stokes) polarized along the fast axis (x) and $v_i(v_s)$ represents the amplitude of the Stokes (anti-Stokes) polarized along the slow axis (y). Introducing Eqs. 3.6 in Eqs. 3.5 and ignoring the non phase-matched waves, we obtain the following differential system [104]:

$$\frac{\partial}{dz}\begin{bmatrix} u_s \\ u_i^* \end{bmatrix} = iM\begin{bmatrix} v_s \\ v_i^*, \end{bmatrix} \tag{3.7}$$

where M is the vectorial stability matrix of the system given by:

$$M = \begin{pmatrix} +\frac{\gamma P_0}{3} & +\frac{\Delta\kappa}{2} \\ -\frac{\Delta\kappa}{2} & -\frac{\gamma P_0}{2}, \end{pmatrix} \tag{3.8}$$

where P_0 is the total input power, given by $P_0 = 2P_1 = 2P_2$ for a pump polarized at 45° of the fiber's axes. Furthermore, the phase-matching is given by:

$$\Delta\kappa = -\frac{\delta n}{c}\Omega + \beta_2\Omega^2 + \gamma P_0. \tag{3.9}$$

From this equation, one can understand in the case of a highly birefringent fiber, in normal dispersion regime, the phase-matching is possible when the birefringent term compensates both the dispersion and the nonlinearity. In these conditions, the phase-matched waves will be the Stokes one polarized along the slow axis and the anti-Stokes one polarized along the fast axis. The perturbation v_s and u_i^*, from Eqs. 3.7, are exponentially amplified during the propagation if the matrix of stability M has eigenvalues with an imaginary part different to zero. Using $det(M - \lambda I)$ to obtain the eigenvalues, the XPMI gain in a highly birefringent fiber is given by:

$$G(\Omega) = 2|\lambda| = 2g, \tag{3.10}$$

where g is the amplitude gain by unit of length of the XPMI given by:

$$g = \sqrt{\left(\frac{\gamma P_0}{3}\right)^2 - \left(\frac{\Delta\kappa}{2}\right)^2}. \tag{3.11}$$

According to this equation, we can obtain the maximum gain of the XPMI process, when $\Delta\kappa = 0$, $g_{max} = \gamma P_0/3$. Furthermore, using Eq. 3.9, the angular frequency shift of the XPMI, compared to the pump, is given by:

$$\Omega_\pm = \frac{\Delta\beta_1}{2\beta_2}\left(1 \pm \sqrt{1 - \frac{4\beta_2\gamma P}{\Delta\beta_1^2}}\right) = \frac{\delta n}{2c\beta_2}\left(1 \pm \sqrt{1 - \frac{4c^2\beta_2\gamma P}{\delta n^2}}\right). \tag{3.12}$$

3.3/ NUMERICAL INVESTIGATION OF XPMI GENERATION

To simulate the SC generation in the PM-ANDi fiber, we use a Matlab code solving the two coupled generalized nonlinear Schrodinger equations (CGNLSE) for highly birefringent fibers as described in Eqs. 1.39. We used as input parameters a pump wavelength of 1040 nm, a pulse duration of 200 fs, 12 kW peak power, a longer fiber length of 60 cm for better visibility, the loss profile as described in Fig. 3.2 (green curve) and the birefringence values are taken from the inset. Fig. 3.9 shows the simulated SC spectrum generated on each axis (blue and pink) and the sum of both (red).

We observe a very good agreement between the spectral bandwidth of our simulation and our experiment (430 nm vs 420 nm at -20 dB). Furthermore, with these parameters, we can't see any XPMI sideband generation around 1360 nm. To investigate this, we

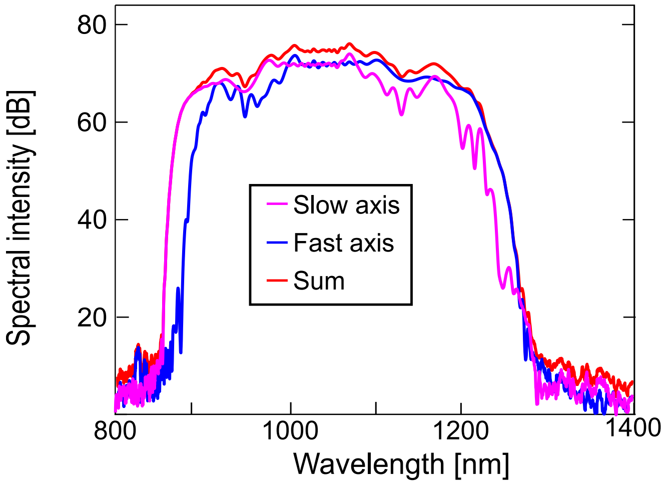

Figure 3.9: Simulated SC generation with the following input parameters: 200 fs input pulse duration, 12 kW peak power centered at 1040 nm and a fiber length of 60cm. The slow axis is shown in pink, the fast one in blue and the sum of both in red.

use Eq. 3.12 to plot the theoretical XPMI sidebands as a function of pump wavelength (Fig. 3.10) for the dispersion profile depicted in Fig. 3.2 in solid blue for different input peak power going from 0 kW to 7.5 kW. In this figure, we find, when the nonlinear term in Eq. 3.12 is set to zero, a signal can be generated at 1360 nm with a degenerated pump located at 1110 nm and an idler at 990 nm (both in the SPM area). Furthermore, we can observe the wavelength combination of the pump and idler are red-shifted when the peak power increases (as expected from Eq. 3.12 to obtain a signal at 1360 nm. Thus, we can assume the XPMI sideband is not generated spontaneously and the SPM broadening plays a major role in this phenomenon.

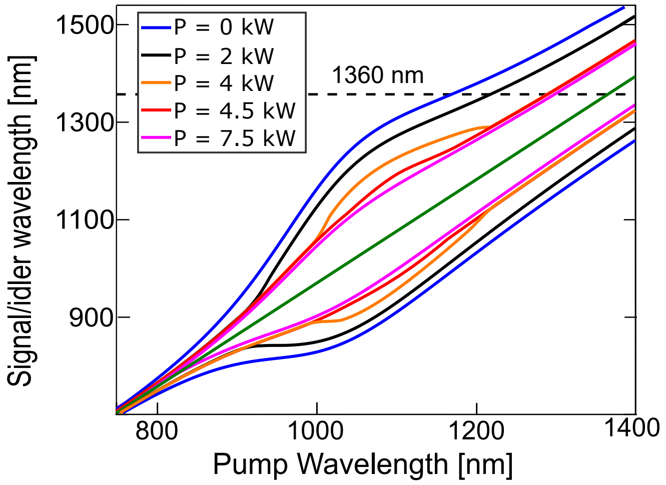

Figure 3.10: Phase-matching map as a function of total peak power, from low (0 kW) to high (735 kW) power. The horizontal dashed black line indicates the expected XPMI sideband at 1360 nm.

Therefore, the numerical modeling using the experimental dispersion data did not reproduce the experimental results; this is probably due to the uncertainties on this dispersion curve that increases when the dispersion is close to zero. Thus, we considered the dispersion given by the brown curve in Fig. 3.2, which is shifted upwards in the center as the dispersion approaches zero. This is still within the measurement uncertainties and is able to reproduce the experiments as we will demonstrate.

Using this new modified dispersion curves, we obtained a better agreement between simulation and experimental results. This is shown in Figs. 3.11 (a-d) that depicts both the spectral and temporal intensity dynamics on each axis when pumping at 45° the PM-ANDi fiber. First, the numerical SC bandwidth at -20 dB level is estimated as large as 450 nm which is very close to the experimental one (430 nm). Second, we can clearly see the generation of a small signal at 1360 nm polarized on the slow axis, as described previously (See Fig. 3.11 (b). We can also notice the sideband appears after 20 cm of propagation exactly where the OWB starts to rise [97]. Interestingly, the temporal trace

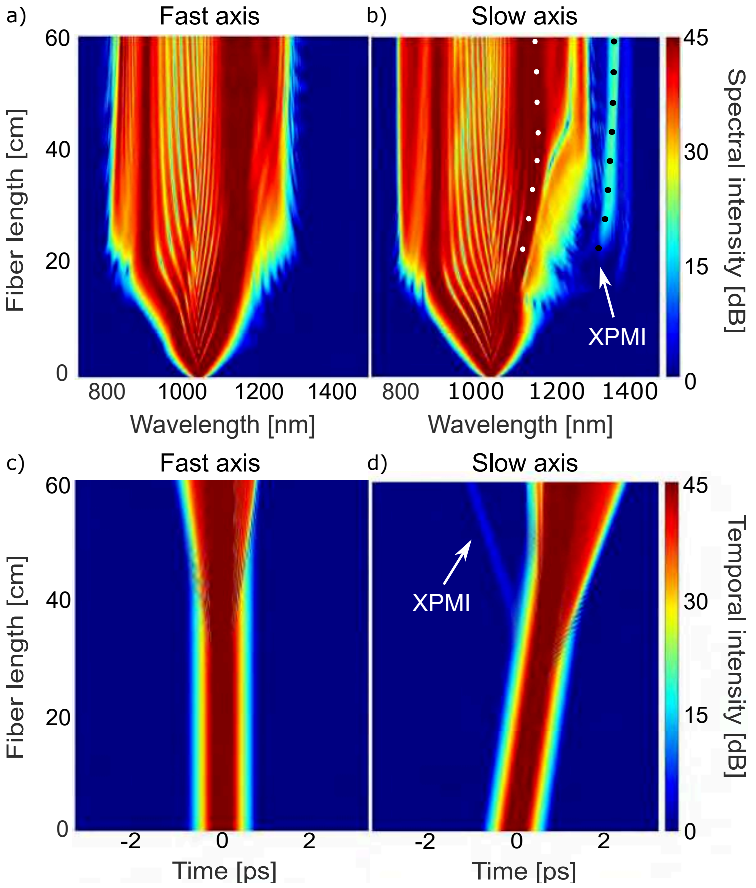

Figure 3.11: Simulated spectral (top) and temporal (bottom) SC evolution on each fiber axis as a function of fiber length. The dots represent the theoretical XPMI wavelength (black) using the redder SPM wavelength (white) as a pump.

plotted in Fig. 3.11 (d) reveals that the signal at 1360 nm behaves like a small dispersive wave (DW) shed by the pump pulse on the slow axis, in a way akin to the DW emission by OWB in the anomalous dispersion regime [105, 106].

Likewise, the slow axis XPMI generation is seen to be closely linked to the long-wavelength SPM lobe in the slow axis, marked with white dots in Fig. 3.11(b). According to this conjecture, the XPMI gain is only efficient when the red-shift of the SPM lobe, acting as the pump, slows down, and for lengths not much longer than the walk-off length of 22 cm. This is exactly what is observed in Fig. 3.11(b): the XPMI peak is first growing after about 20 cm when the red-shift of the SPM lobe is stopped by OWB, and after about 30 cm the power in the XPMI peak does not grow anymore. Looking in more detail we find that the peak power decreases from 12 kW at z=0 to 1.5 kW at z=60 cm.

Now that we obtained good agreement between the simulated and the experimental spectra, we replot Fig. 3.10 showing the XPMI wavelengths, using the modified dispersion curve and , for an increasing peak power from 0 kW to 12 kW. From those new phase-matching curves shown in Fig. 3.12, we see that the XPMI phase-matched to the center wavelength of the SPM lobe initially at 2787 nm (P_0=12 kW, λ_{SPM}=1040 nm), then it rapidly decreases because of the red-shift of the SPM lobe. The observed final SPM lobe wavelength of 1152 nm is seen to generate an XPMI Stokes sideband at 1360 nm. In such process, the idler sideband wavelength is at 910 nm within the SC bandwidth. We can observe we obtain this combination in the valley of the linear phase-matching curve, which nicely corresponds to the numerically and experimentally observed XPMI

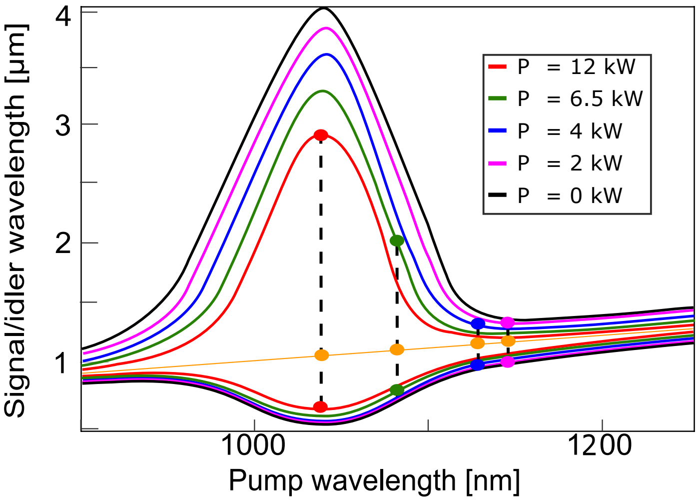

Figure 3.12: Phase-matching map as a function of total peak power, from 0 kW (black) to 12 kW (red). The orange dots on the straight line for the pump wavelength show the numerically observed red SPM wavelength [white dots in Fig. 6(b)], and the other colored dots mark the corresponding XPMI wavelength.

wavelength (Fig. 3.12 pink dots). The observed SCG induced XPMI generation thus requires a delicate balance between strong SPM stopped sufficiently before say twice the walk-off length by OWB.

In addition, we plot in Fig. 3.13 the spectrogram of our SC simulation after two meters of propagation while pumping at 45° to both axes. As expected, we can observe the two polarized waves walk-off from each other due to the birefringent of the fiber. Furthermore, as explained before the XPMI sideband is polarized along the slow axis and walk-off as well from the main pulse and acts as a dispersive wave.

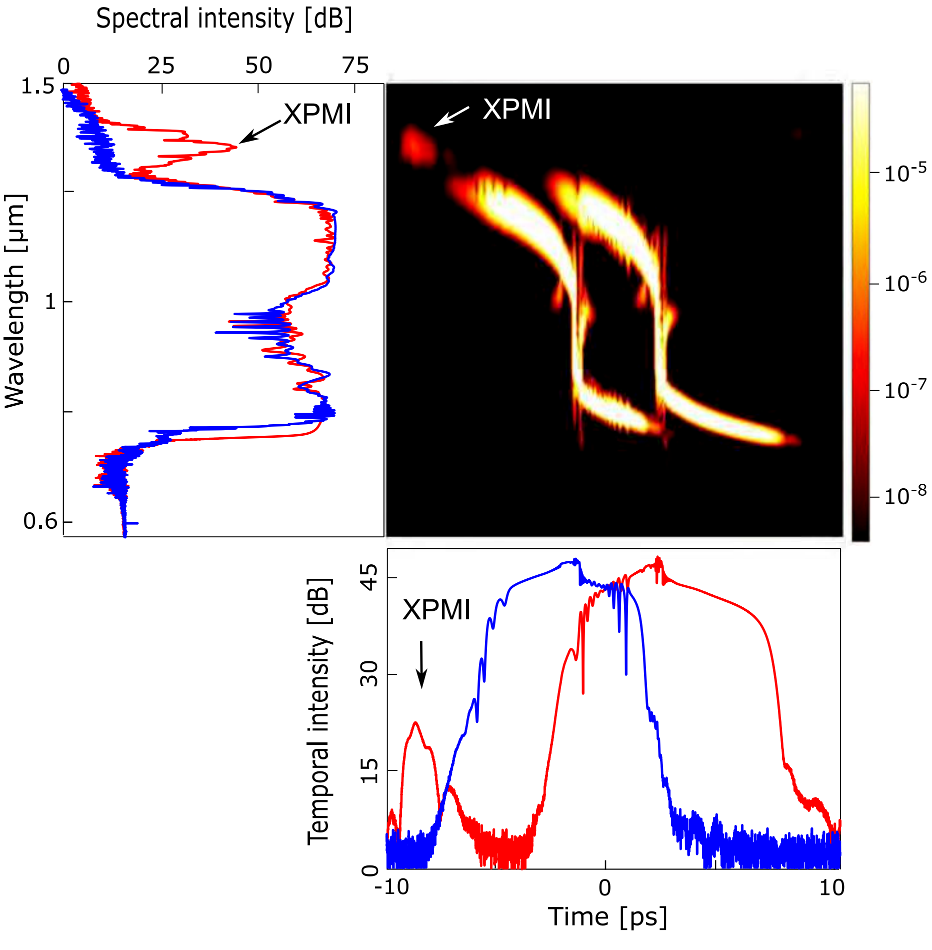

Figure 3.13: Spectrogram of the XPMI spectrum with $T_0 = 200$ fs, $P_0 = 12$ kW, and $L = 2$ m. The red curve represents the temporal trace and the spectrum generated on the fast axis while the blue curve represents the fast axis ones.

In conclusion, we have reported the observation of cross-phase modulation instability while pumping a PM-ANDi PCF with a femtosecond mode-locked laser tuned at 1040 nm. A strong sideband was generated through an XPMI process at 1360 nm during coherent supercontinuum generation spanning from 870 nm to 1300 nm. We demonstrated this sideband cannot be generated while pumping on the fast axis and is itself polarized along the fiber's slow axis. Further, clarifying that we were observing XPMI, theoretical calculation and simulation performed solving the GNLSE confirmed the degenerated four-wave mixing between a pump corresponding to the red edge of the SPM on the fiber's slow axis, an anti-Stokes idler pump in the central SPM area on the fiber fast's axis and a signal at 1360 nm polarized on the fiber's slow axis. XPMI generation could be used to extend the bandwidth of the SC spectrum at the cost of the polarization control. Indeed, injecting the beam at 45° to both axes means the PER at the output fiber is strongly degraded.

3.4/ REAL-TIME NOISE SC MEASUREMENTS

After explaining the phenomenon of XPMI generation, we want to investigate the impact of the input polarization on the ANDI SC RIN and coherence. Thus, we will simulate 20 SC generations using the parameters described in the previous section without any addition of technical noise sources to investigate the impact of the XPMI only on the SC coherence.

Figure 3.14 shows the average simulated SC spectrum (blue curve) using the parameters described previously (200 fs input pulse duration, 12 kW input peak power, and input beam polarized at 45° to both axes) with the modified dispersion profile (Figure 3.2 brown curve) and the spectrally resolved coherence function g_{12} (red curve), given by Eq. 2.3. The results show an extremely high degree of coherence, equal to 1 across the whole SC bandwidth including the XPMI sideband, when including only the quantum noise.

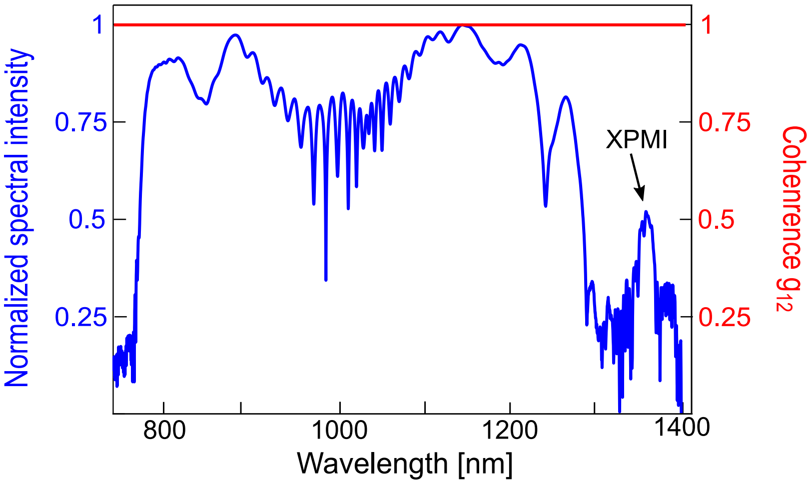

Figure 3.14: Simulated average SC spectrum (blue curve) using an ensemble of 20 independent SC spectrum and coherence function g_{12} (red curve) using the same parameters described in our experiment: 200 fs input pulse duration, 12 kW input peak power, and input beam polarized at 45° to both axes.

Thus, we observed a stimulated XPMI process which is seeded by SC, both including the pump and the idler.

To explore the decoherence process of the ANDi SC spectrum, in the context of XPMI generation, we repeat the same set of simulations but including an amplitude noise of 1 % as described in Sec. 2.4. Thereby, Fig. 3.15 shows the average simulated SC spectrum (blue curve) using 200 fs input pulse duration, 12 kW input peak power, and input beam polarized at 45° to both axes) with the modified dispersion profile (Figure 3.2 brown curve) and the spectrally resolved coherence function g_{12} (red curve), given by Eq. 2.3. Adding the amplitude noise in our modeling, we find the average coherence ($\langle |g_{12}\rangle$) is equal to 0.68, highlighting the impact of technical noise on the ANDi SC coherence. Furthermore, we observe the coherence spectrum follows the SC one. Indeed, we see the modulations on the SC spectrum on the SPM area are present, as well, on the coherence spectrum, same for the deep and small peak around 1260 nm. Also, the most surprising point of this figure is the discovery of a high coherence area on the XPMI bandwidth. Indeed, the average coherence on the XPMI bandwidth is up to 0.85, which means the XPMI generation is barely affected by the technical noise. Thus, we can conclude the amplitude noise only affects the moment when the XPMI sideband is generated but barely the coherence of this nonlinear effect.

In order to investigate experimentally the stability of our SC generation as a function of the input polarization, we build a dispersive Fourier transform (DFT) setup depicted in Fig. 3.16, as described in Sec. 2.1. This setup is composed of the tunable femtosecond

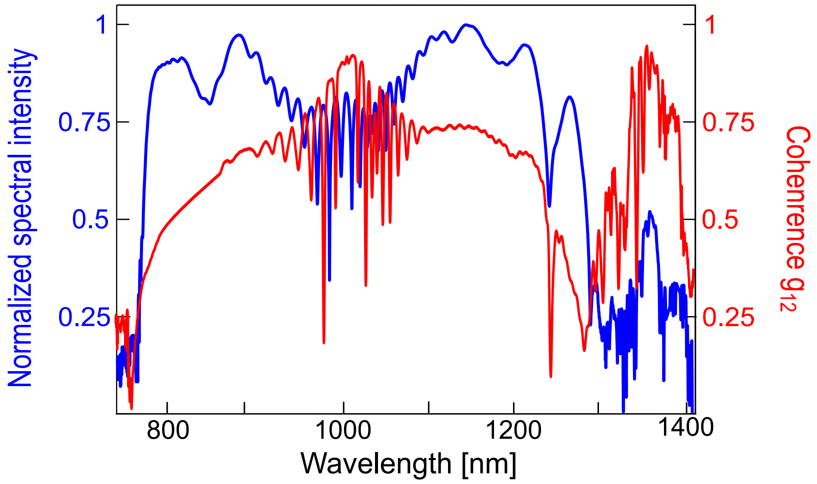

Figure 3.15: Simulated average SC spectrum (blue curve) using an ensemble of 20 independent SC spectrum and coherence function g_{12} (red curve) using the same parameters described in our experiment: 200 fs input pulse duration, 12 kW input peak power, input beam polarized at 45° to both axes and input amplitude noise value of 1 %.

laser, the SC generation stage then by 150 m of dispersion-shifted fiber (DSF) to stretch the pulses while ensuring there is no overlap between each pulse (duration between two pulses is 12.5 ns), a flip-mirror to inject the light either in the OSA or in a fast photodiode connected to a real-time oscilloscope. Before the photodiode, we use a neutral density to avoid damaging it and especially to ensure a linear propagation inside the stretching DSF (the maximum average power handled by the photodiode is 8 mW). The DSF has a D parameter equal to 80 ps/nm/km at 1040 nm, which provides a total dispersion of 12 ps/nm. The detector, from Newfocus (model 1414), has a bandwidth of 25 GHz and a detection range from 630 nm to 1620 nm. Thus, the equivalent spectral resolution of our DFT setup is equal to 7 nm at 1040 nm (see Sec. 2.1). The oscilloscope is the DSA91204A from Agilent, which has a maximum sample rate of 40 GSa/s and a real-time full bandwidth of 12 GHz.

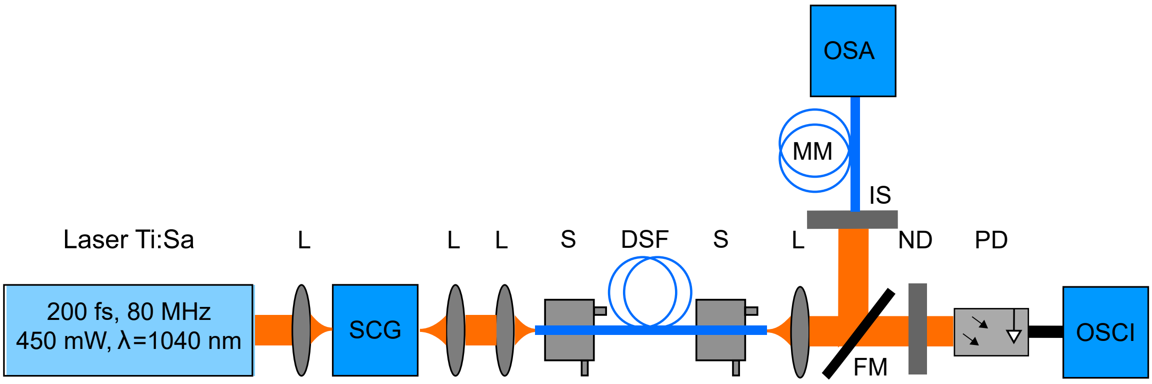

Figure 3.16: Schematic of the DFT setup, including the Ti:Sa femtosecond laser, the SCG setup, aspheric lenses (L), 3D translation stages (S), 150 m of DSF fiber (DSF), a flip mirror (FM), a fast photodiode (PD), an oscilloscope (OSCI), 2 m of multimode pick-up fiber (MM), an integrating sphere (IS), and an optical spectrum analyzer (OSA).

Using the oscilloscope and the OSA, we recorded the SC spectrum and the temporal profile at the output of our stretching fiber and superpose them to check the linear behavior of our stretching fiber. To superimpose both OSA and oscilloscope spectrum, we used a Matlab code, and the total dispersion ($\beta_2 \times z$) allowing a match between the different spectral data (as explained in Sec. 2.1). Thus, Fig. 3.17, shows the different steps of our Matlab code for the different input polarization (slow axis, fast axis, and at 45° to both axes).

The first step, is to stack the 300 oscilloscope spectra and ensure there is no presence of aliasing or tilt, which is confirmed by Figs. 3.17 (a,b,c). Thus, we can analyze the statistics of the pulse-pulse sequences of our stacking in order to conclude if there is an impact of the input polarization on the SC stability. The second step is to compare the average temporal trace obtained via the recorded pulse train on the oscilloscope. Thereby, Fig. 3.17 (d,e,f) shows the superposition between the average oscilloscope

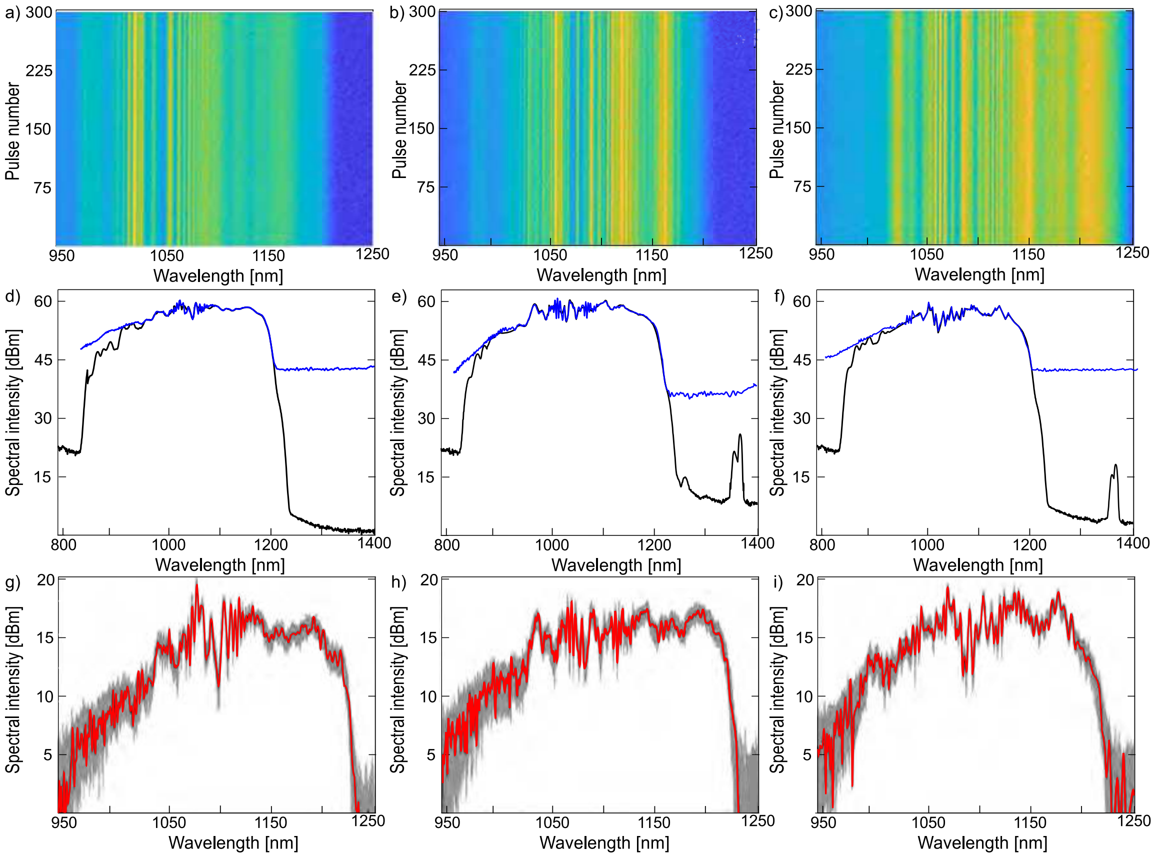

Figure 3.17: Representation of the different steps to analyze the DFT data recorded on the oscilloscope as a function of the input polarization (a,d,g, beam polarized along the fast axis, b,e,h beam polarized at $45°$ to both axes, c,f,i beam polarized along the slow axis). The first row represents the stacking of the 300 spectra recorded on the oscilloscope. The second row shows the comparison between the OSA spectrum (black curve) and the average oscilloscope trace (blue curve). The last row displays the average (red curve) and individual (grey curve) traces recorded on the oscilloscope.

(blue curve) and the OSA spectrum (black curve). We can observe a quite good match between both spectra for wavelengths going from 950 nm to 1250 nm. We advance the lack of matching below 950 nm is due to a lower responsivity of the photodetector. Furthermore, we find the maximum dynamic range of our DFT setup is up to 18 dB. Also, as expected, there is no XPMI sideband generated when pumping along the fast axis (Fig. 3.17 (d)) but there is one when pumping on the slow and off-axis (Fig. 3.17 (e,f)). This XPMI sideband is detected on the OSA but is below the noise floor of the photodetector. The last step is to analyze the statistic of the pulse-to-pulse sequence. Figure 3.17 (g,h,i) shows the superposition of each independent DFT SC spectrum (300 in total) in gray and the average DFT SC spectrum in red. On these spectra, we find out a higher standard deviation of our ensemble for wavelengths shorter than 950 nm, i.e. where the DFT spectrum deviated from the OSA spectrum. Furthermore, as expected from ANDi SC generation, we don't observe any discontinuities in the grey trace characteristic of rogue wave generation, as shown in [107].

Furthermore, we can measure the spectrally resolved RIN of our DFT traces for our different input polarization, as depicted in Fig. 3.18. Again, the data below 950 nm are hard to analyze due to the drift between the OSA and the DFT spectrum but we can still analyze them between 950 nm to 1250 nm. From these spectra, we can extract the following information. The three spectra have the same behavior: the RIN increases linearly on the blue side on the spectrum and exponentially on the red side, as demonstrated in Sec. 2.4. Furthermore, the RIN spectrum is modulated on the SPM area (going from 1050 nm to 1125 nm) and rather flat on the OWB area on the red side. The noise floor is the same so we are limited by our electronic components (responsivity/maximum detected power) Finally, all three spectra have an average RIN equal to 6.5 % and the minimum RIN is as low as 3.9 %. Thus, it looks like, pumping at 45 ° and therefore generating XPMI sideband has no real impact on the SC RIN as we predicted earlier. To confirm this assumption, we would require the use of a photodiode with a higher responsivity or the ability to handle a higher input power to analyze the whole SC bandwidth.

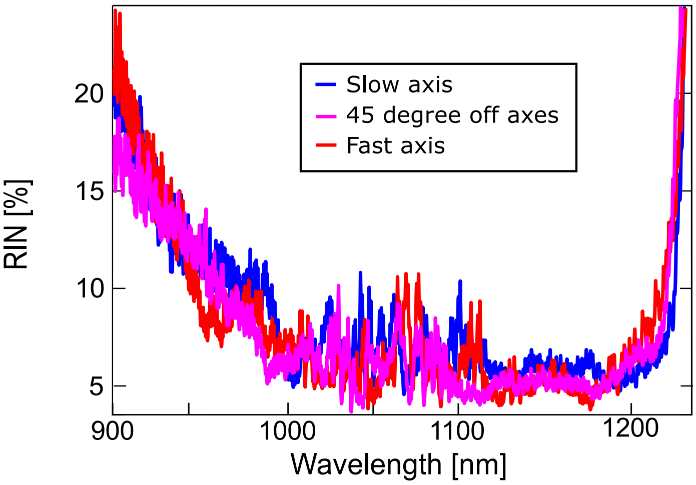

Figure 3.18: Measured spectrally resolved RIN using DFT method when pumping on fast axis (red curve), slow axis (blue curve) and at 45° to both axes (pink curve).

In order to measure experimentally the RIN of our SC spectrum, we use the setup depicted in Fig. 2.3. To obtain a spectrally resolved RIN spectrum, we replaced the bandpass filters by a monochromator (from Princeton Instrument). A monochromator is an optical device based on gratings to diffract and select a specific spectral bandwidth centered at a given wavelength. Furthermore, for this experiment, we use a 190 fs laser centered at 1049 nm with an output peak power of 122 kW (more details in Sec. 4.3). Fig. 3.19 depicts a zoom of the spectrally resolved RIN while pumping at 45° to both axes using 10000 individual recorded pulses and a spectral filter bandwidth of 1 nm. In this figure, and as demonstrated numerically in Sec. 2.4, we observe the RIN increases drastically on the spectrum edges due to the reduction of the SC power and/or bigger fluctuations at these wavelengths. Finally, we remark the RIN value is, as well, quite low on the XPMI area (equal to 10.1 %), which we guess could be lower due to the small power detected at these wavelengths by the detector (low signal-to-noise ratio induces a higher noise floor limit). Thus, as demonstrated numerically, and experimentally via the DFT method, we confirm with the oscilloscope method a low RIN on the XPMI area.

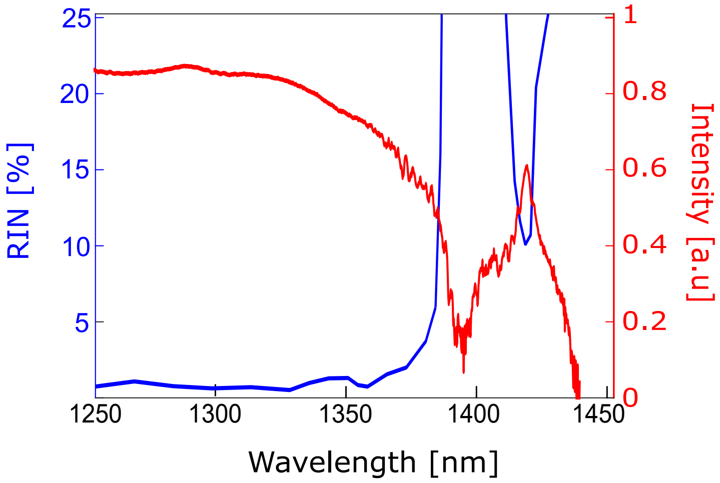

Figure 3.19: Zoom on measured spectrally resolved RIN using monochromator and oscilloscope method with an InGaAs photodiode and corresponding average normalized SC spectrum (solid red), pumping at 45° to both axes.

To conclude this chapter, we investigated experimentally the SC generation when pumping the PM-ANDi fiber with a Ti:Sa femtosecond laser. We obtained a spectral bandwidth of 460 nm, measured at -20 dB, centered at 1040 nm, linearly polarized with a PER up to 17 dB. Then, we look over the impact of the input polarization on the ANDi SC spectrum. We discovered the bandwidth of the output spectrum is slightly smaller when pumping along the fast axis due to a lower nonlinear coefficient. Furthermore, while pumping at 45° to both axes, we observed the generation of a sideband identify as XPMI. After a theoretical, numerical and experimental investigation of the XPMI phenomenon, we demonstrated (based on the phase-matching equation) the XPMI is generated via the interaction of a pump located in the red-lobe of the SPM (polarized along both axes), at 1152 nm, and an idler located in the fringes area of the SPM (polarized along the fast axis) at 990 nm. Also, the phenomenon of XPMI could be used to increase the SC bandwidth with a good engineering of the fiber's dispersion and birefringent profile at the cost of a PER degradation (equal to 0 when pumping at 45° to both axes). Finally, using numerical simulation and experimental noise measurement methods (DFT and oscilloscope), we demonstrated that the input polarization has no real impact on the RIN and coherence of the fs ANDi SC spectrum. A deeper investigation of the experimental noise properties is given in the next chapter.

4

DEVELOPMENT OF A LOW-NOISE SUPERCONTINUUM SYSTEM

One of the main objectives of this Ph.D is to develop a "low-cost", low-noise, coherent supercontinuum source using an all-normal dispersion optical fiber for several applications such as optical coherent tomography (OCT), spectroscopy, metrology [5, 108–112]. The targets for the developed system are: broadest spectrum as possible, ideally octave-spanning, output power higher than 5 mW, average pulse-to-pulse fluctuations below 5 %. Thus, in this chapter, we will discuss about three different SC systems I have developed using different pump lasers and experimental arrangements. We remind the PCF used for all our experimental setups is the PM-PCF from NKT photonics and is called, in the whole manuscript, by PM-ANDi PCF. Furthermore, we will show and discuss about the different RIN levels of the lasers/SCs obtained. Finally, we will present the "best" SC system that could be used for several applications and compare it to the existing ANDi SC systems. Indeed, in the literature, few ANDi SC compact systems have already been published [**?**, 10, 11] using different input pulse duration, peak powers, central wavelengths. We will demonstrate that our final developed system will be the broader, the flatter, the most stable and with the higher polarization extinction ratio.

4.1/ FIRST SYSTEM: LOW-AVERAGE POWER LASER

The first seed laser used during this Ph.D is the Origami 10 LP (for low power) from NKT photonics. This laser is an ytterbium solid-state mode-locked by semiconductor saturable absorber mirror [91], a picture of this laser can be found in App. 4. According to the datasheet, produces femtosecond hyperbolic secant pulses with a duration around 100 fs at a repetition rate of 80 MHz with an average power of 11 mW centered at 1054 nm and a bandwidth of 11.5 nm. In order to be sure of the manufacturer's specifications, we decided to double-check them using different devices including an optical spectrum analyzer (OSA), a powermeter, and an autocorrelator. Figure 4.1 (a) shows the output spectrum of the Origami 10 LP recorded via an integrating sphere and an OSA. We observe it is well centered at 1054 nm with a small Kelly sideband at 1005 nm and a bandwidth of 12 nm at -3 dB. Furthermore, Fig. 4.1 (b) shows the autocorrelation trace of the Origami 10 LP using a PulseCheck autocorrelator from APE, which can measure pulse duration between 10 fs to 12 ps, a wavelength range going from 700 nm to 1100 nm and a sensitivity of 10^{-4} W^2. This autocorrelator is sensitive to the input polarization of the beam thus a half-wave plate was added before the input of the autocorrelator to maximize the intensity of the detected signal. The autocorrelation (AC) trace factor for a secant hyperbolic profile is 0.65 and therefore the measured AC trace (intensity profile) provides a pulse duration of around 103 fs at FWHM. Using this measurement, we can determine the time-bandwidth product (TBP) of this system using the following formula:

$$\Delta t \Delta \nu = 0.315 = \frac{\Delta t \lambda^2}{c \Delta \lambda}, \tag{4.1}$$

where Δt is the pulse duration at FWHM of the laser, λ the central wavelength and $\Delta\lambda$ the spectral bandwidth at FWHM (12 nm). Thus, we obtain a TBP of 0.338 which means this laser system is almost transform-limited and can not be further linearly compressed.

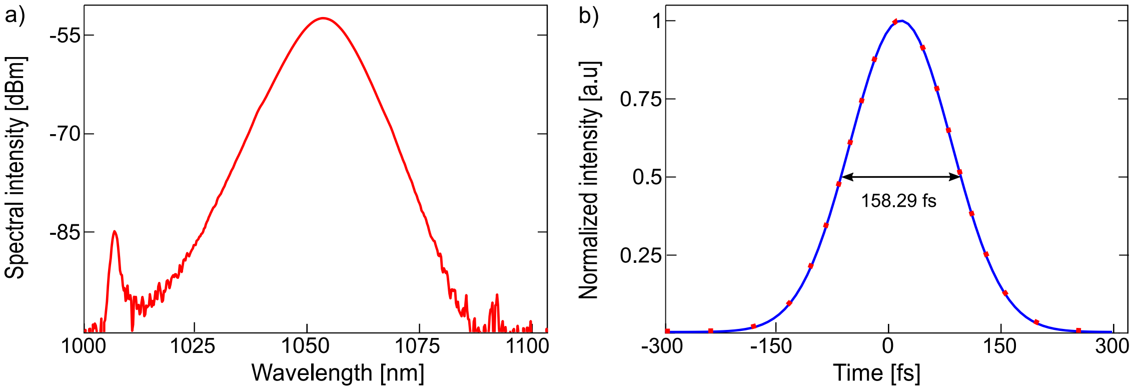

Figure 4.1: a) Output spectrum of the Origami 10 LP b) Autocorrelation trace (solid blue) and corresponding sech^2 fit (red dots) of the Origami 10 LP laser. The AC trace measured at FWHM is 158.29 fs.

This laser is a turn-key system thus in order to control the output power we used a variable neutral density. Using a powermeter, we measure a maximum average power of 10 mW which gives an output peak power for this laser of 1.07 kW and a pulse energy of 0.13 nJ. An extra advantage of this system is that it is the cheapest of the Origami laser product line (~ 15 k€). Thus, this system could be attractive for different applications such as OCT where SC systems are in direct competition with the swept-sources.

The first experiment made with this seed laser was to couple directly the output beam of the Origami LP into the PM-ANDi fiber to observe and analyze the SC generation. The whole setup is shown in Fig. 4.2. A half-wave plate was used to turn the input polarization state at the fiber input while the polarizer at the output of the fiber was used to observe the spectral content of the light of each polarization axis. A set of aspheric lenses is used to couple the light into 170 cm of PM-ANDi PCF and to collimate the output beam of the fiber. This seed laser is not isolated, thus in order to protect it from back reflections, we had to collapse the air holes of the PM-ANDi PCF to limit the amount of power going back in the laser cavity. We have chosen on purpose a long PCF length (170 cm) to ensure the ripples induced by SPM are smoothed by the OWB.

Figure 4.3 shows the evolution of the SC generation as a function of the input polarization

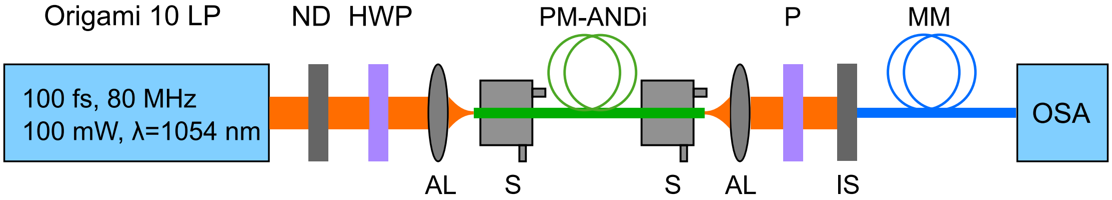

Figure 4.2: Schematic of the setup, including an Origami LP femtosecond laser, a variable neutral density filter (ND), a half-wave plate (HWP), two aspheric lenses, two 3D translation stages (S), 170 cm of all-normal dispersion PCF (PM-ANDi), a polarizer (P), 1 m of multimode pick-up fiber (MM), an integrating sphere (IS), and an optical spectrum analyzer (OSA).

for a maximum coupled power of 6 mW (the coupling efficiency is around 60 %). Therefore, the coupled peak power inside the PM-ANDi PCF is up to 0.64 kW. We find, at maximum coupled power, the output spectrum is broader when the input beam is aligned on the slow axis of the fiber (pink curve) with a bandwidth of 45 nm at -3 dB. This result is expected because the nonlinear coefficient is higher on the slow axis than on the fast axis (blue curve), as discussed in Section 2.3, which has a bandwidth at -3 dB of 42 nm. Furthermore, the spectrum is narrower when the beam is aligned at 45 ° of the optical axes (red curve), as explained in Sec. 1.2.9 and Sec. 3.1 with a bandwidth of 37 nm at -3 dB. The SC spectrum is quite symmetric whatever the input angle due to the parabolic shape of the fiber dispersion (Fig. 2.9). Also, we remark the Kelly sideband of the seed laser is still present during the SC generation at 1005 nm. Then, we highlight the output power of this laser being rather small, the output bandwidth of our SC (slight broadening) is extremely weak compared to octave-spanning SC generation. The broadening is limited but can still be useful for some applications such as OCT.

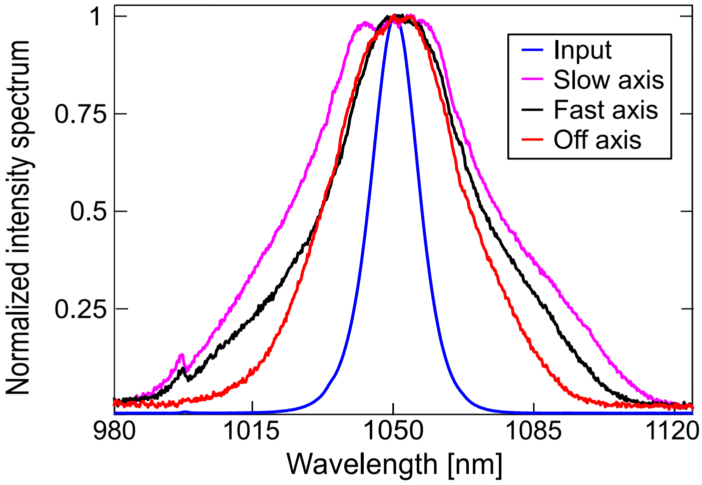

Figure 4.3: Comparison between the input seed laser spectrum and SC spectra for different input polarizations: slow axis (pink curve), fast axis (blue curve) and at 45° of the optical axes (red curve), with 10 mW average input power.

To understand the dynamic of this weak broadening, we performed some simulations using a Matlab code resolving the CGNLSEs, as described in Eqs. 1.39, and using the same input parameter than in our experiment: 103 fs input pulse duration, 0.64 kW input coupled peak power, 170 cm of PM-ANDi PCF and input polarization aligned along the slow axis. Therefore, Fig. 4.4 (a) compares the output experimental spectrum (blue curve) with the simulated one (red curve). We observe the bandwidth of both spectra is rather similar at -3 dB (45 nm for the experimental and 50 nm for the simulation), which means the parameters used are accurate for this simulation. Furthermore, we can clearly notice the broadening induced by the SPM and the OWB on the simulated spectrum (harder on the experimental one). Fig. 4.4 (b) displays the output temporal profile. We observe a typical ANDi SC temporal trace after the rising of the OWB as shown in Fig. 1.15. Therefore, with a fiber length of 170 cm, the maximal broadening is achieved for an input pulse duration of 103 fs.

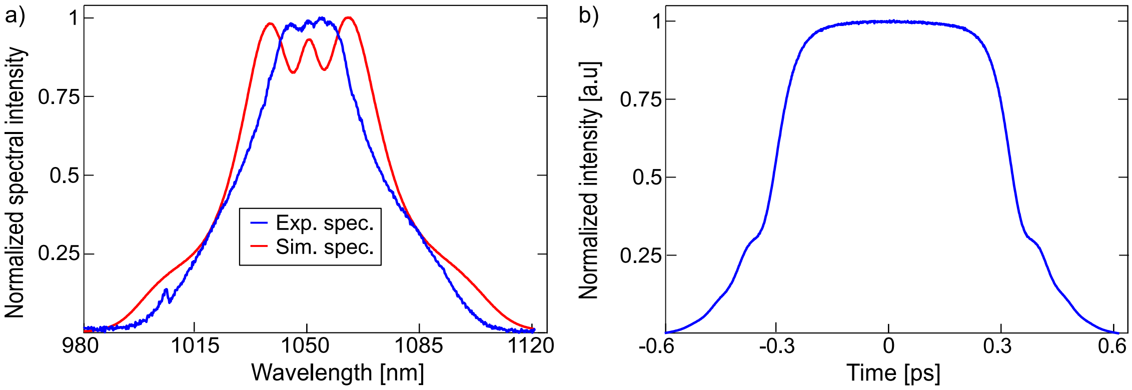

Figure 4.4: a) Simulated (red curve) and experimental (blue curve) spectrum at the output of 170 cm of PM-ANDi PCF with an input pulse duration of 103 fs and input peak power of 0.64 kW. b) Simulated temporal profile at the output of the 170 cm of PM-ANDi PCF.

Aligning the input beam polarization on one of the principal axes and using the output polarizer, we can measure the PER of our SC. Figure 4.5 shows the recorded SC spectrum for different orientations of the polarizer when the input beam is aligned on the slow axis. As expected, we can clearly see the spectrum is broader and more powerful when the polarizer is aligned on the slow axis as well (blue curve). When it is aligned at 45° degrees to both axes (red curve), we observe the spectrum is highly modulated due to the interference of the two polarizations. The beating period over the spectrum provides an estimation of the group birefringence as $\delta n = c/L/d\nu$ where $d\nu$ is the free spectral range of the interference pattern. Using this formula, we obtain a group birefringent of 3.7×10^{-4} at 1054 nm. Furthermore, the power of this spectrum is 3 dB below the higher intensity level because only half of the power present on the slow axis is detected. Finally, when the polarizer is aligned on the fast axis, the spectrum is the narrower and the weaker (purple curve). Subtracting the purple to the blue spectrum yields an estimate of the PER of 17 dB. The measured PER of the laser is up to 26 dB so we observe a small deviation of the input polarization during the coupling. Thus, with this configuration, we are able to generate a linearly polarized SC with a bandwidth up to 45 nm at -3 dB.

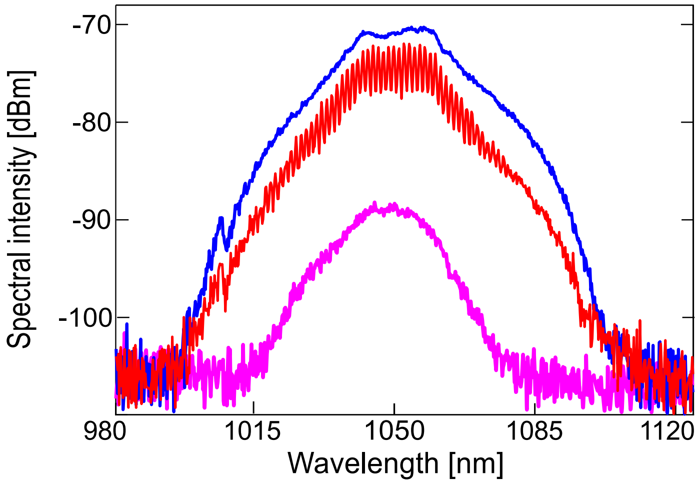

Figure 4.5: SC evolution for different polarizer orientations while pumping on the slow axis. Polarizer aligned on slow axis (blue curve), fast axis (purple curve) and at 45° to both axes (red curve)

In order to increase the SC bandwidth, we added to the input pump laser an all-fiber amplification stage followed by a compression stage. The amplification stage is schematically depicted in Fig. 4.6. It is composed of: two isolators (to prevent back-reflections in the laser cavity), two wavelength-division multiplexers for pump diodes (one at the input and one at the output), two 1 W butterfly InGaAs pump diodes and 1 meter of PLMA-YSF-10/125 doped-fiber from Nufern. All these components were spliced together using a 90 S Fujikura splicer. We built this amplifier using both backward and forward pumping configuration (one pump diode at each side of the amplifier, separated by the ytterbium gain fiber), to limit the maximum power handled by the first wavelength division multiplexers (WDM).

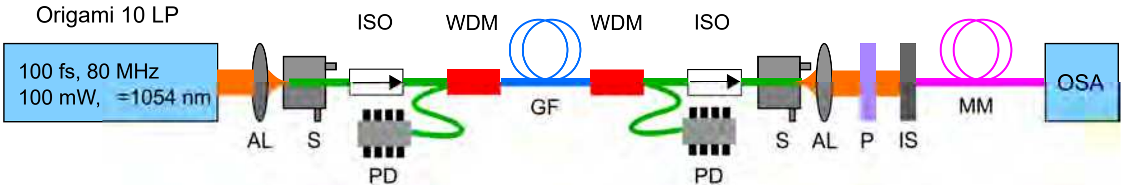

Figure 4.6: Scheme of the pulse amplification stage, including an Origami 10 LP femtosecond laser, two aspheric lenses (AL), two 3D translation stages (S), two isolators (ISO), two wavelength-division multiplexers (WDM), two pump diodes (PD), one meter of ytterbium gain fiber (GF), a polarizer (P), 1 m of multimode pick-up fiber (MM), an integrating sphere (IS), and an optical spectrum analyzer (OSA).

Our amplifier follows the parabolic pulse amplification architecture since it operates in the normal dispersion regime. In a fiber amplifier, chirped parabolic pulses can be generated when the pulse is affected by optical gain, normal dispersion and Kerr nonlinearity [113, 114]. Using this parabolic pulse amplification, it can be easy to obtain nearly transform-limited pulses after pulse compression, due to the linear chirp acquired during the propagation inside the gain fiber.

The average power at the output of the amplifier stage, when both pump diodes are turned on, is up to 920 mW (460 mW when only one pump diode is turned on). The output spectrum after the second isolator is shown in Fig. 4.7 (a) when the pump diodes are turned on (blue curve) and off (red curve). When the pump diodes are turned off, the output average power after the amplification stage is 0.8 mW while when both pump diodes are turned on the output this one goes up to 920 mW. Thus, the gain of this amplifier stage is up to 21 dB. We can remark a blue shift when the pump diodes are turned on up to 30 nm and an amplification of the diode pump residue at 980 nm. After measuring the output spectrum of the amplifier stage, we measure the output pulse duration of our amplified pulse using the same autocorrelator. Figure 4.7 (b) shows the measured AC trace (intensity profile) corresponding to a pulse duration of around 5.1 ps at FWHM, which is well longer than the input pulse (103 fs).

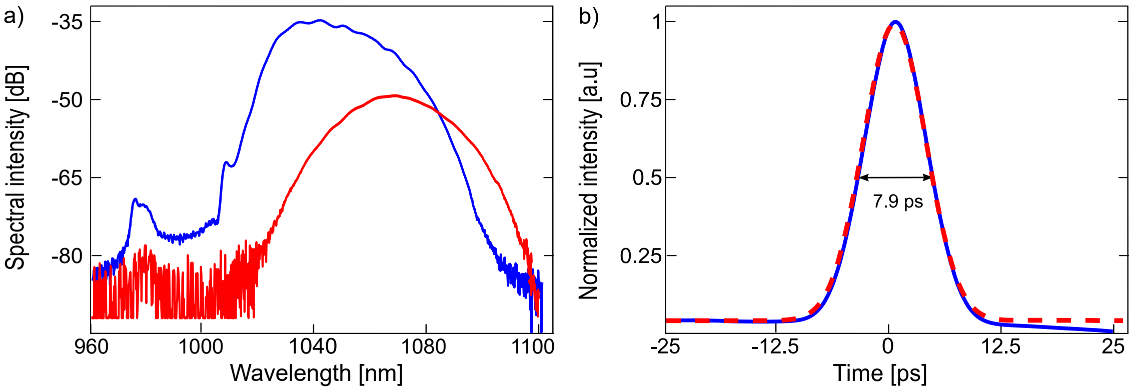

Figure 4.7: a) Experimental spectra at the output of the amplifier stage when pump diodes are turn off (solid red) and turn on (solid blue). (b) Autocorrelation trace (solid blue) and corresponding sech^2 fit (red dots) of the Origami 10 LP laser after amplification. The AC trace measured at FWHM is 7.9 ps.

After the amplification stage, we need to compress the output pulse to maximize the peak power available for the SC generation. The experimental set-up is sketched in Fig. 4.8. We used linear compression based on a hollow core fiber (HCF). The set-up includes a set of two aspheric lenses to collimate and focus the laser beam inside our HCF. This

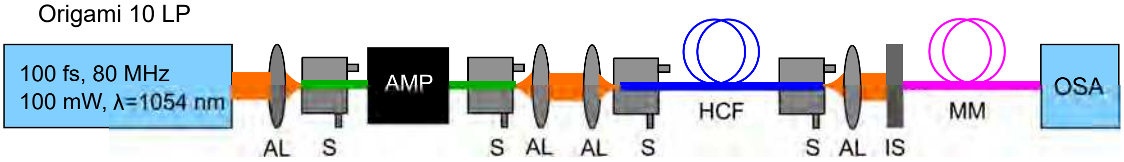

Figure 4.8: Schematic of the compression stage optical set-up, including an Origami LP femtosecond laser, four aspheric lenses, four 3D translation stages (S), one amplification stage (AMP), 195 cm of HCF, an integrating sphere (IS), 1 m of multimode pick-up fiber (MM) and an optical spectrum analyzer (OSA).

HCF is the HC 1060-2 from NKT Photonics which has an anomalous dispersion over the full pulse bandwidth after our amplifier stage as shown in Fig. 4.9. Furthermore, the average power after our compression stage is 586 mW (coupling efficiency of 63 %). The TBP of our system after the amplification is equal to 43 for a bandwidth of 31 nm centered at 1040 nm. Thus, we can theoretically decrease the pulse duration down to 37 fs.

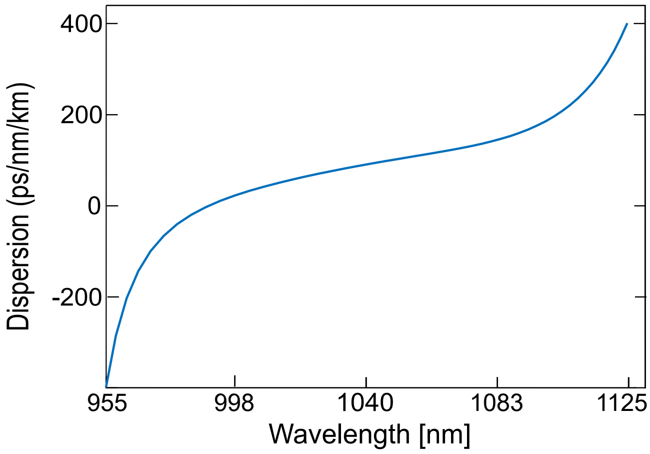

Figure 4.9: Measured dispersion curve of the HCF 1060-2 from NKT Photonics.

To estimate the optimal fiber length of the HCF, we measure the output pulse duration for different fiber lengths with a cut-back method. Figure 4.10 (a) shows the measured AC traces of the output pulse of the HCF for a total amplification stage length of 260 cm while Fig. 4.10 (b) shows the deconvolved pulse duration as a function of the HCF length for a total amplification length of 260 cm (red dots) and 135 cm (blue dots). The 135 cm amplification stage is obtained by removing 125 cm of passive fiber (PM-980 form Nufern). We can notice the output pulse duration decreases for fiber length going from 100 cm to 110 cm (165 cm to 195 cm) and increases for fiber length longer than 120 cm (195 cm) for a total amplification stage length of 135 cm (260 cm). The shortest pulse duration obtained via this cut-back measurement is 90 fs using a total amplification stage length of 135 cm, which highlights the need to remove as much as possible of passive fiber. Thus, the peak power available after our steps of amplification/compression is now

73 kW (gain of a factor 11 with the amplification/compression stages).

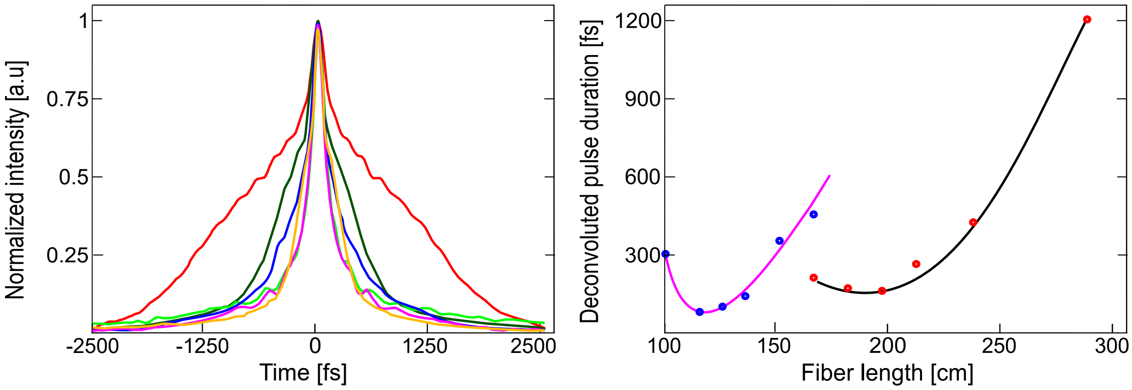

Figure 4.10: a) AC traces at the output of the compression stage, for a total amplification stage length of 135 cm, for different HCF lengths: 285 cm (red), 235 cm (dark green), 210 cm (yellow), 195 cm (light green), 180 cm (purple) and 165 cm (blue). (b) deconvolved output pulse duration as a function of HCF length and amplification stage length (135 cm blue dots and 260 cm red dots) and their respective fitting.

From this higher available peak power, we can expect a broader bandwidth for the SC generation. Figure 4.11 depicted the experimental set-up. Again, we use a set of two aspheric lenses to couple the light inside the PM-ANDi fiber and to collimate the output beam, and 170 cm of PM-ANDi PCF. The output power of the PM-ANDi PCF is 310 mW (coupling efficiency of 57 %). The coupling efficiency is rather similar than the one without the amplification/compression stages (60 %), which means we keep a good beam quality during the propagation.

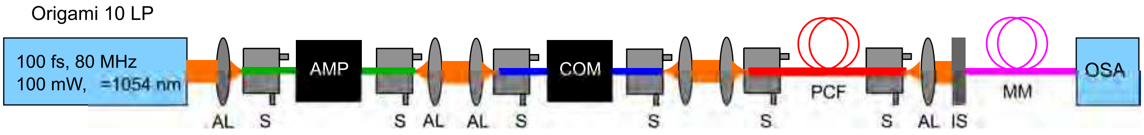

Figure 4.11: Schematic of the SC generation optical set-up, including an Origami 10 LP femtosecond laser, six aspheric lenses, six 3D translation stages (S), one amplification stage (AMP), one compression stage (COM), 160 cm of PM-ANDi fiber (PCF), an integrating sphere (IS), 1 m of multimode pick-up fiber (MM) and an optical spectrum analyzer (OSA).

Figure 4.12 shows the SC spectrum at the output of the PM-ANDi fiber with the maximum of power injected. We can observe the SC bandwidth spans is going from 980 nm to 1130 nm at -30 dB which is barely broader than our first attempt. Furthermore, we can observe the SC spectrum is highly modulated, which is due to the interaction of the two linear polarizations inside the OSA. The assumption emitted to explain the weak improvement of the SC bandwidth are: a lack of polarization control between each stage and a chirped induced by the compression stage which limits the available peak power for the SC generation.

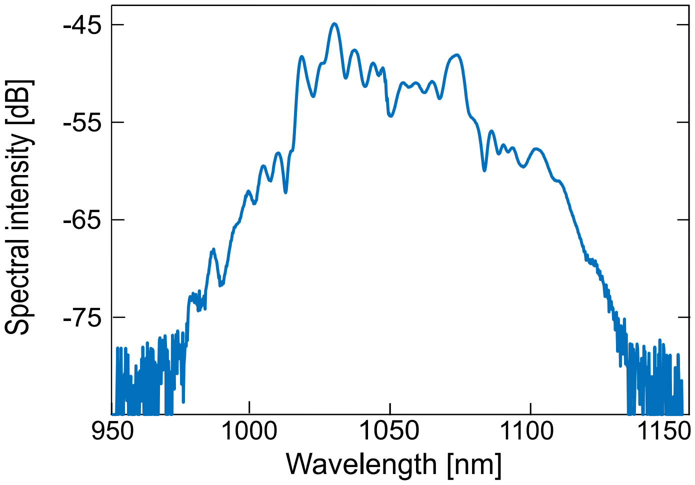

Figure 4.12: Experimental SC spectrum at the output of the PM-ANDi PCF with an output power of 460 mW.

Figure 4.13, compares the experimental spectrum with the expected one assuming a ideal amplified, transform-limited pulse (pulse duration of 90 fs, coupled input peak power of 38 kW and 170 cm of PM-ANDi PCF), linearly polarized along the slow axis. We observe the drastic bandwidth difference between the two spectra. We propose, to explain this drastic change in the spectral bandwidth, that the pulse might be still very chirped even after the compression stage and/or a lack of the polarization control through the amplification/compression stages.

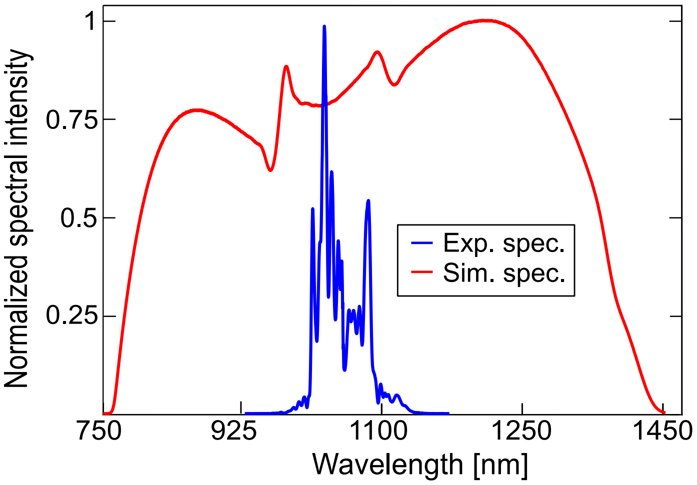

Figure 4.13: Comparison between experimental and simulated SC spectra at the output of the PM-ANDi PCF with an input pulse duration of 90 fs, coupled input peak power of 38 kW and 170 cm of PM-ANDi PCF.

To conclude, this first SC system could be used as a compact/cheap SC source mainly for OCT application. The tentative to improve this system, using parabolic pulse amplification and linear compression, was not really successful when we take a look at the SC bandwidth obtained with the amplified and compressed pulse. Thus, this amplified setup should be improved before a new attempt for SC generation.

4.2/ SECOND SYSTEM: HIGH-POWER, LONG PULSE DURATION AND NONLINEAR COMPRESSION

The second system used during this Ph.D is the Origami 10 XP (for extra power) from NKT photonics. This laser, according to the datasheet, produces femtosecond pulses with a duration around 400 fs at a repetition rate of 100 kHz with an average power of 4 W centered at 1030 nm and a bandwidth of 3 nm (maximum peak power of 88 MW and pulse energy of 40 μJ). Again, we performed different measurements to check the laser specifications. to be sure of the laser datasheet. Figure 4.14 (a) shows the output spectrum of this laser recorded via an integrating sphere and an OSA, we find this spectrum has a bandwidth of 3 nm at -3 dB centered at 1030 nm. Figure 4.14 (b) represents the AC trace of the laser. After deconvolution of this AC trace, we calculated a pulse duration of 398 fs. Thus, the TBP of this laser is 0.338, which means this laser can not be linearly compressed anymore (close to being transform-limited).

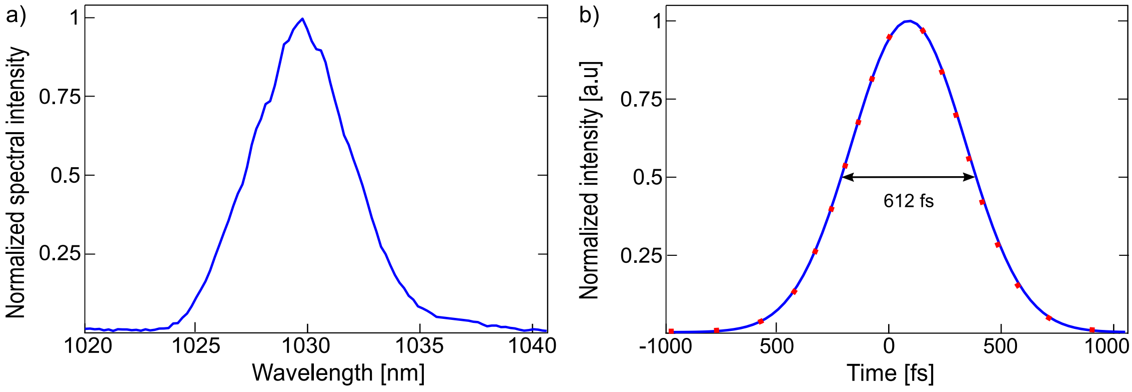

Figure 4.14: a) Output spectrum of the Origami 10 XP b) Autocorrelation trace (solid blue) and corresponding sech^2 fit (red dots) of the Origami 10 XP laser. The AC trace measured at FWHM is 612 fs.

As in the first system, we coupled directly the laser beam inside 2 m of PM-ANDi PCF to investigate our SC generation using an aspheric lens. Our setup is similar to the one depicted in Fig. 4.2 with the new high power laser.

Figure 4.15 shows the evolution of the SC spectrum for an increasing input coupled power from 3 mW to 12 mW (peak power going from 45 kW to 183 kW). We reduced drastically the output power of the laser, by use of the neutral density, to avoid burning the fiber facet. Furthermore, for average power higher than 15 mW the spectrum doesn't evolve anymore. Also, the laser beam state of polarization is aligned on the slow axis of the fiber to maximize the spectral bandwidth. We remind the XPMI has no real impact on the noise properties of the SC, as demonstrated in Sec. 3.4. As expected, when we increase the input coupled power, the spectrum broader symmetrically and is quite flat. Thus, the SC bandwidth spans from 359 nm for an input coupled peak power of 45 kW to 710 nm for an input coupled peak power of 183 kW (690 nm to 1400 nm at -3 dB), with this power the SC spectrum covers more than one octave. We can observe, on all these spectra, some ripples on the anti-Stokes side around 950 nm corresponding to the signature of SRS components, as described earlier and in [9, 74]. This phenomenon was expected because the output pulse duration of this laser is around 400 fs, which is long enough to observe it. Furthermore, we can see on the blue curve (input power of 9 mW) the XPMI sideband composed of two small peaks at 1366 nm and 1377 nm, respectively. Finally, this sideband is swallowed when the coupled power is increased due to the broadening toward longer wavelengths. Thus, XPMI generation could be used to increase the SC bandwidth of a SC spectrum.

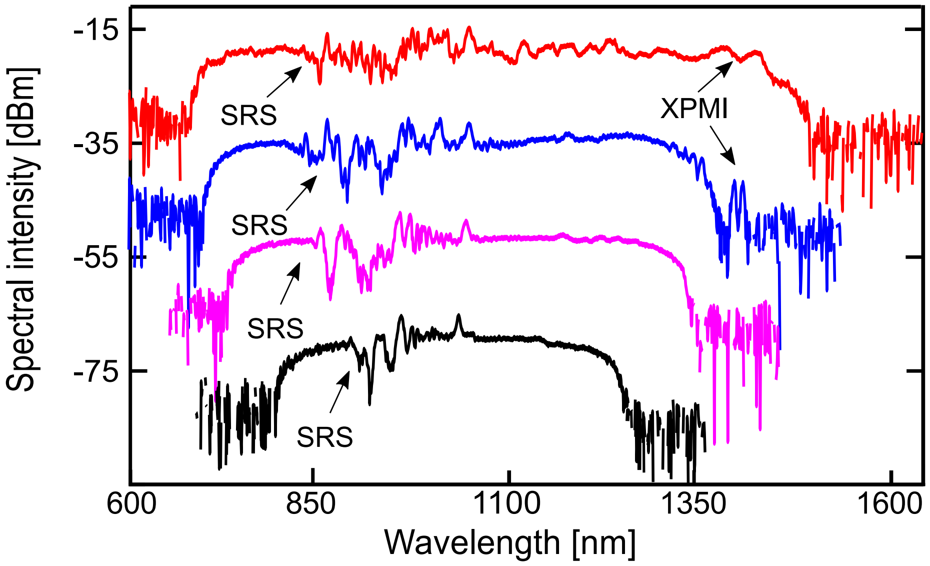

Figure 4.15: Experimental SC spectra at the output of the PM-ANDi PCF for input average power of: 3 mW (black curve), 6 mW (pink curve), 9 mW (blue curve) and 12 mW (red cruve) with an input pulse duration of 400 fs.

By use of a polarizer and a powermeter, we can measure the average PER of our SC spectra. This PER decreases drastically when the coupled power increases, this one is equal to 16.3 dB when $P_{in} = 3$ mW and equal to 2.5 dB when $P_{in} = 12$ mW. This degradation confirms the emergence of SRS components during our SC generation. Thus, we can expect this SC spectrum to be very noisy and its applications could be limited due to the presence of SRS components, as described in Ref. [9, 74].

In order to reduce the pulse duration of the laser, we built a stage of nonlinear compression. This stage is composed by 4 cm of LMA fiber (for the nonlinear spectral broadening), the LMA-PM-15 from NKT photonics, and 2 chirped mirrors (for the compression) from Edmund Optics. This technique of nonlinear compression leads to the anti-correlation between the pulse duration and the spectral bandwidth, which is given by the TBP equation. When the spectral bandwidth of a laser increases, we can compress down its initial pulse duration. The optical set-up for this nonlinear compression stage is depicted in Fig. 4.16.

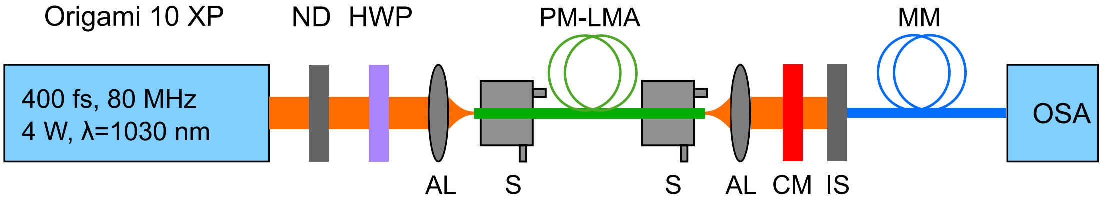

Figure 4.16: Schematic of the experimental setup for nonlinear pulse compression, including an Origami XP femtosecond laser, a variable neutral density filter (ND), a half-wave plate (HWP), two aspheric lenses, two 3D translation stages (S), 4 cm of PM-LMA, 2 chirped mirrors (CM), 1 m of multimode pick-up fiber (MM), an integrating sphere (IS), and an optical spectrum analyzer (OSA).

The output spectrum of the PM-LMA is shown in Fig. 4.17 (a). We can notice the features of the SPM spectrum including three peaks and two dips. This SPM has a bandwidth of 28 nm at -3 dB and is centered at 1030 nm. Thus, the theoretical minimum pulse duration which can be obtained after compression is 40 fs. Using our two chirped mirrors, we reduce the output pulse duration down to 90 fs with a total of four bounces (total GDD = -4000 fs^2). The AC trace of this SPM spectrum is shown in Fig. 4.17 (b) and we measure a pulse duration of 90 fs (pulse not transform-limited) using a secant hyperbolic approximation. Thus, the peak power available is 4 times higher than the previous system therefore we use another neutral density to reduce the average power before the PM-ANDi fiber.

After compressing our laser, we inject its beam inside our PM-ANDi fiber using another 3D stage and aspheric lenses. Figure. 4.18 shows the SC evolution for different input average power going from 300 μW to 1.4 mW (peak power going from 46 kW to 183 kW). These values are the same ones than our previous experiment. First of all, we notice the dynamic range is smaller than the previous experiment but was expected

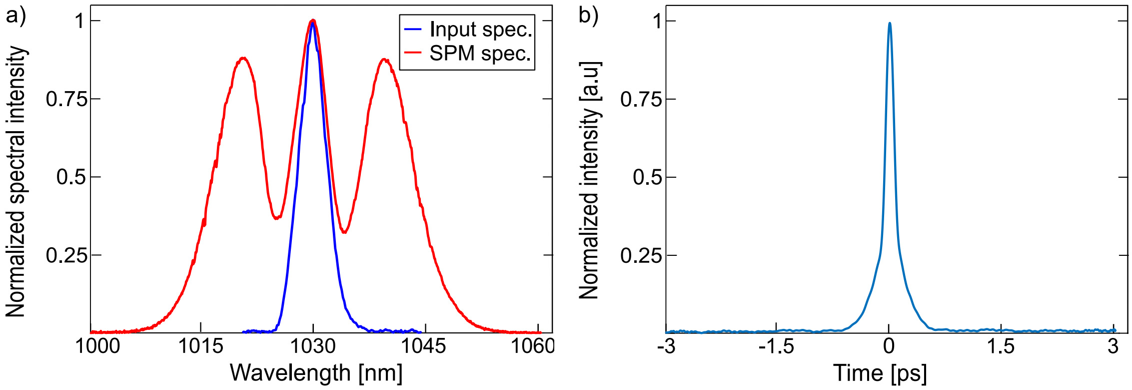

Figure 4.17: a) Experimental SPM spectrum at the output of the PM-LMA fiber with an output power of 13.5 mW. (b) Autocorrelation trace of compressed pulse. The AC trace measured at FWHM is 138 fs.

because the power detected by the OSA is 10 times smaller. Then, for an input coupled average power at the fiber entrance of 300 μW, the spectral bandwidth goes from 800 nm to 1240 nm at -3 dB (440 nm). When we increase the injected power the spectral bandwidth goes up to 730 nm (from 680 nm to 1410 nm) for an input power of 1.4 mW. As demonstrated in Ref. [77], in ANDi SC generation, the spectral bandwidth is independent of the input pulse duration if the fiber length is long enough (longer than the OWB length). We can confirm this statement because the spectral bandwidth obtained using a 90 fs and a 400 fs input pulse duration is rather similar (710 nm VS 730 nm). Furthermore, we can remark there are no ripples on the blue side of the spectrum anymore. Thus, we can confirm there are due to SRS. Furthermore,

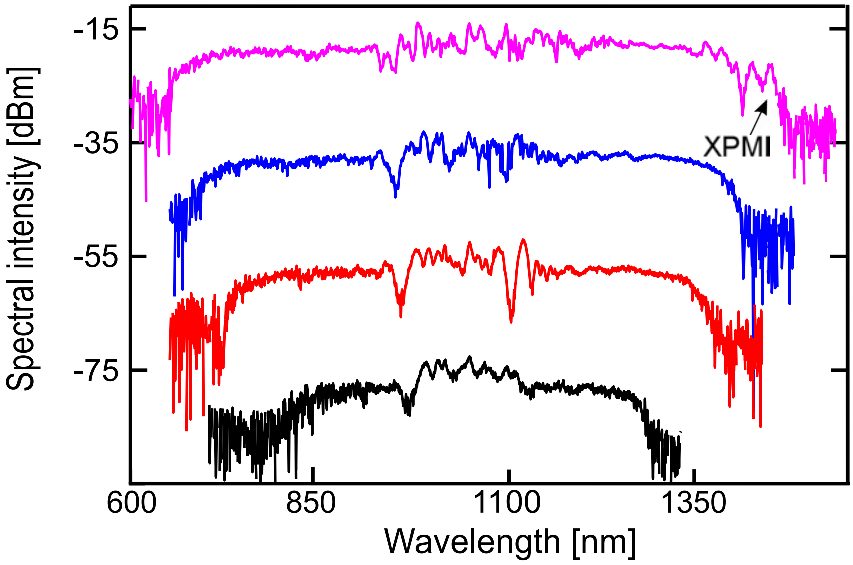

Figure 4.18: Experimental SC spectra at the output of the PM-ANDi PCF for input coupled average power going from 300 μW to 1.3 mW with an input pulse duration of 90 fs. Power offset between the spectra for better clarity.

the fine structures in the SPM area can be attributed to the chirp of our compressed pulse. Also, we observe some ripples in the SPM area, which could be produced by the fine structures present in the input spectrum. Finally, we observe on the pink spectrum the presence of XPMI sideband, which has not been swallowed by the SC spectrum.

After investigating the different SC spectra generated, we decided to look over the RIN in the context of low-noise ANDi SC generation. To do so, we used different noise measurement setups composed either by band-pass spectral filters (as described in section 2.1) or using a monochromator. The monochromator has the advantage to allow control over the spectral width of the filters but we have to be careful because when we reduce this one the resolution is higher but the signal-to-noise ratio decreases as well [115].

In order to measure the RIN of the seed laser, we collimated the output beam laser onto an InGaAs photodiode (5 GHz DET08CFC from Thorlabs) after reducing its power using some neutral densities. Then, we connected this fast photodiode to an oscilloscope (4 GHz HDO9404 from Teledyne LeCroy) to record the output pulse train. Fig. 4.19 (a) shows a single pulse of the Origami 10 XP laser recorded via our oscilloscope. As expected, each individual pulse has the shape of the waveform distorted and duration (70 ps) limited by the rise and fall times of the photodiode. To measure the RIN of this laser, we took the maximum of each intensity peak and plot the histogram of the maximum of our 5000 pulses, as shown in Fig. 4.19 (b), with its Gaussian fit (in red). Using this representation, we obtain the average (1.2449) and the standard deviation (0.0119) of our Gaussian distribution. Thus, the RIN of the seed laser is equal to 0.96 %, which is similar to other femtosecond lasers proposed by Coherent.

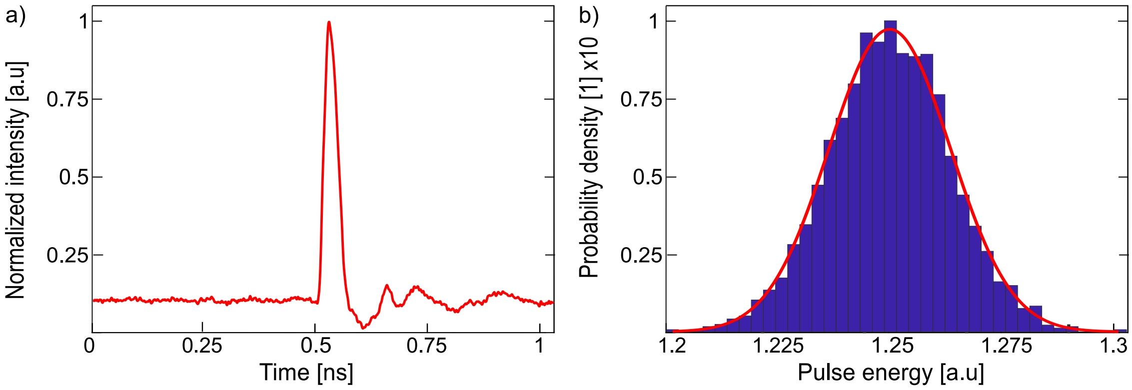

Figure 4.19: a) Single pulse of the Origami 10 XP laser recorded on the oscilloscope. b) Histogram of the variation of the maximum intensity of 5000 pulses. The red curve represents a Gaussian fit of the distribution.

After measuring the RIN of our seed laser, we investigated its impact on the RIN of the SPM spectrum. Using the same method, we measured an average RIN of the SPM spectrum of 0.99 %, which is very close to the seed laser RIN. Then, we used the monochromator to obtain a spectrally resolved RIN. We adjusted the spectral filter to have a bandwidth of 5 nm and we took RIN every 2.5 nm. Figure 4.20 shows the SPM spectrum (red curve) and its corresponding spectrally resolved RIN spectrum (blue curve). The RIN values go from 0.92 % near the center to 3.88 % at the edges. We can find, as in Fig. 2.20, a correlation between the RIN and the SPM spectra. Indeed, we determine the minimum RIN values are located at the maxima and minima of the SPM spectrum while the maximum RIN values are located on the inflection points of the spectrum. Furthermore, the RIN spectrum grows exponentially on the edges of the spectrum as demonstrated in Sec. 2.4.

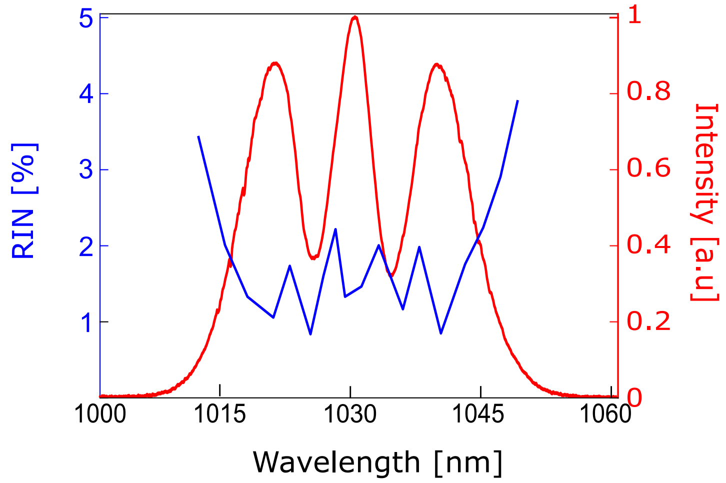

Figure 4.20: Spectrally resolved RIN spectrum (solid blue) and its corresponding intensity spectrum at the output of the LMA-PM 15 PCF for an input average power of 14 mW (solid red).

Now, we will investigate the SC RIN for two different cases (input pulse duration of 90 fs and 400 fs). For this, we use a set of spectral band-pass filters with a bandwidth of 10 nm going from 700 nm to 1300 nm, and we measure the RIN value every 50 nm. Figure 4.21 shows the spectrally resolved RIN for both cases for a similar input coupled peak power (≈ 183 kW). It is difficult to notice a correlation between the RIN and the intensity spectrum due to the bandwidth of these filters and the gap between two wavelengths across the whole SC span. Otherwise, we can clearly observe the RIN is more than 20 times higher, on the blue side of the spectrum, for an input pulse duration of 400 fs compared to a 90 fs pumping, which confirms the presence of SRS components. Indeed, the RIN values, for the long pulse duration case, varies from 1.5 % to 32 % with a mean value of 11.6 % while, for the 90 fs case, the RIN values vary from 1.5 % to 9.4 % with a mean value of 4.5 %.

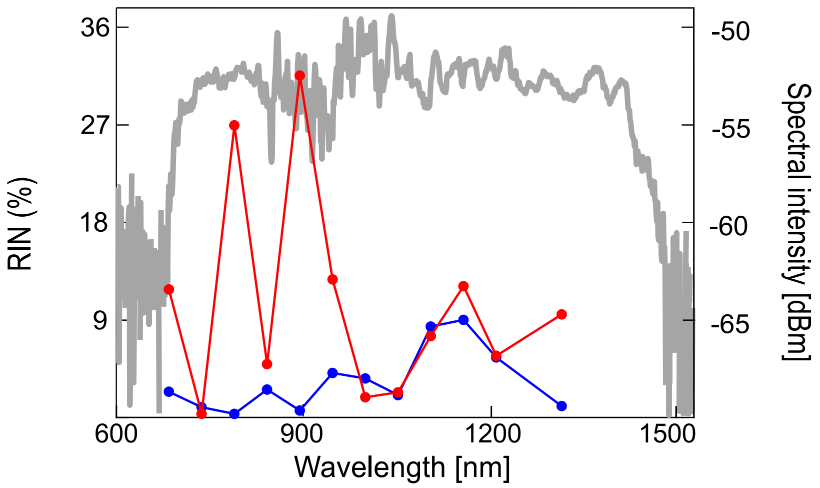

Figure 4.21: Spectrally resolved SC RIN spectrum for an input peak power of 183 kW for a input pulse duration of 90 fs (solid blue) and 400 fs (solid red), and SC spectrum for a coupled input peak power of 183 kW and input pulse duration of 400 fs (solid grey).

To conclude, as demonstrated numerically in Refs. [9,74,88], a 400 fs input pulse duration is too long to obtain a low-noise ANDi SC generation. Indeed, the SC spectrum is affected by the SRS for a case of high input peak power, which is required to obtain a large bandwidth (we generated an octave-spanning SC). After using a nonlinear compression stage, we have been able to reduce the pulse duration of our seed laser down to 90 fs. The bandwidth of our SC generation remains the same for a similar input peak power but the average RIN level is reduced by a factor of almost 3, highlighting the necessity of a short input pulse duration to obtain a low-noise SC system. Finally, this compressed system could be used for different applications such as OCT and metrology.

4.3/ THIRD SYSTEM: HIGH POWER, SHORT PULSE DURATION

The third seed laser used during this Ph.D is the Origami 10 HP (for high power) from NKT photonics. This laser, according to the datasheet, produces pulses with a duration of around 120 fs at a repetition rate of 80 MHz with an average power of 4 W centered at 1054 nm and a bandwidth of 10 nm (maximum input peak power of 367 kW and maximum energy of 50 nJ). Once more, we checked all these laser specifications using our experimental setups to be sure of the laser datasheet. Figure 4.22 (a) shows the output spectrum of this laser. We can notice this spectrum has a bandwidth of 9 nm center at 1049 nm. Figure 4.22 (b) represents the AC trace of this laser. After deconvolution of this AC trace, we calculate a pulse duration of 180 fs, which is quite longer than the value provided in the laser datasheet. Thus, the TBP of this laser is 0.4417, which means this laser is slightly chirped and could be compressed to shorter pulse duration. However, its output peak power (244 kW) is high enough to obtain a broadband SC spectrum. Thus, to keep a compact system, we decided to not compress it further down.

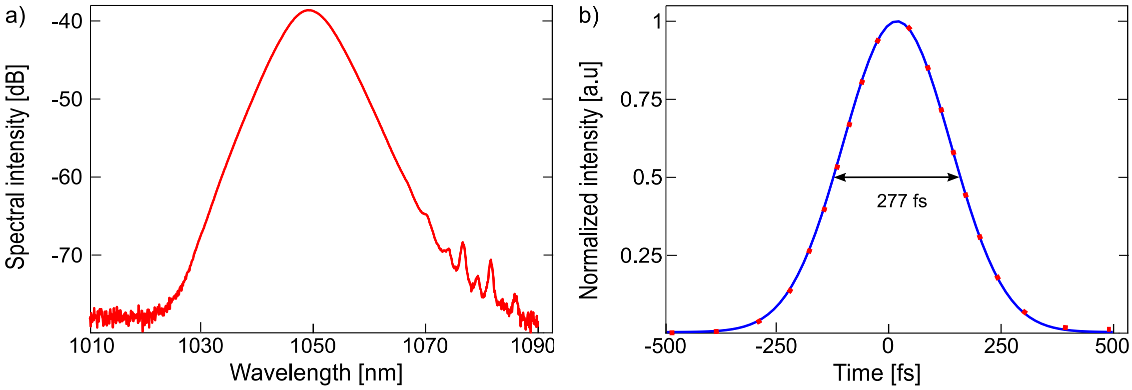

Figure 4.22: a) Output spectrum of the Origami 10 HP laser b) Autocorrelation trace (solid blue) and corresponding sech^2 fit (red dots). The AC trace measured at FWHM is 277 fs.

Again, using a similar setup to the one depicted in Fig. 4.2 with the new high power laser, we inject the seed laser beam via an aspheric lens inside 2 m of PM-ANDi PCF to generate our SC light. Figure 4.23 shows the evolution of the SC spectrum as a function of the input polarization angle for an average coupled input power of 640 mW (peak power of 37 kW). This seed laser was a demo system and we had a lot of troubles to couple the output beam inside our PFC with a maximum coupling efficiency of 30 %. Furthermore, we use a higher average power compared to the previous system due to the higher repetition rate of the laser. Furthermore, the output beam of this laser was not ideal and we obtained a maximum coupling efficiency of 30 %. We obtain a broader bandwidth while pumping along the slow axis (red curve), with a spectrum

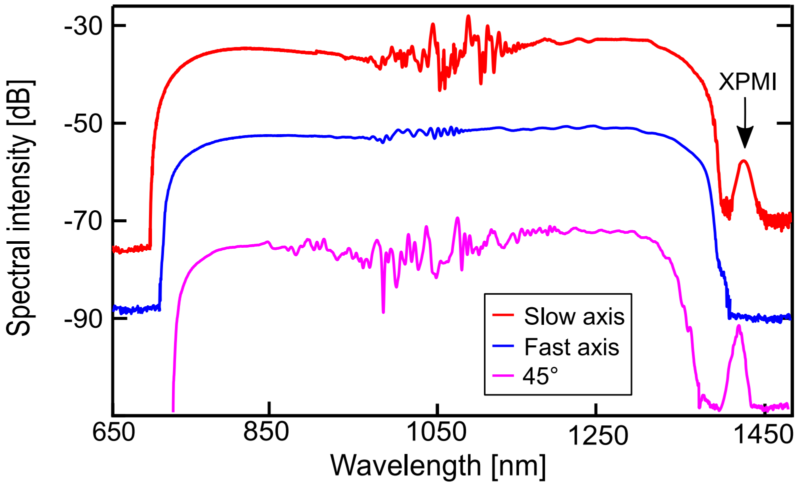

Figure 4.23: Experimental SC spectra at the output of the PM-ANDi PCF for input coupled average power of 640 mW with an input pulse duration of 180 fs while pumping along slow axis (red curve), fast axis (blue curve) and at 45° to both axes (pink curve). Power offset for better understanding.

going from 685 nm to 1395 nm at -3 dB, which is consistent with our previous results. We can find the spectrum is quite modulated in the SPM area (from 1000 nm to 1100 nm). Furthermore, the XPMI sideband is still present at 1400 nm. The spectrum is the narrower when pumping at 45 ° to both axes (pink curve) with a spectrum going from 700 nm to 1370 nm at -3 dB. We see the spectrum is highly modulated from 870 nm to 1120 nm, which is probably due to the XPM effect. The XPMI sideband is again present and slightly stronger than the one obtained on the red curve, as expected from the theory (see Chapter 3). Then, we obtain an extremely flat spectrum when pumping on the fast axis (blue curve) with a spectrum spanning from 670 nm to 1390 nm at -3 dB without any trace of a sideband at 1400 nm.

Figure 4.24 shows the evolution of the SC generation for an input coupled average power increasing from 1 mW to 640 W (peak power going from 6 W to 37 kW). We can clearly notice two SPM fringes on the pink curve (for an input average power of 6 W). Then, by increasing further up the power, we can remark the rising of the OWB for an output average power higher than 110 mW (purple spectrum). Furthermore, the SC bandwidth goes from 9 nm (in the linear regime) to 720 nm (going from 670 nm to 1390 nm) at -3 dB which is more than one octave. Next, as expected from coherent ANDi SC generation, the spectrum broadens symmetrically and is extremely flat (the maximum amplitude of the ripples in the SPM area is 1.65 dB). Finally, we can not observe any modulations in the final spectra (brown, red and black spectra), indicating the presence of SRS components. Thus, we can expect this SC generation to be low-noise.

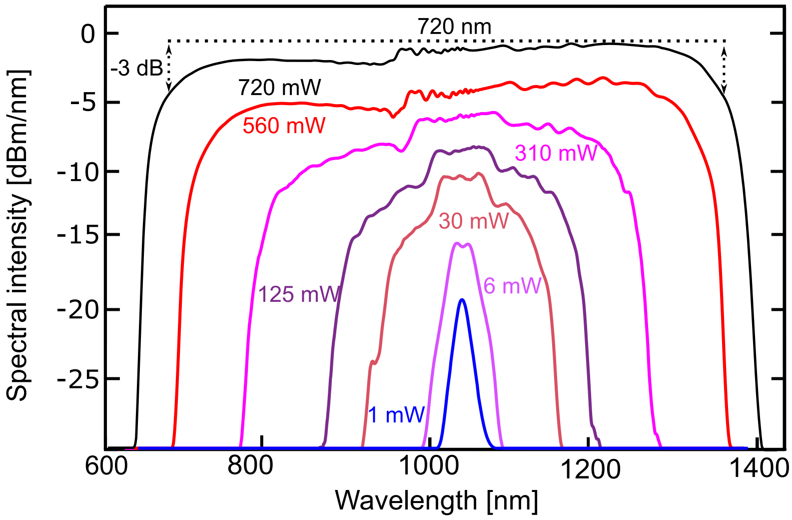

Figure 4.24: Experimental SC spectrat at the output of the PM-ANDi PCF for input coupled average power of 1 mW to 640 mW with an input pulse duration of 180 fs and an input beam polarized along the fast axis.

Also, using a polarizer at the output of the fiber, we measured the polarization extinction ratio (PER) of our SC spectrum. Thus, Fig. 4.25 depicts the SC spectra while the input beam is polarized along the fast axis and the output polarizer is aligned on the fast axis (red curve) and the slow axis (blue curve). Thus, we can measure an average PER for our SC spectrum of 16.9 dB, which means we are able to generate a SC spectrum linearly polarized. Again, we noticed a degradation of the PER at the output of the PCF (input one up to 31 dB), but this result is consistent with the previous SC PER values, which means the degradation is only induced by either the collapse of the air holes, the coupling of the laser beam or the fiber itself.

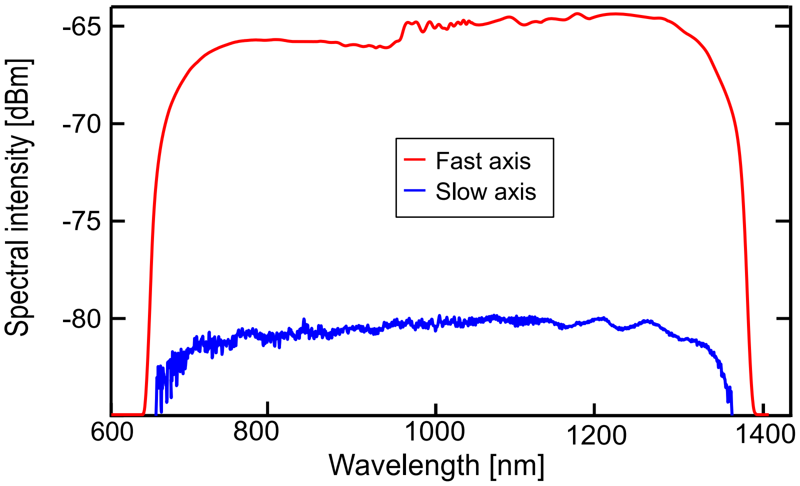

Figure 4.25: Experimental SC spectra with a half-wave plate aligned on the fast axis. The red curve shows the spectrum recorded when the polarizer is aligned on the fast axis while the blue curve shows the one recorded when it is aligned on the slow axis. The difference between both curves provides the PER.

Then, we measured the noise level of the seed laser and the SC spectrum. For the seed noise measurement, we used an ESA thus we were able to compare the noise value given by this instrument to the one given by the oscilloscope method. After using the methods described in Sec. 2.1, we calculated a RIN value from the ESA spectrum, shown in Fig. 4.26 (a), of 0.28 % (integrated from 1 Hz to 80 MHz). Furthermore, using the approximate Eq. 2.14, we obtain the exact same result, which confirms its validity. Also, after recording 2500 pulses on an oscilloscope, we obtain the histogram depicted in Fig. 4.26 (b). Using a Gaussian fit of this distribution, we extract a mean value of 2.5 and a standard deviation of 0.011. Thus, calculating the ratio of both values, we obtain a RIN value of 0.46 % using this method, which is slightly higher than our previous measurement using the ESA.

After measuring the pump laser noise, we further investigated the RIN over the whole

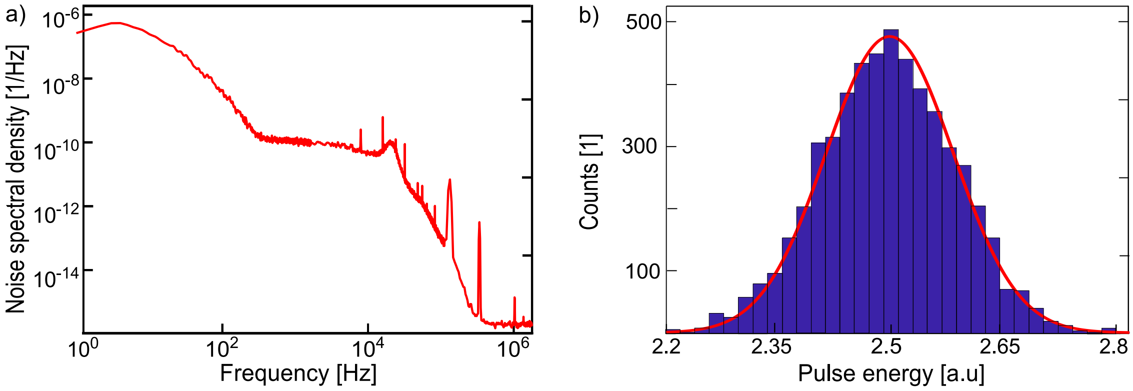

Figure 4.26: a) Electrical spectrum of the Origami 10 HP laser. b) Histogram of the variation of the maximum intensity of 2500 pulses measured with the oscilloscope. The red curve represents a Gaussian fit of our distribution.

SC bandwidth. To this end, we used a monochromator (from Princeton instrument) as a tunable spectral filter and the spectrally-sliced SC was sent to the photodetector and oscilloscope. We specifically used two photodetectors to cover the SC bandwidth: a silicon photodetector from 650 to 1100 nm and an InGaAs photodetector for longer wavelengths. The SC RIN was still measured using the Gaussian fit method by saving 10000 pulses onto an oscilloscope (PicoScope) every 10 nm, with a 3 nm bandwidth for the silicon photodetector and a 1 nm bandwidth for the InGaAs one. Fig. 4.27 depicts the two spectrally-resolved RIN measurements as red dots (silicon) and as green dots (InGaAs), while the blue curve shows the related SC spectrum while pumping the fiber at 45° off the axes. Unfortunately, we were not able to measure the RIN of the SC spectrum while pumping on the fast/slow axis due to some problems with this seed laser (demo system). Nevertheless, We find an average RIN from 700 nm to 1100 nm

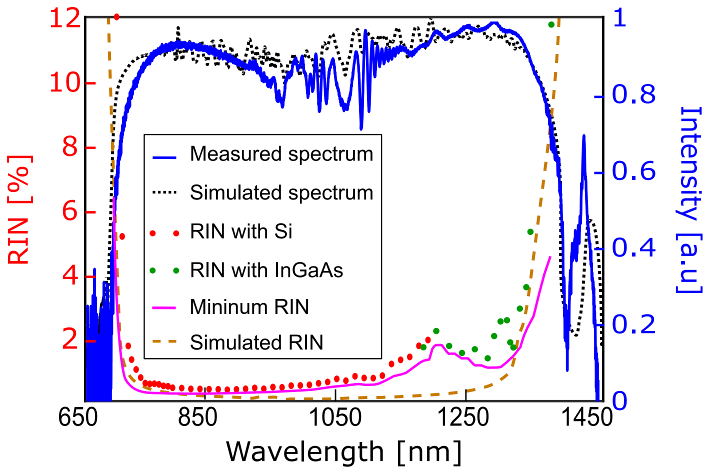

Figure 4.27: Measured spectrally resolved RIN using monochromator and oscilloscope method with silicon (blue curve) and InGaAs (pink curve) photodiode and corresponding average normalized SC spectrum (solid red), pumping at 45° to both axes.

down to 0.54 %, when we omit the high edge RIN values. The results also show that the RIN increases drastically on the SC edges due to both the reduction of the SC power and the strong effect of laser peak power fluctuations on the supercontinuum bandwidth [88]. Furthermore, the pink curve in Fig. 4.27 depicts the estimated minimum RIN values measured by our system as a function of wavelength. Indeed, our scope has an estimated dark noise standard deviation of 1 mV. Thus, if we divide this number by the mean of our Gaussian distribution, for each spectrally resolved bin, we obtain a minimum estimated spectrally resolved RIN value of 0.14 %. Finally, we observe that our measured spectrally RIN values are all slighty above the estimated minimum.

These experimental measurements have been further compared to numerical simulations of the two-coupled generalized nonlinear Schrödinger equations (CGNLSEs), as those described in Ref. [48] for highly-birefringent PM fibers. We performed SC and RIN simulations solving the CGNLSEs using the split-step method and the initial conditions as described in [88] with an input pulse duration of 180 fs (full width half maximum), an input peak power of 48 kW, an input amplitude noise value of 0.22 % (amplitude noise $\approx$ RIN/2) and associated anti-correlated pulse duration fluctuations to keep the energy of the mode-locked laser constant. To plot the simulated RIN, we use an ensemble size of 50 independent pulses, which is sufficient to minimise modelling error.

Table 1 compares the noise performances of our SC source to those of the literature [**?**, 10, 11]. The second column indicates the SC bandwidth at -3 dB. The third one explained the method used to measure the RIN of the SC system, either based on an oscilloscope in the time domain or on an Electric spectrum analyser (ESA) in the frequency domain. The fourth and fifth ones stipulate the measurement and filter bandwidth to obtain the average RIN specified in the last column. Few methods have indeed been implemented to measure the coherence or the RIN of ANDi SC generation [**?**, 10, 11]. For the coherence, in [**?**], the authors used a dispersive Fourier transform technique to highlight the stability of ANDi SC generation. Then, using a fiber-based unequal-path Michelson interferometer, they demonstrate a high fringe visibility meaning a high degree of coherence for the ANDi SC generation. Also, in Refs. [10] and [11], the authors used a setup composed of bandpass filters (10/12 nm), a fast photodiode and an oscilloscope to measure the spectrally-resolved RIN of the SC spectrum. In [10], the authors reported an average RIN of 33 %. This value can be considered high but, in this study, the coherence of ANDi SC generation was degraded by the PMI effect. In [11], the authors reported a very low average RIN of 1.2 %, due to the low input peak power used to obtain their ANDI SC and the large bandwidth of their filters.

System	$\lambda_{0,in}$	$\Delta\lambda_{SC}$	Method	$\Delta\lambda_{RIN}$	ΔRIN_{filter}	RIN
Ref. [10]	1054 nm	620 nm, -10 dB	Osci.	600 nm	10 nm	33 %
Ref. [11]	1550 nm	480 nm, -30 dB	Osci.	200 nm	12 nm	1.2 %
Ref. [**?**]	1550 nm	300 nm, -3dB	ESA	300 nm		0.07 %
Ti:Sa sys.	1040 nm	453 nm, -3 dB	DFT	325 nm	7 nm	6.5 %
XP sys.	1029 nm	710 nm, -3 dB	Osci.	500 nm	10 nm	15 %
XPc sys.	1029 nm	730 nm, -3 dB	Osci.	500 nm	10 nm	4.5 %
HP sys.	1049 nm	720 nm, -3 dB	Osci.	400 nm	3 nm	0.54 %

Table 4.1: Average RIN values in ANDi SC generation from the current literature and our system.

From Table 1, we see that we obtain the lowest average RIN value using the oscilloscope measurement method. About the value reported by [**?**], it is not possible to compare directly our RIN value to the 0.07 % announced because they don't use any passband filters and limit their ESA measurement bandwidth from 10 Hz to 20 MHz while the repetition rate of their laser is up to 80 MHz. Thus, it reduces the overall RIN value. Finally, we underline the setup composed by the Origami 10 HP laser and the PM-ANDi silica PCF is the system with the lowest average RIN to our knowledge and the highest PER (measured PER of 10 dB in [**?**]), and thus it can be also considered as one of the state-of-the-art systems.

In conclusion, we developed several coherent SC sources using different seed lasers (different input pulse duration and peak powers). We observed the input pulse duration has a crucial impact on the SC coherence and RIN due to the SRS. Furthermore, using a compact ytterbium mode-locked laser producing 180 fs pulses and a highly-nonlinear polarization-maintaining ANDi PCF, we were able to generate an ultra-flat octave-spanning SC spectrum with a bandwidth up to 720 nm (from 670 nm to 1390 nm) and associated PSD higher than 0.4 mW/nm. We have shown that the SC is linearly polarized with a PER of 17 dB across the whole spectrum bandwidth and with a spectrally-resolved RIN below 0.54 % from 700 nm to 1100 nm, which is, to the best of our knowledge, the lowest average SC ANDi RIN value ever reported with this measurement method. This system could find many applications in OCT, metrology, or as a wavelength-tunable fs laser source based on its octave-spanning bandwidth, flatness, low-noise, high coherence, polarization and near-linear chirp properties.

5

GENERAL CONCLUSION

The goal of this thesis was to develop a state-of-the-art low-noise supercontinuum system using femtosecond laser and all-normal dispersion silica photonic crystal fiber for several applications including spectroscopy, OCT, and metrology. Indeed, the coherent nonlinear effects responsible for the spectral broadening in the context of all-normal dispersion pumping allow, in theory, to generate a highly coherent and stable supercontinuum. In this work, the numerical and experimental limits of all-normal dispersion supercontinuum generation have been studied in depth using different Matlab codes solving the generalized nonlinear Shrodinger equations and several femtosecond lasers.

In theory, all-normal supercontinuum generation is stable for pump pulse duration shorter than 500 fs when considering only the quantum fluctuations of the system. based on several simulations considering the real-world technical noise sources of the system (timing jitter, amplitude noise and pulse duration fluctuations), we demonstrated that it is possible to get a highly coherent supercontinuum spectrum for pulse duration shorter than 120 fs (with an input amplitude noise of 0.3 %). Furthermore, we found the relative intensity noise of the supercontinuum remains low in the middle part of the spectrum and increases drastically on the edges. Finally, we have shown a correlation between the features of the intensity spectrum and its corresponding spectrally resolved relative intensity noise. From this numerical study, we decided to restrain our choice of seed lasers and use only the one with an output pulse duration lower than 400 fs.

In the FEMTO-ST institute, I was able to use their titanium-sapphire femtosecond laser. This laser delivers 200 fs pulses at an 80 MHz repetition rate and is tunable from 680 nm to 1080 nm. Pumping at the minimum dispersion of our polarization-maintaining all-normal dispersion fiber allows us to obtain a broad and flat linearly-polarized supercontinuum with a bandwidth up to 460 nm and a polarization extinction ratio of more than 17 dB. After an investigation of the impact of the input polarization on the supercontinuum generation, we discovered the emergence of a sideband at 1360 nm, polarized along the slow axis, corresponding to a cross-phase modulation instability process. We further discovered this XPMI sideband can be suppressed while pumping along the fast axis of the fiber. We found out it is very tricky to obtain the cross-phase modulation instability sideband via the supercontinuum generation, only a very limited parameter space is possible to observe it. Through the phase-matching equation of the cross-phase modulation instability process, we notice this nonlinear effect involves a degenerate pump at 1152 nm polarized along both axes and an idler located at 910 nm. Furthermore, we demonstrated this cross-phase modulation instability sideband evolves like a dispersive wave and walk-off from the main pulse. Then, we determined numerically and experimentally the cross-phase modulation instability sideband is low-noise/highly coherent, which highlights the stimulated generation of this process. Also, using the dispersive Fourier transform method, we demonstrated the input polarization has no real impact on the noise level of our femtosecond all-normal dispersion supercontinuum generation.

After these promising results, we pursued our goal to develop an ultra low-noise supercontinuum system. For this, we investigated the bandwidth and noise level of our all-normal dispersion supercontinuum generation using several seed lasers, all centered around 1040 nm. The first one was a low-cost low peak power laser, which delivers 103 fs pulses at an 80 MHz repetition rate. With this system, we obtained a linearly polarized supercontinuum spectrum with a polarization extinction ration up to 17 dB and a spectral bandwidth going up to 112 nm, for an input peak power of 30 kW. Although, the spectral bandwidth of this supercontinuum was quite small, it can still be useful for applications in optical coherent tomography. The second system was composed of a seed laser producing 400 fs pulses at an 1 MHz repetition rate. With this laser, we obtained an octave-spanning spectrum with a spectral bandwidth going up to 730 nm for an input peak power of 183 kW). Then, we observed experimentally the impact of the pulse length (i.e. of stimulated Raman scattering) on the supercontinuum and relative intensity noise spectrum. Indeed, the supercontinuum lost its flatness and the average relative intensity noise goes up to 12 % (recent measurements obtained via a spectrally resolved spectrum using a 3 nm spectral filter bandwidth indicates the relative intensity noise is close to 25 %). Using a nonlinear compression stage, we reduced the pulse duration of our seed laser down to 90 fs. With this shorter pulse duration, we obtained an average relative intensity noise of 4.5 %, highlighting the impact of pulse length on the supercontinuum noise level, for the same spectral bandwidth and input peak power. Our last seed laser produces 190 fs pulses at a repetition rate of 80 MHz. With this seed laser, we obtained an octave-spanning, smooth and extremely flat spectrum going from 685 nm to 1395 nm, and linearly polarized with a polarization extinction ratio of 17 dB. Furthermore, we obtained an ultra low-noise supercontinuum with an average relative intensity noise of 1.47 % for a spectral filter bandwidth of 1 nm, which is to the best of our knowledge the most stable all-normal dispersion supercontinuum spectrum ever demonstrated.

Unfortunately, by lack of time, we did not get the opportunity to test our SC systems for several applications as OCT and metrology. Nevertheless, it is forecast to investigate the performance of our third system for eye and skin imaging with the Research Center for Non-Destructive Testing in Austria through the collaboration given by the SUPUVIR European project. Furthermore, the Centre Suisse d'Electronique et de Microtechnique (CSEM) is very interested to use it to produce ultra-stable frequency combs. Indeed, a smooth, ultra-flat, low-noise and polarized supercontinuum could be extremely useful for both applications.

6

BIBLIOGRAPHY

BIBLIOGRAPHY

[1] DUDLEY, J. M., GENTY, G., AND COEN, S. **Supercontinuum generation in photonic crystal fiber**. *Reviews of Modern Physics 78*, 4 (2006), 1135–1184.

[2] ALFANO, R., AND SHAPIRO, S. **Emission in the region 4000 to 7000 Å via four-photon coupling in glass**. *Physical Review Letters 24*, 11 (1970), 584–588.

[3] ALFANO, R. R., AND SHAPIRO, S. **Observation of self-phase modulation and small-scale filaments in crystals and glasses**. *Physical Review Letters 24*, 11 (1970), 592–596.

[4] BIRKS, T., ROBERTS, P., RUSSELL, P. S. J., ATKIN, D., AND SHEPHERD, T. **Full 2-D photonic bandgaps in silica/air structures**. *Electronics Letters 31*, 22 (1995), 1941–1943.

[5] UDEM, T., HOLZWARTH, R., AND HÄNSCH, T. W. **Optical frequency metrology**. *Nature 416*, 6877 (2002), 233–237.

[6] HEIDT, A. M., HARTUNG, A., BOSMAN, G. W., KROK, P., ROHWER, E. G., SCHWOERER, H., AND BARTELT, H. **Coherent octave spanning near-infrared and visible supercontinuum generation in all-normal dispersion photonic crystal fibers**. *Optics Express 19*, 4 (2011), 3775–3787.

[7] ANDERSON, D., DESAIX, M., LISAK, M., AND QUIROGA-TEIXEIRO, M. L. **Wave breaking in nonlinear-optical fibers**. *Journal of the Optical Society of America B 9*, 8 (1992), 1358–1361.

[8] FINOT, C., KIBLER, B., PROVOST, L., AND WABNITZ, S. **Beneficial impact of wave-breaking for coherent continuum formation in normally dispersive nonlinear fibers**. *Journal of the Optical Society of America B 25*, 11 (2008), 1938–1948.

[9] HEIDT, A. M., FEEHAN, J. S., PRICE, J. H., AND FEURER, T. **Limits of coherent supercontinuum generation in normal dispersion fibers**. *Journal of the Optical Society of America B 34*, 4 (2017), 764–775.

[10] GONZALO, I. B., ENGELSHOLM, R. D., SØRENSEN, M. P., AND BANG, O. **Polarization noise places severe constraints on coherence of all-normal dispersion femtosecond supercontinuum generation**. *Scientific reports 8*, 1 (2018), 1–13.

[11] DS, S. R., ENGELSHOLM, R. D., GONZALO, I. B., ZHOU, B., BOWEN, P., MOSELUND, P. M., BANG, O., AND BACHE, M. **Ultra-low-noise supercontinuum generation with a flat near-zero normal dispersion fiber**. *Optics Letters 44*, 9 (2019), 2216–2219.

[12] PETERSEN, C. **2-10 μm Mid-infrared Supercontinuum Light Sources**. PhD thesis, 2016.

[13] AGRAWAL, G. P. **Nonlinear fiber optics**. In *Nonlinear Science at the Dawn of the 21st Century*. Springer, 2000, pp. 195–211.

[14] SALEH, B. E., AND TEICH, M. C. **Fundamentals of photonics**. John Wiley & sons, 2019.

[15] NEWPORT. https://www.newport.com/medias/sys_master/images/images/hd5/ha2/8797095919646/Fiber-Basics.pdf.

[16] KNIGHT, J., BIRKS, T., RUSSELL, P. S. J., AND ATKIN, D. **All-silica single-mode optical fiber with photonic crystal cladding**. *Optics Letters 21*, 19 (1996), 1547–1549.

[17] RUSSELL, P. **Photonic crystal fibers**. *Science 299*, 5605 (2003), 358–362.

[18] NKT. www.nktphotonics.com/lasers-fibers/technology/photonic-crystal-fibers/.

[19] BIRKS, T. A., KNIGHT, J. C., AND RUSSELL, P. S. J. **Endlessly single-mode photonic crystal fiber**. *Optics Letters 22*, 13 (1997), 961–963.

[20] MORTENSEN, N. A., FOLKENBERG, J. R., NIELSEN, M. D., AND HANSEN, K. P. **Modal cutoff and the V parameter in photonic crystal fibers**. *Optics Letters 28*, 20 (2003), 1879–1881.

[21] SAITOH, K., AND KOSHIBA, M. **Numerical modeling of photonic crystal fibers**. *Journal of Lightwave Technology 23*, 11 (2005), 3580–3590.

[22] FOLKENBERG, J. R., MORTENSEN, N. A., HANSEN, K. P., HANSEN, T. P., SIMONSEN, H. R., AND JAKOBSEN, C. **Experimental investigation of cutoff phenomena in nonlinear photonic crystal fibers**. *Optics Letters 28*, 20 (2003), 1882–1884.

[23] WADSWORTH, W., PERCIVAL, R., BOUWMANS, G., KNIGHT, J., AND RUSSELL, P. S. J. **High power air-clad photonic crystal fibre laser**. *Optics Express 11*, 1 (2003), 48–53.

[24] GOWAR, J. **Optical communication systems**. Prentice-Hall, 1984.

[25] Finazzi, V., Monro, T. M., and Richardson, D. J. **The role of confinement loss in highly nonlinear silica holey fibers**. *IEEE Photonics Technology Letters 15*, 9 (2003), 1246–1248.

[26] Zhou, J., Tajima, K., Nakajima, K., Kurokawa, K., Fukai, C., Matsui, T., and Sankawa, I. **Progress on low loss photonic crystal fibers**. *Optical Fiber Technology 11*, 2 (2005), 101–110.

[27] Moselund, P. M., Frosz, M. H., Thomsen, C. L., and Bang, O. **Picosecond supercontinuum generation with back seeding of different spectral parts**. In *OECC/ACOFT 2008-Joint Conference of the Opto-Electronics and Communications Conference and the Australian Conference on Optical Fibre Technology* (2008), IEEE, pp. 1–2.

[28] Mogilevtsev, D., Birks, T. A., and Russell, P. S. J. **Group-velocity dispersion in photonic crystal fibers**. *Optics Letters 23*, 21 (1998), 1662–1664.

[29] Marcuse, D. **Light transmission optics**. *Van Nostrand Reinhold New York* (1972).

[30] Malitson, I. H. **Interspecimen comparison of the refractive index of fused silica**. *Journal of the Optical Society of America 55*, 10 (1965), 1205–1209.

[31] FiberLabs. https://www.fiberlabs.com/glossary/polarization-maintaining-fiber/.

[32] Boyd, R. W. **Nonlinear optics**. *Academic press* (2019).

[33] Butcher, P. N., and Cotter, D. **The elements of nonlinear optics**. *Cambridge University Press* (1990).

[34] Shen, Y.-R. **The principles of nonlinear optics**. *Wi* (1984).

[35] Bloembergen, N. **Nonlinear optics, 3rd printing**. *Benjamin, New York* (1977).

[36] Diament, P. **Wave transmission and fiber optics**. *Macmillan* (1990).

[37] Stolen, R., and Lin, C. **Self-phase-modulation in silica optical fibers**. *Physical Review A 17*, 4 (1978), 1448–1454.

[38] Stolen, R. **Phase-matched-stimulated four-photon mixing in silica-fiber waveguides**. *IEEE Journal of Quantum Electronics 11*, 3 (1975), 100–103.

[39] Carman, R., Chiao, R., and Kelley, P. **Observation of degenerate stimulated four-photon interaction and four-wave parametric amplification**. *Physical Review Letters 17*, 26 (1966), 1281–1284.

[40] Emplit, P., Hamaide, J.-P., Reynaud, F., Froehly, C., and Barthelemy, A. **Picosecond steps and dark pulses through nonlinear single mode fibers**. *Optics Communications 62*, 6 (1987), 374–379.

[41] Akhmediev, N., and Karlsson, M. **Cherenkov radiation emitted by solitons in optical fibers**. *Physical Review A 51*, 3 (1995), 2602–2607.

[42] Gorbach, A. V., and Skryabin, D. V. **Light trapping in gravity-like potentials and expansion of supercontinuum spectra in photonic-crystal fibres**. *Nature Photonics 1*, 11 (2007), 653–657.

[43] Travers, J., and Taylor, J. **Soliton trapping of dispersive waves in tapered optical fibers**. *Optics Letters 34*, 2 (2009), 115–117.

[44] Stolen, R. H., Gordon, J. P., Tomlinson, W., and Haus, H. A. **Raman response function of silica-core fibers**. *Journal of the Optical Society of America B 6* (1989), 1159–1166.

[45] Lin, Q., and Agrawal, G. P. **Raman response function for silica fibers**. *Optics Letters 31*, 21 (2006), 3086–3088.

[46] Gordon, J. P. **Theory of the soliton self-frequency shift**. *Optics Letters 11*, 10 (1986), 662–664.

[47] Herrmann, J., and Nazarkin, A. **Soliton self-frequency shift for pulses with a duration less than the period of molecular oscillations**. *Optics Letters 19*, 24 (1994), 2065–2067.

[48] Venck, S., St-Hilaire, F., Brilland, L., Ghosh, A. N., Chahal, R., Caillaud, C., Meneghetti, M., Troles, J., Joulain, F., Cozic, S., Poulain, S., Huss, G., Rochette, M., Dudley, J. M., and Sylvestre, T. **2–10 µm mid-infrared fiber-based supercontinuum laser source: Experiment and simulation**. *Laser & Photonics Reviews*, 20000011 (2020).

[49] Hartung, A., Heidt, A. M., and Bartelt, H. **Design of all-normal dispersion microstructured optical fibers for pulse-preserving supercontinuum generation**. *Optics Express 19*, 8 (2011), 7742–7749.

[50] Heidt, A. M. **Pulse preserving flat-top supercontinuum generation in all-normal dispersion photonic crystal fibers**. *Journal of the Optical Society of America B 27*, 3 (2010), 550–559.

[51] Heidt, A. M., Rothhardt, J., Hartung, A., Bartelt, H., Rohwer, E. G., Limpert, J., and Tünnermann, A. **High quality sub-two cycle pulses from compression of supercontinuum generated in all-normal dispersion photonic crystal fiber**. *Optics Express 19*, 15 (2011), 13873–13879.

[52] Li, F., Li, Q., Yuan, J., and Wai, P. **Highly coherent supercontinuum generation with picosecond pulses by using self-similar compression**. *Optics Express 22*, 22 (2014), 27339–27354.

[53] Frosz, M. H., Bang, O., and Bjarklev, A. **Soliton collision and Raman gain regimes in continuous-wave pumped supercontinuum generation**. *Optics Express 14*, 20 (2006), 9391–9407.

[54] Mussot, A., Lantz, E., Maillotte, H., Sylvestre, T., Finot, C., and Pitois, S. **Spectral broadening of a partially coherent CW laser beam in single-mode optical fibers**. *Optics Express 12*, 13 (2004), 2838–2843.

[55] Sørensen, S. T., Larsen, C., Møller, U., Moselund, P. M., Thomsen, C. L., and Bang, O. **The role of phase coherence in seeded supercontinuum generation**. *Optics Express 20*, 20 (2012), 22886–22894.

[56] Zhu, Z., and Brown, T. G. **Polarization properties of supercontinuum spectra generated in birefringent photonic crystal fibers**. *Journal of the Optical Society of America B 21*, 2 (2004), 249–257.

[57] Dudley, J. M., and Coen, S. **Coherence properties of supercontinuum spectra generated in photonic crystal and tapered optical fibers**. *Optics Letters 27*, 13 (2002), 1180–1182.

[58] Frosz, M. H. **Validation of input-noise model for simulations of supercontinuum generation and rogue waves**. *Optics Express 18*, 14 (2010), 14778–14787.

[59] Corwin, K. L., Newbury, N. R., Dudley, J. M., Coen, S., Diddams, S. A., Washburn, B. R., Weber, K., and Windeler, R. S. **Fundamental amplitude noise limitations to supercontinuum spectra generated in a microstructured fiber**. *Applied Physics B 77*, 2-3 (2003), 269–277.

[60] Drummond, P., and Corney, J. F. **Quantum noise in optical fibers. i. stochastic equations**. *Journal of the Optical Society of America B 18*, 2 (2001), 139–152.

[61] Corney, J. F., and Drummond, P. **Quantum noise in optical fibers. ii. Raman jitter in soliton communications**. *Journal of the Optical Society of America B 18*, 2 (2001), 153–161.

[62] Smith, R. G. **Optical power handling capacity of low loss optical fibers as determined by stimulated Raman and Brillouin scattering**. *Applied optics 11*, 11 (1972), 2489–2494.

[63] Genty, G., Surakka, M., Turunen, J., and Friberg, A. T. **Complete characterization of supercontinuum coherence**. *Journal of the Optical Society of America B 28*, 9 (2011), 2301–2309.

[64] Wetzel, B., Stefani, A., Larger, L., Lacourt, P.-A., Merolla, J.-M., Sylvestre, T., Kudlinski, A., Mussot, A., Genty, G., Dias, F., and Dudley, J. **Real-time full bandwidth measurement of spectral noise in supercontinuum generation**. *Scientific reports 2* (2012), 882–889.

[65] Wong, T. C., Rhodes, M., and Trebino, R. **Single-shot measurement of the complete temporal intensity and phase of supercontinuum**. *Optica 1*, 2 (2014), 119–124.

[66] Heidt, A. M., Spangenberg, D.-M., Brügmann, M., Rohwer, E. G., and Feurer, T. **Improved retrieval of complex supercontinuum pulses from XFROG traces using a ptychographic algorithm**. *Optics Letters 41*, 21 (2016), 4903–4906.

[67] Okamura, A., Sakakibara, Y., Omoda, E., Kataura, H., and Nishizawa, N. **Experimental analysis of coherent supercontinuum generation and ultrashort pulse generation using cross-correlation frequency resolved optical gating (x-frog)**. *Journal of the Optical Society of America B 32*, 3 (2015), 400–406.

[68] Pellat-Finet, P. **Optique de Fourier: Théorie métaxiale et fractionnaire**. Springer Science & Business Media, 2009.

[69] Grigoryan, G., Lima Jr, I., Yu, T., Grigoryan, V., and Menyuk, C. **Using color to understand light transmission**. *Optics and Photonics News 11*, 8 (2000), 44–50.

[70] Goda, K., and Jalali, B. **Dispersive fourier transformation for fast continuous single-shot measurements**. *Nature Photonics 7*, 2 (2013), 102–112.

[71] Kyei, K., Jensen, M., Engelsholm, R. D., Dasa, M. K., Deepak, J., Bowen, P., Moselund, P. M., Petersen, C. R., and Ole, B. **In-amplifier and cascaded mid-infrared supercontinuum sources with low noise through gain-induced soliton spectral alignment**. *Scientific Reports (Nature Publisher Group) 10*, 1 (2020), 1–11.

[72] Sørensen, S. T., Bang, O., Wetzel, B., and Dudley, J. M. **Higher-order moment characterisation of rogue wave statistics in supercontinuum generation**. In *Nonlinear Photonics* (2012), Optical Society of America, pp. JTu5A–22.

[73] Engelsholm, R. **Low Noise Supercontinuum Lasers for Optical Coherence Tomography Systems**. PhD thesis, 2018.

[74] Gonzalo, I. B., and Bang, O. **Role of the Raman gain in the noise dynamics of all-normal dispersion silica fiber supercontinuum generation**. *Journal of the Optical Society of America B 35*, 9 (2018), 2102–2110.

[75] Coen, S., Wardle, D. A., and Harvey, J. D. **Observation of non-phase-matched parametric amplification in resonant nonlinear optics**. *Physical Review Letters 89*, 27 (2002), 273901–273905.

[76] Bloembergen, N., and Shen, Y. **Coupling between vibrations and light waves in Raman laser media**. *Physical Review Letters 12*, 18 (1964), 504–507.

[77] Alfano, R. R. **The supercontinuum laser source: the ultimate white light**. Springer, 2016.

[78] Hellwarth, R. **Third-order optical susceptibilities of liquids and solids**. *Progress in Quantum Electronics 5* (1977), 1–68.

[79] Stolen, R., and Ippen, E. **Raman gain in glass optical waveguides**. *Applied Physics Letters 22*, 6 (1973), 276–278.

[80] Blow, K. J., and Wood, D. **Theoretical description of transient stimulated Raman scattering in optical fibers**. *IEEE Journal of Quantum Electronics 25*, 12 (1989), 2665–2673.

[81] Golovchenko, E., and Pilipetskii, A. **Unified analysis of four-photon mixing, modulational instability, and stimulated Raman scattering under various polarization conditions in fibers**. *Journal of the Optical Society of America B 11*, 1 (1994), 92–101.

[82] Vanholsbeeck, F., Emplit, P., and Coen, S. **Complete experimental characterization of the influence of parametric four-wave mixing on stimulated Raman gain**. *Optics Letters 28*, 20 (2003), 1960–1962.

[83] Domingue, S. R., and Bartels, R. A. **Overcoming temporal polarization instabilities from the latent birefringence in all-normal dispersion, wave-breaking-extended nonlinear fiber supercontinuum generation**. *Optics Express 21*, 11 (2013), 13305–13321.

[84] Liu, Y., Zhao, Y., Lyngsø, J., You, S., Wilson, W. L., Tu, H., and Boppart, S. A. **Suppressing short-term polarization noise and related spectral decoherence in all-normal dispersion fiber supercontinuum generation**. *Journal of Lightwave Technology 33*, 9 (2015), 1814–1820.

[85] Murdoch, S., Leonhardt, R., and Harvey, J. **Polarization modulation instability in weakly birefringent fibers**. *Optics Letters 20*, 8 (1995), 866–868.

[86] Tu, H., Liu, Y., Lægsgaard, J., Sharma, U., Siegel, M., Kopf, D., and Boppart, S. A. **Scalar generalized nonlinear schrödinger equation-quantified continuum generation in an all-normal dispersion photonic crystal fiber for**

broadband coherent optical sources. *Optics Express 18*, 26 (2010), 27872–27884.

[87] Tu, H., Liu, Y., Liu, X., Turchinovich, D., Lægsgaard, J., and Boppart, S. A. **Nonlinear polarization dynamics in a weakly birefringent all-normal dispersion photonic crystal fiber: toward a practical coherent fiber supercontinuum laser**. *Optics Express 20*, 2 (2012), 1113–1128.

[88] Genier, E., Bowen, P., Sylvestre, T., Dudley, J. M., Moselund, P., and Bang, O. **Amplitude noise and coherence degradation of femtosecond supercontinuum generation in all-normal-dispersion fibers**. *Journal of the Optical Society of America B 36*, 2 (2019), A161–A167.

[89] Genier, E., Ghosh, A. N., Bobba, S., Bowen, P., Moselund, P. M., Bang, O., Dudley, J. M., and Sylvestre, T. **Cross-phase modulation instability in PM andi fiber-based supercontinuum generation**. *Optics Letters 45*, 13 (2020), 3545–3548.

[90] Diddams, S., and Diels, J.-C. **Dispersion measurements with white-light interferometry**. *Journal of the Optical Society of America B 13*, 6 (1996), 1120–1129.

[91] NKTPhotonics. https://www.nktphotonics.com/lasers-fibers/product/onefive-origami-ultra-low-noise-femtosecond-laser/.

[92] Gurland, J., and Tripathi, R. C. **A simple approximation for unbiased estimation of the standard deviation**. *The American Statistician 25*, 4 (1971), 30–32.

[93] Buccoliero, D., Steffensen, H., Ebendorff-Heidepriem, H., Monro, T. M., and Bang, O. **Midinfrared optical rogue waves in soft glass photonic crystal fiber**. *Optics Express 19*, 19 (2011), 17973–17978.

[94] Sierro, B., and Heidt, A. M. **Noise amplification in all-normal dispersion fiber supercontinuum generation and its impact on ultrafast photonics applications**. *OSA Continuum 3*, 9 (Sep 2020), 2347–2361.

[95] Tarnowski, K., Martynkien, T., Mergo, P., Poturaj, K., Anuszkiewicz, A., Béjot, P., Billard, F., Faucher, O., Kibler, B., and Urbanczyk, W. **Polarized all-normal dispersion supercontinuum reaching 2.5 μm generated in a birefringent microstructured silica fiber**. *Optics Express 25*, 22 (2017), 27452–27463.

[96] Tarnowski, K., Martynkien, T., Mergo, P., Sotor, J., and Soboń, G. **Compact all-fiber source of coherent linearly polarized octave-spanning supercontinuum based on normal dispersion silica fiber**. *Scientific Reports 9*, 1 (2019), 1–8.

[97] Rothenberg, J. E. **Observation of the buildup of modulational instability from wave breaking**. *Optics Letters 16*, 1 (1991), 18–20.

[98] Kudlinski, A., Bendahmane, A., Labat, D., Virally, S., Murray, R., Kelleher, E., and Mussot, A. **Simultaneous scalar and cross-phase modulation instabilities in highly birefringent photonic crystal fiber**. *Optics Express 21*, 7 (2013), 8437–8443.

[99] Drummond, P., Kennedy, T., Dudley, J., Leonhardt, R., and Harvey, J. **Cross-phase modulational instability in high-birefringence fibers**. *Optics Communications 78*, 2 (1990), 137–142.

[100] Hlubina, P., Ciprian, D., and Kadulová, M. **Wide spectral range measurement of modal birefringence in polarization-maintaining fibres**. *Measurement Science and Technology 20*, 2 (2008), 025301–025305.

[101] Thibaut, S., and Etienne, G. **Combined spectral effects of pulse walk-off and degenerate cross-phase modulation in birefringent fibers**. *Journal of Nonlinear Optical Physics and Materials 6*, 03 (1997), 313–320.

[102] Chen, J., Wong, G., Murdoch, S., Kruhlak, R., Leonhardt, R., Harvey, J., Joly, N., and Knight, J. **Cross-phase modulation instability in photonic crystal fibers**. *Optics Letters 31*, 7 (2006), 873–875.

[103] Sylvestre, T., Maillotte, H., Lantz, E., and Gindre, D. **Combined spectral effects of pulse walk-off and degenerate cross-phase modulation in birefringent fibers**. *Journal of Nonlinear Optical Physics & Materials 6*, 03 (1997), 313–320.

[104] Seve, E., Dinda, P. T., Millot, G., Remoissenet, M., Bilbault, J., and Haelterman, M. **Modulational instability and critical regime in a highly birefringent fiber**. *Physical review A 54*, 4 (1996), 3519–3534.

[105] Conforti, M., and Trillo, S. **Dispersive wave emission from wave breaking**. *Optics Letters 38*, 19 (2013), 3815–3818.

[106] Webb, K., Xu, Y., Erkintalo, M., and Murdoch, S. **Generalized dispersive wave emission in nonlinear fiber optics**. *Optics Letters 38*, 2 (2013), 151–153.

[107] Sørensen, S. T., Bang, O., Wetzel, B., and Dudley, J. M. **Describing supercontinuum noise and rogue wave statistics using higher-order moments**. *Optics Communications 285*, 9 (2012), 2451–2455.

[108] Maria, M., Gonzalo, I. B., Feuchter, T., Denninger, M., Moselund, P. M., Leick, L., Bang, O., and Podoleanu, A. **Q-switch-pumped supercontinuum**

for ultra-high resolution optical coherence tomography. *Optics Letters 42*, 22 (2017), 4744–4747.

[109] Dasa, M. K., Markos, C., Maria, M., Petersen, C. R., Moselund, P. M., and Bang, O. **High-pulse energy supercontinuum laser for high-resolution spectroscopic photoacoustic imaging of lipids in the 1650-1850 nm region**. *Biomedical Optics Express 9*, 4 (2018), 1762–1770.

[110] Petersen, C. R., Prtljaga, N., Farries, M., Ward, J., Napier, B., Lloyd, G. R., Nallala, J., Stone, N., and Bang, O. **Mid-infrared multispectral tissue imaging using a chalcogenide fiber supercontinuum source**. *Optics Letters 43*, 5 (2018), 999–1002.

[111] Israelsen, N. M., Maria, M., Mogensen, M., Bojesen, S., Jensen, M., Haedersdal, M., Podoleanu, A., and Bang, O. **The value of ultrahigh resolution oct in dermatology-delineating the dermo-epidermal junction, capillaries in the dermal papillae and vellus hairs**. *Biomedical Optics Express 9*, 5 (2018), 2240–2265.

[112] Povazay, B., Bizheva, K., Unterhuber, A., Hermann, B., Sattmann, H., Fercher, A. F., Drexler, W., Apolonski, A., Wadsworth, W., Knight, J., and others. **Submicrometer axial resolution optical coherence tomography**. *Optics Letters 27*, 20 (2002), 1800–1802.

[113] Fermann, M., Kruglov, V., Thomsen, B., Dudley, J., and Harvey, J. **Self-similar propagation and amplification of parabolic pulses in optical fibers**. *Physical Review Letters 84*, 26 (2000), 6010–6013.

[114] Kruglov, V. I., and Harvey, J. D. **Asymptotically exact parabolic solutions of the generalized nonlinear schrödinger equation with varying parameters**. *Journal of the Optical Society of America B 23*, 12 (2006), 2541–2550.

[115] Skoog, D. A., Holler, F. J., and Crouch, S. R. **Principles of instrumental analysis**. Cengage learning, 2017.

APPENDIX

1. DERIVATION OF THE COHERENCE FORMULA

In this section, we derive the coherence formula to obtain a simpler form. It is straightforward to show that, in general, the imaginary part of $|g_{12}(\omega)|$ is negligible compared to its real part (except in the incoherent case but then both parts are essentially equal to zero). We can thus rewrite the spectral coherence function as []:

$$|g_{12}(\omega)| \simeq \Re\left[g_{12}\right] = \frac{\left\langle \tilde{A}_i^*(\omega)\tilde{A}_j(\omega)\right\rangle_{i\neq j}}{\left\langle\left|\tilde{A}(\omega)\right|^2\right\rangle} + \frac{\left\langle \tilde{A}_j^*(\omega)\tilde{A}_i(\omega)\right\rangle_{j\neq i}}{\left\langle\left|\tilde{A}(\omega)\right|^2\right\rangle}. \tag{1}$$

For a given set of N realizations and writing specifically the summation over all possible pairs in the numerator we have:

$$|g_{12}(\omega)| = \frac{1}{n_{pairs}}\frac{\sum_{i\neq j}^{N}\left[\tilde{A}_i^*(\omega)\tilde{A}_j(\omega) + \tilde{A}_i(\omega)A_j^*(\omega)\right]}{\left\langle\left|\tilde{A}(\omega)\right|^2\right\rangle} \tag{2}$$

Using the binomial formula one obtains:

$$|g_{12}(\omega)| = \frac{1}{n_{pairs}}\frac{\left|\sum_{i=1}^{N}\tilde{A}_i(\omega)\right|^2 - \sum_{i=1}^{N}\left|\tilde{A}_i(\omega)\right|^2}{\left\langle\left|\tilde{A}(\omega)\right|^2\right\rangle} \tag{3}$$

And it follows that:

$$|g_{12}(\omega)| = \frac{1}{n_{pairs}}\frac{\left|N\left\langle\tilde{A}(\omega)\right\rangle\right|^2 - N\left\langle\left|\tilde{A}(\omega)\right|^2\right\rangle}{\left\langle\left|\tilde{A}(\omega)\right|^2\right\rangle} \tag{4}$$

As the number of pairs corresponding to an ensemble of N realizations is $N^2 - N$, we finally obtain for the measured spectral coherence function:

$$|g_{12}(\omega)| = \frac{1}{N^2 - N}\frac{N^2\left|\left\langle\tilde{A}(\omega)\right\rangle\right|^2 - N\left\langle\left|\tilde{A}(\omega)\right|^2\right\rangle}{\left\langle\left|\tilde{A}(\omega)\right|^2\right\rangle} \tag{5}$$

.

For N sufficiently high enough, we finally obtain:

$$|g_{12}(\omega)| = \frac{\left|\left\langle\tilde{A}(\omega)\right\rangle\right|^2}{\left\langle\left|\tilde{A}(\omega)\right|^2\right\rangle} \tag{6}$$

2. CORRELATION BETWEEN AMPLITUDE NOISE AND PULSE DURATION NOISE

Through the time-bandwidth product equation, there is a direct correlation between wavelength and time. According to the laser datasheet, there is a correlation between average power and bandwidth thus between average power and pulse duration if we assume the pulse remains transform-limited. Now, if we consider this relations holds during the fluctuations, we have:

$$\delta t_0 = \frac{0.317}{\frac{c}{\lambda^2}\Delta\lambda_1} - \frac{0.317}{\frac{c}{\lambda^2}\Delta\lambda_2}, \tag{7}$$

where δt_0 represents the pulse duration fluctuations and $\Delta\lambda_{1,2}$ the bandwidth of the laser for a given power given by:

$$\Delta\lambda_1 = \Delta\lambda(P_1), \quad P_1 = P_0(1 + \delta_{AN}) \tag{8}$$

$$\Delta\lambda_2 = \Delta\lambda(P_2), \quad P_2 = P_0. \tag{9}$$

Using the value given by the datasheet and depicted in Fig. 2.14, we obtain:

$$\frac{\delta t_0}{t_0} = -0.8\% \tag{10}$$

3. COLLAPSE OF THE FIBER

This section of the appendix shows a picture of the PM-ANDi fiber before and after collapsing the holes of the PCF. We use a FFS-2000 Fusion Splicing Workstation with the following parameters: duration of 2.5 s and power of 19 W.

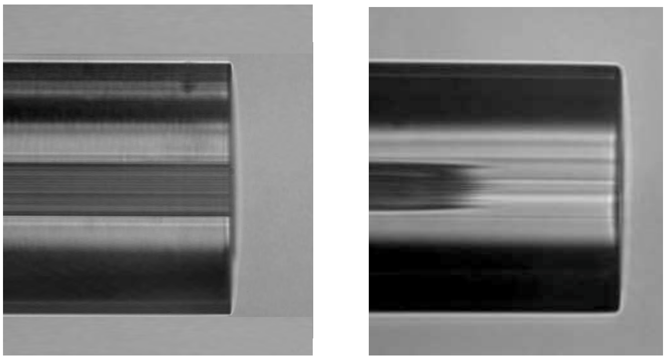

Figure 1: Image taken from the Vytran showing the PM-ANDi PCF left) before collapse and right) after collapse

4. ORIGAMI 10 LP LASER

Technical drawing of the Origami 10 LP femtosecond laser, more information can be found in [91]:

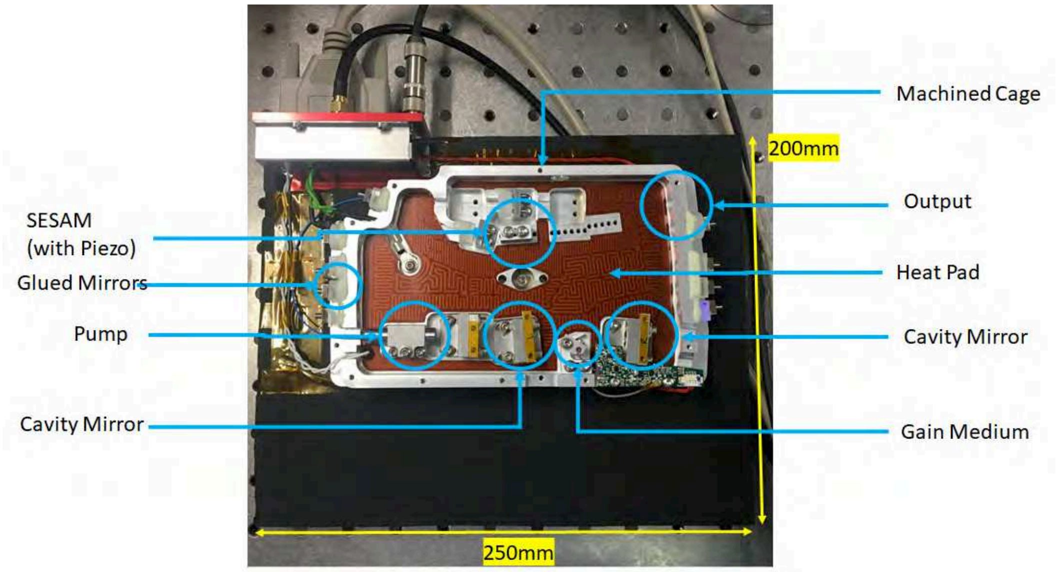

Figure 2: Technical drawing of the Origami 10 LP femtosecond laser

5. EVOLUTION OF THE SPECTRAL FILTER BANDWIDTH

The monochromator used in Sec. 3.4, 4.2 and 4.3. has two gratings, one for each detector (Silicon and InGaAs). As discussed in Sec. 3.4, the spectral filter bandwidth evolves as a function of wavelength and grating. The following picture shows this evolution:

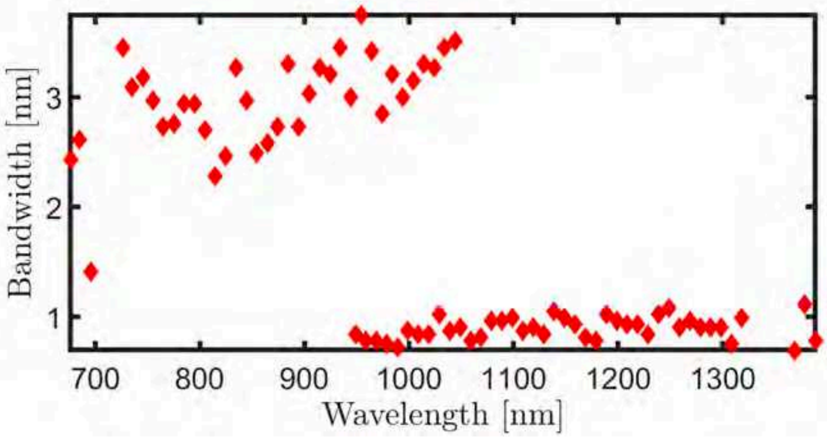

Figure 3: Evolution of the filter spectral bandwidth of the monochromator as a function of central wavelength.

Research Article Vol. 36, No. 2 / February 2019 / *Journal of the Optical Society of America B* **A161**

Journal of the Optical Society of America B

OPTICAL PHYSICS

Amplitude noise and coherence degradation of femtosecond supercontinuum generation in all-normal-dispersion fibers

Etienne Genier,[1,*] Patrick Bowen,[1] Thibaut Sylvestre,[2] John M. Dudley,[2] Peter Moselund,[1] and Ole Bang[1,3]

[1]*NKT Photonics A/S, Blokken 84, DK-3460 Birkerød, Denmark*
[2]*Institut FEMTO-ST, UMR 6174 CNRS-Université de Franche-Comté, 25030 Besançon, France*
[3]*DTU Fotonik, Department of Photonics Engineering, Technical University of Denmark, 2800 Kgs. Lyngby, Denmark*
**Corresponding author: etge@nktphotonics.com*

Received 3 October 2018; revised 20 December 2018; accepted 23 December 2018; posted 3 January 2019 (Doc. ID 347414); published 28 January 2019

Supercontinuum (SC) generation via femtosecond (fs) pumping in all-normal-dispersion (ANDi) fiber is predicted to offer completely coherent broadening mechanisms, potentially allowing for substantially reduced noise levels in comparison to those obtained when operating in the anomalous dispersion regime. However, previous studies of SC noise typically treat only the quantum noise, typically in the form of one-photon-per-mode noise, and do not consider other technical noise contributions, such as the stability of the pump laser, which become important when the broadening mechanism itself is coherent. In this work, we discuss the influence of the amplitude and pulse length noise of the pump laser, both added separately and combined. We show that for a typical mode-locked laser, in which the peak power and pulse duration are anticorrelated, their combined impact on the SC noise is generally smaller than in isolation. This means that the supercontinuum noise is smaller than the noise of the mode-locked pump laser itself, a fact that was recently observed in experiments but not explained. Our detailed numerical analysis shows that the coherence of ANDi SC generation is considerably reduced on the spectral edges when realistic pump laser noise levels are taken into account.

https://doi.org/10.1364/JOSAB.36.00A161

1. INTRODUCTION

Highly nonlinear photonic crystal fibers (PCFs) having all-normal dispersion (ANDi) have only recently emerged as attractive fibers to generate low-noise, octave-spanning supercontinua (SCs) [1–4]. This is due to the facts that these PCFs are difficult to fabricate (e.g., requiring submicrometer holes) and that broadband low-noise ANDi SC generation requires high peak power femtosecond (fs) lasers. It has been shown that low-noise ANDi SC generation cannot be achieved using long pulses because the Raman effect is just as noisy as modulation instability [5]. Despite these obstacles, fs-pumped ANDi SC generation has received significant attention because of its ability to generate temporally coherent SC pulses, a feature that is unachievable in the anomalous dispersion regime. This gives such systems potential in a range of fields including optical coherence tomography (OCT), optical metrology, photoacoustic imaging, and spectroscopy [6–11].

The reason for this high coherence comes from the coherent spectral broadening mechanisms of self-phase modulation (SPM) and optical wave-breaking [12,13]. In fs-pumped ANDi SC generation these mechanisms are considerably more efficient than the incoherent nonlinear effects of noise-seeded modulation instability and stimulated Raman scattering [1], allowing for octave-spanning SC generation in which these incoherent effects are suppressed for sufficiently short fiber lengths and input pulse durations [12,14].

Several theoretical studies about SC coherence have been reported in anomalous dispersion fiber, covering pulse durations from fs up to continuous wave, and including several kinds of noise, such as one-photon-per-mode (OPM) quantum noise added as pure phase noise in the frequency domain, Wigner-representation based quantum noise is added in the time domain as amplitude and phase noise, Raman noise, and polarization noise [15–26]. This is not the case for theoretical studies of ANDi SC generation, which have mostly considered only the OPM noise [1,12,20], except for a recent work of Gonzalo *et al.* [14], in which relative intensity noise (RIN) was experimentally and numerically compared for ANDi SC generation with 170 fs pump pulses. In this study, it was found that OPM noise was too weak to describe the experimentally observed noise, whereas adding 1% amplitude fluctuations of the laser gave better agreement with the experimental results. This important result underlines that while pump laser noise traditionally has contributed little to the noise levels in incoherently broadened anomalous dispersion fiber SC generation [20,27], it is extremely important in coherently broadened ANDi SC generation.

Unfortunately Gonzalo *et al.* just briefly mentioned the effect of pure amplitude noise of the pump laser for one specific pulse duration and fiber length, and no specific simulation including the amplitude noise was shown and no general study conducted [14]. In this work, we therefore present a comprehensive study of the influence of the noise of a mode-locked pump laser on the coherence and RIN of the SC spectrum generated in an ANDi fiber. We focus on single polarization SC generation because it allows us to more clearly demonstrate the impact of technical laser noise. In particular we consider fluctuations in both the amplitude and pulse length, which typically are anticorrelated in a mode-locked laser. We show both numerically and analytically that their combined impact on the SC noise is generally smaller than in isolation, which explains that the SC noise generally is smaller than the noise of the pump laser itself, as was observed recently [28].

These results show that the limits for high coherence, in terms of pulse duration and fiber length, suggested in previous publications change substantially when technical pump laser noise is included. Indeed, we find that while a high coherence can be maintained for a pulse duration below 1.2 ps in a system without technical pump laser noise and only with one polarization [12], a pulse duration of ~50 fs will begin to lose coherence even when a relatively low noise pump laser is properly described.

2. NUMERICAL MODEL AND NOISE SOURCES

In the numerical study we use a single-polarization scalar model in the form of the standard generalized nonlinear Schrödinger equation to model the propagation of the envelope function $A = A(z, T)$, with initial condition $A(0, t) = \sqrt{P_0}\,\mathrm{sech}(t/T_0)$, in a highly nonlinear single mode optical fiber. This includes dispersion (described by a Taylor expansion up to β_{10}), spectrally dependent linear loss $\alpha(\omega)$, and the nonlinear response of the material as well as the dispersion of the nonlinearity and the Raman response, $R(T)$ [20]:

$$\frac{\partial A}{\partial z} = -\frac{\alpha(\omega)}{2}A + \sum_{k\geq 2}\frac{i^{k+1}}{k!}\beta_k\frac{\partial^k A}{\partial T^k} + i\gamma\left(1 + i\tau_0\frac{\partial}{\partial T}\right)\left(A\int_{-\infty}^{+\infty}R(T')|A(z, T - T')|^2\mathrm{d}T'\right), \quad (1)$$

where γ is the nonlinear coefficient and $\tau_0 = 1/\omega_0$ represents the characteristic time scale of self-steepening [20]. The Raman response is modeled using the real experimentally measured Raman gain profile as described in [29].

In this study we consider two sources of noise. The first is the well-known quantum noise δ_{QN}, modeled semiclassically as the standard OPM noise, which is added to the initial condition in the Fourier domain as one photon of energy $\hbar\omega_m$ and random phase Φ_m in each spectral bin with angular frequency ω_m and bin size $\Delta\Omega$ [26]. The OPM noise in the frequency domain is given by $\delta_{\mathrm{QN}} = \sqrt{\hbar\omega_m/\Delta\Omega}\exp(i2\pi\Phi_m)$, where $\hbar$ is Planck's constant and Φ_m is a random number Gaussian distributed in the interval [0,1]. In our simulations we used 2^{15} points, and thus $m \in [1, 2^{15}]$.

The second noise source is the laser amplitude fluctuations described by $\delta_{\mathrm{AN}} = \Psi$, where Ψ is a single random value for each input pulse, extracted from a Gaussian distribution with a unit mean and a standard deviation equal to the rms amplitude noise of the modeled laser, given by the manufacturer of the laser. In this paper, we will consider a range of rms amplitude noises from 0.1% to 2% (0.2% representing a Onefive Origami 10 fs laser and 1% a Fianium fs laser, both from NKT Photonics).

To correctly consider the effects of laser amplitude fluctuations on the SC, it is important to take into account any correlated fluctuations of the pulse duration which occur in a mode-locked laser. This is important to model, as pulse duration fluctuations will subtly affect the efficiency of SPM, and thus the output spectral shape and width. To estimate the correlation of the fluctuations, we use the deterministic correlation between average power and spectral bandwidth experimentally measured in an Origami 10 fs mode-locked laser. Assuming a fixed repetition rate and a state of anomalous dispersion soliton mode-locking, producing approximately transform-limited sech-shaped pulses, we then find the linearized relation between peak power and pulse length. Assuming then that this relation holds during the fluctuations, we obtain the following relationship:

$$\delta_{T_0} = -0.8 * (\delta_{\mathrm{AN}} - 1), \quad (2)$$

where δ_{T_0} is a Gaussian distribution centered in 0 having a standard deviation equal to 0.8 times δ_{AN}. The peak power and pulse duration of a mode-locked laser are thus anticorrelated, which is extremely important for the SC noise, as we shall see in the following. We note that the value of 0.8 is specific to the laser considered but can be generalized for other kinds of lasers. With both noise terms included, our initial condition becomes

$$A(0,t) = \sqrt{P_0}\delta_{\mathrm{AN}}\,\mathrm{sech}(t/(T_0(1-0.8(\delta_{\mathrm{AN}}-1)))) + F^{-1}\{\delta_{\mathrm{QN}}\}, \quad (3)$$

where F^{-1} represents the inverse Fourier transform. Here and in the following the Fourier transform of a function is denoted by a tilde and defined as $\tilde{A}(z, \omega) = \int_{-\infty}^{\infty} A(z, t)\exp(i[\omega - \omega_0]t)\mathrm{d}t$, where ω_0 is the pump angular frequency.

3. RESULTS

As explained previously, we want to focus on just the effect of laser technical noise compared to the conventional OPM noise and therefore use a single-polarization scalar code. This is still highly accurate for polarization maintaining (PM) fibers, which is why we choose the specific PM ANDi PCF NL-1050-NE-PM from NKT Photonics. This PCF has a relative hole size of $d/L = 0.45$, a small hole-to-hole pitch of 1.44 μm, and a stress-induced birefringence of 4×10^{-4}. Its classical ANDi dispersion profile, shown in Fig. 1(a), was calculated with

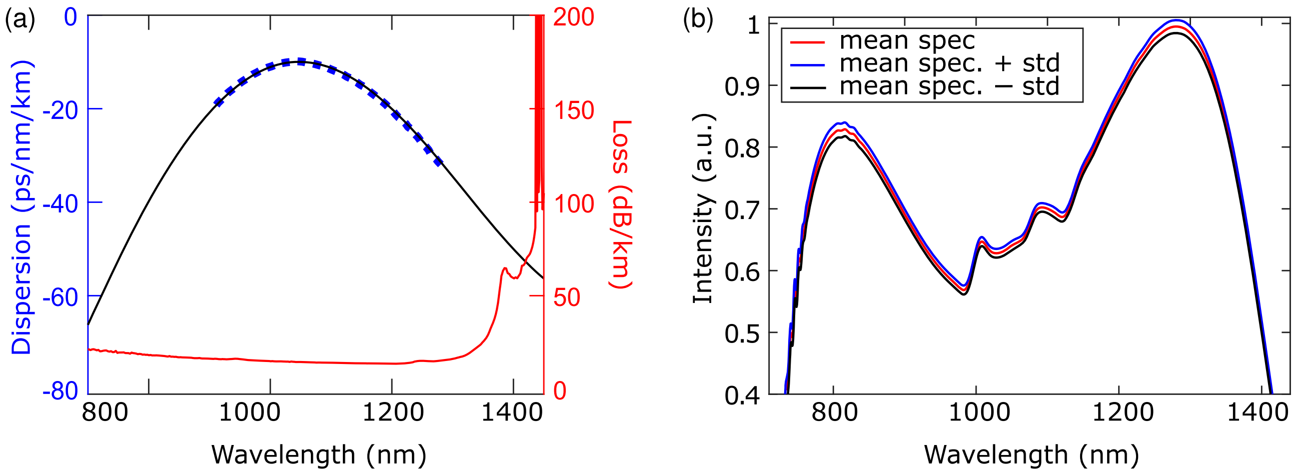

Fig. 1. (a) Measured (dashed blue) and modeled (solid black) dispersion profile, and fiber losses (solid red) of the NL-1050-NE-PM ANDi PCF. (b) Numerical SC spectra generated in 1 m of ANDi fiber with a 1054 nm pump with an average peak power and pulse duration of $P_0 = 100$ kW and $T_0 = 50$ fs, respectively. An amplitude noise of 0.5% was used, corresponding to a pulse duration noise of 0.4%.

COMSOL and confirmed experimentally in the region 900–1300 nm using white light interferometry. The measurements of dispersion were done without controlling polarization, which is typically sufficient for stress-induced birefringence that does not significantly alter the mode profile. As expected, the small holes of the PCF give a confinement loss edge significantly below the material loss edge, here found to be at 1450 nm using COMSOL [see Fig. 1(a)]. This will significantly influence the long wavelength part of the intensity and noise profiles, as we will see in the following. The dispersion has a maximum of −13 ps/nm/km at 1040 nm and is rather symmetrical within the low-loss window. However, we pump just above the maximum dispersion at 1054 nm, because we want to consider realistic noise values of a specific laser—the Origami 10.

In Fig. 1(b) we show the numerically found SC spectrum out of 1 m of ANDi fiber generated by a pump laser with an average peak power and pulse duration of $P_0 = 100$ kW and $T_0 = 50$ fs, respectively, and an amplitude and corresponding anticorrelated pulse duration noise of 0.5% and 0.4%, respectively. We used an ensemble of 20 simulated pulses to calculate the mean and standard deviation for each wavelength and show in Fig. 1(b) the mean and the mean +/− the standard deviation. The results show that with only a small pump laser amplitude noise of 0.5%, fluctuations in the SC spectrum are already noticeable. The calculations were repeated with 40 and 80 pulses in the ensemble, and no noticeable change was found, which means that the statistics can be trusted.

In ANDi SC generation, it has been shown that the pulse duration, fiber length, and peak power have a critical influence on the noise properties [12,14], for example, the anticipated coherent spectra are only obtained for sufficiently short pulse durations and fiber lengths. To see the effect of pump laser amplitude noise on the coherence and the requirements on the fiber length and pulse parameters, we simulate a wide parameter space and calculate for each case the spectrally averaged coherence given by [12,20]

$$|g_{12}(\omega)| = \left| \frac{\langle \tilde{A}_i^*(\omega)\tilde{A}_j(\omega)\rangle_{i\neq j}}{\sqrt{\langle |\tilde{A}_i(\omega)|^2\rangle \langle |\tilde{A}_j(\omega)|^2\rangle}} \right|,$$
$$\langle |g_{12}|\rangle = \frac{\int_0^\infty |g_{12}(\omega)| \langle |\tilde{A}_i(\omega)|^2\rangle \mathrm{d}\omega}{\int_0^\infty \langle |\tilde{A}_i(\omega)|^2\rangle \mathrm{d}\omega}, \tag{4}$$

where $\tilde{A}_i(\omega) = \tilde{A}_i(z, \omega)$, $\langle \tilde{A}_i(\omega)\rangle$ denotes an ensemble average and subscripts $(i, j) \in [1, 20]$ run over the ensemble. This gives a single number characterizing the coherence for each set of parameters. In Fig. 2(a) we plot the color coded spectrally averaged coherence $\langle |g_{12}|\rangle$ versus the pulse duration and fiber length for a fixed weak amplitude noise of 0.3% (giving an anticorrelated pulse duration noise of 0.24%). As is typical of ANDi-SC sources, the coherence decreases when either the pulse duration or fiber length is increased [12,14]. However, unlike earlier single-polarization studies without amplitude noise, we observe in Fig. 2(a) a considerably limited range of parameters where the noise is low, defined as when the spectrally averaged coherence $\langle |g_{12}|\rangle$ is higher than 0.9 [dashed line in Fig. 2(a)]. In particular, good coherence is seen to require pulse durations below 100 fs, which is an order of magnitude shorter than the corresponding limit found without even this weak laser amplitude noise of 0.3% [12,14].

In Fig. 2(b) we show the low noise limit $\langle |g_{12}|\rangle = 0.9$ for amplitude noise levels between 0.1% and 1% (pulse duration noise from 0.08% to 0.8%). From Fig. 2(b) we see that for amplitude noise levels higher than 1% an average coherence of 0.9 cannot be obtained for any reasonable fiber length. From this, we can see clearly the dramatically limiting effect that the addition of standard laser noise levels has on the coherence parameter space. Significantly, Fig. 2(b) does not show a contour line for the case when only OPM noise is present because there is no loss of coherence observable until pulse durations as long as 1.2 ps, as also shown by Heidt *et al.* [12].

It is interesting to look into the specific spectral structure of the ANDi noise. To do so we consider the experimentally more

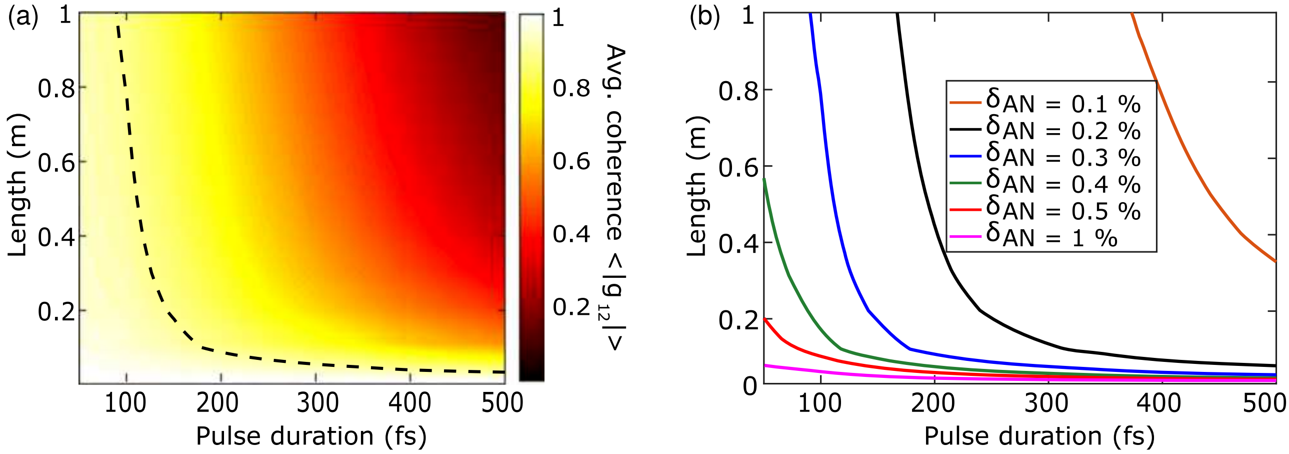

Fig. 2. (a) Average spectral coherence $\langle |g_{12}| \rangle$ of SC pulses generated with $P_0 = 100$ kW peak power pump pulses as a function of pump pulse duration T_0 and propagation distance for an amplitude noise value of 0.3% (pulse duration noise 0.24%). The dotted line indicates the limit $\langle |g_{12}| \rangle = 0.9$. (b) Limit $\langle |g_{12}| \rangle = 0.9$ for a range of amplitude noise values from 0.1% to 1% (pulse duration noise 0.08%–0.8%).

relevant RIN, which is typically used to characterize the noise of an SC source. The frequency-dependent profile, RIN(ω), is defined as [14]

$$\mathrm{RIN}(\omega) = \sqrt{\langle (|\tilde{A}(\omega)|^2 - \langle |\tilde{A}(\omega)|^2 \rangle)^2 \rangle} / \langle |\tilde{A}(\omega)|^2 \rangle. \quad \textbf{(5)}$$

Figure 3(a) shows the mean of the intensity spectrum and the RIN(ω) of an SC generated with 100 kW, 50 fs pulses at 1054 nm for a reasonably long fiber length of 1 m for pump laser amplitude noise levels of 0.1%, 0.5%, and 1.0%. We again used 20 pulses in the ensemble.

We see that in all cases the RIN is low for the majority of the bandwidth but increases strongly at the edges as expected. Two things are interesting to note: First, for the weaker amplitude noise levels of 0.1% and 0.5%, the RIN at the red edge is significantly lower than the RIN at the corresponding blue edge (e.g., the 0.6 intensity level for 0.5% noise). This is because the loss at the red edge is much higher than at the blue edge due to the strongly increasing confinement loss at 1450 nm. Indeed, if we omit fiber losses from our model, we find similar RIN values at the two spectral edges. We note that the impact of the long-wavelength loss edge was studied previously in conventional anomalous dispersion SC generation, in which it was also found to reduce the noise, here by suppressing rogue wave generation [30].

Second, we see in Fig. 3(a) a signature of peaks in the spectrum being correlated with peaks in the RIN profile. This correlation becomes even more pronounced at shorter fiber lengths where SPM is dominating and generates a periodic spectrum and RIN profile, as is visible in the initial 20 cm of the propagation shown in Fig. 3(b), which is a color map of the spectral RIN evolution as a function of the fiber length. We note that while the average RIN increases during the propagation, the spectrally resolved RIN in the central region of the spectrum decreases with the propagation, with the higher RIN quotients being pushed to the edges of the spectrum.

In Fig. 4(a) we show the mean spectrum and the RIN profile after 10 cm of propagation and draw vertical lines from the

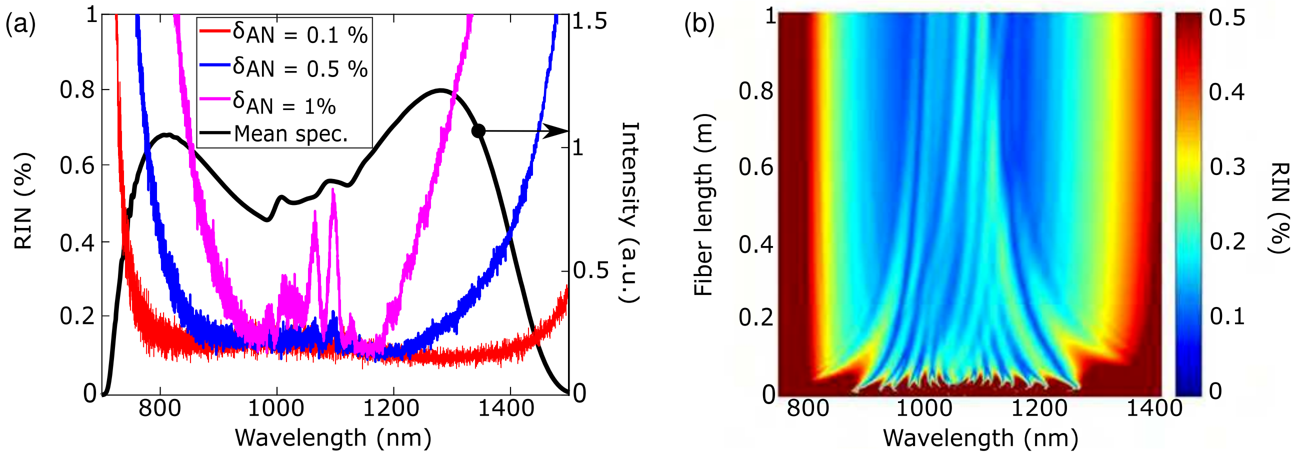

Fig. 3. (a) RIN profiles for different amplitude noise values and mean spectral profile out of 1 m of ANDi fiber pumped with 100 kW peak power, 50 fs long pulses at 1054 nm. (b) Evolution of the RIN along the fiber length for an amplitude noise value of 0.5% (pulse duration noise 0.4%). Note: The color map has a dynamic range limited to a RIN equal to 0.5%, meaning RIN data is only visible for wavelengths 800–1430 nm.

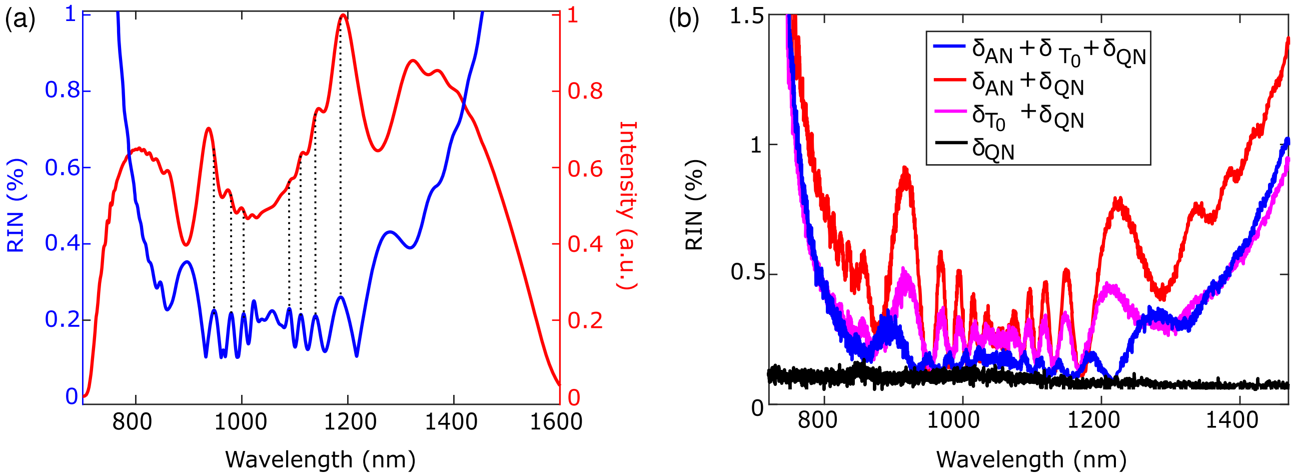

Fig. 4. (a) RIN profile (blue line) and mean spectrum (red line) of an ensemble of 20 pulses after 10 cm of fiber with 100 kW peak power, 50 fs pulse duration at 1054 nm for an amplitude noise value of 0.5% (pulse duration noise of 0.4%). (b) RIN spectrum as a function of the input noise: OPM only (black line), amplitude noise plus OPM noise (red line), pulse duration noise plus OPM (pink line), and amplitude noise plus pulse duration noise and OPM (blue line).

peaks in the RIN profile to the corresponding point in the mean spectrum (OPM noise was removed for better clarity). The correlation is very clear here as a closely matched periodicity, and it appears that when SPM is dominating, the influence of amplitude and pulse duration noise is to generate strong RIN peaks close to the fringes with maximum slope in the spectrum. We again used 20 pulses in the ensemble, and the calculations were repeated with 40 and 80 pulses in the ensemble, which revealed no noticeable change. This means that the RIN statistics converged and can be trusted.

A very interesting and counterintuitive fact seen in Figs. 3(a) and 4(a) is that across the bandwidth, away from the edges, the noise level of the generated ANDi SC is lower than the laser amplitude noise imposed on the initial condition. This has in fact also been observed experimentally in a recent work on ANDi SC generation with a 1550 nm mode-locked laser [28] but never explained. To explain it we need to look deeper into the SPM-based SC generation and the effects of the anticorrelated amplitude and pulse duration noise separately and together.

Let us consider the exact solution for SPM, which with our initial condition is given by $A(z,t) = \sqrt{P_0}\,\mathrm{sech}(t/T_0)$ $\exp(i\gamma P_0\,\mathrm{sech}^2(t/T_0)z)$. Expanding the sech^2 function in the exponent around its maximum derivative, which corresponds to the maximum frequency shift, one finds $\phi(x) = \mathrm{sech}^2(x) \approx \phi_0 + \phi_1(x - x_0) + \phi_2(x - x_0)^2$, where $x_0 = 0.66$, $\phi_1 = -0.77$, and $\phi_2 = 0$. This gives the Fourier transform

$$|\tilde{A}(\omega)|^2 = P_0 T_0^2 \left| \int_0^{+\infty} \mathrm{sech}(x)\left(e^{i(\omega-\omega_0+\Delta\omega)T_0 x} + e^{-i(\omega-\omega_0-\Delta\omega)T_0 x}\right)\mathrm{d}x \right|^2, \tag{6}$$

where the frequency shift is given by $\Delta\omega = -0.77\gamma P_0 z/T_0$. This expression can be used to study the RIN due to amplitude and pulse duration noise, which is basically how much $|\tilde{A}(\omega)|^2$ changes under a change in P_0 and/or T_0.

First of all we see that the frequency shift increases with increasing peak power and/or decreasing pulse duration, as is well known. Thus an increasing (decreasing) peak power and correlated decreasing (increasing) pulse duration will act together on the frequency shift and lead to a strongly increasing (decreasing) frequency shift. This will in itself lead to a periodic change in the spectral intensity $|\tilde{A}(\omega)|^2$ and thus a periodic RIN.

Let us now look at two simple special cases: (1) At the input $z = 0$ the frequency shift is zero and the solution becomes $|\tilde{A}(\omega)|^2 = \pi^2 P_0 T_0^2\,\mathrm{sech}^2(\pi T_0[\omega - \omega_0]/2)$. Since T_0 will decrease when P_0 increases (and vice versa) according to Eq. (2), we see that at the center frequency the amplitude and anticorrelated pulse duration noise act against each other, that is, they will tend to eliminate each other. (2) If we consider sufficiently large propagation distances, so that the frequency shift $\Delta\omega$ is large, then we can neglect the first (second) exponential in Eq. (6) when $\omega \approx \omega_0 + \Delta\omega$ $(\omega \approx \omega_0 - \Delta\omega)$, because the exponential will be rapidly oscillating. In other words, the two outer lopes in the SPM spectrum can be treated in isolation. In this case the approximate solution for the long wavelength SPM slope is $|\tilde{A}(\omega)|^2 = (\pi^2/4)P_0 T_0^2\mathrm{sech}^2$ $(\pi T_0[\omega - \omega_0 + \Delta\omega]/2)$. At the peak we therefore see that again the amplitude and anticorrelated pulse duration will act oppositely and tend to cancel each other. The fact that the RIN is lower than the pump laser amplitude noise is thus to be expected from theory and is due to the anticorrelated pulse duration noise.

Finally, Fig. 4(b) compares the impact of the different noise sources including OPM, pulse duration, and amplitude noise on the RIN spectrum. We clearly see when all the noise sources are included (blue curve) the RIN level is lower than in isolation (red and pink curves), except for OPM noise (black curve).

4. CONCLUSION

We have presented a detailed numerical study of the impact of pump laser amplitude noise on the coherence of the SC generated in ANDi PCFs with fs high peak power mode-locked pump lasers. In particular, we have shown that considering nominal values of amplitude noise drastically affects the SC coherence on the spectral edges. Indeed, when only one-photon-per-mode quantum noise is taken into account, the coherence first starts to degrade for pulse durations above 1.2 ps, while if a weak pump laser amplitude noise of 0.5% is taken into account, the degradation starts already at a pulse duration of ~50 fs.

We have looked into the specific spectral profile of the RIN of a typical low-noise ANDi SC (50 fs pulse duration, 100 kW peak power) and found that it is strongly increasing toward the spectral edges of the SC, as expected, but much less so on the red edge than the blue edge. We found that this is due to the noise suppression effect of the long wavelength confinement loss edge of the ANDi PCF, occurring already at 1450 nm due to the small holes of the typical ANDi PCF we considered.

In the central part of the low-noise ANDi SC we demonstrated that the peaks in the SC spectrum are correlated with the peaks in the RIN spectrum and that this correlation is especially apparent at shorter fiber length where SPM is dominating and the RIN profile is periodic. In particular, we demonstrated numerically that the SC noise in the central part is lower than the considered pump laser amplitude noise and that this is due a competition between the amplitude and anticorrelated pulse duration noise, which in combination gives a lower noise than in isolation. We confirmed analytically that this should be so and that it is due to the anticorrelation of the amplitude and pulse duration of the pump laser.

Our study of the absolute values and finer details of SC noise in ANDi fibers is of substantial value to potential applications, such as OCT and metrology, which require ultralow-noise SC light sources. Indeed, this study constitutes the first in-depth look into the effect of technical noise sources on the ANDi SC process and provides grounds for further research to achieve a better understanding of these physically complex processes.

Funding. European Union's Horizon 2020 Research and Innovation Programme, FP7 People: Marie-Curie Actions (PEOPLE) (SUPUVIR Project) (722380); FP7 Information and Communication Technologies (ICT) (GALAHAD Project) (7326); Agence Nationale de la Recherche (ANR) (ANR-15-IDEX-0003, ANR-17-EURE-0002).

Acknowledgment. The authors thank A. Heidt for his helpful discussions. T. Sylvestre and J. Dudley thank the support of ANR.

REFERENCES

1. A. M. Heidt, A. Hartung, G. W. Bosman, P. Krok, E. G. Rohwer, H. Schwoerer, and H. Bartelt, "Coherent octave spanning near-infrared and visible supercontinuum generation in all-normal dispersion photonic crystal fibers," Opt. Express **19**, 3775–3787 (2011).
2. A. Hartung, A. Heidt, and H. Bartelt, "Design of all-normal dispersion microstructured optical fibers for pulse-preserving supercontinuum generation," Opt. Express **19**, 7742–7749 (2011).
3. L. Liu, T. Cheng, K. Nagasaka, H. Tong, G. Qin, T. Suzuki, and Y. Ohishi, "Coherent mid-infrared supercontinuum generation in all-solid chalcogenide microstructured fibers with all-normal dispersion," Opt. Lett. **41**, 392–395 (2016).
4. R. Alfano, *The Supercontinuum Laser Source*, 3rd ed. (Springer, 2016).
5. U. Møller and O. Bang, "Intensity noise in normal-pumped picoseconds supercontinuum generation, where higher-order Raman lines cross into the anomalous dispersion regime," Electron. Lett. **49**, 63–65 (2013).
6. M. Maria, I. B. Gonzalo, T. Feuchter, M. Denninger, P. M. Moselund, L. Leick, O. Bang, and A. Podoleanu, "*Q*-switch-pumped supercontinuum for ultra-high resolution optical coherence tomography," Opt. Lett. **42**, 4744–4747 (2017).
7. T. Udem, R. Holzwarth, and T. Hänsch, "Optical frequency metrology," Nature **416**, 233–237 (2002).
8. M. K. Dasa, C. Markos, M. Maria, C. R. Petersen, P. M. Moselund, and O. Bang, "High-pulse energy supercontinuum laser for high-resolution spectroscopic photoacoustic imaging of lipids in the 1650–1850 nm region," Biomed. Opt. Express **9**, 1762–1770 (2018).
9. C. R. Petersen, N. Prtljaga, M. Farries, J. Ward, B. Napier, G. R. Lloyd, J. Nallala, N. Stone, and O. Bang, "Mid-infrared multispectral tissue imaging using a chalcogenide fiber supercontinuum source," Opt. Lett. **43**, 999–1002 (2018).
10. N. M. Israelsen, M. Maria, M. Mogensen, S. Bojesen, M. Jensen, M. Haedersdal, A. Podoleanu, and O. Bang, "The value of ultrahigh resolution OCT in dermatology—delineating the dermo-epidermal junction, capillaries in the dermal papillae and vellus hairs," Biomed. Opt. Express **9**, 2240–2265 (2018).
11. B. Povazay, K. Bizheva, A. Unterhuber, B. Hermann, H. Sattmann, A. F. Fercher, W. Drexler, A. Apolonski, W. J. Wadsworth, J. C. Knight, P. St.J. Russell, M. Vetterlein, and E. Scherzer, "Submicrometer axial resolution optical coherence tomography," Opt. Lett. **27**, 1800–1802 (2002).
12. A. M. Heidt, J. S. Feehan, J. H. V. Price, and T. Feurer, "Limits of coherent supercontinuum generation in normal dispersion fibers," J. Opt. Soc. Am. B **34**, 764–775 (2017).
13. C. Finot, B. Kibler, L. Provost, and S. Wabnitz, "Beneficial impact of wave-breaking for coherent continuum formation in normally dispersive nonlinear fibers," J. Opt. Soc. Am. B **25**, 1938–1948 (2008).
14. I. Gonzalo, R. Engelsholm, M. Sørensen, and O. Bang, "Polarization noise places severe constraints on coherence of all-normal dispersion femtosecond supercontinuum generation," Sci. Rep. **8**, 6579 (2018).
15. F. Li, Q. Li, J. Yuan, and P. K. A. Wai, "Highly coherent supercontinuum generation with picosecond pulses by using self-similar compression," Opt. Express **22**, 27339–27354 (2014).
16. M. H. Frosz, O. Bang, and A. Bjarklev, "Soliton collision and Raman gain regimes in continuous-wave pumped supercontinuum generation," Opt. Express **14**, 9391–9407 (2006).
17. A. Mussot, E. Lantz, H. Maillotte, T. Sylvestre, C. Finot, and S. Pitois, "Spectral broadening of a partially coherent CW laser beam in single-mode optical fibers," Opt. Express **12**, 2838–2843 (2004).
18. S. T. Sørensen, C. Larsen, U. Møller, P. M. Moselund, C. L. Thomsen, and O. Bang, "The role of phase coherence in seeded supercontinuum generation," Opt. Express **20**, 22886–22894 (2012).
19. Z. Zhu and T. G. Brown, "Polarization properties of supercontinuum spectra generated in birefringent photonic crystal fibers," J. Opt. Soc. Am. B **21**, 249–257 (2004).
20. J. M. Dudley, G. Genty, and S. Coen, "Supercontinuum generation in photonic crystal fiber," Rev. Mod. Phys. **78**, 1135–1184 (2006).
21. J. M. Dudley and S. Coen, "Coherence properties of supercontinuum spectra generated in photonic crystal and tapered optical fibers," Opt. Lett. **27**, 1180–1182 (2002).
22. M. H. Frosz, "Validation of input-noise model for simulations of supercontinuum generation and rogue waves," Opt. Express **18**, 14778–14787 (2010).
23. K. L. Corwin, N. R. Newbury, J. M. Dudley, S. Coen, S. A. Diddams, B. R. Washburn, K. Weber, and R. S. Windeler, "Fundamental amplitude noise limitations to supercontinuum spectra generated in a microstructured fiber," Appl. Phys. B **77**, 269–277 (2003).
24. P. D. Drummond and J. F. Corney, "Quantum noise in optical fibers. I. Stochastic equations," J. Opt. Soc. Am. B **18**, 139–152 (2001).

25. J. F. Corney and P. D. Drummond, “Quantum noise in optical fibers. II. Raman jitter in soliton communications,” J. Opt. Soc. Am. B **18**, 153–161 (2001).
26. R. G. Smith, “Optical power handling capacity of low loss optical fibers as determined by stimulated Raman and Brillouin scattering,” Appl. Opt. **11**, 2489–2494 (1972).
27. U. Møller, S. T. Sørensen, C. Jakobsen, J. Johansen, P. M. Moselund, C. L. Thomsen, and O. Bang, “Power dependence of supercontinuum noise in uniform and tapered PCFs,” Opt. Express **20**, 2851–2857 (2012).
28. S. Rao, R. Engelsholm, I. Gonzalo, B. Zhou, P. Bowen, P. Moselund, M. Bache, and O. Bang, “Ultra-low noise supercontinuum generation with flat near-zero normal dispersion fiber,” arXiv:1812.03877 (2018).
29. I. Gonzalo and O. Bang, “Role of the Raman gain in the noise dynamics of all-normal dispersion silica fiber supercontinuum generation,” J. Opt. Soc. Am. B **35**, 2102–2110 (2018).
30. D. Buccollero, H. Steffensen, H. Ebendorff-Heidepriem, T. M. Monro, and O. Bang, “Midinfrared optical rogue waves in soft glass photonic crystal fiber,” Opt. Express **19**, 17973–17978 (2011).

Optics Letters

Cross-phase modulation instability in PM ANDi fiber-based supercontinuum generation

Etienne Genier,[1,2,*] Amar N. Ghosh,[2] Swetha Bobba,[2] Patrick Bowen,[1] Peter M. Moselund,[1] Ole Bang,[1,3] John M. Dudley,[2] and Thibaut Sylvestre[2]

[1]*NKT Photonics A/S, Blokken 84, DK-3460, Birkerød, Denmark*
[2]*Institut FEMTO-ST, UMR 6174 CNRS-Université Bourgogne Franche-Comté, 25030 Besançon, France*
[3]*DTU Fotonik, Department of Photonics Engineering, Technical University of Denmark, 2800 Kgs. Lyngby, Denmark*
*Corresponding author: etienne.genier@nktphotonics.com

Received 7 May 2020; revised 22 May 2020; accepted 22 May 2020; posted 26 May 2020 (Doc. ID 397106); published 24 June 2020

We demonstrate broadband supercontinuum generation in an all-normal dispersion polarization-maintaining photonic crystal fiber and report the observation of a cross-phase modulation instability sideband generated outside of the supercontinuum bandwidth. We demonstrate that this sideband is polarized on the slow axis and can be suppressed by pumping on the fiber's fast axis. We theoretically confirm and model this nonlinear process using phase-matching conditions and numerical simulations, obtaining good agreement with the measured data.

https://doi.org/10.1364/OL.397106

All-normal dispersion (ANDi) optical fibers have recently emerged as attractive platforms to improve the noise and coherence of supercontinuum generation (SC/SCG) beyond the limits of anomalous SC generation [1–4]. ANDi SCG is based on two fully coherent nonlinear effects: self-phase modulation (SPM) and optical wave breaking (OWB) [2,5] while anomalous SCG is typically susceptible to or even generated by incoherent nonlinear effects [6]. Despite this, ANDi SCG has its own limitations, being both very sensitive to Raman noise [2–4,7] and requiring low and flat fiber dispersion engineering that is technically challenging to achieve [1]. When pumping with femtosecond pulses, it has been shown that other factors should be considered including polarization modulation instability (PMI) or the amplitude noise of the laser, both of which can drastically degrade the relative intensity noise (RIN) and coherence [3,4,8]. These factors limit the available parameter space for coherent SCG; however, fs-pumped ANDi SC generation still has significant potential to generate temporally coherent SC with realistic laser parameters, a feature hard to come by in the anomalous dispersion regime. This gives such systems potential in a range of fields including optical coherence tomography (OCT), optical metrology, photoacoustic imaging, and spectroscopy [9–11].

In this work, we investigate SCG in a polarization-maintaining (PM)-ANDi silica photonic crystal fiber (PCF) with a femtosecond stable optical parametric oscillator (OPO) with intention to suppress PMI. However, in doing this, we discovered the generation of a sideband outside the SC bandwidth that was not observed in previous PM-ANDi SCG [12,13]. We identify this sideband as the result of a cross-phase modulation instability (XPMI) process that builds up from coherent SCG and OWB. As described in [14,15], XPMI is usually observed when a beam is launched at a 45° angle from the principal axis of a highly birefringent fiber. This beam is then split into two linearly polarized modes on each axis that will nonlinearly interact with each other to generate two frequency-detuned and cross-polarized four-wave mixing (FWM) sidebands [14]. However, this XPMI process has never been observed before through the stimulation of fs-SC generation but only via spontaneous generation of the interaction of picosecond or nanosecond pulses.

Our results show that we can generate a stimulated XPMI sideband in a PM-ANDi PCF using femtosecond pulses. As expected, this sideband is most powerful while pumping the fiber at 45° off the axes. We also demonstrate this sideband can be completely suppressed when pumping the fiber on the fast axis.

The experimental setup used to observe and analyze SC and XPMI generation in the PM-ANDi PCF is shown in Fig. 1. As a pump laser, we used a Ti:Sa femtosecond pulsed laser (Coherent Chameleon) tunable from 680–1080 nm, delivering 200 fs pulse duration at an 80 MHz repetition rate with a maximum average power of 450 mW at 1040 nm. The output power is controlled using a variable neutral density filter (ND). A half-wave plate is used to turn the input polarization state , while the polarizer at the fiber's output is used to observe the spectral content on the light of each axis. A 40x microscope objective is used to couple the light into the 40 cm of PM ANDi PCF—the NL-1050-NE-PM from NKT Photonics. This fiber has a relative hole size of $d/L = 0.45$, a small hole-to-hole pitch of 1.44 μm, and a nonlinear coefficient of $\gamma = 26.8\ \mathrm{W}^{-1}\ \mathrm{km}^{-1}$ at 1040 nm. A set of two aspheric lenses is used to collimate the output beam and then focus it to the multimode pick-up fiber.

The dispersion was measured using white-light interferometry and calculated for an idealized structure with a uniform hole structure with fixed pitch and hole diameter using COMSOL.

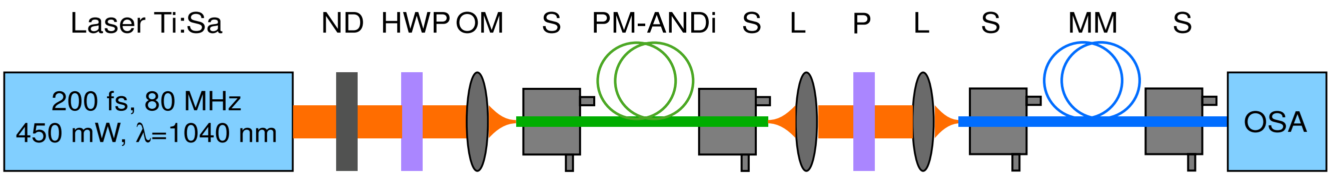

Fig. 1. Schematic of the setup, including a wavelength tunable Ti:Sa femtosecond laser, variable neutral density filter (ND), half-wave plate (HWP), 40x microscope objective (OM), aspheric lenses (L), 3D translation stages (S), 40 cm of all-normal dispersion PCF (PM-ANDi), a polarizer (P), 2 m of multimode pick-up fiber (MM), and an optical spectrum analyzer (OSA).

The calculation fits the measurements well and is shown as the blue curve in Fig. 2. The numerical modeling using the experimental dispersion data did not reproduce the experimental results; this is probably due to the uncertainties on this dispersion curve that increase when the dispersion is close to zero. We therefore considered the dispersion given by the brown curve, which is shifted upwards in the center as the dispersion approaches zero. This is still within the measurement uncertainties and is able to reproduce the experiments as we will demonstrate. As expected, the small holes of the PCF give a confinement loss edge wavelength significantly below the material loss edge wavelength, calculated to be at 1450 nm using COMSOL (see Fig. 2, green curve). The dispersion profile has a minimum of -13 ps/nm/km at 1040 nm and is rather symmetrical within the low-loss window. The PM effect of this fiber is stress-rod induced, with a slight degree of core-ellipticity that causes a linearly increasing birefringence [16], which goes from $2.5 \cdot 10^{-4}$ at 850 nm to $6.8 \cdot 10^{-4}$ at 1300 nm, as shown in Fig. 2 (red circles).

We pumped the fiber at 1040 nm, at the minimum dispersion wavelength (MDW); thus we should expect the broadest SC. Figure 3 shows the spectral evolution while pumping on the slow axis, fast axis, and at 45°. The broadest SC spectrum (bandwidth at -20 dB is 460 nm) is obtained by pumping on the slow axis, while the narrowest is obtained by pumping at 45° because only half the power is available for spectral broadening in each axis and due to the temporal walk-off, which tends to eliminate the influence of cross-phase modulation [17]. Also, the SC spectrum is quite symmetric whatever the input angle due to the parabolic shape of the fiber dispersion. Interestingly a sideband appears at 1360 nm, which is strongest when pumping at 45° and which we identify as XPMI. When pumping on the slow axis, the sideband intensity is reduced by 12 dB but is still clearly observable. Finally, when pumping on the fast axis, the sideband appears to be completely suppressed with an extinction of at least 25 dB. To understand the appearance of this sideband and the efficiencies regarding the input polarization angle, let us recall that the phase-matching condition for XPMI should give rise to a Stokes sideband on the slow axis and an anti-Stokes sideband on the fast axis because of positive (normal) group-velocity dispersion (GVD) [6,18]. This means to stimulate the generation of an idler-pumped sideband in the Stokes side of the spectrum, we need energy in the pump (on both axes) and energy in the anti-Stokes sideband (aligned to the fast axis). Experimentally, we use a pump laser with a polarization extinction ratio (PER) of 40 dB and inject the light into the PM-ANDi fiber, whose input face was end-collapsed to remove back reflections into the Ti:Sa laser. At the output, we measure a maximum achievable PER of 17 dB, which has a relatively even distribution over the whole SC bandwidth. This shows that at some point in the propagation, light has deviated from the input axis to become distributed more over both axes, probably due to the collapse of the fiber holes. This can explain why it is possible to observe a Stokes sideband at 1360 nm even when the input beam is almost aligned on the slow axis, as shown in Fig. 3.

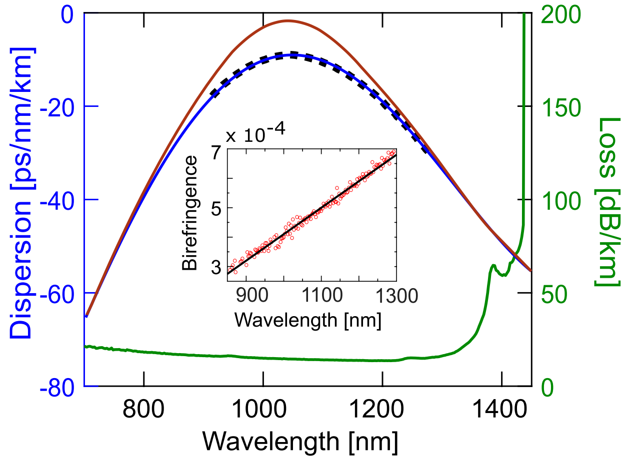

Fig. 2. Numerical (solid blue), experimental (black dots) and modeled (dashed brown) dispersion profiles, and fiber losses (solid green) of the NL-1050-NE-PM ANDi PCF. The inset shows the group birefringence: linear fitting (solid black) and measured data (circles red).

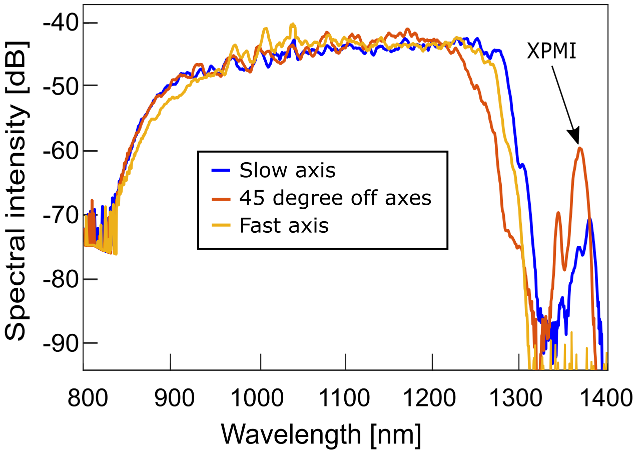

Fig. 3. Experimental SC spectra for different input polarizations with 220 mW output power.

Figure 4 shows the evolution of the SC spectrum as a function of the pump power for an input polarization at 45° off axes. The SC bandwidth is 430 nm at -20 dB (845–1275 nm) for an average output power of 220 mW. The XPMI sideband grows

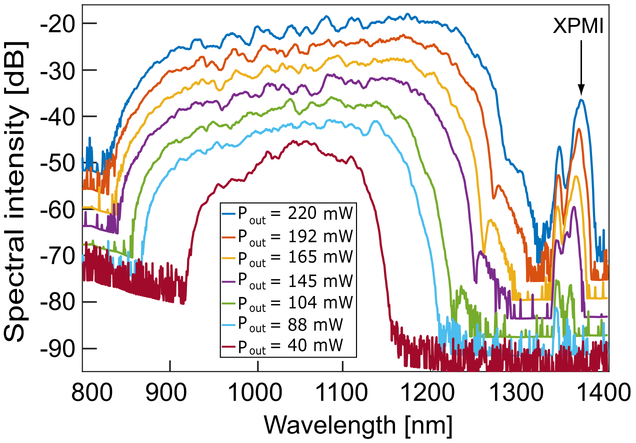

Fig. 4. SC evolution for different pump powers while pumping at 45° from the two axes (power offset for clarity).

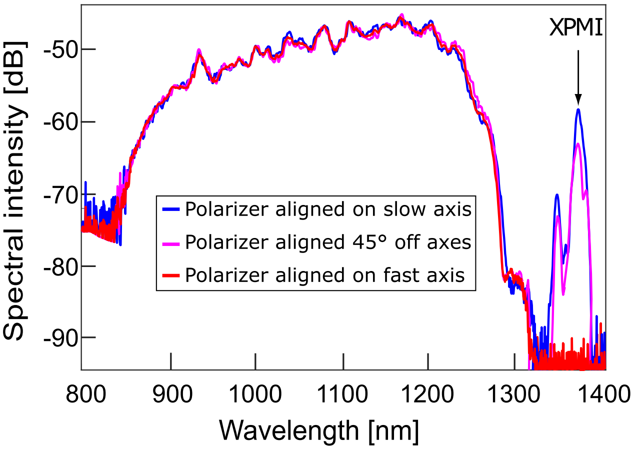

Fig. 5. SC evolution for different polarizer orientations while pumping at 45° from the two axes.

and slightly broadens to longer wavelengths when increasing the coupled power. It starts to appear only when SC extends past 1200 nm and when the OWB also starts to appear (see the green spectrum in Fig. 4). In addition, there is no observable anti-Stokes sideband outside the SC, even when observing the spectrum over a wide bandwidth (600–2000 nm).

Adding a polarizer at the output of the fiber to analyze the sideband polarization angle, we show in Fig. 5 the SC spectrum measured after the polarizer as a function of the polarizer angle at maximum output power (220 mW average power). We notice that the three spectra obtained by aligning the polarizer on the slow axis (blue curve), fast axis (red curve), and at 45° of the axes (pink curve) have a similar bandwidth and shape. We observe the most powerful sideband when the polarizer is aligned on the slow axis and a 10 dB suppression when aligning the polarizer at 45° of the axes. Finally, aligning the polarizer on the fast axis totally suppresses the sideband, confirming that the sideband is polarized along the slow axis.

To simulate the SCG in the PM-ANDi fiber, we use a MATLAB code solving the two coupled generalized nonlinear Schrodinger equations (CGNLSEs) for highly birefringent fibers as described in [19]. We used as input parameters a pump wavelength of 1040 nm, a sech-shaped pump pulse with duration of 200 fs (full width half maximum intensity), 12 kW peak power, a longer fiber length of 60 cm for better visibility, the loss profile as described in Fig. 2 (green curve), and the birefringence values taken from the inset. One-photon-per-mode noise and intensity noise of 1% was added to our input condition, and the results were sampled average over 20 simulations. Using these parameters, we obtain a quite good agreement between simulation and experimental results. This is shown in Figs. 6(a)–6(d), which depict both the spectral and temporal intensity dynamics on each axis when pumping the PM-ANDi fiber at 45°. First, the numerical SC bandwidth at −20 dB level is estimated to be 450 nm, which is very close to the experimental one (430 nm). Second, we can clearly see the generation of a small signal at 1360 nm polarized on the slow axis, which fits with the experimentally observed XPMI sideband [see Fig. 6(b)]. We also notice that the sideband appears after 20 cm of propagation exactly where the OWB sets in and stops the red-shift of the SPM lobes. Interestingly, the temporal trace plotted in Fig. 6(d) reveals that the signal at 1360 nm behaves as a small dispersive wave (DW) shed by the pump pulse on the slow axis, in a way akin to the DW emission by OWB in the anomalous dispersion region [20,21].

To go further into detail, in Fig. 7, we plot the theoretical XPMI sidebands as a function of pump wavelength using the well-known formula for the XPMI frequency shift [22]

$$\Omega_s(\lambda, z) = \frac{\delta n(\lambda)}{2c\beta_2(\lambda)}\left(1+\sqrt{1-4\beta_2(\lambda)\gamma P_0(z)\left(\frac{c}{\delta n(\lambda)}\right)^2}\right),$$

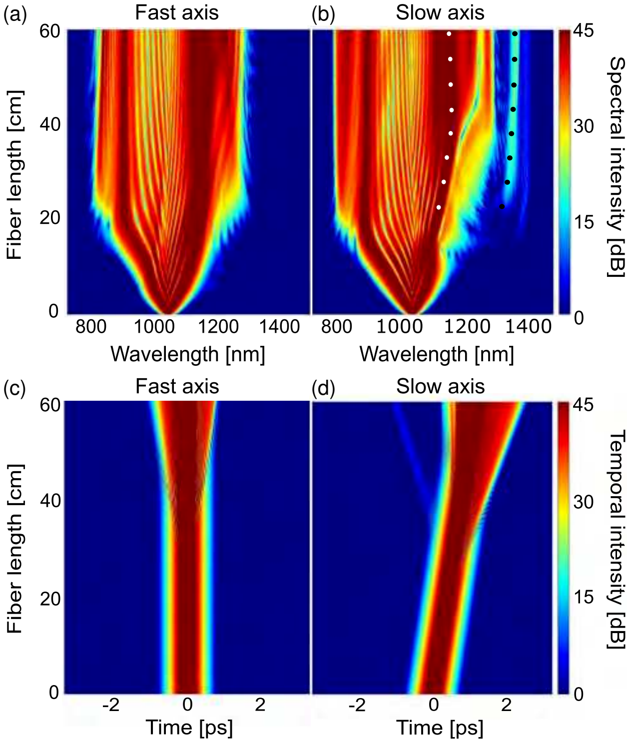

Fig. 6. Simulated spectral (top) and temporal (bottom) SC evolution on each fiber axis as a function of fiber length. The dots represent the theoretical XPMI wavelength (black) using the redder SPM wavelength (white) as a pump.

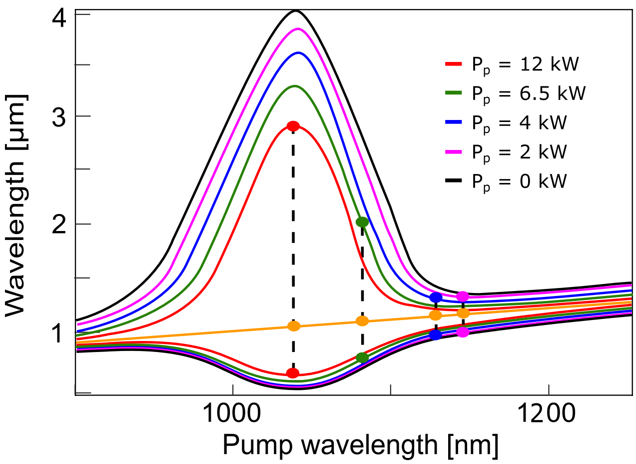

Fig. 7. Phase-matching map as a function of total peak power, 12 kW (red), 6.5 kW (green), 4 kW (blue), 2 kW (pink), and 0 kW (black). The orange dots on the straight line for the pump wavelength show the numerically observed red SPM wavelength [white dots in Fig. 6(b)], and the other colored dots mark the corresponding XPMI wavelength.

where δn is the group birefringence, P_0 the total peak power, and β_2 the wavelength-dependent GVD. The XPMI wavelengths are plotted in Fig. 7 for different peak powers. From the modeling, the slow axis XPMI generation is seen to be closely linked to the long wavelength SPM lobe in the slow axis, marked with white dots. According to this conjecture, the XPMI gain is efficient only when the red shift of the SPM lobe, acting as the pump, slows down, and for lengths not much longer than the walk-off length of 22 cm. This is exactly what is observed: the XPMI peak is first growing after about 20 cm when the red-shift of the SPM lobe is stopped by OWB, and after about 30 cm, the power in the XPMI peak does not grow anymore. Looking into more detail, we find that the peak power decreases from 12 kW at $z = 0$ to 1.5 kW at $z = 60$ cm. From the corresponding phase-matching curves in Fig. 7, we see that the XPMI phase-matches to the center wavelength of the SPM lobe initially at 2787 nm ($P_0 = 12\,\mathrm{kW}$, $\lambda_{\mathrm{SPM}} = 1040\,\mathrm{nm}$), then it rapidly decreases because of the red-shift of the SPM lobe. The observed final SPM lobe wavelength of 1152 nm is seen to generate XPMI at 1360 nm in the valley of the linear phase-matching curve, which corresponds nicely to the numerically and experimentally observed XPMI wavelength, for the adjusted dispersion profile. The observed SCG-induced XPMI generation thus requires a delicate balance between strong SPM stopped sufficiently before, say, twice the walk-off length by OWB.

In conclusion, we have reported the observation of XPMI while pumping a PM-ANDi PCF with a femtosecond laser. A sideband was generated through a XPMI process at 1360 nm during coherent SCG from SPM and OWB. We demonstrated this sideband cannot be generated while pumping on the fast axis and is itself polarized along the fiber's slow axis. Further clarifying that we were observing XPMI, theoretical calculation and simulation performed solving the CGNLSE confirmed the degenerate FWM between a pump corresponding to the red edge of the SPM on the fiber's slow axis, an anti-Stokes idler pump in the central SPM area on the fiber fast's axis, and a signal at 1360 nm polarized on the fiber's slow axis. Our study is of substantial value to potential applications, such as OCT and metrology, which require ultra-low-noise SC light sources. To achieve low noise in these future SC sources, a high degree of suppression of XPMI will be required and for this a solid understanding of the underpinning physics. Indeed, this study shows that controlling the input polarization is very important to avoid noise the amplification effect and thus keep the noise-free/stability given by fs PM-ANDi SCG.

Funding. Horizon 2020 Framework Programme (722380); Agence Nationale de la Recherche (ANR-15-IDEX-0003).

Disclosures. The authors declare no conflicts of interest.

REFERENCES

1. A. Hartung, A. M. Heidt, and H. Bartelt, Opt. Express **19**, 7742 (2011).
2. A. M. Heidt, J. S. Feehan, J. H. V. Price, and T. Feurer, J. Opt. Soc. Am. B **34**, 764 (2017).
3. I. B. Gonzalo, R. D. Engelsholm, M. P. Sørensen, and O. Bang, Sci. Rep. **8**, 6579 (2018).
4. E. Genier, P. Bowen, T. Sylvestre, J. M. Dudley, P. Moselund, and O. Bang, J. Opt. Soc. Am. B **36**, A161 (2019).
5. C. Finot, B. Kibler, L. Provost, and S. Wabnitz, J. Opt. Soc. Am. B **25**, 1938 (2008).
6. J. M. Dudley, G. Genty, and S. Coen, Rev. Mod. Phys. **78**, 1135 (2006).
7. U. Møller and O. Bang, Electron. Lett. **49**, 63 (2013).
8. A. Loredo-Trejo, Y. López-Diéguez, L. Velázquez-Ibarra, A. Díez, E. Silvestre, J. M. Estudillo-Ayala, and M. V. Andrés, IEEE Photon. J. **11**, 7104208 (2019).
9. M. K. Dasa, C. Markos, M. Maria, C. R. Petersen, P. M. Moselund, and O. Bang, Biomed. Opt. Express **9**, 1762 (2018).
10. C. R. Petersen, N. Prtljaga, M. Farries, J. Ward, B. Napier, G. R. Lloyd, J. Nallala, N. Stone, and O. Bang, Opt. Lett. **43**, 999 (2018).
11. B. Povazay, K. Bizheva, A. Unterhuber, B. Hermann, H. Sattmann, A. Fercher, W. Drexler, A. Apolonski, W. Wadsworth, J. Knight, P. St.J. Russell, M. Vetterlein, and E. Scherzer, Opt. Lett. **27**, 1800 (2002).
12. K. Tarnowski, T. Martynkien, P. Mergo, K. Poturaj, A. Anuszkiewicz, P. Béjot, F. Billard, O. Faucher, B. Kibler, and W. Urbanczyk, Opt. Express **25**, 27452 (2017).
13. K. Tarnowski, T. Martynkien, P. Mergo, J. Sotor, and G. Soboń, Sci. Rep. **9**, 1 (2019).
14. A. Kudlinski, A. Bendahmane, D. Labat, S. Virally, R. Murray, E. Kelleher, and A. Mussot, Opt. Express **21**, 8437 (2013).
15. P. Drummond, T. Kennedy, J. Dudley, R. Leonhardt, and J. Harvey, Opt. Commun. **78**, 137 (1990).
16. P. Hlubina, D. Ciprian, and M. Kadulová, Meas. Sci. Technol. **20**, 025301 (2008).
17. T. Sylvestre, H. Maillotte, E. Lantz, and D. Gindre, J. Nonlinear Opt. Phys. Mater. **6**, 313 (1997).
18. J. Chen, G. Wong, S. Murdoch, R. Kruhlak, R. Leonhardt, J. Harvey, N. Joly, and J. Knight, Opt. Lett. **31**, 873 (2006).
19. A. N. Ghosh, M. Meneghetti, C. R. Petersen, O. Bang, L. Brilland, S. Venck, J. Troles, J. M. Dudley, and T. Sylvestre, J. Phys. Photon. **1**, 044003 (2019).
20. M. Conforti and S. Trillo, Opt. Lett. **38**, 3815 (2013).
21. K. E. Webb, Y. Q. Xu, M. Erkintalo, and S. G. Murdoch, Opt. Lett. **38**, 151 (2013).
22. G. P. Agrawal, *Nonlinear Fiber Optics* (Springer, 2000), pp. 195–211.

An ultra-flat, low-noise and linearly polarized fiber supercontinuum source covering 670 nm-1390 nm

ETIENNE GENIER[1,2,*], **SACHA GRELET**[1], **RASMUS D. ENGELSHOLM**[1], **PATRICK BOWEN**[1], **PETER M. MOSELUND**[1], **OLE BANG**[1,3], **JOHN M. DUDLEY**[2], AND **THIBAUT SYLVESTRE**[2]

[1] *NKT Photonics A/S, Blokken 84, DK-3460, Birkerød, Denmark*
[2] *Institut FEMTO-ST, UMR 6174 CNRS-Université de Franche-Comté, 25030 Besançon, France*
[3] *DTU Fotonik, Department of Photonics Engineering, Technical University of Denmark, 2800 Kgs. Lyngby, Denmark*
[*] *Corresponding author: etienne.genier@nktphotonics.com*

Compiled January 22, 2021

We report an octave-spanning coherent supercontinuum (SC) fiber laser with excellent noise and polarization properties. This was achieved by pumping a highly birefringent all-normal dispersion (ANDi) photonic crystal fiber with a compact high-power ytterbium femtosecond laser at 1049 nm. This system generates an ultra-flat SC spectrum from 670 nm to 1390 nm with a power spectral density higher than 0.4 mW/nm and a polarization extinction ratio of 17 dB across the entire bandwidth. An average pulse-to-pulse relative intensity noise (RIN) down to 0.54% from 700 nm to 1100 nm has been measured and found to be in good agreement with numerical simulations. This highly-stable broadband source could find strong potential applications in biomedical imaging and spectroscopy where improved signal to noise ratio is essential.

http://dx.doi.org/10.1364/ao.XX.XXXXXX

Supercontinuum (SC) generation in all-normal dispersion (ANDi) photonic crystal fibers (PCF) has recently been investigated due to its ability to generate a low-noise broadband coherent spectrum [1–6], with a noise level much lower than typical SC sources using anomalous dispersion. The main issues with typical soliton-based SC generation is the poor flatness and the coherence degradation for a soliton number higher than 16, associated with large pulse-to-pulse fluctuations due to noise amplification by modulation instability (MI), soliton fission and rogue wave generation [7]. On the contrary, ANDi SC generation, which is essentially based on nonlinear coherent effects such as self-phase modulation (SPM) and subsequently optical wave breaking (OWB), has a high degree of coherence and pulse to pulse stability [8, 9]. ANDi SC generation is thus a topic being extensively investigated for several applications such as optical coherent tomography [10], coherent amplification [11], nonlinear microscopy [12], hyperspectral stimulated Raman scattering microscopy [13] , and coherent anti-Stokes Raman scattering (CARS) spectroscopy [14]. Several recent studies have however shown some limitations on the input pulse duration due to stimulated Raman scattering (SRS) and polarization modulation instability (PMI) [5, 6, 9, 15, 16]. Specifically, it has been shown that for input pulse duration longer than $\sim$ 500 fs, SRS-induced noise amplification impacts on the SC pulse coherence and spectral flatness [9]. Furthermore, for input pulse duration longer than $\sim$ 120 fs, PMI can take place between the two orthogonal eigenmodes of the fiber, thus degrading the relative intensity noise (RIN) and the output polarization for non-polarization maintaining (PM) fibers [5].

In this work, we overcome these limitations by using a silica-based PM ANDi PCF pumped with a low-noise, short pulse duration (180 fs) compact ytterbium mode-locked laser at 1049 nm. Using this system, symmetrically flat and ripple-free SC generation has been generated from 670 nm to 1390 nm with a maximum output power of 720 mW. It is shown in particular that pumping on the fast axis of the fiber provides the flattest and most stable SC while removing the cross-phase modulation instability (XPMI) that has recently been evidenced in PM ANDi fibers [17]. A polarization extinction ratio (PER) of 17 dB and an average RIN of 0.54 % from 700 nm to 1100 nm were further measured. We finally compare the spectrally-resolved RIN of our ANDi-fiber-based SC source with those recently published in the literature and we show excellent noise and polarization characteristics.

The experimental setup used to observe and analyze coherent SC generation in the PM-ANDi PCF is shown in Fig. 1. As a pump laser, we used a femtosecond ytterbium solid-state mode-locked laser (Origami 10 HP, NKT Photonics) centered at 1049 nm, delivering a 180 fs pulse train at an 80 MHz repetition rate with a maximum average power of 4 W, a low RIN of 0.5%, and a PER of 31 dB. The laser output power was controlled using a variable neutral density (ND) filter. A half-wave plate was used to rotate the field polarization state at the fiber input. An aspheric lens with a focal length of 6 mm was used to couple the light into the fiber core. The fiber is a PM ANDi PCF from NKT Photonics (Model NL-1050-NEG-PM). This fiber has a core diameter of 2.4 μm, a relative hole diameter of $d/\Lambda = 0.45$, a small hole-to-hole pitch of $\Lambda = 1.44$ μm, and a nonlinear coefficient of

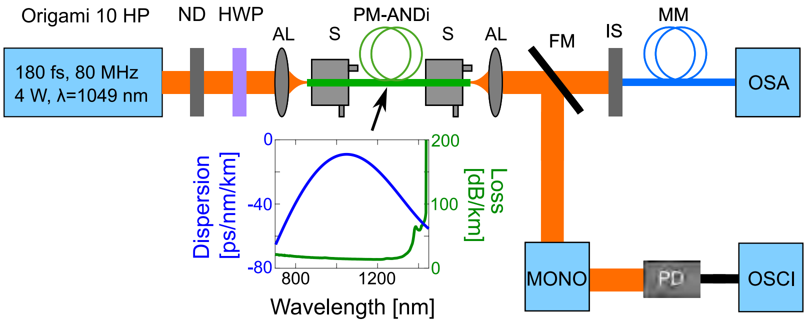

Fig. 1. Schematic of the setup, including ytterbium femtosecond mode-locked laser (ORIGAMI 10 HP), variable neutral density filter (ND), half wave plate (HWP), aspheric lenses (AL), 3D translation stages (S), 2 m of PM-ANDi PCF, flip-mirror (FM), integrating sphere (IS), 2 m of multimode pick-up fiber (MM), optical spectrum analyzer (OSA), monochromator (MONO), photodiode (PD), and oscilloscope (OSCI).

γ=26.8 $W^{-1}km^{-1}$ at 1040 nm. The fiber's dispersion and loss profiles are shown as an inset in Fig. 1 [17]. The dispersion has an all-normal parabolic profile with a peak at -13 ps/nm/km at 1040 nm. The PM property of the PCF is mainly stress-rod induced and it has a slightly elliptic core, which together gives it a high birefringence of $4.7\ 10^{-4}$ at the pump wavelength. The output spectrum is recorded using an optical spectrum analyser (OSA) and analysed as a function of input polarization and pump power, while the RIN was measured in another path using a monochromator as filter passband, two different fast photodetectors to cover the whole SC bandwidth and an oscilloscope.

Figure 2 shows the spectral intensity profile for 3 selected polarizations and an average output power from the fiber of 720 mW (estimated input peak power of 48 kW, including losses and Fresnel reflections). We obtain the broadest bandwidth while pumping along the slow axis (red curve), with a spectrum going from 685 nm to 1395 nm at -3 dB if we disregard the oscillations in the central part of the spectrum. We find the spectrum becomes more noticeably modulated as we move closer to the center of the spectrum. Furthermore, the modulations appear together with the observation of an XPMI peak [17] when pumping along the slow axis. This clarifies the importance of avoiding XPMI, since the modulation can be detrimental to interference based imaging. The spectrum is the narrowest when pumping at 45° from the principal axes (pink curve) spanning from 700 nm to 1370 nm at -3 dB, which is expected because only half of the power is available on each axis. We observe that the spectrum for 45° is highly modulated from 870 nm to 1120 nm. The XPMI sideband is again present and slightly stronger than the one obtained on the red curve, as expected from the theory [17–19]. Then, we obtain an extremely flat spectrum when pumping on the fast axis (blue curve) with a spectrum spanning from 670 nm to 1390 nm at -3 dB without any trace of an XPMI sideband around 1400 nm.

We now investigate the case with pumping along the fast axis, for which we observed the best spectrum with the least ripples. Thus, Fig. 3 shows the evolution of the SC generation for a fiber output average power increasing from 1 mW to 720 mW (peak power going from 8 W to 48 kW). We observe two SPM fringes on the pink curve (for a power of 6 mW). Then, by increasing further the power up to 30 mW (brown spectrum), we can clearly see the appearance of OWB on the edges. Furthermore, the SC bandwidth goes from 9 nm (in the linear regime) to 720 nm (going from 670 nm to 1390 nm) at -3 dB, which is more than one octave with a power spectral density (PSD) higher than 0.4 mW/nm (-4 dBm/nm). Next, as expected from coherent ANDi SC generation, the spectrum broadens symmetrically and is extremely flat (the maximum amplitude of the ripples in the SPM area is 1.65 dB). Finally, we do not observe any SRS compo-

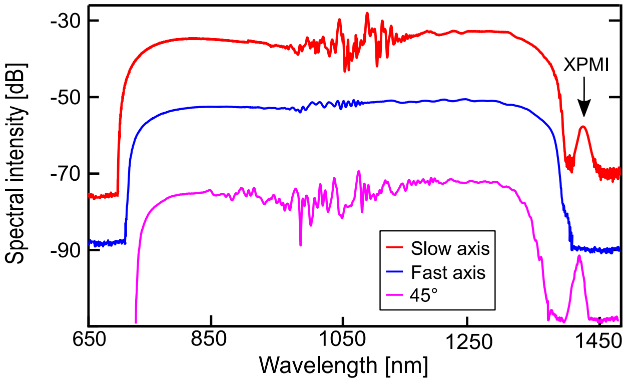

Fig. 2. Experimental SC spectra at the output of the PM-ANDi PCF for output average power of 720 mW with an input pulse duration of 180 fs while pumping along the slow axis (red curve), fast axis (blue curve) and at 45 ° from the axes (pink curve). The blue and red curves are offset by 15 dB and 30 dB from the pink curve, respectively.

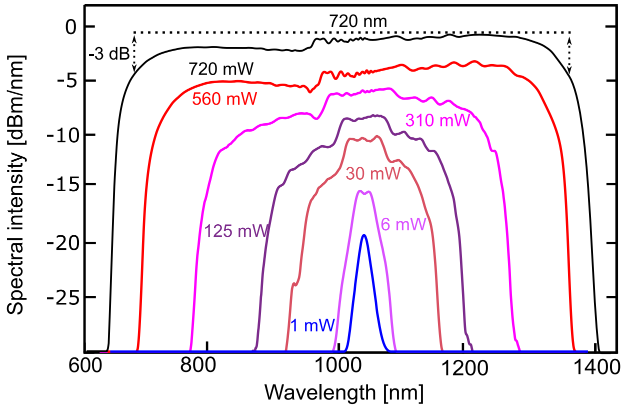

Fig. 3. Experimental SC spectra at the output of the PM-ANDi PCF for output average power of 1 mW to 720 mW with an input pulse duration of 180 fs and an input beam polarized along the fast axis.

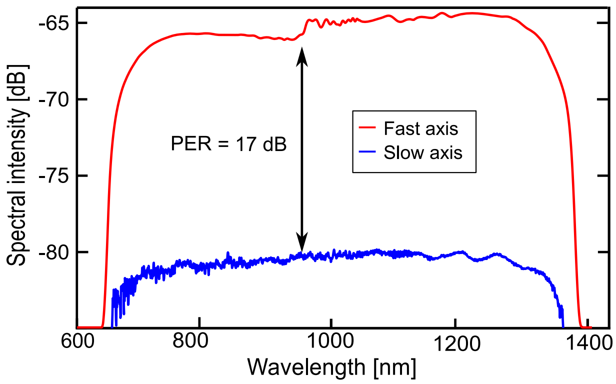

Fig. 4. Experimental SC spectra when pumping on the fiber's fast axis and using a polarizer aligned either on the fast axis (red) or on the slow axis (blue). The difference between the flat parts of the spectra gives a PER of about 17 dB.

nents in the final spectra at high power (red and black spectra) across the whole bandwidth [5, 9]. Thus, we can expect this SC generation to be extremely low-noise and highly stable.

Using a polarizer at the output of the ANDi-PCF, we measured the PER of the generated SC using the OSA. Fig. 4 depicts the SC spectra when the input beam is polarized along the fast axis and the output polarizer is aligned either on the fast axis (red curve) or on the slow axis (blue curve). Specifically, the polarizer is rotated to measure the minimum power including the whole spectrum and then the spectrum is measured at this angle and at a 90 degree rotation. This way, we can measure an average PER of 17 dB over the full SC bandwidth, which means that the SC output is nearly linearly polarized. We noticed however a PER degradation of 14 dB compared to the input pump laser (PER of 31 dB). This degradation of 14 dB is also measured at low power (no spectral broadening) and may be explained by the collapse of the air holes at the entrance of the fiber required to remove back-reflection in the laser cavity.

Let us now turn our attention to the noise properties of the pump and the generated supercontinuum. For the pump noise measurement, we coupled the output beam onto a silicon photodiode connected to a fast oscilloscope (DSA91204A from Agilent). After recording 10000 pulses, we obtained the histogram depicted in Fig. 5. Using a Gaussian fit of this distribution, we extract a mean value of 2.5 and a standard deviation of 0.011.

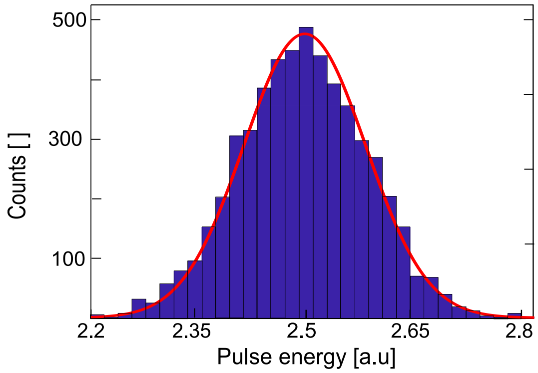

Fig. 5. Histogram of the variation of the energy of 10000 pulses measured with the oscilloscope. The red curve represents a Gaussian fit of the distribution.

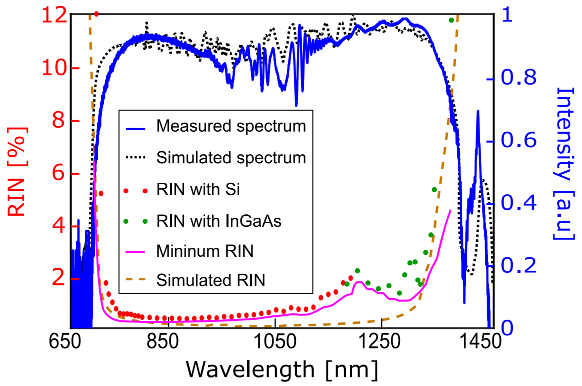

Fig. 6. Measured spectrally-resolved RIN using the oscilloscope method with silicon (red dots) and InGaAs (green dots) photodetector and corresponding average normalized SC spectrum (solid blue), pumping at 45° from the principal axes plus simulated SC (black dots) and RIN spectra (dashed brown). The pink curve shows the estimated minimum RIN values from our measurement system.

Thus, calculating the ratio of the standard deviation to the mean, we obtain a RIN value of 0.44 % using this method, in rather good agreement with the laser manufacturer data (0.5 %).

After measuring the pump laser noise, we further investigated the RIN over the whole SC bandwidth. To this end, we used a monochromator (from Princeton instrument) as a tunable spectral filter and the spectrally-sliced SC was sent to the photodetector and oscilloscope. We specifically used two photodetectors to cover the SC bandwidth: a silicon photodetector from 650 to 1100 nm and an InGaAs photodetector for longer wavelengths. The SC RIN was still measured using the Gaussian fit method by saving 10000 pulses onto an oscilloscope (PicoScope) every 10 nm, with a 3 nm bandwidth for the silicon photodetector and a 1 nm bandwidth for the InGaAs one. Fig. 6 depicts the two spectrally-resolved RIN measurements as red dots (silicon) and as green dots (InGaAs), while the blue curve shows the related SC spectrum while pumping the fiber at 45° off the axes. We find an average RIN from 700 nm to 1100 nm down to 0.54 %, when we omit the high edge RIN values. The results also show that the RIN increases drastically on the SC edges due to both the reduction of the SC power and the strong effect of laser peak power fluctuations on the supercontinuum bandwidth [6]. Furthermore, the pink curve in Fig. 6 depicts the estimated minimum RIN values measured by our system as a function of wavelength. Indeed, our scope has an estimated dark noise standard deviation of 1 mV. Thus, if we divide this number by the mean of our Gaussian distribution, for each spectrally resolved bin, we obtain a minimum estimated spectrally resolved RIN value of 0.14 %. Finally, we observe that our measured spectrally RIN values are all slighty above the estimated minimum.

These experimental measurements have been further compared to numerical simulations of the two-coupled generalized nonlinear Schrödinger equations (CGNLSEs), as those described in Ref. [20] for highly-birefringent PM fibers. We performed SC and RIN simulations solving the CGNLSEs using the split-step method and the initial conditions as described in [6] with an input pulse duration of 180 fs (full width half maximum), an input peak power of 48 kW, an input amplitude noise value of 0.22 % (amplitude noise ≈ RIN/2) and associated anti-correlated pulse duration fluctuations to keep the energy of the mode-locked laser constant. To plot the simulated RIN, we used the following equation with an ensemble size of 50 independent pulses, which is sufficient to minimise modelling error:

$$\mathrm{RIN}(\lambda) = \sqrt{\left\langle \left(|\tilde{A}(\lambda)|^2 - \left\langle |\tilde{A}(\lambda)|^2 \right\rangle \right)^2 \right\rangle} / \left\langle |\tilde{A}(\lambda)|^2 \right\rangle . \quad \mathbf{(1)}$$

The simulation results are shown in Fig. 6 (black dots for the spectrum and dashed brown for the RIN). As can be seen, the agreement is excellent with the experimental spectrum, both for the shape and bandwidth, with a highly modulated spectrum and the generation of an XPMI sideband near 1400 nm. This agreement is also rather good between the measured and simulated RIN.

Ref	$\Delta\lambda_{SC}$	Method	$\Delta\lambda_{RIN}$	$\Delta\lambda_{filter}$	RIN
[5]	620 nm, -10 dB	Osci.	600 nm	10 nm	33 %
[21]	480 nm, -30 dB	Osci.	200 nm	12 nm	1.2 %
[11]	300 nm, -3 dB,	ESA	300 nm		0.07 %
Ours	720 nm, -3 dB	Osci.	400 nm	3 nm	0.54 %

Table 1. Average RIN values in ANDi SC generation from the current literature and our system.

Table 1 compares the noise performances of our SC source to those of the literature [5, 21]. The second column indicates the SC bandwidth. The third one explained the method used to measure the RIN of the SC system, either based on an oscilloscope in the time domain or on an Electric spectrum analyser (ESA) in the frequency domain. The fourth and fifth ones stipulate the measurement and filter bandwidth to obtain the average RIN specified in the last column. Few methods have indeed been implemented to measure the coherence or the RIN of ANDi SC generation [5, 21, 22]. For the coherence, in [22], the authors used a dispersive Fourier transform technique to highlight the stability of ANDi SC generation. Then, using a fiber-based unequal-path Michelson interferometer, they demonstrate a high fringe visibility meaning a high degree of coherence for the ANDi SC generation. Also, in Refs. [5] and [21], the authors used a setup composed of bandpass filters (10/12 nm), a fast photodiode and an oscilloscope to measure the spectrally-resolved RIN of the SC spectrum. In [5], the authors reported an average RIN of 33 %. This value can be considered high but, in this study, the coherence of ANDi SC generation was degraded by the PMI effect. In [21], the authors reported a very low average RIN of 1.2 %, due to the low input peak power used to obtain their ANDI SC and the large bandwidth of their filters.

From Table 1, we see that we obtain the lowest average RIN value using the oscilloscope measurement method. About the value reported by [11], it is not possible to compare directly our RIN value to the 0.07 % announced because they don't use any passband filters and thus measure a single RIN value for the whole SC spectrum. Furthermore, they limit their ESA measurement bandwidth from 10 Hz to 20 MHz while the repetition rate of their laser is up to 80 MHz. Therefore, it reduces the overall RIN value. Finally, we underline the setup composed by the Origami 10 HP laser and the PM-ANDi silica PCF is the system with the lowest average RIN to our knowledge and the highest PER (measured PER of 10 dB in [11]), and thus it can be also considered as one of the state-of-the-art systems.

In conclusion, using a compact ytterbium mode-locked laser producing 180 fs pulses and a highly-nonlinear polarization-maintaining ANDi PCF, we were able to generate an ultra-flat octave-spanning SC spectrum with a bandwidth up to 720 nm (from 670 nm to 1390 nm) and associated PSD higher than 0.4 mW/nm. We have shown that the SC is linearly polarized with a PER of 17 dB across the whole spectrum bandwidth and with a spectrally-resolved RIN below 0.54 % from 700 nm to 1100 nm, which is, to the best of our knowledge, the lowest average SC ANDi RIN value ever reported with this measurement method. This system could find many applications in OCT, metrology, or as a wavelength-tunable fs laser source thanks to its octave-spanning bandwidth, flatness, low-noise, high coherence, polarization and near-linear chirp properties.

Funding. Horizon 2020 Framework Programme (722380); Agence Nationale de la Recherche (ANR) (ANR-15-IDEX-0003, ANR-17-EURE-0002).

Disclosures. The authors declare no conflicts of interest.

REFERENCES

1. T. Hori, J. Takayanagi, N. Nishizawa, and T. Goto, Opt. Express **12**, 317 (2004).
2. L. E. Hooper, P. J. Mosley, A. C. Muir, W. J. Wadsworth, and J. C. Knight, Opt. Express **19**, 4902 (2011).
3. K. Tarnowski, T. Martynkien, P. Mergo, K. Poturaj, A. Anuszkiewicz, P. Béjot, F. Billard, O. Faucher, B. Kibler, and W. Urbanczyk, Opt. Express **25**, 27452 (2017).
4. A. Hartung, A. M. Heidt, and H. Bartelt, Opt. Express **19**, 7742 (2011).
5. I. B. Gonzalo, R. D. Engelsholm, M. P. Sørensen, and O. Bang, Sci. Reports **8**, 6579 (2018).
6. E. Genier, P. Bowen, T. Sylvestre, J. M. Dudley, P. Moselund, and O. Bang, J. Opt. Soc. Am. B **36**, A161 (2019).
7. J. M. Dudley, G. Genty, and S. Coen, Rev. Mod. Phys. **78**, 1135 (2006).
8. C. Finot, B. Kibler, L. Provost, and S. Wabnitz, J. Opt. Soc. Am. B **25**, 1938 (2008).
9. A. M. Heidt, J. S. Feehan, J. H. V. Price, and T. Feurer, J. Opt. Soc. Am. B **34**, 764 (2017).
10. M. Jensen, I. B. Gonzalo, R. D. Engelsholm, M. Maria, N. M. Israelsen, A. Podoleanu, and O. Bang, J. Opt. Soc. Am. B **36**, A154 (2019).
11. A. M. Heidt, J. M. Hodasi, A. Rampur, D.-M. Spangenberg, M. Ryser, M. Klimczak, and T. Feurer, Sci. Reports **10**, 1 (2020).
12. G. Dwapanyin, D. Spangenberg, A. Heidt, T. Feurer, G. Bosman, P. Neethling, and E. Rohwer, J. Opt. Soc. Am. B **37**, A285 (2020).
13. P. Abdolghader, A. F. Pegoraro, N. Y. Joly, A. Ridsdale, R. Lausten, F. Légaré, and A. Stolow, Opt. Express **28**, 35997 (2020).
14. R. Viljoen, P. Neethling, D. Spangenberg, A. Heidt, H.-M. Frey, T. Feurer, and E. Rohwer, J. Opt. Soc. Am. B **37**, A259 (2020).
15. U. Møller and O. Bang, Electron. Lett. **49**, 63 (2013).
16. J. S. Feehan and J. H. Price, J. Opt. Soc. Am. B **37**, 635 (2020).
17. E. Genier, A. N. Ghosh, S. Bobba, P. Bowen, P. M. Moselund, O. Bang, J. M. Dudley, and T. Sylvestre, Opt. Lett. **45**, 3545 (2020).
18. A. Kudlinski, A. Bendahmane, D. Labat, S. Virally, R. Murray, E. Kelleher, and A. Mussot, Opt. Express **21**, 8437 (2013).
19. P.D. Drummond, T.A.B. Kennedy, J.M. Dudley, R. Leonhardt, and J.D. Harvey, Opt. Commun. **78**, 137 (1990).
20. A. N. Ghosh, M. Meneghetti, C. R. Petersen, O. Bang, L. Brilland, S. Venck, J. Troles, J. M. Dudley, and T. Sylvestre, J. Physics: Photonics **1**, 044003 (2019).
21. S. Rao D.S., R. D. Engelsholm, I. B. Gonzalo, B. Zhou, P. Bowen, P. M. Moselund, O. Bang, and M. Bache, Opt. Lett. **44**, 2216 (2019).
22. K. Tarnowski, T. Martynkien, P. Mergo, J. Sotor, and G. Soboń, Sci. Reports **9**, 1 (2019).

école doctorale sciences pour l'ingénieur et microtechniques

Title: Development of a low-noise visible near-infrared fiber-based supercontinuum source

Keywords: Photonic crystal fiber, supercontinuum generation, all-normal dispersion, noise, coherence

Abstract:

This Ph.D thesis focuses on the development of a low-noise visible near-infrared fiber-based supercontinuum source. First, we provide a complete theoretical, numerical and experimental description of coherent supercontinuum generation in a polarization-maintaining all-normal dispersion photonic crystal fibers. Then, exploiting several numerical simulations, we investigate the short available parameter space to obtain an ultra-low-noise supercontinuum source. This parameter space is extremely limited by the technical laser noise such as amplitude noise, phase noise, and pulse duration fluctuations. The limiting factor is mainly the input pulse duration of the laser which can induce the generation of stimulated Raman scattering components for long pulse duration. Through a detailed experimental and numeral analysis of the impact of input polarization on supercontinuum generation, we present, for the first time to our knowledge, the possibility to generate cross-phase modulation instability in an all-normal dispersion polarization-maintaining fiber. Finally, we develop different all-normal dispersion supercontinuum generation systems using commercially available femtosecond seed lasers. Using different noise measurement setups, we demonstrate an ultra-low-noise (RIN<0.54 %) and linearly polarized (PER>17 dB) all-normal dispersion supercontinuum source. Our works represent a fundamental study of low-noise supercontinuum generation in all-normal dispersion fiber and lead to the development of industrial systems for biomedical and metrology applications.

Titre : Development of a low-noise visible near-infrared fiber-based supercontinuum source

Mots-clés : Fibre à cristaux photoniques, génération de spectre supercontinuum, dispersion normale, bruit, cohérence

Résumé :

Cette thèse de doctorat porte sur le développement d'une source supercontinuum fibrée, visible proche-infrarouge et faiblement bruitée. Nous apportons une description complète théorique, numérique, expérimentale de la génération de supercontinuum cohérent dans les fibres à cristaux photoniques à maintien de polarisation et à dispersion normale. En exploitant des simulations numériques, nous démontrons que les conditions pour obtenir une source supercontinuum à faible bruit sont extrêmement restrictives. Cette restriction varie en fonction du bruit technique du laser : bruit d'amplitude, de phase et de durée d'impulsion. De plus, la durée d'impulsion du laser est un paramètre important qui supprime ou accentue la présence de la diffusion Raman stimulée. Grâce à une étude exhaustive de l'impact de la polarisation d'entrée sur la génération de supercontinuum, nous avons démontré, pour la première fois à notre connaissance, la possibilité de générer de l'instabilité modulationnelle vectorielle. De plus, nous présentons divers systèmes de génération de supercontinuum cohérent utilisant des lasers femtosecondes disponibles dans le commerce. Finalement, nous démontrons que certains de nos sytèmes cohérents possèdent un bruit relatif d'intensité extrêmement faible. Ce manuscrit présente donc une étude approfondie de la génération de source supercontinuum faiblement bruitée en régime de dispersion normale et a conduit au développement de plusieurs prototypes utilisables pour de nombreuses applications comme l'imagerie biomédical, la spectroscopie, et la métrologie.

Université Bourgogne Franche-Comté
32, avenue de l'Observatoire
25000 Besançon, France